Nonlinear optics at nanoscale: frequency conversion at interfaces

A thesis submitted by

Laura Rodríguez Suñé

in fulfillment of the requirements of the degree of Doctor in Computational and Applied Physics

Supervisors

Jose Trull and Crina Cojocaru

Department of Physics, "Nonlinear Dynamics, Nonlinear Optics and Lasers (DONLL)"

Universitat Politècnica de Catalunya
June, 2023

Per al Manolo.

Abstract

The use of semiconductors, metals, or ordinary dielectrics in the process of fabrication of nanodevices is at the front edge of nowadays technology. In the last decade an impressive technological progress has been made towards the miniaturization process, giving birth to the field of nanotechnology. Currently, nanostructures are routinely fabricated and integrated in different photonic devices for a variety of purposes and applications. At the nanoscale, light-matter interaction can display new phenomena, different from those occurring in homogeneous materials or even micrometer-scale optical structures and devices. This scenario makes conventional approximations to the dynamics of light-matter interactions to break down and new strategies must be sought in order to study, understand, and ultimately harness the performance of subwavelength nonlinear optical materials. This is the case of nonlinear interactions and in particular, of nonlinear frequency conversion, a fundamental physical process that lies on the basis of many modern disciplines, from bioimaging in nanomedicine to material characterization in material science and nanotechnology. Nonlinear photonics also holds great promise in laser physics with applications in information technology for optical signal processing and in the development of

novel coherent light sources. Thus, a deep understanding of the specific aspects of light-matter interaction at the nanoscale is crucial if one is to properly engineer nanodevices.

In this thesis we report comparative experimental and theoretical studies of nonlinear frequency conversion in different strategic materials for photonics having nanoscale dimensions. We start our study with homogeneous layers and project our results to nanostructures, where second and third harmonic conversion efficiencies drastically decrease compared to typical nonlinear optics working conditions. We have developed novel experimental set-ups capable of measuring second and third harmonic generation efficiencies arising from semicondutors, conductive oxides and metal nanolayers and nanostructures. Our experimental approach allows us to estimate very low conversion efficiencies (down to 10^{-13}), and it is designed to perform an exhaustive study of harmonic generation by analyzing the nonlinear signals as a function of incident angle, wavelength and polarization, important parameters that determine and distinguish the origin of the nonlinear process. At the nanoscale phase matching conditions and even absorption no longer play a primary or significant role, and new linear and nonlinear sources become relevant, including magnetic dipole and electric quadrupole (surface) nonlinearities arising from both free and bound electrons, as well as nonlocal effects, convection, and hot electrons nonlinearities, associated with free electron dynamics, pump depletion, and phase-locking. We perform numerical simulations based on a unique microscopic hydrodynamic model that considers all these contributions to the nonlinear polarization. By comparing experimental results with numerical simulations we are able to identify and distinguish the different mechanisms that trigger the harmonic generated signals at visible and UV wavelengths, while extracting basic physical properties of the material. With this knowledge we are able to make a step forward and predict conversion efficiencies in complex structures which are specifically designed to enhance harmonic generation. The capability to efficiently generate harmonics at the nanoscale will have an enormous impact in the fields of nanomedicine and nanotechnology, since it would allow one to realize much more compact devices and to interrogate matter in extremely confined volumes.

Resum

L 'ús de semiconductors, metalls o dielèctrics en el procés de fabricació de nanodispositius es troba al davant de la tecnologia actual. Durant l'última dècada s'ha fet un impressionant progrés tecnològic cap al procés de miniaturització, donant lloc al camp de la nanotecnologia. Actualment, nanoestructures es fabriquen rutinàriament i s'integren en diferents dispositius fotònics per a una varietat de propòsits i aplicacions. A l'escala nanomètrica, la interacció llum-matèria pot mostrar nous fenòmens, diferents dels que ocorren en materials homogenis o fins i tot en estructures i dispositius òptics micromètrics. En aquest escenari les aproximacions convencionals per descriure la dinàmica de les interaccions llum-matèria deixen de ser aplicables i s'han de buscar noves estratègies per estudiar, entendre i, en última instància, aprofitar el rendiment dels materials òptics no lineals de dimensions més petites que la longitud d'ona. Aquest és el cas de les interaccions no lineals i, en particular, de la conversió de freqüència no lineal, un procés físic fonamental que es troba a la base de moltes disciplines modernes, des de la bioimatge en nanomedicina fins a la caracterització de materials en ciència de materials i nanotecnologia. La fotònica no lineal també te futur potencial en la física del làser amb aplicacions en tecnologia de la informació per al processament de senyals òptics i en el desenvolupament de noves fonts de

llum coherent. Per tant, una comprensió profunda dels aspectes específics de la interacció llum-matèria a l'escala nanomètrica és crucial per tal de dissenyar adequadament nanodispositius.

En aquesta tesi presentem estudis comparatius experimentals i teòrics de conversió de freqüència no lineal en diferents materials estratègics per a la fotònica amb dimensions nanomètriques. Comencem el nostre estudi amb capes homogènies i projectem els nostres resultats a nanoestructures, on les eficiències de conversió de segon i tercer harmònic disminueixen dràsticament en comparació amb les condicions típiques de treball d'òptica no lineal. Hem desenvolupat muntatges experimentals capaços de mesurar eficiències de generació de segon i tercer harmònic que sorgeixen de semiconductors, òxids conductors i metalls. El nostre enfocament experimental ens permet estimar eficiències de conversió molt baixes, i està dissenyat per realitzar un estudi exhaustiu de la generació d'harmònics analitzant les senyals no lineals com a funció de l'angle d'incidència, longitud d'ona i polarització, paràmetres importants que determinen i distingeixen l'origen del procés no lineal. A l'escala nanomètrica, les condicions d'acoplament de fase i fins i tot l'absorció ja no juguen un paper primordial o significatiu, i noves fonts lineals i no lineals esdevenen rellevants, incloent les no linealitats de dipol magnètic i quadrupol elèctric (superfície) que sorgeixen tant dels electrons lliures com dels lligats, així com els efectes no locals, la convecció i les no linealitats dels electrons calents, associats amb la dinàmica dels electrons lliures, i el fenòmen de *phase-locking*. Hem realitzat simulacions numèriques basades en un model hidrodinàmic microscòpic únic que considera totes aquestes contribucions a la polarització no lineal. Comparant els resultats experimentals amb les simulacions numèriques, som capaços d'identificar i distingir els diferents mecanismes que generen les senyals harmòniques generades en longituds d'ona visibles i ultraviolades, mentre extraiem propietats físiques bàsiques del material. Amb aquest coneixement, som capaços de fer un pas endavant i predir les eficiències de conversió en estructures complexes que estan dissenyades específicament per millorar la generació harmònica. La capacitat de generar harmònics eficientment a escala nanomètrica tindrà un enorme impacte en els camps de la nanomedicina i la nanotecnologia, ja que permetria realitzar dispositius molt més compactes.

Agraïments

Moltes persones m'han donat suport i m'han acompanyat d'una manera o una altra durant la realització d'aquesta tesi. Primer de tot m'agradaria agraïr a la Crina Cojocaru i al Jose Trull, els quals m'han donat la oportunitat de treballar al grup de recerca de dinàmica no lineal, òptica no lineal i làsers (DONLL), m'han ensenyat a treballar en un laboratori i m'han guiat i aconsellat per dur a terme aquesta tesi. També al Michael Scalora, qui tot i la distància també m'ha guiat i aconsellat durant aquests anys, i al Kent Hallman per ser tan bon company de treball durant la meva estada a Alabama. Als altres investigadors del grup, al Ramon Vilaseca, al Ramon Herrero, a la Muriel Botey, al Kestas Staliunas, a la Cristina Masoller i al Toni Pons. Als companys de grup, a la Judith, a la primera Maria, al Riccardo, al Giulio, al Jordi, a la Shroddha, al Nayeem, a la Eva, a la segona Maria, al Raul, al Juan i al Guillermo. I especialment al Salim, amb qui vam començar aquest camí a primer de carrera, m'ha ajudat amb el disseny gràfic d'aquesta tesi, i amb qui som veïns, amics i companys de viatge. També m'agradaria donar les gràcies a la meva germana, l'Arrikitiki, a la meva mare, la Carme, i al meu pare, el Manolo, qui em va donar l'empenta inicial per entrar en el mon de la física. També a la Sílvia, a la Judit i al Jordi. M'agradaia donar les gràcies també als amics d'enginyeria física, a la Maria,

a l'Ignasi, al Sergi i a la Natàlia, amb qui després d'anar soles a la recuperació de física 1 ja res podia anar malament. A les companyes del barri perquè son lo mas, a la Mireia, a l'Aina, a l'Ester, a la Sara, al Miquel, al Cristian, al Xavi, i en definitiva, a tothom amb qui he compartit estones a l'ateneu. A la Victòria per fer del pisito una casa i a la Dalilulu per fer-nos companyia. També a la Marta, a la Tesa, a la Clara, a la Lauri i a la Gemma, qui em dona sempre els millors consells de vida. I finalment, al Jose i al Jaume, els quals tot i no visitar-los amb tanta freqüència segueixen sent els millors cambrers de la història.

Preface

Recent years have witnessed and impressive progress in the design and fabrication of structures with nanometric size that are produced and integrated in different devices and applications. At this scale light-matter interaction displays completely new phenomena. Linear and nonlinear nonlocal pressure and viscosity effects, quantum tunneling and screening, propagation of electromagnetic radiation below the absorption limit of certain materials and nonlinear harmonic generation processes are only a few examples. Understanding how light interacts at the nanoscale with metals and semiconductors is pivotal if one is to properly engineer and implement nanoantennas, filters and, more generally, devices that aim to harness the effects of new physical phenomena that manifest themselves at the nanoscale.

Most of the theoretical models that describe light-matter interaction at the nanoscale are based on classical electrodynamics, considering the medium as a continuum where macroscopic fields are averaged over a volume of space containing millions of atoms or dipoles. These approaches do not properly describe the observed effects at nanometric scale since at these dimensions the medium loses this continuity and fluctuating microscopic fields created by atoms and dipoles

have to be taken into account. To properly describe this situation, different models are needed to describe the light-matter interaction at the nanoscale.

For what harmonic generation is concerned, most current theoretical models rely on assigning effective volume and surface second order susceptibilities for second harmonic generation and effective volume third order susceptibilities for third harmonic generation. However, while harmonic generation triggered by surface and magnetic nonlinearities is always present in all materials, they are preemptively neglected in most theoretical descriptions of metasurfaces and other nanometric structures in favor of bulk second order susceptibility without properly assessing their relevance. In addition, typical approaches focus on an instantaneous medium response that lacks a detailed dynamical description of light-matter interactions, that ultimately neglect aspects relating to the microscopic origin of the generated signals, temporal dynamics, the presence of nonlinear dispersion and competing nonlinearities, possible contributions beyond the third order nonlinearity, pump depletion, and frequency down-conversion. At the nanoscale, these phenomena compete and can even overcome the bulk contribution, and thus require special attention.

In this thesis we have performed an experimental study of second and third harmonic generation in different samples with nanoscale dimensions made of strategic materials for nanophotonics. These are semiconductors, metals and conductive oxides. To this end, we have developed experimental set-ups capable of measuring second and third harmonic generation efficiencies arising from different nanolayers and nanostructures. Our experimental approach has allowed us to estimate low conversion efficiency processes and perform an exhaustive study of harmonic generation by analyzing the nonlinear signals as a function of incident angle, wavelength and polarization. The experimental observations have been compared with numerical simulations based on a theoretical model that embraces full-scale, time-domain coupling of matter to the macroscopic Maxwell's equations. Our approach consists in formulating a microscopic, hydrodynamic model in order to understand linear and nonlinear optical properties of metals and semiconductors by accounting for competing surface, magnetic, and bulk nonlinearities arising

from both free and bound electrons. Just as importantly, the model preserves linear and nonlinear material dispersion, nonlocal effects due to pressure and viscosity, and the influence of hot electrons. With this experimental-theoretical comparative investigation, we study the basic properties of simple layers only a few tens of nanometers in thickness in order to ascertain basic physical characteristics that may transfer to more complicated nanostructured geometries. The samples that have been studied consist of a Gallium arsenide (GaAs) wafer, a crystalline silicon wafer, an amorphous silicon nanolayer, crystalline silicon membranes, an Indium tin oxide (ITO) nanolayer, gold nanolayers, and a gold nanograting.

The outline of the thesis is as follows:

Chapter 1 provides an overview of the most relevant aspects of the theoretical background in which this thesis is based. First, we will show how nonlinear optical interactions in bulk materials are described through the nonlinear polarization of the system. Then, we will introduce the concepts of surface and phase-locked second harmonic generation. After that, we will talk about the classical models used to explain optical properties of semiconductors and metals. Then, we will overview the research that has been done on nonlinear optics at the nanoscale. We will talk about harmonic generation in gold, GaAs, silicon and ITO nanostructures. Finally, we will introduce a description of the theoretical approach in which our numerical simulations are based.

In Chapter 2 we report experimental and theoretical results of phase-locked harmonic generation in the opaque region of a GaAs wafer. These harmonic components, which are generated close to the surface, can propagate through an opaque material and correspond to the inhomogeneous solutions of Maxwell's equations with nonlinear polarization sources. We will show that measurements of the angular and polarization dependence of the observed harmonic components allows us to infer the different nonlinear mechanisms that trigger these processes. In order to be able to take the measurements we have developed an experimental set-up capable of measuring the angular and polarization dependence of harmonic signals generated from a GaAs wafer in transmission and in reflection. A description of this experimental set-up will be given at the

beginning of this chapter. We will also introduce an explanation of our calibration procedure to estimate harmonic generation conversion efficiencies. This will be followed by a brief description of the sample. Then, we will explain how the theoretical model explained in Chapter 1 is adapted to the particular case of a semiconductor such as GaAs. Finally, experimental and predicted second and third harmonic generation results will be reported, followed by some concluding remarks.

In Chapter 3 we show results of harmonic generation from different silicon samples in the visible and ultraviolet (UV) ranges of the spectrum, showing that judicious exploitation of the nonlinear dispersion of ordinary semiconductors can provide reasonable nonlinear efficiencies and transformational device physics well into the UV. This chapter is divided in three parts. The first part 3.1 will include a comparison of the nonlinear response of amorphous and crystalline silicon, while the second part 3.2 will introduce results of harmonic generation in crystalline silicon membranes. Using experimental results and simulations we identify basic physical properties of the material with which we can then accurately predict the nonlinear optical properties of complex structures. For this reason, the third part of this chapter 3.3 will present preliminary predicted results of harmonic generation from a nanostructure made of silicon nanowires with the aim of showing that harmonic generation conversion efficiencies can be enhanced in this kind of arrangements. Each of these parts will include a description of the experimental and theoretical approach used to take the measurements and perform the numerical simulations, respectively, a brief description of the samples, and a section including the results that have been obtained. The chapter will end with some conclusions.

In Chapter 4 we analyze second and third harmonic generation from an ITO nanolayer in proximity of its epsilon-near-zero condition, and we demonstrate an enhancement of harmonic generation conversion efficiencies close to this particular point. We investigate the influence of nonlocal effects and hot electrons on the nonlinear response, as well as an induced anisotropy in the material caused by the presence of nonlocal effects. Following the structure of the previous chapters, we will first introduce a description of the experimental approach and of the samples.

Then, we will explain how the theoretical approach explained in Chapter 1 is adapted to the case of conductive oxides and finally, we will show the experimental and predicted results that have been obtained. The conclusions extracted from this study will be introduced at the end of the chapter.

Chapter 5 includes results on the nonlinear optical response of gold. It is divided in two parts. In the first part we will report second and third harmonic generation experimental and theoretical results from gold nanolayers having different thicknesses, and we will discuss the impact of bound and hot electrons in the generated third harmonic conversion efficiencies. In the second part we will demonstrate harmonic generation enhancement from a gold nanograting. We will see that second harmonic generation conversion efficiencies increase more than three orders of magnitude, while a third harmonic generation conversion efficiency enhancement factor of 3200 is obtained. In both parts, the experimental and theoretical approach developed to carry out this study will be specified. The samples will be briefly described and experimental and theoretical results will be introduced at the end of each part. To finish the chapter we will include some concluding remarks.

In Chapter 6 we present a practical, combined experimental and theoretical approach based on our theoretical model that uses experimental results of harmonic generation conversion efficiencies to retrieve complex, nonlinear dispersion curves. We will provide examples of the materials that have been studied in the previous chapters and are of special interest for nanophotonics: silicon, gold, and ITO.

Finally, Chapter 7 presents our conclusions.

In the Appendices, specifications of optical elements used in the experimental set-ups and measurements, and the method of solution implemented to perform the numerical simulations will be included. We will also provide a list of publication and research activities that have been developed during this thesis.

Contents

1
Introduction

1.1 Nonlinear optical interactions in bulk materials

Optics is the field in physics in which the interaction between light and matter is studied. In our everyday experience we can observe linear optical phenomena, such as light being reflected, transmitted and absorbed by a material. This kind of phenomena occurs at low light intensities that normally occur in nature. However, when light intensities increase, nonlinear light-matter interaction becomes relevant.

Nonlinear optics is the study of phenomena that occur as a consequence of the modification of the optical properties of a material system due to the presence of intense light. The intensities needed to observe these effects can be obtained by using the output of a coherent light source such as a laser. The field of nonlinear optics started shortly after the demonstration of the first working laser by Maiman in 1960 [1], with the discovery of second harmonic generation in 1961 [2], and the theoretical work of Bloembergen *et al.* on optical wavemixing in 1962 [3, 4]. Over the following decades, the field of nonlinear optics witnessed enormous growth, leading to the observation of new physical phenomena and giving rise to novel concepts and applications including high-harmonic generation and frequency mixing that can act as new light sources or as amplification schemes, light modulators for controlling the phase or amplitude of a light beam, optical switches, optical logic, optical limiters, and numerous ways of processing the

information content of data images, which created revolutionary change in photonics technology in the 20th century. Almost all those achievements were made on conventional bulk crystals where the phase-mismatch, imposed by material dispersion, limits the efficiency of the nonlinear processes. However, as it will be reviewed in Chapter 1.4, the current research trend in nonlinear optics has moved toward miniaturized optical materials in truly compact optical devices.

Nowadays, second and third harmonic generation are well known nonlinear effects. Efficient second or third harmonic light can be generated in bulk nonlinear crystals such as BBO (Barium borate) and KTP (Potassium titanyl phosphate) crystals under phase-matching conditions. Bulk-generated second harmonic generation is used, for instance, to characterize an ultrashort pulse through autocorrelation measurements [5], and in imaging microscopy [6]. It is also applied in the laser industry to make green 532 nm lasers from a 1064 nm source. One application of third harmonic generation is the generation of ultraviolet (UV) light, and it is also used in microscopy [7].

To describe these processes, Maxwell's equations use the nonlinear polarization of the system. In this section we will describe how light propagates through a nonlinear bulk material and how nonlinear bulk interactions can be described by means of the nonlinear polarization.

1.1.1 Electromagnetic waves propagating through materials

As it is well known, four equations constitute the fundamentals of the electromagnetic wave theory, which are known universally as Maxwell's equations. They provide physical insights about the scattering properties and local field distributions of a system. They can be formulated in differential and integral form. The former will be used in the discussion that follows and can be written as (in MKS units):

$$\nabla \times \mathbf{E} = -\frac{\partial \mathbf{B}}{\partial t} \tag{1.1.1}$$

$$\nabla \times \mathbf{H} = \frac{\partial \mathbf{D}}{\partial t} + \mathbf{J} \tag{1.1.2}$$

$$\nabla \cdot \mathbf{B} = 0 \tag{1.1.3}$$

$$\nabla \cdot \mathbf{D} = \rho \tag{1.1.4}$$

where $\mathbf{E}\,(\mathrm{V/m})$ and $\mathbf{H}\,(\mathrm{A/m})$ are the electric and magnetic fields, respectively, and $\mathbf{D}\,(\mathrm{C/m^2})$ and $\mathbf{B}\,(\mathrm{T})$ correspond to electric displacement and magnetic flux density, respectively. Generally, these variables are time and position dependent and they are created by electric charges and electric currents and thus expressed by the local charge density per unite volume $\rho\,(\mathrm{C/m^3})$ and the current density $\mathbf{J}\,(\mathrm{A/m^2})$. From a macroscopic point of view, Eqs. 1.1.1 and 1.1.2 describe Faraday's law of induction and Ampère's circuital law, respectively, while Eqs. 1.1.3 and 1.1.4 give Gauss' laws for magnetic and electric fields.

The electric field $\mathbf{E}$ and displacement field $\mathbf{D}\,(\mathrm{C/m^2})$, as well as the magnetic field $\mathbf{H}\,(\mathrm{A/m})$ and magnetic flux density $\mathbf{B}$, are related through the constitutive equations. The instantaneous electromagnetic response of a homogeneous dielectric medium at a certain time depends on the fields at that time and the evolutionary progress over a period of past time. So, the constitutive relations involve the time evolutionary variation as:

$$\mathbf{D}(t) = \varepsilon_0\mathbf{E}(t) + \mathbf{P}(t) = \varepsilon_0\mathbf{E}(t) + \varepsilon_0\int_{-\infty}^{t}\chi_e^{(1)}(t-\tau)\mathbf{E}(\tau)d\tau \tag{1.1.5}$$

$$\mathbf{B}(t) = \mu_0\mathbf{H}(t) + \mu_0\mathbf{M}(t) = \mu_0\mathbf{H}(t) + \mu_0\int_{-\infty}^{t}\chi_m^{(1)}(t-\tau)\mathbf{H}(\tau)d\tau \tag{1.1.6}$$

where $\mathbf{P}\,(\mathrm{C/m^2})$ and $\mathbf{M}\,(\mathrm{A/m})$ are the polarization and the induced magnetization within dielectric media, respectively, $\varepsilon_0 \approx 8.85\cdot 10^{-12}\,\mathrm{F/m}$ and $\mu_0 \approx 4\pi\cdot 10^{-7}\,\mathrm{H/m}$ are the electric permittivity and magnetic permeability of free space, respectively, and $\chi_e^{(1)}$ and $\chi_m^{(1)}$ are the linear electric and magnetic susceptibilities, respectively. Expression 1.1.5 is valid in the case of non dispersive (or monochromatic), isotropic, homogeneous and linear interactions. The polarization vector represents the macroscopic electric dipole moment. If we consider a material as a collection of charged particles, they will move when an electric field is applied: positive charges will move in the direction of the field, while negative charges will move the opposite way. Comparing to electrons, the atomic nuclei are very massive, so the electronic motion will dominate the dynamics. In dielectric materials, the charged particles are bound together, although the bonds do have a certain elasticity. Therefore, the motion of the charges is transitory when the field is first applied: they are displaced slightly from their usual positions. This small movement

results in a collection of induced electric-dipole moments. In other words, the effect of the field on a dielectric medium is to induce a polarization.

The relative permittivity and permeability, which are different for each material, are denoted as $\varepsilon_r = 1 + \chi_e^{(1)}$ and $\mu_r = 1 + \chi_m^{(1)}$. In the linear approximation, $\mathbf{P}$ and $\mathbf{E}$ are related through: $\mathbf{P} = \varepsilon_0 \chi_e^{(1)} \mathbf{E}$.

Equations 1.1.5 and 1.1.6 can also be written in the frequency domain as:

$$\mathbf{D}(\omega) = \varepsilon_0(1 + \chi_e^{(1)})\mathbf{E}(\omega) = \varepsilon(\omega)\mathbf{E}(\omega) \tag{1.1.7}$$

$$\mathbf{B}(\omega) = \mu_0(1 + \chi_m^{(1)})\mathbf{H}(\omega) = \mu(\omega)\mathbf{H}(\omega) \tag{1.1.8}$$

$\varepsilon(\omega) = \varepsilon_0\varepsilon_r(\omega)$ and $\mu(\omega) = \mu_0\mu_r(\omega)$ are the absolute permittivity and permeability, respectively. In homogeneous materials, ε and μ are constant values throughout the media, while in inhomogeneous materials, they are position dependent within the material. For anisotropic materials (different depending on directions), ε and μ are in the form of tensors, while for isotropic materials they are denoted as scalars. Also, as general materials are dispersive, both ε and μ depend on the frequency of the electromagnetic field. As a consequence, $\chi_e^{(1)}$ is denoted as scalar in isotropic materials, while in anisotropic materials it is represented as a matrix known as susceptibility tensor, and it also depends on the frequency of the electromagnetic field. In the discussion that follows in the rest of this thesis, we will omit the subindex e when referring to the electric susceptibility $\chi^{(1)}$.

1.1.2 Wave equation for nonlinear optical media

In the previous section we assumed that the polarization $\mathbf{P}$ depends linearly upon the electric field $\mathbf{E}$ through the expression $\mathbf{P} = \varepsilon_0 \chi^{(1)} \mathbf{E}$. For now on, we will consider a nonlinear material so that the polarization vector depends nonlinearly with the electric field. So, we will split $\mathbf{P}$ into its linear and nonlinear parts:

$$\mathbf{P} = \mathbf{P}^{(1)} + \mathbf{P}^{\mathrm{NL}} \tag{1.1.9}$$

Let's now consider a space without free charges and currents, so that $\rho = 0$ and $\mathbf{J} = 0$. Let's also assume that the material is nonmagnetic, so that the induced magnetization $\mathbf{M}$ in Eq.

1.1.6 vanishes. In order to extract the optical wave equation, we take the curl of Eq. 1.1.1 and interchange the order of space and time derivatives. Then, using Eq. 1.1.2 and the constitutive relations we get:

$$\nabla \times \nabla \times \mathbf{E} + \frac{1}{c^2}\frac{\partial^2 \mathbf{E}}{\partial t^2} = -\frac{1}{\varepsilon_0 c^2}\frac{\partial^2 \mathbf{P}}{\partial t^2} \tag{1.1.10}$$

where $1/(\varepsilon_0 c^2) = \mu_0$, and c is the speed of light. Equation 1.1.10 is the most general form of the wave equation in nonlinear optics. However, it can be simplified. Using the identity $\nabla \times \nabla \times \mathbf{E} = \nabla(\nabla \cdot \mathbf{E}) - \nabla^2 \mathbf{E}$ and assuming the slowly varying amplitude approximation so that the term $\nabla(\nabla \cdot \mathbf{E})$ can be neglected [8], Eq. 1.1.10 becomes:

$$\nabla^2 \mathbf{E} - \frac{1}{c^2}\frac{\partial^2}{\partial t^2}\mathbf{E} = \frac{1}{\varepsilon_0 c^2}\frac{\partial^2 \mathbf{P}}{\partial t^2} \tag{1.1.11}$$

Now, writing Eq. 1.1.11 in terms of the linear part of the displacement field $\mathbf{D}^{(1)} = \varepsilon_0 \mathbf{E} + \mathbf{P}^{(1)}$, we get:

$$\nabla^2 \mathbf{E} - \frac{1}{\varepsilon_0 c^2}\frac{\partial^2 \mathbf{D}^{(1)}}{\partial t^2} = \frac{1}{\varepsilon_0 c^2}\frac{\partial^2 \mathbf{P}^{\mathrm{NL}}}{\partial t^2} \tag{1.1.12}$$

In the case of a lossless, dispersionless and isotropic medium, so that $\mathbf{D}^{(1)} = \varepsilon_0 \varepsilon_r \mathbf{E}$ and ε_r is real, frequency independent and a scalar quantity, Eq. 1.1.12 becomes:

$$\nabla^2 \mathbf{E} - \frac{\varepsilon_r}{c^2}\frac{\partial^2 \mathbf{E}}{\partial t^2} = \frac{1}{\varepsilon_0 c^2}\frac{\partial \mathbf{P}^{\mathrm{NL}}}{\partial t^2} \tag{1.1.13}$$

Expression 1.1.13 has the form of an inhomogeneous wave equation. The nonlinear response of the medium, described through $\mathbf{P}^{\mathrm{NL}}$, acts as a source term. In the absence of this source term, Eq. 1.1.13 admits solutions of the form of free waves propagating with velocity c/n, where n is the refractive index of the medium, which satisfies $n^2 = \varepsilon_r$.

For the case of a dispersive medium, each frequency component of the field should be considered separately.

1.1.3 Nonlinear polarization: the electric dipole approximation

In the previous sections, we have seen that $\mathbf{P}^{\mathrm{NL}}$ acts as a source term in the wave equation. We have also seen how $\mathbf{P}$ depends on the strength of the applied field $\mathbf{E}$ in the linear approximation,

i.e., at low light intensities. In nonlinear optics, the optical response can often be described by expressing the polarization $\mathbf{P}$ as a power series of $\mathbf{E}$:

$$P_i = \sum_j \varepsilon_0 \chi_{ij}^{(1)} E_i + \sum_{jk} \varepsilon_0 \chi_{ijk}^{(2)} E_j E_k + \sum_{jkl} \varepsilon_0 \chi_{ijkl}^{(3)} E_j E_k E_l + ... \tag{1.1.14}$$

where $\chi_{ijk}^{(2)}\,(\mathrm{m/V})$ and $\chi_{ijkl}^{(3)}\,(\mathrm{m^2/V^2})$ are components of the second and third order nonlinear susceptibility tensors, respectively, and they are usually complex and frequency-dependent quantities. The indices i, j, k, l vary on the Cartesian components x, y, z. This expression is known as the electric dipole approximation and is valid for describing the nonlinear interactions in bulk materials and under phase-matching conditions [8]. As we will see later in this thesis, this expression will not be an accurate description of the $\mathbf{P}^{\mathrm{NL}}$ when, for instance, the thickness of the nonlinear material is reduced to the atomic scale, as bulk interactions will be minimized. In Eq. 1.1.14 we have assumed that the polarization at time t depends only on the instantaneous value of the electric field strength. This implies, through Kramers-Kronig relation [8], that the medium must be lossless and dispersionless. In Eq. 1.1.14 we have treated the fields as vectors, which makes the susceptibilities $\chi^{(n)}$ tensors of order $n+1$. However, in the discussion that follows, for simplicity, we will assume that the nonlinear material is isotropic, so we will take the fields P and E to be scalar quantities. As a consequence, the susceptibilities will be taken as scalars. We will also assume a dispersionless medium so that they will be independent of frequency. With this, Eq. 1.1.14 can be written as:

$$\begin{aligned} P &= \varepsilon_0(\chi^{(1)}E + \chi^{(2)}E^2 + \chi^{(3)}E^3 + ...) = \\ &= P^{(1)} + P^{(2)} + P^{(3)} + ... = \\ &= P^{(1)} + P^{\mathrm{NL}} \end{aligned} \tag{1.1.15}$$

where $P^{(2)}$ and $P^{(3)}$ are the second and third order nonlinear polarization. As we will see, the physical processes that occur as a result of $P^{(2)}$ tend to be different from those that occur as a result of $P^{(3)}$.

An order of-magnitude estimate can be done to predict the values of $\chi^{(2)}$ and $\chi^{(3)}$ under highly nonresonant conditions [8]: $\chi^{(2)} \sim 10^{-12}\,\mathrm{m/V}$ and $\chi^{(3)} \sim 10^{-24}\,\mathrm{m^2/V^2}$.

1.1.4 Second order nonlinear processes

Second order bulk nonlinear interactions occur in non-centrosymmetric crystals, i.e., crystals that do not display inversion symmetry. In centrosymmetric materials, such as liquids, gases, amorphous solids (such as glass), and even many crystals, $\chi^{(2)}$ vanishes. However, a number of second order bulk nonlinear interactions can be produced by non-centrosymmetric crystals. We will now discuss briefly some of them.

Let's consider an optical field having two frequency components that is incident upon a $\chi^{(2)}$ material. We can represent it in the form:

$$E_{in} = E_1 e^{-i\omega_1 t} + E_2 e^{-i\omega_2 t} + c.c. \tag{1.1.16}$$

where E_1 and E_2 are field amplitudes and ω_1 and ω_2 the carrier frequencies. The second order contribution to the nonlinear polarization will be:

$$\begin{aligned} P^{(2)} &= \varepsilon_0 \chi^{(2)} E_{in}^2 \\ &= \varepsilon_0 \chi^{(2)} (E_1^2 e^{-2i\omega_1 t} + E_2^2 e^{-2i\omega_2 t} + 2E_1 E_2 e^{-i(\omega_1+\omega_2)t} \\ &+ 2E_1 E_2^* e^{-i(\omega_1-\omega_2)t} + c.c.) + 2\varepsilon_0 \chi^{(2)} (E_1 E_1^* + E_2 E_2^*) \end{aligned} \tag{1.1.17}$$

As it can be seen, $P^{(2)}$ has developed new frequency components not present in the incident field. Representing the second order nonlinear polarization as:

$$P^{(2)} = \sum_n P_{\omega_n} e^{-i\omega_n t} \tag{1.1.18}$$

we can write the amplitudes of the new frequency components of the nonlinear polarization as:

$$\begin{aligned} P_{2\omega_1} &= \varepsilon_0 \chi^{(2)} E_1^2 \quad \text{SHG} \\ P_{2\omega_2} &= \varepsilon_0 \chi^{(2)} E_2^2 \quad \text{SHG} \\ P_{\omega_1+\omega_2} &= 2\varepsilon_0 \chi^{(2)} E_1 E_2 \quad \text{SFG} \\ P_{\omega_1-\omega_2} &= 2\varepsilon_0 \chi^{(2)} E_1 E_2^* \quad \text{DFG} \\ P_0 &= 2\varepsilon_0 \chi^{(2)} (E_1 E_1^* + E_2 E_2^*) \quad \text{OR} \end{aligned} \tag{1.1.19}$$

Four different nonzero frequency components are generated through second harmonic generation (SHG), sum frequency generation (SFG) and difference frequency generation (DFG). OR states

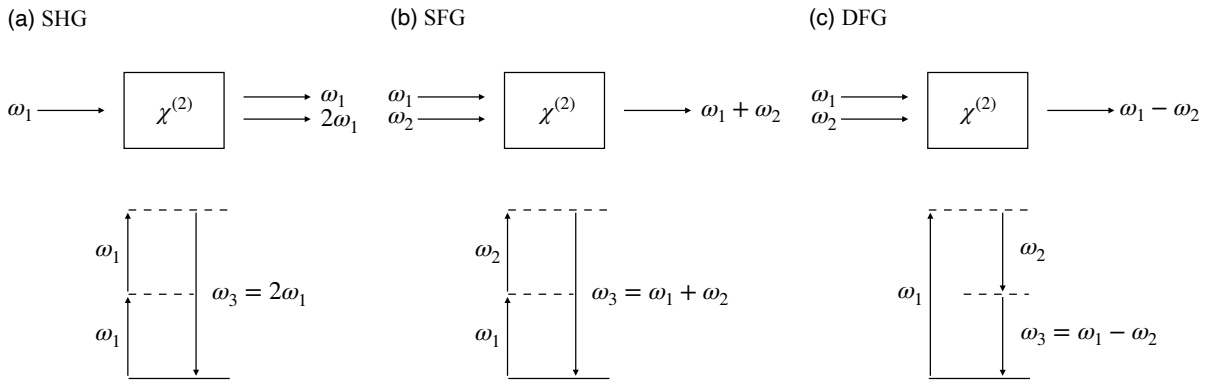

Figure 1.1.1: Geometry representation (top) and energy level diagram (bottom) describing (a) second harmonic generation (SHG), (b) sum frequency generation (SFG), and (c) difference frequency generation (DFG).

for optical rectification, a process in which a static electric field is created across the nonlinear crystal. In Fig. 1.1.1 we show the geometry representation and the energy level description of the different nonlinear processes. For instance, in SHG, two photons at frequency ω_1 are combined and generate a new photon with twice the frequency of the initial photons.

Typically, no more than one of these processes will occur simultaneously, at least with any appreciable intensity. This is due to the fact that the nonlinear polarization can efficiently produce an output signal only if a certain phase-matching condition is satisfied, and usually this condition cannot be satisfied for more than one frequency component of the nonlinear polarization. In other words, some phase-mismatch should be close to zero in order to obtain an efficient nonlinear interaction. The conversion efficiency of the process can be defined as $\eta_{SHG} = I_{2\omega}/I_{\omega}$, were I_{ω} and $I_{2\omega}$ are the intensities of the fundamental and the generated second harmonic (SH) fields, respectively. For SHG, the phase-mismatch factor is given by $\Delta\mathbf{k} = \mathbf{k}_{2\omega} - 2\mathbf{k}_{\omega}$, where $\mathbf{k}_{\omega}$ and $\mathbf{k}_{2\omega}$ are the wavevectors of the fundamental and SH beam, respectively. Perfect phase-matching is achieved when $\Delta\mathbf{k} = 0$, a condition that requires both fundamental and SH fields to have the same phase velocity. So, phase-matching is a condition that essentially requires conservation of linear momentum that allows continuous energy flow from the pump to the SH, generating high efficiency signals. However, this is a condition that

does not generally occur naturally, and so the literature abounds with contributions that contain techniques and stratagems attempting to circumvent a naturally occurring phase-mismatch, in order to bring the interacting waves closer to ideal, phase-matched conditions [9–13].

In Fig. 1.1.2 we have plotted with a solid curve the normalized SHG efficiency (η_{SHG}) as a function of material thickness L when perfect phase-matching ($\Delta\mathbf{k} = 0$) exists. In this case, the efficiency of the nonlinear process grows exponentially with the thickness of the nonlinear material. However, when the fundamental and SH beams start to mismatch ($\Delta\mathbf{k} \neq 0$), this dependence is lost and the process becomes more inefficient. This situation is depicted with dashed curves in Fig. 1.1.2, for different mismatched scenarios.

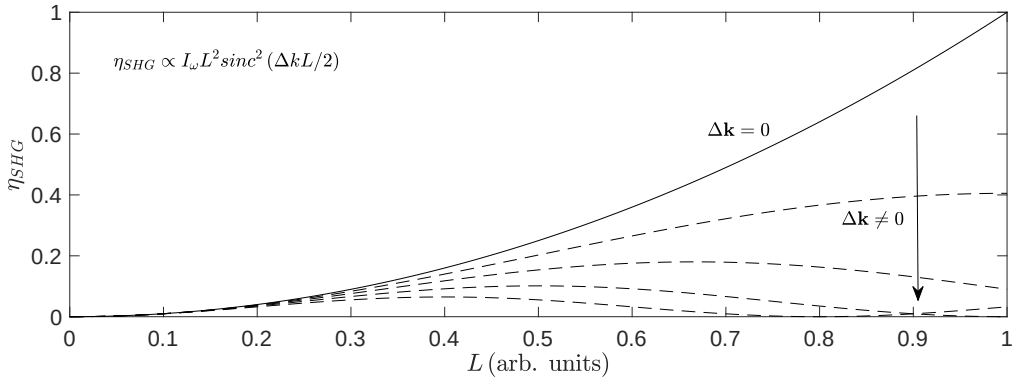

Figure 1.1.2: Normalized SHG efficiency as a function of material thickness when there exists perfect phase-matching between the fundamental and SH beams (solid curves), and when a certain phase-mismatch start to appear (dashed curves).

Generally, it is necessary to account for the vector nature of the fields, which is the case when an anisotropic material is assumed. Consequently, the second order nonlinear susceptibility becomes a tensor of order 3 that couples the different components of the field and polarization. Usually, it is practical to introduce the tensor:

$$d_{ijk} = \frac{1}{2}\chi^{(2)}_{ijk} \tag{1.1.20}$$

This notation is only used when Kleinman's symmetry condition is valid: whenever dispersion of the susceptibility can be neglected [8]. Assuming the interaction of three waves of frequencies

ω_1, ω_2, and $\omega_3 = \omega_1 + \omega_2$, the second order nonlinear polarization can be written as:

$$P_{i,\omega_n+\omega_m} = \varepsilon_0 \sum_{jk} \sum_{(nm)} \chi^{(2)}_{ijk} E_{j,\omega_n} E_{k,\omega_m} = 2\varepsilon_0 \sum_{jk} \sum_{(nm)} d_{ijk} E_{j,\omega_n} E_{k,\omega_m} \tag{1.1.21}$$

where $E_{j,k,\omega_{n,m}}$ are field amplitudes ($\mathbf{E} = \sum_n \mathbf{E}_{\omega_n} e^{-i\omega_n t}$), the indices i, j, k refer to Cartesian components of the field, and the indices n and m refer to the frequencies. The notation (nm) indicates that, in performing the summation over n and m, the sum $\omega_n + \omega_m$ is to be held fixed, although ω_n and ω_m are each allowed to vary.

If we assume that d_{ijk} is symmetric in its last two indices, which is valid whenever Kleinman's symmetry condition is valid, the notation can be simplified using a contracted matrix d_{il}. With this, we can describe the nonlinear polarization leading to SHG in terms of d_{il} by the matrix equation:

$$\begin{pmatrix} P_{x,2\omega} \\ P_{y,2\omega} \\ P_{z,2\omega} \end{pmatrix} = 2\varepsilon_0 \begin{pmatrix} d_{11} & d_{12} & d_{13} & d_{14} & d_{15} & d_{16} \\ d_{21} & d_{22} & d_{23} & d_{24} & d_{25} & d_{26} \\ d_{31} & d_{32} & d_{33} & d_{34} & d_{35} & d_{36} \end{pmatrix} \begin{pmatrix} E^2_{x,\omega} \\ E^2_{y,\omega} \\ E^2_{z,\omega} \\ 2E_{y,\omega}E_{z,\omega} \\ 2E_{x,\omega}E_{z,\omega} \\ 2E_{x,\omega}E_{y,\omega} \end{pmatrix} \tag{1.1.22}$$

If now Kleinman's symmetry condition is introduced explicitly (all the indices d_{ijk} can be freely permuted) we find that d_{il} has only 10 independent elements. Moreover, this number can be reduced depending on the crystalline symmetry of the nonlinear material. For instance, for (001) Gallium arsenide (GaAs) the d_{il} tensor is given by:

$$d_{il} = \begin{pmatrix} 0 & 0 & 0 & d_{14} & 0 & 0 \\ 0 & 0 & 0 & 0 & d_{14} & 0 \\ 0 & 0 & 0 & 0 & 0 & d_{14} \end{pmatrix} \tag{1.1.23}$$

In some cases, once the nonlinear interaction is known, it can be represented in terms of a single effective nonlinear coefficient d_{eff} [8].

1.1.5 Third order nonlinear processes

In the case of third order nonlinear interactions, a study similar to that performed in the previous section can be done to analyse the different frequency components that would be generated due to the third order contribution to the nonlinear polarization $P^{(3)}$. However, as now it is a four-wave mixing problem, and so it can be quite extensive, we will limit the discussion to the case of

a monochromatic applied field $E = 2E_1 cos(\omega t)$. The third order contribution to the nonlinear polarization will be:

$$P^{(3)} = \varepsilon_0 \chi^{(3)} (2E_1 cos(\omega t))^3 = \\ = \frac{1}{2}\varepsilon_0 \chi^{(3)} E_1^3 cos(3\omega t) + \frac{3}{2}\varepsilon_0 \chi^{(3)} E_1^3 cos(\omega t) \tag{1.1.24}$$

The first term in Eq. 1.1.24 describes a response at frequency 3ω that is generated by an applied field at frequency ω, which is called third harmonic generation (THG). In Fig. 1.1.3 we show the geometry representation (a) and the energy level diagram (b) of this third order nonlinear process. The third harmonic (TH) frequency can be obtained directly due to the cubic nonlinearity of the material, as exemplified by Eq. 1.1.24, and/or due to the combination of fundamental and SH beams still via the quadratic nonlinearity, which is called cascaded THG. In the first case three photons of the fundamental field annihilate to create directly a TH photon ($\omega + \omega + \omega \rightarrow 3\omega$), as shown in Fig. 1.1.3. In the second case a two-step process occurs: first two photons of the fundamental field annihilate to create a SH photon ($\omega + \omega \rightarrow 2\omega$) and then one photon from the fundamental field and one photon from the SH field combine to create a TH photon ($\omega + 2\omega \rightarrow 3\omega$).

Apart from THG, there are other third order nonlinear effects. For instance, the second term in Eq. 1.1.24 describes a nonlinear contribution to the polarization at the frequency of the incident field, so this term leads to a nonlinear contribution to the refractive index experienced by a wave at frequency ω. In the presence of this type of nonlinearity the refractive index is intensity-dependent. This is called the optical Kerr effect.

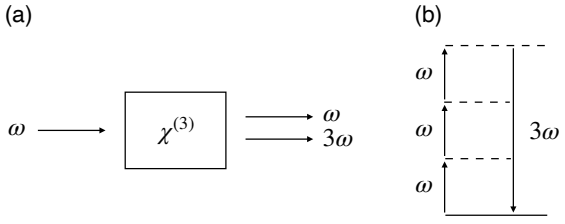

Figure 1.1.3: (a) Geometry representation and (b) energy level diagram describing third harmonic generation (THG).

1.2 Surface and phase-locked harmonic generation

The first observation of SHG [2] belonged to a mismatched bulk second order nonlinear optical process which, in general, is observed in the volume of non-centrosymmetric nonlinear media. In fact, SHG has been widely studied in thick nonlinear materials with high nonlinearities, low material absorption and phase-matching conditions, in order to achieve high conversion efficiencies. However, later it was shown that SHG can be observed at an interface between two centrosymmetric media with different material properties [14–16]. The reason of this is that the symmetry is broken in the vicinity of this interface. Put it another way, the surface of a material lacks inversion symmetry and so the nonlinear polarization generates a SH field, even though the material is centrosymmetric. This is known as surface SHG. This process was investigated for the first time assuming non-centrosymmetric media by Bloembergen *et al.* in [4], where they outlined that energy transfer between the fundamental and its generated harmonic, far from phase-matching conditions, always happens near the interface. The expression "near the interface" makes reference to the walk-off distance, i.e., the distance until the harmonic pulse is no longer under the spatial influence of the fundamental pulse due to differences in group velocities. The more mismatch between fundamental and harmonic beams, the faster walk off is observed. This work was successfully experimentally verified in [17], where measurements of SHG from a $NaClO_3$ (Sodium hypochlorite) crystal were reported, which agreed well with Bloembergen's theory.

As it was explained in Section 1.1.3, in the electric dipole approximation, when the nonlinear material is centrosymmetric, second order bulk nonlinearities are forbidden as $\chi^{(2)}$ vanishes. So, one would expect that in this case, only surface-generated SHG would take place. However, volume SHG is not completely prohibited in centrosymmetric media if magnetic dipole and electric quadrupole contributions exist. This was first pointed out in [18]. Later, in [19], it was shown that the quadrupole source term was equivalent to a nonlinear surface contribution. It is well known now that the nonlinear polarization of a medium can be written according to a well-established order where the electric dipole contribution is much larger than the combination

of electric quadrupole and magnetic dipole, which in turn is much larger than the combination of electric octupole and magnetic quadrupole, and so on. Using this classification, Eq. 1.1.14 can be modified and written as:

$$\begin{aligned} P_i = \sum_j \varepsilon_0 \chi_{ij}^{(1)} E_i + \sum_{jk} \varepsilon_0 \chi_{ijk}^{(2),ed} E_j E_k + \sum_{jkl} \varepsilon_0 \chi_{ijkl}^{(3),ed} E_j E_k E_l + \\ + \sum_{jk} \frac{1}{c} \chi_{ijk}^{(2),md} E_j H_j + \sum_{jkl} \varepsilon_0 \chi_{ijkl}^{(2),eq} E_j \nabla_k E_l + ... \end{aligned} \tag{1.2.1}$$

where i, j, k, l are Cartesian coordinates, $\chi_{ijk}^{(2),ed}$ and $\chi_{ijkl}^{(3),ed}$ are the tensor components of second and third order nonlinear coefficients, the superscripts *ed*, *md*, *eq* stand for electric dipole, magnetic dipole, and electric quadrupole, respectively, and E_{ijk} and H_{ijk} are the Cartesian components of the electric and magnetic fields.

The primary reason to investigate SHG has consistently been the achievement of efficient frequency doubling. Thus, the emphasis has been on phase-matched interactions between the fundamental and SH beams, and relatively few studies of SHG under phase-mismatch conditions have been done. In this case, researchers have been confronted with situations where, in addition to the usual SH beam, a second component is observed. This was first revealed by J. A. Armstrong *et al.* [3] and N. Bloembergen *et al.* [4] in 1962, where they studied the creation of SH waves when a monochromatic plane wave at frequency ω was incident on a plane boundary of a crystal that lacked inversion symmetry. With the wave equation at the SH frequency:

$$\nabla \times \nabla \times \mathbf{E}(2\omega) + \frac{\varepsilon(2\omega)}{c} \frac{\partial^2 \mathbf{E}(2\omega)}{\partial t^2} = -\frac{4\pi}{c^2} \frac{\mathbf{P}^{\mathrm{NLS}}(2\omega)}{\partial t^2} \tag{1.2.2}$$

they found that the general solution consisted of the solution of the homogeneous equation plus one particular solution of the inhomogeneous equation:

$$\begin{aligned} \mathbf{E}^{\mathrm{T}}(2\omega) = \mathbf{e}_{\mathrm{T}} \mathcal{E}^{\mathrm{T}}(2\omega) e^{i(\mathbf{k}^{\mathrm{T}}(2\omega)\cdot\mathbf{r} - 2\omega t)} \\ - \frac{4\pi P^{\mathrm{NLS}}(2\omega)(4\omega^2/c^2)}{(k^{\mathrm{T}}(2\omega))^2 - (k^{\mathrm{S}}(2\omega))^2} \left(\mathbf{p} - \frac{\mathbf{k}^{\mathrm{S}}(2\omega)(\mathbf{k}^{\mathrm{S}}(2\omega)\cdot\mathbf{p})}{(k^{\mathrm{T}}(\omega))^2} \right) e^{i(\mathbf{k}^{\mathrm{S}}(2\omega)\cdot\mathbf{r} - 2\omega t)} \end{aligned} \tag{1.2.3}$$

for the transmitted electric field $\mathbf{E}^{\mathrm{T}}(2\omega)$, and

$$\mathbf{E}^{\mathrm{R}}(2\omega) = \mathbf{e}_{\mathrm{R}} \mathcal{E}^{\mathrm{R}}(2\omega) e^{i(\mathbf{k}^{\mathrm{R}}(2\omega)\cdot\mathbf{r} - 2i\omega t)} \tag{1.2.4}$$

for the reflected electric field $\mathbf{E}^{\mathrm{R}}(2\omega)$. Similar equations were obtained for the magnetic field and can be found in [4]. In Eqs. 1.2.3 and 1.2.4, $\mathbf{e}_{\mathrm{T}}$ and $\mathbf{e}_{\mathrm{R}}$ are the polarization vectors, $\mathcal{E}^{\mathrm{T}}(2\omega)$ and $\mathcal{E}^{\mathrm{R}}(2\omega)$ are the transmitted and reflected amplitudes of the SH field, $\mathbf{k}^{\mathrm{T}}(2\omega)$ is the wavevector of the transmitted homogeneous SH wave, $\mathbf{k}^{\mathrm{S}}(2\omega) = 2\mathbf{k}^{\mathrm{T}}(\omega)$ is the wavevector of the transmitted inhomogeneous SH wave where $\mathbf{k}^{\mathrm{T}}(\omega)$ is the wavevector of the incident wave, and $\mathbf{k}^{\mathrm{R}}(2\omega)$ is the wavevector of the reflected SH wave. In Eqs. 1.2.3 and 1.2.4 it can be seen that the general solution for SHG from a boundary layer displays a reflected signal, and two forward propagating components, one displaying a k-vector that is a solution of the homogeneous wave equation, i.e., the expected wave vector at the SH frequency, and the other k-vector that is the solution of the inhomogeneous wave equation, equal to twice the pump's wave vector. This fact is also illustrated in Fig. 1.2.1, which is extracted from [4]. As it can be seen, the reflected SH goes in the same direction as the reflected fundamental wave, as vacuum does not have dispersion. However, in the transmitted case, while the inhomogeneous source wave $\mathbf{k}^{\mathrm{S}}(2\omega)$ goes in the same direction as the transmitted fundamental $\mathbf{k}^{\mathrm{T}}(\omega)$, the homogeneous transmitted harmonic $\mathbf{k}^{\mathrm{T}}(2\omega)$ will in general go in a different direction due to material dispersion. In the case of exact

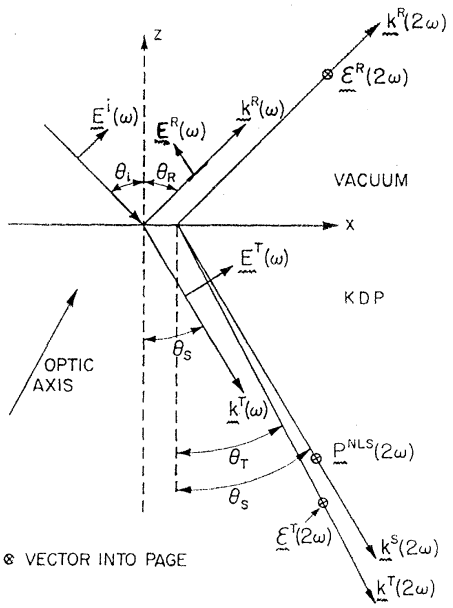

Figure 1.2.1: Incident, reflected and refracted rays at the fundamental and SH frequencies near the boundary between vacuum and a nonlinear crystal [4].

phase-matching ($\Delta\mathbf{k} = 0$), the two rays will be parallel.

More research on this phenomenon followed the next years. In 1969, in a mathematical treatment, Glenn [20] provided a general solution of the SH field that also showed two contributions, one arising as a surface term, traveling with the characteristic group velocity expected at the SH frequency, and a second component that instead appeared to travel with the group velocity of the fundamental beam. In 1987, it was theoretically shown in [21] that, in the weak conversion efficiency regime and in the presence of group velocity dispersion, the SH signal was characterized by a double-peaked structure. Then in 1990, Noordam *et al.* [22] reported that under conditions of a phase and group velocity mismatch, the SH signal indeed displayed two prominent features. This was the first experimental observation of the phenomenon, which, in the years that followed was again reported theoretically and experimentally. In 2006 [23] additional theoretical and experimental evidence that a purely second order process could lead to a double peaked structure in the time domain profile of the SH beam was introduced. The effect was attributed to induced group velocity dispersion, under conditions of negligible group velocity mismatch. They argued that, as the pump and SH beams co-propagate, the pump is able to impress its dispersive properties on the SH pulse. Also, in [24], the double peaked structure in the SH signal was discussed theoretically in the context of femtosecond pulse propagation in a birefrigent nonlinear material, under phase-mismatched conditions. Their results suggested that the SH signal splits into two components, one that travels at the pump's group velocity, and a second component that walks off, consistent with all previous predictions and observations of the phenomenon. We could say that what we have learnt from these studies is the following: when a pump pulse crosses an interface between a linear and a nonlinear medium there will be always three distinguishable SH components. One component is generated backward (reflection) into the linear medium; the other two components are generated forward. These forward-propagating components arise from the homogeneous and inhomogeneous solutions of the wave equation at the SH frequency. For example, in the absence of absorption, the homogeneous component

travels with the group velocity given by material dispersion:

$$k_{2\omega}^{\mathrm{HOM}} = k_{0,2\omega} n_{2\omega} \tag{1.2.5}$$

where $k_{0,2\omega} = 2\omega/c$ is the wavenumber expression for the SH in vacuum; while the inhomogeneous component is captured by the pump pulse and experiences its same effective dispersion:

$$k_{2\omega}^{\mathrm{INH}} = 2k_{0,\omega} n_{\omega} \tag{1.2.6}$$

where $k_{0,\omega} = \omega/c$ is the wavenumber of the fundamental field in vacuum. In this case it is said that the SH pulse is *phase-locked*. We remark that, in order to better distinguish both the homogeneous and the phase-locked components, it is important to work far from phase-matching conditions and use very short pulses. For instance, femtosecond pulses propagating in millimeters long sample. This way, the fundamental and SH pulses will have enough time to walk off. This situation is schematically shown in Fig. 1.2.2, where the propagation of a pump Gaussian ultrashort pulse into a nonlinear material is depicted. The SH signal is characterized by a reflected pulse and two forward-propagating pulses, one traveling at the normal group velocity, which walks off and lags behind the other phase-locked, and located under the pump, and traveling at the pump's group velocity.

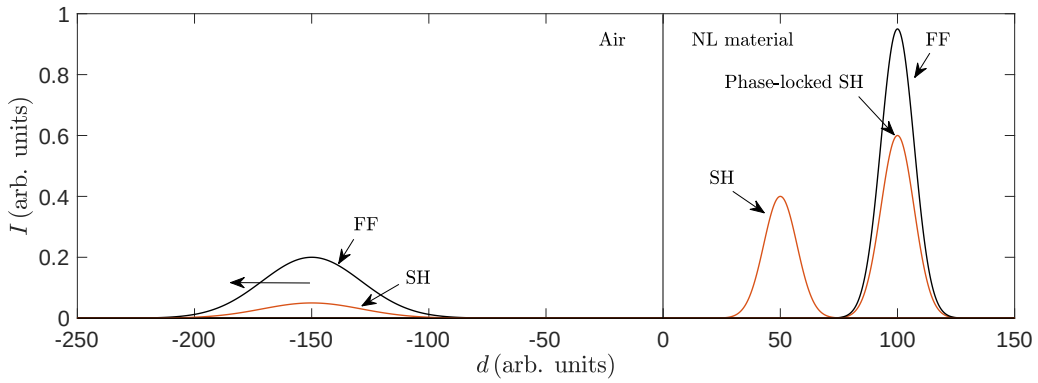

Figure 1.2.2: A Gaussian pump pulse (black) propagates into a nonlinear material. The SH signal (red) is characterized by a reflected pulse and two forward-propagating pulses, one traveling at the normal group velocity, which walks off and lags behind the other phase-locked, and located under the pump, and traveling at the pump's group velocity.

After the above mentioned studies, V. Roppo *et al.* reported in 2007 [25] a theoretical study of the phase-locking mechanism in negative index media. They found that the phase-locking phenomenon caused the forward moving, phase-locked SH pulse to experience the same negative index as the pump pulse, even though the index of refraction at the SH wavelength was positive. They also found that the phase-locking mechanism characterizes not only SHG, but also $\chi^{(3)}$ processes, as shown previously in [26] where the phase-locking mechanism was first discussed in the context of intense field propagation and filamentation in the atmosphere.

To practically appreciate this double nature of the SH, a way to separate the two components in time or in space is needed. In 2009 it was reported in [27] an experimental verification of the phenomenon. A fundamental field tuned at 800 nm was incident to a $LiNbO_3$ (Lithium niobate) crystal, which was transparent for both fundamental and SH wavelengths. The exit interface of the crystal was cut 20° respect to the orientation of the entry interface. In Fig. 1.2.3 we show the simulated and experimental results reported in [27], as well as the experimental set-up used to measure the SH signals. In the experiment, the fundamental beam impinged normally to the entry of the interface of the crystal and then it was refracted at a certain angle at the

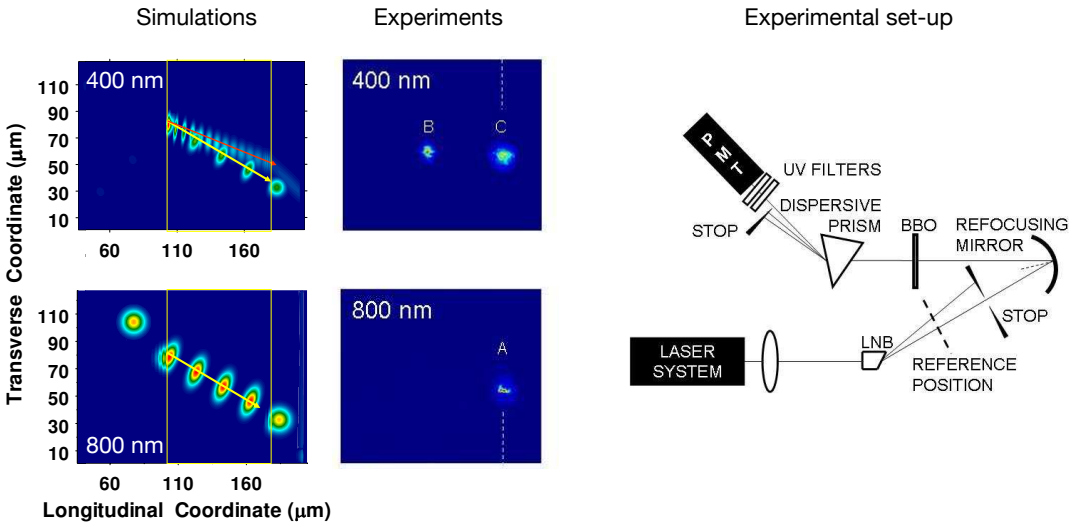

Figure 1.2.3: Results on SHG in a $LiNbO_3$ crystal reported in [27]. Numerical simulations (left), experimental results (center) and experimental set-up (right).

exit accordingly to Snell's law corresponding to n_ω. The generated SH was decomposed and recorded in two spots: one refracted accordingly to Snell's law at $n_{2\omega}$ and the other followed the fundamental beam direction. With this, they concluded that the SH "read" the index of refraction imposed by the dispersion value $n_{2\omega}$, but the inhomogeneous SH component "read" the same refractive index as the fundamental beam.

A more intriguing situation arises when the fundamental beam is tuned in the transparency range of the material, while the harmonic wavelengths fall well below the absorption edge. Based on the nature of the inhomogeneous solution, which travels with the phase and group velocities of the fundamental wave, one may then expect from the Kramers-Kronig relations that the imaginary part of the refractive index experienced by the phase-locked harmonic component should match that of the fundamental. This conclusion leads to the counter-intuitive hypothesis that the phase-locked harmonic component should be able to propagate inside the material regardless of material dispersion and absorption at the harmonic wavelengths in the opaque region of the spectrum, as long as the pump is at least partially transmitted. In [28] it was experimentally reported for the first time the inhibition of linear absorption for phase and group velocity mismatched SHG and THG in GaAs, at frequencies above the absorption edge. A 100 fs pump pulse tuned to 1300 nm generated 650 nm and 435 nm SH and TH pulses, respectively, that propagated across a 450 μm-thick GaAs substrate without being absorbed. This was attributed to a phase-locking mechanism that causes the pump to trap the harmonics and to impress on them its dispersive properties. Later, it was shown in [29] that the phase-locked SH component generated in opaque materials can be significantly amplified by three orders of magnitude in a GaAs cavity that displays a resonance only at the fundamental wavelength. Later, in 2011, V. Roppo *et al.* also reported in [30] the generation of a TH field tuned at 223 nm from a GaP (Gallium phosphide) substrate 500 μm-thick. The results showed that a phase-locking mechanism that triggers transparency at the harmonic wavelengths persists regardless of the dispersive properties of the medium, and that the fields propagate hundreds of microns without being absorbed even when the harmonics are tuned to portions of the spectrum that display

metallic behavior. During this thesis, we have continued the study of phase-locked harmonic generation in an opaque material and the results will be shown in Chapters 2 and 3 for the case of a GaAs wafer and different silicon samples.

1.3 Optical properties of semiconductors and metals

Nowadays, metals and semiconductors are usually embedded in nanostructures which are routinely fabricated and integrated in different photonic devices for a variety of purposes and applications. The optical response of metals and semiconductors is different. In this section we will describe it following the theoretical models for free and bound (valence) electrons.

1.3.1 Free electrons and interband transitions

In the band theory of solids there are conduction electrons and interband transition (or bound) electrons. Conduction electrons are freely to move within bulk metals, while interband transition electrons can only be induced by incident photons having energy greater than the bandgap energy. Both of them can determine the complex dielectric function of the material, which describes its optical properties.

Conduction electrons are associated principally with free carriers within metal media, and they are described by the Drude model. Interband transitions consist of electrons jumping from the energy band below the Fermi level (valence band) to the conduction band when being excited by photons with enough energy. This interband transitions often occur in the light-matter interaction at the visible or infrared (IR) wavelengths, and they can be described as an harmonic oscillator through the Lorentz model.

Materials can be divided depending on their band structure. For an insulator, a large energy gap exists between the valence and the conduction band. Semiconductor materials have a similar band structure, but their bandgap is much smaller, so lower energy photons will be able to excite electrons from the valence to the conduction band. The energy gap depends on the semiconductor and it can be temperature dependent. In the case of metals, the energy bands overlap each other. The overlap of valence bands and free conduction bands enables electrons

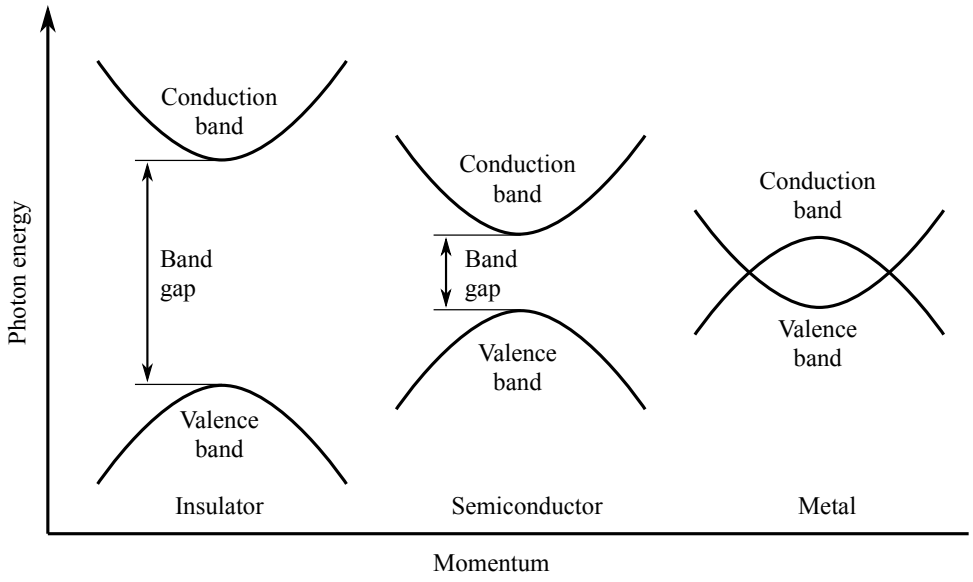

Figure 1.3.1: (a) Geometry representation and (b) energy level diagram describing third harmonic generation

to move freely across the bands. In semiconductors, like GaAs, free carrier doping ranges from $10^{14}\,\mathrm{cm}^{-3}$ to $10^{17}\,\mathrm{cm}^{-3}$, so they can be neglected in the description of their dielectric function. Typical free carrier densities in metals are much higher, of the order $10^{22}\,\mathrm{cm}^{-3}$. So, the optical properties in semiconductors are described by the Lorentz model, while the Drude (or a combined Drude-Lorentz) model is used to describe the dielectric function of metals.

1.3.2 Classical harmonic oscillator: Lorentz model

The Lorentz model treats the atom as an harmonic oscillator, and it is known to provide a good description of the linear optical properties of nonmetallic solids. This model describes a point electron that is bound to a nucleus as though by a spring, as depicted in Fig. 1.3.2. The electron is under the action of a linear restoring force, which can be written as $\mathbf{F}^{\mathrm{L}}_{\mathrm{Restoring}} = -m\omega_0^2\mathbf{r}$, were m is the mass of the electron, ω_0 is the resonance frequency of the oscillation, and $\mathbf{r}$ determines the position of the electron. However, the model can be extended by adding a nonlinearity in the restoring force, which will be discussed later.

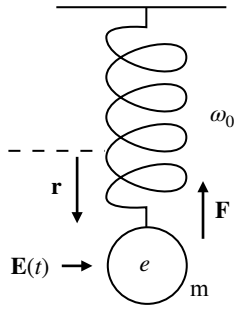

Figure 1.3.2: Schematic representation of the Lorentz model of the atom, consisting of an electron bound to the atom by a spring that provides a restoring force.

The equation of motion of a bound electron in the presence of an applied electromagnetic field can be expressed as:

$$\ddot{\mathbf{r}} + \gamma\dot{\mathbf{r}} + \omega_0^2\mathbf{r} = \frac{e}{m}\left(\mathbf{E} + \dot{\mathbf{r}} \times \mathbf{B}\right) \tag{1.3.1}$$

The right hand side of Eq. 1.3.1 contains the Lorentz force, where $\mathbf{E}$ and $\mathbf{B}$ are the applied electric and magnetic fields, respectively. In the left hand side of Eq. 1.3.1 there is a damping force of the form $-m\gamma\dot{\mathbf{r}}$, where γ is the damping coefficient, as well as a linear restoring force, where ω_0 is the resonant frequency. The damping coefficient γ is introduced in the model to explain absorption.

We now wish to connect the microscopic dynamics of the electron driven by Eq. 1.3.1 to a macroscopic dynamical equation. This connection is done through the polarization $\mathbf{P}$ of the medium. The microscopic quantity of interest is the dipole moment, defined as:

$$\mathbf{p} = e\mathbf{r} \tag{1.3.2}$$

where e is the charge of the electron. When the dipoles are distributed throughout the volume with a dipole density n per unit volume, the polarization of the medium is:

$$\mathbf{P} = n\mathbf{p} = ne\mathbf{r} \tag{1.3.3}$$

So, Eq. 1.3.1 can be written in terms of the polarization $\mathbf{P}$ as:

$$\ddot{\mathbf{P}} + \gamma\dot{\mathbf{P}} + \omega_0^2\mathbf{P} = \frac{ne^2}{m}\left(\mathbf{E} + \dot{\mathbf{r}} \times \mathbf{B}\right) = \omega_p^2\varepsilon_0\left(\mathbf{E} + \dot{\mathbf{r}} \times \mathbf{B}\right) \tag{1.3.4}$$

where $\omega_p = (ne^2/m\varepsilon_0)^{1/2}$ is the plasma frequency and $\dot{\mathbf{P}} = \mathbf{J}$ is the current density. By Fourier transforming Eq. 1.3.4, assuming a monochromatic field, and neglecting the magnetic part of the Lorentz force we get:

$$\mathbf{P}_\omega = \frac{\omega_p^2 \varepsilon_0}{\omega_0^2 - \omega^2 - i\gamma\omega}\mathbf{E}_\omega \tag{1.3.5}$$

where $\mathbf{P}_\omega$ and $\mathbf{E}_\omega$ are polarization and field amplitudes, respectively. Now, comparing Eq. 1.3.5 with the expression $\mathbf{P}_\omega = \varepsilon_0 \chi_\omega^{(1)} \mathbf{E}_\omega = \varepsilon_0(\varepsilon_r - 1)\mathbf{E}_\omega$, we can write the (relative) permittivity function as:

$$\varepsilon_r = 1 - \frac{\omega_p^2}{\omega^2 - \omega_0^2 - i\gamma\omega} \tag{1.3.6}$$

We note here that, in the absence of a damping coefficient ($\gamma = 0$), the permittivity of the material would be purely real and the model would not take absorption into account.

As mentioned before, Eq. 1.3.1 can be modified by adding a nonlinearity in the restoring force. For a non-centrosymmetric material, the equation of motion of the electron position $\mathbf{r}$ can be written as:

$$\ddot{\mathbf{r}} + \gamma\dot{\mathbf{r}} + \omega_0^2\mathbf{r} + a\mathbf{r}\cdot\mathbf{r} = \frac{e}{m}\left(\mathbf{E} + \dot{\mathbf{r}} \times \mathbf{B}\right) \tag{1.3.7}$$

In Eq. 1.3.7 we have added a nonlinear restoring force of the form $\mathbf{F}^{\mathrm{NL}}_{\mathrm{Retsoring}} = -ma\mathbf{r}\cdot\mathbf{r}$, where a is a parameter that characterizes the strength of the second order nonlinearity. We can assume that the nonlinear term becomes important when linear and nonlinear internal restoring forces are of the same order of magnitude. So, for a given spring deformation $\mathbf{r}_0$, one should have $\omega_0^2\mathbf{r}_0 \approx a\mathbf{r}_0\cdot\mathbf{r}_0$ which yields $a \approx \omega_0^2/|\mathbf{r}_0|$. If we assume that the maximum spring deformation is comparable to the size of the atom, which would give us a large, upper estimate of the oscillation amplitude, and note that this distance is of the order of the separation between atoms, that is, of the lattice constant L, we have that $a \approx \omega_0^2/L$.

The nature of this form of the restoring force can be understood by noting that it corresponds to the following potential energy function (for simplicity we analyse it in one dimension):

$$U(x) = -\int (F^{\mathrm{L}}_{\mathrm{Restoring}} + F^{\mathrm{NL}}_{\mathrm{Restoring}})dx = \frac{1}{2}m\omega_0^2x^2 + \frac{1}{3}max^3 \tag{1.3.8}$$

which contains both even and odd powers of x. This means that the present model describes only non-centrosymmetric materials as the condition $U(x) = U(-x)$ is not fulfilled. The first term in Eq. 1.3.8 corresponds to an harmonic potential, while the second term corresponds to an anharmonic correction term.

For centrosymmetric media, the equation of motion of electrons can be given by:

$$\ddot{\mathbf{r}} + \gamma\dot{\mathbf{r}} + \omega_0^2\mathbf{r} - b(\mathbf{r}\cdot\mathbf{r})\mathbf{r} = \frac{e}{m}\left(\mathbf{E} + \dot{\mathbf{r}}\times\mathbf{B}\right) \tag{1.3.9}$$

where now a nonlinear restoring force of the form $\mathbf{F}^{\mathrm{NL}}_{\mathrm{Restoring}} = mb(\mathbf{r}\cdot\mathbf{r})\mathbf{r}$ is considered. The parameter b represents the strength of the third order nonlinearity and can be estimated to be of the order $b \approx \omega_0^2/L^2$. In this case, the potential energy function corresponding to this nonlinear restoring force will be symmetric under the operation $x \to -x$, which it must be for a medium that possesses a center of inversion symmetry.

The parameters a and b can be related to $\chi^{(2)}_\omega$ and $\chi^{(3)}_\omega$, respectively [8].

1.3.3 Drude model

The Drude model is used to describe the linear optical properties of metals, which are treated as a gas of free electrons with density n per unit volume. In this case, the electrons are not bound to any particular nucleus and are considered to move freely around the metal lattice in the absence of a restoring force.

In the presence of an external electromagnetic field, the equation of motion of free electrons is given by:

$$\ddot{\mathbf{r}} + \gamma\dot{\mathbf{r}} = \frac{e}{m}\left(\mathbf{E} + \dot{\mathbf{r}}\times\mathbf{B}\right) \tag{1.3.10}$$

where m, e and $\mathbf{r}$ are the electron mass, charge and position, respectively, and $\mathbf{E}$ and $\mathbf{B}$ are the electric and magnetic fields. In this model, the electron motion is damped by collisions with ions ($\gamma \sim 100\,\mathrm{THz}$ for noble metals). Electron-electron interactions and the effects of crystal lattice potential are neglected. The first term on the right-hand side of Eq. 1.3.10 is the Coulomb interaction between the electron charge and the electric field $\mathbf{E}$, while the second term is the Lorentz force due to the presence of the magnetic flux density $\mathbf{B}$. Similarly to what we did with

the case of bound electrons, the relation between the microscopic dynamics described by Eq. 1.3.10 and the macroscopic response of the medium is given by the polarization $\mathbf{P} = en\mathbf{r}$. As a consequence, the macroscopic version of Eq. 1.3.10 can be written as:

$$\ddot{\mathbf{P}} + \gamma\dot{\mathbf{P}} = \varepsilon_0\omega_p^2\left(\mathbf{E} + \dot{\mathbf{r}} \times \mathbf{B}\right) \tag{1.3.11}$$

where $\omega_p = \left(ne^2/\varepsilon_0 m\right)^{(1/2)}$ is the plasma frequency of the electron gas. It is important to note that the mass m in the free electron model is an optical effective mass. Such mass, which mainly depends on the band structure of the medium, may significantly differ from the electron rest mass m_e. If we now assume a monochromatic field, apply Fourier transform to Eq. 1.3.11, and neglect the magnetic part of the Lorentz force, we get:

$$\mathbf{P}_\omega = -\frac{\varepsilon_0\omega_p^2}{\omega^2 + i\gamma\omega}\mathbf{E}_\omega \tag{1.3.12}$$

where we have assumed that n does not depend on time. Finally, by comparing Eq. 1.3.12 with $\mathbf{P}_\omega = \varepsilon_0(\varepsilon_r - 1)\mathbf{E}_\omega$, the following expression for the permittivity function is obtained:

$$\varepsilon_r(\omega) = 1 - \frac{\omega_p^2}{\omega^2 + i\gamma\omega} \tag{1.3.13}$$

Eq. 1.3.13 is known as the Drude dispersion model for an ideal gas of free electrons. It can be shown that, for frequencies below $\left(\omega_p^2 - \gamma^2\right)^{(1/2)}$ the real part of the dielectric function is negative. For media with damping coefficient γ much smaller than the plasma frequency, ω_p is approximately the zero-crossing frequency for the dielectric function.

Interband transitions in metals, such as gold and copper, can occur in the visible range of the spectrum. In order to take them into account, the usual approach consists in adding a number N of Lorentz oscillators to the free electron response, so that the permittivity function becomes:

$$\varepsilon(\omega) = \varepsilon_f(\omega) + \varepsilon_b(\omega) = 1 - \frac{\omega_p^2}{\omega^2 + i\gamma\omega} - \sum_{j=1}^{N}\frac{f_j\omega_p^2}{\omega^2 - \omega_j^2 + i\gamma_j\omega} \tag{1.3.14}$$

where $\varepsilon_f(\omega)$ and $\varepsilon_b(\omega)$ are the Drude and the Lorentz portion of the total dielectric function, respectively, and ω_j, f_j and γ_j are resonant frequency, strength and damping coefficient of the j-th oscillator, respectively. Equation 1.3.14 is known as the Drude-Lorentz model. A simplified

version of it is obtained considering ε_b constant and by writing $\varepsilon(\omega) = \varepsilon_\infty - \frac{\omega_p^2}{\omega^2 + i\gamma\omega}$. Although this correction improves the free electron Drude model, it does not provide an accurate description of the optical response in the frequency region where interband transitions occur.

When metallic structures reach the nanometer size, or when the distances between metallic regions are smaller than a few nanometers, additional effects must be included in the description of the free electron gas. The simplicity and effectiveness of the Drude and the Drude-Lorentz models reside in their local nature. These models predict that the response of the metal at a certain location in space is proportional to the field evaluated at that specific location. In other words, the induced polarization at position $\mathbf{r}$ is simply proportional to the applied field, as shown in Eq. 1.3.12.

A more accurate representation of the optical response of metals is provided by the hydrodynamic model of the free electron gas. This model corrects the constitutive relation for metals by adding a dependence on the spatial derivative of the field. The equation of motion for a hydrodynamic gas can be written as:

$$m\ddot{\mathbf{r}} + m\gamma\dot{\mathbf{r}} = e\left(\mathbf{E} + \dot{\mathbf{r}} \times \mathbf{B}\right) - \frac{1}{n}\nabla p \tag{1.3.15}$$

In Eq. 1.3.15 there is an additional force, $\nabla p/n$, due to spatial differences of gas pressure p that drives the conduction electrons from higher to lower density regions. For a three dimensional gas, the quantum pressure can be written as $p = p_0(n/n_0)^{5/3}$, where $p_0 = n_0 E_F$ is the Fermi pressure (the pressure of the quantum electron gas at zero temperature), n_0 is the equilibrium free electron density, and E_F is the Fermi energy. From Eq. 1.3.15, the following expression for the field amplitudes at the fundamental frequency can be obtained, as explained in detail in [31]:

$$\beta^2 \nabla(\nabla \cdot \mathbf{P}_\omega) - \omega^2 \mathbf{P}_\omega - i\omega\gamma \mathbf{P}_\omega = \varepsilon_0 \omega_p^2 \mathbf{E}_\omega \tag{1.3.16}$$

where β is proportional to the Fermi energy and the expression of the free electron plasma frequency is reintroduced. If one neglects the pressure term ($\beta = 0$), the above expression corresponds to the classical local response of the Drude model, as in Eq. 1.3.12. It is clear that

the pressure term introduces second order spacial derivatives, hence adding to the metal optical response a nonlocal, or spatially dispersive, contribution. If we transform the relation 1.3.16 into the k-space domain, i.e., using the transformation $\nabla \rightarrow ik$, we can obtain the resulting nonlocal permittivity:

$$\varepsilon_{nl}(k,\omega) = 1 - \frac{\omega_p^2}{\omega^2 + i\omega\gamma - |k|^2\beta^2} \tag{1.3.17}$$

The term $|k|^2\beta^2$ in Eq. 1.3.17 introduces a small perturbation of the permittivity that blue-shifts plasmonic resonances.

1.4 Nonlinear optics at nanoscale

In the last decade an impressive technological progress has been made towards the miniaturization process. Nowadays, in the multidisciplinary field of nanotechnology, structures with nanometric and even sub-nanometric size are produced and integrated in different devices and applications. At sub-nanometer scale light-matter interaction displays completely new phenomena, different from those corresponding to the same materials at micron or millimeter size. For example, controlling and guiding light has been one of science's most influential achievements. It affects everyday life in many ways, such as the development of telescopes, microscopes, spectrometers, and optical fibers, to name but a few. These examples exploit the wave nature of light and are based on the reflection, refraction and diffraction of light by optical elements such as mirrors, lenses or gratings. However, the wave nature of light limits the resolution to which an object can be imaged, as well as the size of the transverse cross section of efficient guiding structures to the wavelength dimension. On the contrary, plasmonic resonances in nanoantennas overcome these constraints, allowing unprecedented control of light-matter interactions within subwavelength volumes.

The integration of optical processes at the nanoscale may become fundamental in fields such as quantum optics as well as in biology and medicine. The ability to generate nonlinear optical processes in nanoscale volumes may allow boosting the efficiencies of high throughput screening techniques and squeezing optical logic functions down to electronic chip scales, pointing to-

wards the realization of nonlinear optical sensing probes and photonic sources operating at the nanoscale. For instance, SHG and THG can be used in nonlinear sensing. THG in nanoantenna arrays was the first to be tested as a probe in plasmon-enhanced nonlinear sensing [32], and a preliminary study, reported in [33] on engineered nanoantennas demonstrated that SHG-based plasmonic sensing can be at least as sensitive as the linear one despite the extremely low SHG performance.

The drawback is that, at the nanoscale, conversion efficiencies of nonlinear processes such as SHG and THG may decrease compared to their macroscopic counterparts and phase-matching conditions and even absorption may no longer play a primary or significant role. However, nonlinear optics in nanostructured materials offers possibilities for efficiency enhancement due to strong field confinement by plasmonic resonances at metal-dielectric boundaries, in metamaterials, or under conditions where the dielectric constant of the material approaches zero. So, the research interest has shifted from phase-matched optical interactions that occur over the bulk size with many wavelengths scale toward the optical near-field interactions within a few wavelengths or at sub-wavelength scale [32, 34, 35]. In this case, the efficiency of nonlinear processes is determined not by the quality of phase-matching, but by the degree of confinement and overlap of the optical near-field with the nonlinear nanostructures. As a consequence, major research work over the past decade has been focused on the design and fabrication of optimized configurations of nonlinear nanostructures.

Plasmonic nanostructures are among the first exploited approach to bridge the gap between conventional and modern nonlinear optics as they allow the local field to be significantly enhanced. Metal nanostructures (nanoantennas) are variously shaped objects, with a size as small as few tens of nanometers, typically made of noble metals, such as gold and silver. The combination of the strong near-field intensity in plasmonic systems and the intrinsic nonlinearities of metals result in efficient nonlinear optical processes. Nontheless, recently, dielectric nanostructures have emerged as an alternative to plasmonics due to their much lower loss, high refractive index and high damage threshold. In this new route, the light-matter interaction can be en-

hanced through Mie resonances [36]. Semiconductor Mie-resonators can confine the light inside their volume, allowing for a large overlap of the near-fields of the resonant modes with the semiconductor material. Thereby, nonlinear optical effects can be boosted.

In this section, we will overview the research that has been done on harmonic generation from different materials interesting for nanophotonics: metals, semicondutors and conductive oxides. Specifically, we will focus on the materials that have been studied in this thesis: gold, GaAs, silicon, and Indium tin oxide (ITO).

1.4.1 Metals: gold

Interest in the nonlinear optical properties of metals arches back to the beginning of nonlinear optics, is still a subject of debate, and is now more relevant than ever insofar as nano-plasmonics is concerned. Plasmonics concerns to the investigation of electron oscillations in metallic nanostructures and nanoparticles. Surface plasmons have optical properties, which are very interesting. For instance, they have the unique capacity to confine light at the nanoscale. Moreover, surface plasmons are very sensitive to the surrounding medium and the properties of the materials on which they propagate. In addition to the above, the surface plasmon resonances can be controlled by adjusting the size, shape, periodicity, and material's nature. Thus, all these optical properties of plasmonic systems can enable a great number of applications, such as biosensors [37, 38], optical devices [39, 40], and photovoltaic devices [41, 42].

As mentioned, the electromagnetic resonances associated with these surface plasmons depend on the details of the nanostructure, opening up opportunities for controlling light confinement on the nanoscale. The resulting strong electromagnetic fields allow weak nonlinear processes, which depend superlinearly on the local field, to be significantly enhanced. In addition to providing enhanced nonlinear effects with ultrafast response times, plasmonic nanostructures allow nonlinear optical components to be scaled down in size.

Research of nonlinear interactions in metals, such as SHG and THG, started with the beginning of nonlinear optics. From a historical point of view, it was pointed out in reference [18] that in centrosymmetric media, where bulk $\chi^{(2)}$ vanishes, SHG arises from a magnetic dipole term

and from an electric quadrupole-like contribution. Later, in reference [19], it was shown that the quadrupole source term was equivalent to a nonlinear surface contribution, and it was proposed that SHG in metals may be explained by considering separate bulk and surface contributions having different weights associated with free electron dynamics. Early experimental evidence of SHG in metals may be found in reference [43], where reflected SHG was measured from a silver mirror. In references [44] and [45] experimental results of reflected SHG were reported for silver and gold mirrors. Additional theoretical and experimental studies followed, a small sample of which may be found in references [46–48], where the main approach to explain the generation of SH light was to separate and distinguish between surface and volume nonlinear contributions. For example, based on the idea of identifying surface and volume sources, in reference [49] the magnitude and relative phase of second order susceptibility tensor elements were determined for thin-film metal samples of silver, gold, copper, aluminum and tantalum. However, the interest in metals' potential and usefulness as optical materials, beyond their use as mirrors, started when the field of plasmonics emerged. The combination of the strong near-field intensity obtained with plasmonic systems and the intrinsic nonlinearities of metals readily results in efficient nonlinear optical processes, which have given rise to the new research field of nonlinear plasmonics. Various nonlinear optical processes, including SHG, have been observed in plasmonic nanostructures. For instance, in references [50–52], SHG was investigated experimentally and theoretically from gold nanoparticles. In [53] SHG from gold nanocups was reported, with experimental conversion efficiencies of order 10^{-9}. As another example, in reference [54] SHG was demonstrated from a diffraction grating of symmetric gold nanoparticles, without reporting experimental or theoretical conversion efficiencies. Other experimental studies of SHG from gold are reported in references [55] and [56]. Third order nonlinearities have also been studied in a variety of gold samples in various geometries [57–62].

1.4.2 Semiconductors: GaAs and silicon

Despite the numerous advantages for near-field enhancement, metallic nanostructures suffer from high dissipative losses and inevitable heating effect, leading to irreversible damage under high

intensity light. As a consequence, the exploration of other materials for nonlinear engineering at the nanoscale has been also an active research direction. Recently, dielectric nanostructures have emerged as an alternative to plasmonics due to their much lower loss, high refractive index and high damage threshold. The use of semiconductors such as GaAs, GaP or silicon in the process of fabrication of nanodevices is at the forefront of modern technology, with the aim of exploiting light-matter interactions at the nanoscale in new and sometimes surprising ways. Nonlinear frequency conversion plays a crucial role in advancing the functionality of next generation optical systems. Portable metrology references and quantum networks will demand highly efficient second order nonlinear devices. In order to achieve this efficiency enhancement, several studies reporting SHG from nanostructures made of semiconductors such as GaAs have been done. For instance, in [63], efficient SHG in GaAs-on-insulator waveguides was demonstrated and achieved by minimizing the propagation loss and optimizing phase-matching. Also, in [64], efficient SHG from GaAs microdisk resonators was reported, with conversion efficiencies of order 10^{-6}. Microdisk resonators offer resonant field enhancement, resulting in highly efficient frequency conversion in micrometre-scale volumes. These devices can be integrated in photonic circuits as compact frequency converters, and sources of radiation or entangled photons. In [65], the authors reported SHG in GaAs photonic crystal cavities. Their predictions showed SHG normalized conversion efficiencies of the order of $10\%\,\mathrm{W}^{-1}$, while their experimentally measured values were on the order of $1\%\,\mathrm{W}^{-1}$.

Apart from the numerous published work on efficient SHG from nanostructures made of GaAs, another kind of studies of harmonic generation from this material have been performed in order to investigate the phase-locked component of the SH or TH field. This component was first revealed by J. A. Armstrong *et al.* [3] and N. Bloembergen *et al.* [4] in 1962, and experimentally observed for the first time in 1990 [22]. Experimental and theoretical studies continued in the years that followed [23–27]. In [28] it was experimentally reported for the first time the inhibition of linear absorption for phase and group velocity mismatched SHG and THG in GaAs, at frequencies above the absorption edge. A 100 fs pump pulse tuned to 1300 nm generated 650 nm and 435 nm

SH and TH pulses, respectively, that propagated across a 450 μm-thick GaAs substrate without being absorbed. This was attributed to a phase-locking mechanism that causes the pump to trap the harmonics and to impress on them its dispersive properties. Conversion efficiencies of order 10^{-8} and 10^{-9} were reported for SHG and THG, respectively. Later, it was shown in [29] that the phase-locked SH component generated in opaque materials could be significantly amplified by three orders of magnitude in a GaAs cavity that displayed a resonance at the fundamental wavelength.

Another interesting material for nanophotonics is silicon. Recent years have witnessed impressive progress in the development of functional, nonlinear silicon photonic devices which can emit light, modulate signals electro-optically and process data at speeds higher than electronic chips, and they are highly compatible with CMOS technology at low cost [66, 67]. Applications include frequency conversion [68], optical switched and modulators [69], high-speed optical signal processing [70–72], optical sensing [73], and integrated quantum photonic circuits [74]. Even though silicon is a centrosymmetric material, SHG in media with inversion symmetry has been studied since the early days of nonlinear optics. As already mentioned in previous sections, one of the first detailed theoretical discussions of surface SHG emanating from quadrupole-like and magnetic dipole terms is found in [18]. In [45], reflected SHG was discussed in the context of a thin slab of crystalline silicon. The authors measured and predicted the angular dependence of the SH signal, resulting in a SH peak at a large angle of incidence. In [75], a study of SHG was performed on crystalline silicon samples having different crystallographic orientations. Additional studies of THG were carried out in the years that ensued [76–78]. For instance, in [78], THG was analyzed in reflection from crystalline and amorphous samples of silicon.

Despite the reported experimental and theoretical studies of harmonic generation in silicon, not high enough conversion efficiencies were obtained in order for the material to be adequate for the development of functional nonlinear devices. For this reason, more recently, researchers have taken measures to overcome the absence of a $\chi^{(2)}$ term by depositing either straining layers on top of silicon [79, 80], or by using another $\chi^{(2)}$ nonlinear electro-optic active material as

a cladding [81] in order to break the silicon centrosymmetry. In [79], the authors reported SHG conversion efficiencies of order 10^{-8} from silicon waveguides strained by silicon nitride. In [80] an enhancement of the SHG intensity is reported when an external cylindrical strain is applied to silicon stripes, attributed to the contributions from the strain-induced second order nonlinear susceptibility to the bulk dipole. Studies on THG from silicon samples having different geometries have also been carried out with the aim to enhance the harmonic signal [82–85]. In [82] THG is reported from a two-dimensional silicon photonic crystal waveguide. The authors reported THG efficiencies of order 10^{-7}. A two orders of magnitude enhancement of THG conversion efficiencies from silicon nanodisks was observed in [83], where efficiencies of order 10^{-7} were reported. In [84], the authors experimentally demonstrate THG conversion efficiencies from a silicon metasurface which are about 300 times larger than that of bulk silicon slab.

1.4.3 Conductive oxides: ITO

Another promising way to improve the performance of nonlinear optical devices is provided by a new class of optical materials that display vanishing small real part of the dielectric constant, known as epsilon-near-zero (ENZ) materials [86–98]. These materials enhance the local electromagnetic field through the condition where the longitudinal component of the displacement vector of a TM-polarized field has to be continuous across the boundary between media with different optical properties. For homogeneous, flat structures, this condition may be written as $\varepsilon_{in}E^z_{in} = \varepsilon_{out}E^z_{out}$, where ε_{in} and ε_{out} are dielectric constants inside and outside the medium, respectively, and E^z_{in} and E^z_{out} are the corresponding longitudinal components of the electric field amplitude and require oblique incidence to excite the ENZ point. Therefore, if ε_{in} decreases, then E^z_{in} increases and nonlinear optical phenomena, such as harmonic generation, are enhanced. This situation is schematically shown for a TM-polarized field in Fig. 1.4.1, where $\mathbf{E}_{in(out)}$, $\mathbf{B}_{in(out)}$ and $\mathbf{S}_{in(out)}$ are the electric and magnetic fields and Poynting vector, respectively, inside and outside the ENZ medium.

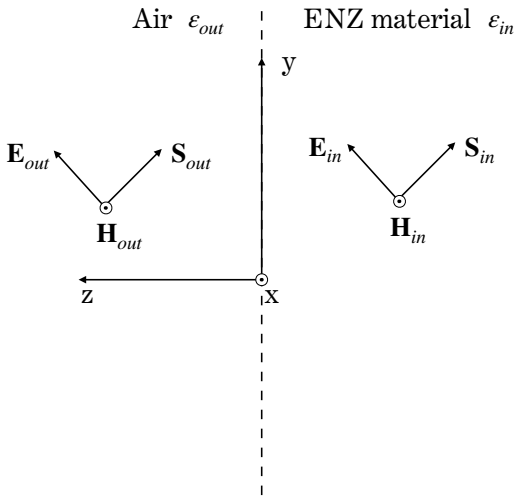

Figure 1.4.1: Geometric representation of TM-polarized light in and outside an ENZ material.

ENZ materials can be made artificially with periodic structures (metamaterials) and waveguides. The issues that arise using these approaches are the presence of scattering and the difficulty of miniaturization. All natural bulk materials that display a Lorentz-like response (see Eq. 1.3.6) also exhibit a real part of the dielectric permittivity that crosses zero, in proximity of either plasma or interband transition frequencies [91]. For instance, semiconductors like GaAs, GaP and silicon display ENZ conditions near 100 nm, deep in the UV range. Metals such as gold, silver and copper have ENZ crossing points in the visible range, while the zero crossing points of conductive oxides, also known as degenerate semiconductors, such as ITO and CdO (Cadmium oxide) fall in the IR regime and can be tuned using thermal post-processing of sputtered samples.

ITO is one of the most studied transparent conductive films. For instance, it is used to make transparent conductive coatings for displays such as liquid crystal displays, OLED displays and touch panels. It is also used in photovoltaic cells [99]. It is a free-electron system characterized by absorption that is typically much smaller than that of noble metals, especially near the ENZ point. As a consequence, conductive oxides may substitute or even supplant metals in certain

applications and spectral wavelength regions, as they can trigger novel, low-intensity nonlinear optical phenomena that can usually be observed only for high local fields.

The linear and nonlinear optical properties of ITO and CdO [100, 101] are under intense investigation because of a easily available ENZ response tunable across the near-IR wavelength range. Despite both metals and conductive oxides are free-electron systems, their linear and nonlinear optical properties have some differences. First, free electron densities of noble metals can be several orders of magnitude larger than that of conductive oxides, leading to significant differences in field penetration and the excitation of surface and volume nonlinearities, and non-local effects [102]. Second, in the case of noble metals, interband excitations lead to an increase of free carrier density and a blueshift of the plasma frequency. On the contrary, conducting oxides are prone to displaying intraband transitions and increased electron gas temperature that lead to increased effective electron mas and a dynamic redshift of the plasma frequency [101].

Recently, several studies of SHG and THG from ITO layers have been reported. For instance, in [87], the ENZ crossing point was exploited for the enhancement of THG in a Kretschmann configuration (i.e., light is prism-coupled to the film). In this work, the authors experimentally and theoretically report an enhancement factor of 200, with values of THG conversion efficiencies of order 10^{-6}. In [88] THG was reported for an ITO nanolayer, along with evidence that enhancement of the generated signal came as a result of an ENZ crossing point. In [89] a comparative study of ITO and TiN (Titanium nitride) nanolayers showed an enhancement of SHG from ITO at the ENZ wavelength. In this study, SHG was examined in two distinct ENZ platforms: an array of 37 nm-thick ITO films with zero-permittivity wavelengths ranging from 1150 nm to 1670 nm, and 40 nm-thick TiN films with zero-permittivity wavelengths ranging from 510 nm to 645 nm. Pumping ITO at the ENZ wavelength resulted in the generation of SH signals with conversion efficiencies comparable to those of a 500 μm-thick quartz crystal reference sample. The generated nonlinear signal peaked at the zero-permittivity wavelength with a substantial reduction elsewhere. Other examples of experimental results of nonlinear optical effects in ENZ materials can be found in [98].

1.5 Hydrodynamic-Maxwell model

In Section 1.4 we have introduced the research that has been done on harmonic generation from metals, conductive oxides and semiconductors, and we have given some examples reporting experimental results on SHG and THG. However, most of the theoretical models that are used to explain these experimental results rely on the introduction of phenomenological or effective surface and bulk parameters. For instance, for SHG, the nonlinear polarization $\mathbf{P}_{2\omega}$ is usually written as:

$$\mathbf{P}_{2\omega} = \mathbf{P}_{2\omega}^{\text{surface}} + \mathbf{P}_{2\omega}^{\text{bulk}} \tag{1.5.1}$$

where $\mathbf{P}_{2\omega}^{\text{surface}}$ and $\mathbf{P}_{2\omega}^{\text{bulk}}$ are the surface and the bulk contributions to the second order nonlinear polarization, respectively, and they are usually written through Eqs. 1.5.2 and 1.5.3 as reported in [16] for centrosymmetric materials:

$$\mathbf{P}_{2\omega}^{\text{surface}} = \chi_{\text{surface}}^{(2)} \mathbf{E}_{\omega}\mathbf{E}_{\omega} \tag{1.5.2}$$

$$\mathbf{P}_{2\omega}^{\text{bulk}} = \gamma\nabla(\mathbf{E}_{\omega}\cdot\mathbf{E}_{\omega}) + \delta(\mathbf{E}_{\omega}\cdot\nabla)\mathbf{E}_{\omega} + \beta\mathbf{E}_{\omega}(\nabla\cdot\mathbf{E}_{\omega}) + \zeta\mathbf{E}_{\omega}\nabla\mathbf{E}_{\omega} \tag{1.5.3}$$

where γ, δ, β and ζ are material parameters, and $\mathbf{E}_{\omega}$ is the electric field at the fundamental frequency. The nonlinear polarization in Eq. 1.5.3 originates from electric quadrupoles and magnetic dipoles located in the bulk. In the case of non-centrosymmetric media, an electric dipole contribution should be added. In Eq. 1.5.2, $\chi_{\text{surface}}^{(2)}$ is the surface second order susceptibility tensor. Usually, the surface of centrosymmetric media possesses an isotropic mirror-symmetry plane perpendicular to the interface. Then, the surface nonlinear susceptibility $\chi_{\text{surface}}^{(2)}$ has only three independent components $\chi_{\perp\perp\perp}^{(2)}$, $\chi_{\perp\parallel\parallel}^{(2)}$, and $\chi_{\parallel\perp\parallel}^{(2)} = \chi_{\parallel\parallel\perp}^{(2)}$. This model for SHG lacks a detailed, microscopic, dynamical description of light propagation and light-matter interaction, and requires *a priori* knowledge of effective second order surface susceptibility tensor components as well as material parameters.

In this section we explain an alternative route to model nonlinear processes in semiconductors and metals. The approach was proposed by Dr. Michael Scalora and it has been reported in [103, 104]. In this thesis it has been adapted to each material case and it has been used to

perform numerical simulations reproducing the experimental situation. The method consists on formulating a microscopic, hydrodynamic model in order to understand linear and nonlinear optical properties of different materials at the nanoscale by accounting for competing surface, magnetic and bulk nonlinearities arising from both free and bound electrons. The model also preserves linear and nonlinear material dispersion, and, in the case of metals and conductive oxides, it accounts for nonlocal effects due to pressure and viscosity, and the influence of hot electrons. We estimate the efficiencies of the nonlinear signals without making assumptions about effective surface and bulk nonlinearities. The only free parameters present in the model are: (1) the effective mass of free and bound electrons, which determines SHG triggered by symmetry braking at the surface, and by the magnetic Lorentz force, (2) the strength of the second and third order bulk nonlinearities, which account for nonlinear material dispersion, and (3) the rate at which electrons are excited from the valence to the conduction band or the rate at which the effective mass of free electrons changes due to temperature.

The model embraces full-scale, time-domain coupling of matter to the macroscopic Maxwell's equations. Its starting point are the equations of motion of free and bound electrons, from which dynamic polarization equations are obtained. Using the solutions of these equations, the total polarization is written as the sum of free and bound electron contributions, $\mathbf{P}_{\text{total}} = \mathbf{P}_f + \mathbf{P}_b$. The polarization equations are integrated together with Maxwell's equations and the integration method outlined in [104] is used. This approach solves Maxwell's equations using a spectral method to advance the field, and a predictor-corrector method to solve material equations, which is explained in Appendix C, using FORTRAN programming code. The propagation of pulses which are plane in the transverse direction and whose temporal duration ranges from 50 fs to 100 fs is considered. Results saturate for longer pulses. Predicted conversion efficiencies are calculated as the ratio between final energy in the scattered pulses (transmitted or reflected) and total initial pump pulse energy.

1.5.1 Bound electrons

In general, the nonlinear polarization of a medium may be written according to a well-established, ascending hierarchy of electric and magnetic dipoles and multipoles, as shown in Eq. 1.2.1. In practical terms this means explicit introduction of a nonlinear polarization that requires *a priori* knowledge of second and third order nonlinear coefficients, in either scalar or tensor form. On the other hand, the nonlinear Lorentz model may be a more instructive starting point that implicitly accounts for linear and nonlinear material dispersion, which turns the polarization into an independent parameter and is able to describe an entire class of nonlinear optical phenomena.

Similarly to Eqs. 1.3.9 and 1.3.7 introduced in Chapter 1.3.2, for bound electrons that occupy a given orbital, Newton's second law may be written as:

$$\ddot{\mathbf{r}} + \gamma_b \dot{\mathbf{r}} + \omega_0^2 \mathbf{r} + a\mathbf{r}\cdot\mathbf{r} - b(\mathbf{r}\cdot\mathbf{r})\mathbf{r} = \frac{e}{m_b^*}(\mathbf{E} + \dot{\mathbf{r}} \times \mathbf{H}) \tag{1.5.4}$$

where $e(\mathbf{E} + \dot{\mathbf{r}} \times \mathbf{H})$ is the Lorentz force, being $\mathbf{E}$ and $\mathbf{H}(= \mathbf{B})$ the electric and magnetic fields, respectively, and e the electron charge. $\mathbf{r}$ is the displacement from orbital equilibrium, m_b^* and γ_b are effective mass and damping coefficient of bound electrons, respectively. ω_0 is the resonant frequency of the oscillator, which is associated with a linear restoring force, and a and b are two parameters associated with a second and a third order nonlinear restoring force, respectively. We already showed in Chapter 1.3.2 that for an oscillator system we can approximate $a \approx \omega_0^2/L$ and $b \approx \omega_0^2/L^2$, where L is the lattice constant. The relationship between these coefficients and the respective nonlinear susceptibilities $\chi^{(2)}_{\omega,2\omega}$, $\chi^{(3)}_{\omega,3\omega}$ may be derived using the nonlinear Lorentz oscillator model and it will be shown for the case of b.

In the discussion that follows we will assume a centrosymmetric material, so that $a = 0$. For the moment, we will just focus on the process of THG, so at the electron position we can write the total field present as a superposition of fundamental and TH fields as follows:

$$\begin{aligned} \mathbf{E} &= \mathbf{E}_\omega e^{-i\omega t} + \mathbf{E}_{3\omega} e^{-3i\omega t} + c.c. \\ \mathbf{H} &= \mathbf{H}_\omega e^{-i\omega t} + \mathbf{H}_{3\omega} e^{-3i\omega t} + c.c. \end{aligned} \tag{1.5.5}$$

where $\mathbf{E}_\omega$, $\mathbf{E}_{3\omega}$, $\mathbf{H}_\omega$ and $\mathbf{H}_{3\omega}$ are complex field amplitudes that for the moment are assumed to be nearly constant in time. As a consequence, a simplified solution for the electron displacement

may also be written as a superposition of fundamental and TH amplitudes that vary relatively slowly in time as compared to the optical cycle:

$$\mathbf{r} = \mathbf{r}_\omega e^{-i\omega t} + \mathbf{r}_{3\omega} e^{-3i\omega t} + c.c. \tag{1.5.6}$$

Substituting Eqs. 1.5.5 and 1.5.6 into Eq. 1.5.4, retaining lowest order terms, neglecting the magnetic term, and equating terms that oscillate at the same frequency, equations for $\mathbf{r}_\omega$ and $\mathbf{r}_{3\omega}$ can be obtained. After solving them, the expressions for the amplitude positions are:

$$\mathbf{r}_\omega = \frac{e}{m_b^*(\omega_0^2 - \omega^2 + i\gamma_b\omega)}\mathbf{E}_\omega + \frac{be^3}{m_b^{*3}(\omega_0^2 - \omega^2 + i\gamma_b\omega)^3(\omega_0^2 - \omega^2 - i\gamma_b\omega)}|\mathbf{E}_\omega|^2\mathbf{E}_\omega \tag{1.5.7}$$

$$\begin{aligned}\mathbf{r}_{3\omega} &= \frac{e}{m_b^*(\omega_0^2 - 9\omega^2 + 3i\gamma_b\omega)}\mathbf{E}_{3\omega} \\ &+ \frac{be^3}{m_b^{*3}(\omega_0^2 - 9\omega^2 + 3i\gamma_b\omega)(\omega_0^2 - \omega^2 + i\gamma_b\omega)^3}(\mathbf{E}_\omega \cdot \mathbf{E}_\omega)\mathbf{E}_\omega\end{aligned} \tag{1.5.8}$$

Recognizing that $\mathbf{P}_{\omega,3\omega} = n_{0,b}e\mathbf{r}_{\omega,3\omega}$ is the polarization, where $n_{0,b}$ is the density of bound electrons (or density of oscillators), and writing $\mathbf{P}_\omega$ and $\mathbf{P}_{3\omega}$ as:

$$\mathbf{P}_\omega = \chi_\omega^{(1)}\mathbf{E}_\omega + \chi_\omega^{(3)}|\mathbf{E}_\omega|^2\mathbf{E}_\omega \tag{1.5.9}$$

$$\mathbf{P}_{3\omega} = \chi_{3\omega}^{(1)}\mathbf{E}_\omega + \chi_{3\omega}^{(3)}(\mathbf{E}_\omega \cdot \mathbf{E}_\omega)\mathbf{E}_\omega \tag{1.5.10}$$

we can extract:

$$\begin{aligned}\chi_\omega^{(1)} &= \frac{n_{0,b}e^2}{m_b^*(\omega_0^2 - \omega^2 + i\gamma_b\omega)} \\ \chi_\omega^{(3)} &= \frac{n_{0,b}be^4}{m_b^{*3}(\omega_0^2 - \omega^2 + i\gamma_b\omega)^3(\omega_0^2 - \omega^2 - i\gamma_b\omega)}\end{aligned} \tag{1.5.11}$$

$$\chi_{3\omega}^{(3)} = \frac{n_{0,b}be^4}{m_b^{*3}(\omega_0^2 - \omega^2 + i\gamma_b\omega)^3(\omega_0^2 - 9\omega^2 + 3i\gamma_b\omega)} \tag{1.5.12}$$

where $\chi_\omega^{(1)}$ and $\chi_{\omega,3\omega}^{(3)}$ are the derived linear and nonlinear susceptibilities experienced by the fundamental and TH fields. We note that we have started using Gaussian units instead of MKS system. The former will be used in the description of the theoretical approach. The second part of Eq. 1.5.11 reveals that the medium is gifted with nonlinear refraction, or self-phase modulation, via the $\mathrm{Re}(\chi_\omega^{(3)})$ portion, and by two-photon absorption via the term $\mathrm{Im}(\chi_\omega^{(3)})$. Also, Eq. 1.5.12 shows that the generated TH field experiences both nonlinear refraction and gain/loss

via the terms $\mathrm{Re}(\chi^{(3)}_{3\omega})$ and $\mathrm{Im}(\chi^{(3)}_{3\omega})$, respectively. The expression for the linear dielectric function shown in Eq. 1.3.6 is recovered with $\varepsilon = 1 + \chi^{(1)}_{\omega}$, and the same strategy may be followed to estimate the second order, nonlinear coefficients of non-centrosymmetric materials, $\chi^{(2)}_{\omega,2\omega}$.

Recognizing that $\mathbf{P}_b = n_{0,b} e \mathbf{r}$ and expanding the fields around an equilibrium, electron position [103, 104], the following polarization equation for bound electrons can be derived from Eq. 1.5.4:

$$\ddot{\mathbf{P}}_b + \tilde{\gamma}_b \dot{\mathbf{P}}_b + \tilde{\omega}_0^2 \mathbf{P}_b + \mathbf{P}_b^{\mathrm{NL}} = \frac{n_{0,b} e^2 \lambda_0^2}{m_b^* c^2} \mathbf{E} + \frac{e\lambda_0}{m_b^* c^2} (\mathbf{P}_b \cdot \nabla)\mathbf{E} + \frac{e\lambda_0}{m_b^* c^2} \dot{\mathbf{P}}_b \times \mathbf{H} \tag{1.5.13}$$

where we have scaled the equation respect to dimensionless time and longitudinal and transverse coordinates: $\tau = ct/\lambda_0$, $\xi = z/\lambda_0$, $\tilde{y} = y/\lambda_0$, where $\lambda_0 = 1\,\mu$m is arbitrarily chosen as the reference wavelength. As a consequence, coefficients have also been scaled: $\tilde{\gamma}_b = \gamma_b \lambda_0 / c$, and $\tilde{\omega}^2_{0,b} = \omega^2_{0,b} \lambda_0^2 / c^2$. $\mathbf{P}_b^{\mathrm{NL}} = \tilde{a}\mathbf{P}_b \cdot \mathbf{P}_b - \tilde{b}(\mathbf{P}_b \cdot \mathbf{P}_b)\mathbf{P}_b$ contains the second $\tilde{a}\mathbf{P}_b \cdot \mathbf{P}_b$ and third $\tilde{b}(\mathbf{P}_b \cdot \mathbf{P}_b)\mathbf{P}_b$ order bulk contributions to the total polarization. The coefficients $\tilde{a}$ and $\tilde{b}$ (or a and b) are tensors that reflect crystal symmetry. If the material is assumed to be isotropic, they can be assumed to be constants, and have the scaled expressions: $\tilde{a} = a\lambda_0^2/(n_{0,b} e c^2)$ and $\tilde{b} = b\lambda_0^2/(n_{0,b}^2 e^2 c^2)$. In general, second and third order bulk nonlinearities can be written as $P_i^{\mathrm{NL}^{(2)}} = \sum_{j=1,3} \sum_{k=1,3} \tilde{a}_{i,j,k} P_j P_k$ and $P_i^{\mathrm{NL}^{(3)}} = \sum_{j=1,3} \sum_{k=1,3} \sum_{l=1,3} \tilde{b}_{i,j,k,l} P_j P_k P_l$, respectively, where P_j are the Cartesian components of the macroscopic polarization. For instance, expanding these summations for isotropic GaAs having (001) symmetry the second and third order bulk contributions can be written as:

$$\begin{pmatrix} P_x^{\mathrm{NL}^{(2)}} \\ P_y^{\mathrm{NL}^{(2)}} \\ P_z^{\mathrm{NL}^{(2)}} \end{pmatrix} = \begin{pmatrix} (\tilde{a}_{x,y,z} + \tilde{a}_{x,z,y}) P_z P_y \\ (\tilde{a}_{y,x,z} + \tilde{a}_{y,z,x}) P_z P_x \\ (\tilde{a}_{z,x,y} + \tilde{a}_{z,y,x}) P_y P_x \end{pmatrix} = \tilde{a} \begin{pmatrix} P_z P_y \\ P_z P_x \\ P_y P_x \end{pmatrix} \tag{1.5.14}$$

and

$$\begin{pmatrix} P_x^{\mathrm{NL}^{(3)}} \\ P_y^{\mathrm{NL}^{(3)}} \\ P_z^{\mathrm{NL}^{(3)}} \end{pmatrix} = \tilde{b} \begin{pmatrix} (P_x^2 + P_y^2 + P_z^2) P_x \\ (P_x^2 + P_y^2 + P_z^2) P_y \\ (P_x^2 + P_y^2 + P_z^2) P_z \end{pmatrix} \tag{1.5.15}$$

For simplicity we have consolidated the constants into a single coefficient.

Equation 1.5.13 contains three main contributions that are expected to participate in the nonlinear process: (i) a nonlinear bulk contribution $\mathbf{P}^{\mathrm{NL}}$; (ii) a purely surface contribution triggered by the spatial derivatives of the field $\frac{e\lambda_0}{m_b^* c^2}(\mathbf{P}_b \cdot \nabla)\mathbf{E}$; and (iii) the nonlinear contribution

from the magnetic portion of the Lorentz force $\frac{e\lambda_0}{m_b^*}\dot{\mathbf{P}}_b \times \mathbf{H}$, which contains intrinsic surface and bulk components since currents flow inside the bulk and at the surface. Put it another way, Eq. 1.5.13 suggests that in the absence of bulk nonlinearities ($a = 0; b = 0 \Rightarrow \mathbf{P}_b^{\mathrm{NL}} = 0$), one still has SHG arising from the spatial derivatives of the field, which are non-zero at each surface crossing, and the magnetic Lorentz force. The effective mass of bound electrons determines the nonlinear gain arising from the surface and the magnetic Lorentz terms, while the parameters $\tilde{a}$ and $\tilde{b}$ determine the amount of bulk-generated nonlinear signals.

1.5.2 Free electrons

Free electrons are described through the hydrodynamic model of the free electron gas, so that their equation of motion may be written as:

$$m_f^* \frac{d\mathbf{v}}{dt} + \gamma_f m_f^* \mathbf{v} = e(\mathbf{E} + \mathbf{v} \times \mathbf{H}) - \frac{\nabla p}{n_f} \tag{1.5.16}$$

where m_f^*, γ_f and n_f are effective mass, damping coefficient and density of free electrons, respectively. $\mathbf{v}$ is the electron velocity and p is the electron gas pressure. $e(\mathbf{E} + \mathbf{v} \times \mathbf{H})$ is the Lorentz force, where e is the electron charge and $\mathbf{E}$ and $\mathbf{H}(=\mathbf{B})$ are the electric and magnetic fields, respectively.

Free electrons are not confined to any specific atomic site, so the temporal derivative of the velocity $\mathbf{v}$ is also position dependent: $\frac{d\mathbf{v}}{dt} = \frac{\partial \mathbf{v}}{\partial t} + (\mathbf{v} \cdot \nabla)\mathbf{v}$. Substituting this expression to Eq. 1.5.16, we get:

$$\frac{\partial \mathbf{v}}{\partial t} + (\mathbf{v} \cdot \nabla)\mathbf{v} + \gamma_f \mathbf{v} = \frac{e}{m_f^*}(\mathbf{E} + \mathbf{v} \times \mathbf{H}) - \frac{\nabla p}{n_f m_f^*} \tag{1.5.17}$$

Identifying the current density with $\mathbf{J} = n_f e \mathbf{v}$ and defining $\dot{\mathbf{P}}_f = \mathbf{J}$, Eq. 1.5.17 becomes:

$$\ddot{\mathbf{P}}_f - \frac{\dot{n}_f}{n_f}\dot{\mathbf{P}}_f + (\dot{\mathbf{P}}_f \cdot \nabla)\left(\frac{\dot{\mathbf{P}}_f}{n_f e}\right) + \gamma_f \dot{\mathbf{P}}_f = \frac{n_f e^2}{m_f^*}\mathbf{E} + \frac{e}{m_f^*}\dot{\mathbf{P}}_f \times \mathbf{H} - \frac{e}{m_f^*}\nabla p \tag{1.5.18}$$

For free electrons the continuity equation $\dot{n}_f(\mathbf{r}, t) = -\frac{1}{e}\nabla \cdot \dot{\mathbf{P}}_f$ supplements the equation of motion. It can be integrated directly to yield:

$$n_f(\mathbf{r}, t) = n_{0,f} - \frac{1}{e}\nabla \cdot \mathbf{P}_f \tag{1.5.19}$$

where $n_{0,f}$ is the equilibrium free electron density, and the initial value of the polarization is $\mathbf{P}_f(\mathbf{r}, t = 0) = 0$ in the absence of any applied field. If we assume that any local variations in the charge density are small compared to the density itself ($|n_{0,f}| \gg |-\frac{1}{e}\nabla \cdot \mathbf{P}_f|$), the ratio $\dot{n}_f/n_f$ can be expanded in powers of $1/(n_{0,f}e)$:

$$\frac{\dot{n}_f}{n_f} = \frac{-\frac{1}{e}\nabla \cdot \dot{\mathbf{P}}_f}{n_{0,f} - \frac{1}{e}\nabla \cdot \mathbf{P}_f} \simeq -\frac{1}{en_{0,f}}\nabla \cdot \dot{\mathbf{P}}_f - \frac{1}{n_{0,f}^2 e^2}(\nabla \cdot \dot{\mathbf{P}}_f)(\nabla \cdot \mathbf{P}_f) + ... \tag{1.5.20}$$

Substituting Eqs. 1.5.19 and 1.5.20 into Eq. 1.5.18 and neglecting terms of order $1/(n_{0,f}e)^2$ and higher, the following expression is obtained:

$$\begin{aligned} \ddot{\mathbf{P}}_f + \gamma_f \dot{\mathbf{P}}_f = \frac{n_{0,f}e^2}{m_f^*}\mathbf{E} - \frac{e}{m_f^*}(\nabla \cdot \mathbf{P}_f)\mathbf{E} + \frac{e}{m_f^*}\dot{\mathbf{P}}_f \times \mathbf{H} \\ -\frac{1}{n_{0,f}e}[(\nabla \cdot \dot{\mathbf{P}}_f)\dot{\mathbf{P}}_f + (\dot{\mathbf{P}}_f \cdot \nabla)\dot{\mathbf{P}}_f] - \frac{e}{m_f^*}\nabla p \end{aligned} \tag{1.5.21}$$

The impact of pressure is treated quantum mechanically. In this case, it takes the form $p = p_0 \left(n_f/n_{0,f}\right)^{\beta}$, where $\beta = (D+2)/D$ and D is the dimensionality of the problem. For $D = 3$ we have $p = p_0 \left(n_f/n_{0,f}\right)^{5/3}$, where $p_0 = n_0 E_F$ and $E_F = \frac{\hbar^2}{2m_f^*}(2\pi^2 n_{0,f})^{2/3}$ is the Fermi energy. With this, the leading pressure term that we will introduce to our polarization equation is:

$$-\frac{e}{m_f^*}\nabla p = -\frac{5E_F}{3m_f^* n_{0,f}^{2/3}} n^{2/3}\nabla n \approx \frac{5E_F}{3m_f^*}\nabla(\nabla \cdot \mathbf{P}_f) \tag{1.5.22}$$

Substituting into Eq. 1.5.21 we get:

$$\begin{aligned} \ddot{\mathbf{P}}_f + \gamma_f \dot{\mathbf{P}}_f = \frac{n_{0,f}e^2}{m_f^*}\mathbf{E} - \frac{e}{m_f^*}(\nabla \cdot \mathbf{P}_f)\mathbf{E} + \frac{e}{m_f^*}\dot{\mathbf{P}}_f \times \mathbf{H} \\ +\frac{5E_F}{3m_f^*}\nabla(\nabla \cdot \mathbf{P}_f) - \frac{1}{n_{0,f}e}[(\nabla \cdot \dot{\mathbf{P}}_f)\dot{\mathbf{P}}_f + (\dot{\mathbf{P}}_f \cdot \nabla)\dot{\mathbf{P}}_f] \end{aligned} \tag{1.5.23}$$

We now scale the equation with respect to dimensionless time and longitudinal and transverse coordinates, as in the previous case of bound electrons. Equation 1.5.23 then becomes:

$$\begin{aligned} \ddot{\mathbf{P}}_f + \tilde{\gamma}_f \dot{\mathbf{P}}_f = \frac{n_{0,f}e^2\lambda_0^2}{m_f^* c^2}\mathbf{E} - \frac{e\lambda_0}{m_f^* c^2}(\nabla \cdot \mathbf{P}_f)\mathbf{E} + \frac{e\lambda_0}{m_f^* c^2}\dot{\mathbf{P}}_f \times \mathbf{H} \\ +\frac{5E_F}{3m_f^* c^2}\nabla(\nabla \cdot \mathbf{P}_f) - \frac{1}{n_{0,f}e\lambda_0}[(\nabla \cdot \dot{\mathbf{P}}_f)\dot{\mathbf{P}}_f + (\dot{\mathbf{P}}_f \cdot \nabla)\dot{\mathbf{P}}_f] \end{aligned} \tag{1.5.24}$$

where the damping coefficient $\tilde{\gamma}_f = \gamma_f \lambda_0/c$ has also been scaled.

In addition to the magnetic Lorentz force, $\frac{e\lambda_0}{m_f^* c^2}\dot{\mathbf{P}}_f \times \mathbf{H}$, Eq. 1.5.24 contains a quadrupole-like Coulomb term that arises from the continuity equation 1.5.19, $-\frac{e\lambda_0}{m_f^* c^2}(\nabla \cdot \mathbf{P}_f)\mathbf{E}$, convective

terms $-\frac{1}{n_{0,f}e\lambda_0}[(\nabla\cdot\dot{\mathbf{P}}_f)\dot{\mathbf{P}}_f+(\dot{\mathbf{P}}_f\cdot\nabla)\dot{\mathbf{P}}_f]$, and nonlocal effects due to pressure, $\frac{5E_F}{3m_f^*c^2}\nabla(\nabla\cdot\mathbf{P}_f)$. Apart from nonlocality induced by the pressure of the electron gas, it is reasonable to expect dissipative effects in the form of viscosity, i.e., friction between particles. By modifying the hydrodynamic model in order to treat the conduction electrons as a viscoelastic fluid [105, 106], a nonlocal term is introduced in Eq. 1.5.24, so that the nonlocal contribution is finally given by: $\frac{5E_F}{3m_f^*c^2}\nabla(\nabla\cdot\mathbf{P}_f+\frac{1}{2}\nabla^2\mathbf{P}_f)$.

The effective free electron mass determines the nonlinear gain arising from Coulomb and magnetic Lorentz terms, while the free electron's density affects the nonlinear gain due to convection. By the same token, m_f^* and $n_{0,f}$ determine the Fermi energy and thus the degree of blueshift of plasmonic resonances, as previously depicted in Eq. 1.3.17.

1.5.3 Method

As mentioned, this model does not need *a priori* knowledge of second and third order susceptibilities. Instead we simulate the nonlinear light-matter interaction using dynamic polarization equations from which, when integrated with Maxwell's equations, harmonic fields can be obtained. In this section we will describe the method we follow to solve the theoretical problem.

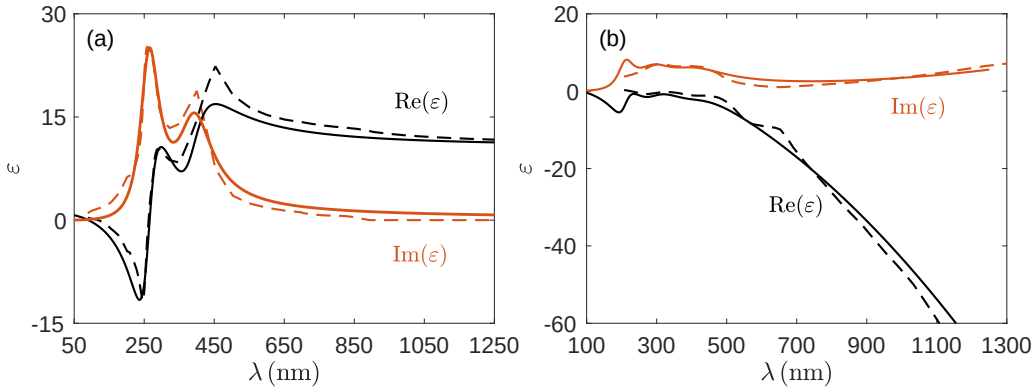

Figure 1.5.1: Real (black dashed curves) and imaginary (red dashed curves) parts of the complex dielectric constant of (a) GaAs and (b) gold found in Palik's handbook [107]. The solid curves are fits to the data through Eqs. 1.5.25 and 1.5.26.

First, we describe the linear dielectric function of the material to be studied using a Drude-Lorentz model, so it will contain a Drude portion followed by one or more Lorentzian resonances,

as shown in Eq. 1.3.14, which we use to fit the data extracted from Palik [107], or from ellipsometry measurements. From this fit we extract values of plasma and resonant frequencies, and damping coefficients. For instance, in Fig. 1.5.1 we have plotted the real and imaginary parts of the complex dielectric constant of (a) GaAs and (b) gold. The dashed curves correspond to experimental data extracted from Palik's handbook [107], which are fitted with theoretical curves of their complex dielectric function. In the case of GaAs free carrier doping is low, ranging from $10^{14}\,\mathrm{cm}^{-3}$ to $10^{17}\,\mathrm{cm}^{-3}$, so that in the visible and near-IR the Drude portion may be neglected and two Lorentzian functions are enough to describe its dielectric behavior. In contrast, in the case of gold a Drude portion must be added as now, a free electron gas and nonlocal effects may contribute to the dielectric constant. This means that the dielectric function of GaAs and gold (Au) can be written through Eqs. 1.5.25 and 1.5.26, respectively:

$$\varepsilon_{\mathrm{GaAs}}(\tilde{\omega}) = 1 - \frac{\tilde{\omega}_{p,b1}^2}{\tilde{\omega}^2 - \tilde{\omega}_{01}^2 + i\tilde{\gamma}_{b1}\tilde{\omega}} - \frac{\tilde{\omega}_{p,b2}^2}{\tilde{\omega}^2 - \tilde{\omega}_{02}^2 + i\tilde{\gamma}_{b2}\tilde{\omega}} \tag{1.5.25}$$

$$\varepsilon_{\mathrm{Au}}(\tilde{\omega}) = 1 - \frac{\tilde{\omega}_{p,f}}{\tilde{\omega}^2 + i\tilde{\gamma}_f\tilde{\omega}} - \frac{\tilde{\omega}_{p,b1}^2}{\tilde{\omega}^2 - \tilde{\omega}_{01}^2 + i\tilde{\gamma}_{b1}\tilde{\omega}} - \frac{\tilde{\omega}_{p,b2}^2}{\tilde{\omega}^2 - \tilde{\omega}_{02}^2 + i\tilde{\gamma}_{b2}\tilde{\omega}} \tag{1.5.26}$$

where $\tilde{\omega} = 1/\lambda$ and it has $\mu\mathrm{m}^{-1}$ units. $\tilde{\omega}_{p,bj} = \omega_{p,bj}^2\lambda_0^2/c^2$ and $\tilde{\omega}_{p,f} = \omega_{p,f}^2\lambda_0^2/c^2$ are the scaled plasma frequencies of free and bound electrons, respectively, with $\omega_{p,bj}^2 = 4\pi n_{0,bj}e^2/m_{bj}^*$ and $\omega_{p,f}^2 = 4\pi n_{0,f}e^2/m_f^*$ (in CGS units). $\tilde{\omega}_{01,02}$ are the scaled resonant frequencies, and $\tilde{\gamma}_b$ and $\tilde{\gamma}_f$ are the scaled damping coefficients for free and bound electrons, respectively. These parameters, which also appear in Eqs. 1.5.13 and 1.5.24 can be extracted by fitting the data shown with dashed curves in Figs. 1.5.1(a) and 1.5.1(b) with Eqs. 1.5.25 and 1.5.26, respectively. In the case of GaAs we obtain $(\tilde{\omega}_{p,b1}, \tilde{\omega}_{01}, \tilde{\gamma}_{b1}) = (5, 2.55, 0.75)$ and $(\tilde{\omega}_{p,b2}, \tilde{\omega}_{02}, \tilde{\gamma}_{b2}) = (9.3, 3.8, 0.95)$, while for gold these parameters correspond to $(\tilde{\omega}_{p,b1}, \tilde{\omega}_{01}, \tilde{\gamma}_{b1}) = (3, 2.75, 0.1)$ and $(\tilde{\omega}_{p,b2}, \tilde{\omega}_{02}, \tilde{\gamma}_{b2}) = (11, 3.3, 0.75)$ for bound electrons, and $(\tilde{\omega}_{p,f}, \tilde{\gamma}_f) = (6.45, 0.05)$ for free electrons. So, in our model, the dielectric constant is not introduced explicitly. Instead, fitting the dielectric constant merely serves the purpose of determining damping coefficients and plasma and resonant frequencies to be inserted in dynamical equations of motion from which a dielectric constant can be retrieved.

Having said that, there are still some parameters in Eqs. 1.5.13 and 1.5.24 to be determined. In the case of bound electrons, the parameters defining the strength of the bulk nonlinearities $\tilde{a} \propto \omega_0^2/L$ and $\tilde{b} \propto \omega_0^2/L^2$ are first approximated considering tabulated values for L and the resonance frequency ω_0. In the cases where two different oscillators (or more) are considered, we assume that $\tilde{a}_1 = \tilde{a}_2$ and $\tilde{b}_1 = \tilde{b}_2$, as the Lorentzian resonances are close to each other. To determine the lattice constant we use average orbital diameters. For solids, L can vary from a fraction of 1 Å to a few Å. For example, the wave function of valence electrons in silicon peaks near 1.32 Å, suggesting that $L_{\mathrm{Si}} \sim 2.6$ Å. However, the highest d-orbital wave function for bound electrons in gold peaks near 0.5 Å, with $L_{\mathrm{Au}} \sim 1$ Å. So, the magnitude of $\tilde{b}$ can change considerably from material to material, and can range between $10^{-6} - 10^{-9}$, depending on atomic orbital radii, densities, and resonant frequencies. As a consequence, the parameters $\tilde{a}$ and $\tilde{b}$ are readjusted taking into account experimental SHG and THG efficiencies, respectively. This means that, once the dielectric constant is fitted to the Lorentzian function, the only free parameters in the equations of motion are the effective mass of electrons, and to some extent the coefficients $\tilde{a}$ and $\tilde{b}$. The effective mass of bound electrons, which determines the strength of the surface and magnetic Lorentz nonlinearities, is extracted from experimental SHG efficiencies.

In the case of free electrons, usually tabulated values for $n_{0,f}$ are used and experimental SHG conversion efficiencies are employed to determine $m^*_{0,f}$. For instance, in gold, the known free electron density $n_{0,f} \sim 5.8 \cdot 10^{22}\,\mathrm{cm}^{-3}$ is used. Since each atom contributes approximately one free electron to the electron density, then it is reasonable to assume that bound electron density may be approximated with the free electron density, so $n_{0,b} \approx n_{0,f}$. The Fermi energy, and so the repercussion of nonlocal effects, depends on both the density and the effective mass of bound electrons, as $E_F = \frac{\hbar^2}{2m^*_{0,f}}(2\pi^2 n_{0,f})^{2/3}$. For typical noble metals and conductive oxides, $\Sigma = \frac{5E_F}{3m^*_f c^2} \sim 10^{-5}$.

2
Harmonic generation in the opaque region of GaAs

In this chapter we present the experimental and numerical simulation results of SHG and THG from a GaAs wafer. Phase-locked harmonic generation in the opaque region of this material is observed and analyzed in transmission and in reflection. As it was explained in Chapter 1.2, these harmonic components are generated close to the surface and can propagate through an opaque material as long as the pump is tuned to a region of transparency or semitransparency and correspond to the inhomogeneous solution of Maxwell's equation with nonlinear polarization sources. While previous studies on harmonic generation from GaAs gave only the total efficiency of the nonlinear signal, in this work we make a step forward to analyze and identify the different nonlinear mechanisms that trigger the processes of SHG and THG, including the second and third order bulk nonlinearities, as well as the surface and the Lorentz contributions to the nonlinear polarization. To this end, we measure the angular and polarization dependence of the harmonic signals.

This chapter is structured as follows. In Section 2.1 we introduce a description of the experimental approach, which includes a description of the experimental set-up and of the laser source that is used. We also explain the calibration procedure we perform to estimate the conversion efficiencies of the nonlinear processes. In Section 2.2 we give a brief description of the sample

that we have studied. Then, in Section 2.3 we present the polarization equations that are used to perform the simulations for the particular case of a semiconductor such as GaAs. We show and comment our results on SHG and THG from GaAs in Section 2.4, and the chapter ends with some conclusions in Section 2.5.

2.1 Experimental approach

2.1.1 Experimental set-up

We pretend to make a detailed experimental study of SH and TH signals generated by a GaAs wafer. Our study includes the measurement of SHG and THG efficiencies and an analysis of their angular and polarization dependence. To this end, we have developed the experimental set-up schematically shown in Fig. 2.1.1. The harmonic fields were generated by exciting the sample with ultrashort pulses coming from a mode-locked fiber laser (FYLA PS50) delivering pulses at 1064 nm with a continuous wave (CW) average output power of 10 W. It emits pulses which are 400 ps in duration at full width half maximum (FWHM) at a repetition rate of 1 MHz. A compressor is used to shorten the duration of the pulses to 13 ps. After that, by means of an acusto-optic modulator, a low frequency train of pulses is selected, usually of the order of kHz. At this point, the average output power has been reduced to 2 W, which corresponds to 2 μJ/pulse. These parameters are summarized in Table 2.1.1.

	λ	τ_{FWHM}	f_{rep}	P_{out}	Energy/pulse
Fiber laser	1064 nm	13 fs	1 MHz	2 W	2 μJ

Table 2.1.1: Fiber laser (FYLA PS50) parameters.

When the fundamental TM-polarized light coming from our laser source enters the set-up, it first faces a half-wave plate which allows the control of polarization of the incident field. Experiments are carried out selecting TM- and TE-polarized fundamental beams. We have to make sure that only fundamental radiation arrives at the sample. To this end, we use a long pass filter (Thorlabs, FGL610) to eliminate any possible SH or TH light eventually generated in the previous elements placed in the beam path. After that, we use a coated plano-convex

lens with focal length f = 200 mm (Thorlabs, LA1708-C) to focus the fundamental beam on the sample plane. As we are dealing with light tuned at 1064 nm, we use a C-coated lens.

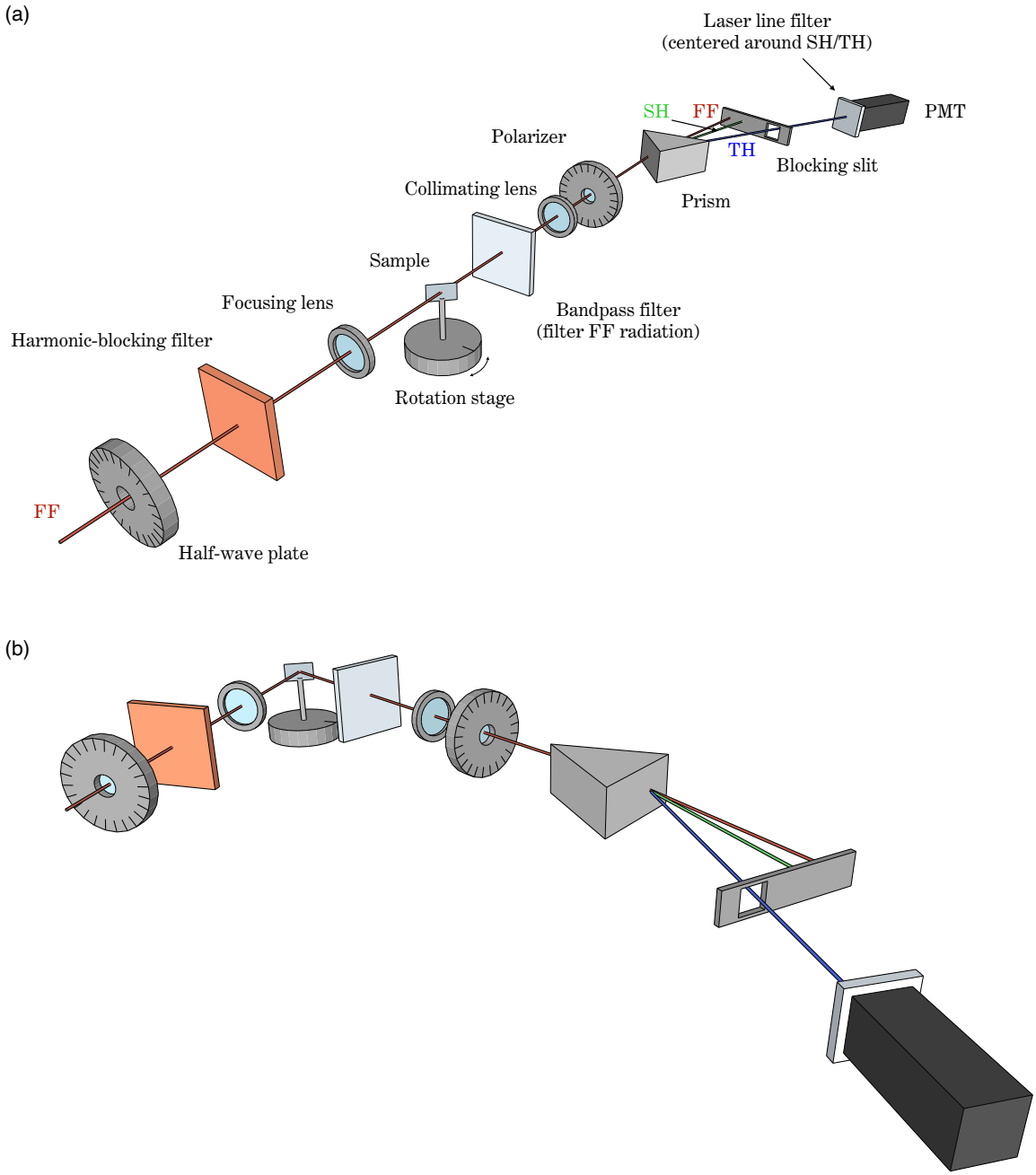

Figure 2.1.1: Schematic representation of the experimental set-up built to measure the angular dependence of SH and TH signals arising from a GaAs wafer in (a) transmission and in (b) reflection.

The sample is mounted on top of a rotation stage that controls the angle at which the fundamental beam is incident to the sample. To make sure that the only harmonic radiation arriving at the detector is the signal generated by the sample, we implement a bandpass filter (Thorlabs, FGS900-A) that attenuates the fundamental beam right after the sample and avoids harmonic generation in other optical elements of the set-up. A plano-convex lens with focal length f = 100 mm (Thorlabs, LA4380-UV) is used to collimate the beam, and with a polarizer (Thorlabs, GTH10M-A) we select the harmonic beam to be either TM- or TE-polarized. Then, by means of a dispersive prism (Thorlabs, PS863) and a blocking slit (Thorlabs, VA100) we separate and obscure the fundamental radiation from the harmonic path. The slit is adjusted depending on weather we want to detect a SH or a TH signal. A lens (Thorlabs, LA4380-UV) between these two objects is sometimes used for a better blocking of the fundamental and TH beam, in case we want to measure SH signals, and of the fundamental and SH beam, in case we want to measure TH signals. Finally, the harmonic radiation arrives at the detector protected with a laser line filter centered around the wavelength we want to detect. We use a laser line filter centered at 532 nm (Thorlabs, FL532-10) for SH measurements, or centered at 355 nm (Thorlabs, FL355-10) for TH measurements. The whole detection system is mounted on top of a rotation arm so that harmonic signals can be measured in transmission, as depicted in Fig. 2.1.1(a), or in reflection, as depicted in Fig. 2.1.1(b). The detector consists of a photomultiplier tube (PMT) (Hamamatsu, H10722-04) whose sensitivity peaks at 400 nm. The PMT is connected to its power supply (Hamamatsu, C10709) through which the control voltage can be changed and the signal can be amplified. The electronic signal arriving at the PMT is recorded by an oscilloscope (Tektronix, DPO3054). The value of the SH (or TH) signal in volts is taken peak-to-peak. In order to properly detect the harmonic signal arriving at the PMT, the source is modulated to deliver a train of N pulses which are repeated at a rate of 1 kHz. In this way, we can integrate on the PMT signal measurement the response of N pulses and obtain a higher signal. The number of selected pulses N is controlled by a software provided by FYLA. The amount of average power arriving at the sample, which is of the order of mW, depends on this

number and is shown in Fig. 2.1.2, in the range of 1 to 16 pulses which were typically used in the experiments.

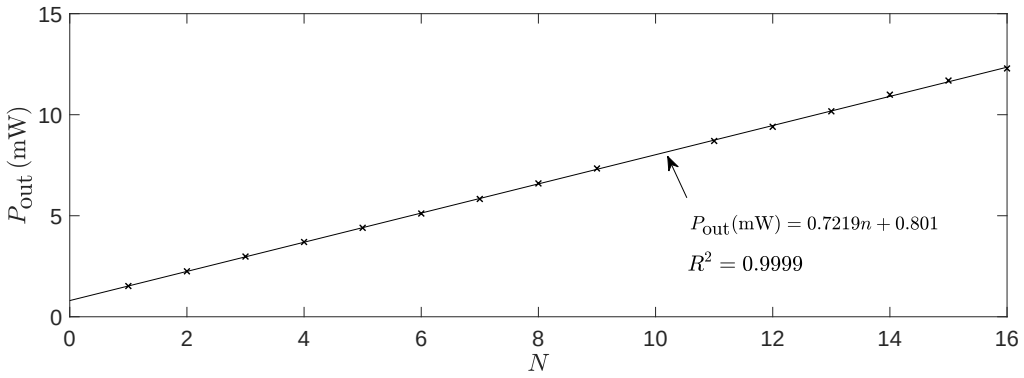

Figure 2.1.2: Output average power as a function of selected pulses measured at the sample place of the set-up. Measurements (cross markers) are well fitted to a line (solid curve).

2.1.2 Description of the calibration procedure

In the previous section we have explained how SH and TH signals arising from a GaAs wafer can be measured. The electronic signal from the PMT is measured with an oscilloscope, from which we obtain a value of the SH or TH signal in volts. If instead, we want to give values of conversion efficiencies of these processes we have to perform a calibration of the system. The calibration is extremely important as we expect to measure very low conversion efficiencies in the range of 10^{-7} to 10^{-13}. This procedure consists of three steps:

1. Measure the responsivity of the PMT at each wavelength to obtain the power/energy of the harmonic signal.
2. Measure the losses in the detection arm (from the sample to the PMT).
3. Calculate the conversion efficiency as the ratio between harmonic and fundamental power (or energy).

We briefly describe the procedure bellow:

1. Measure the responsivity of the PMT. In Fig. 2.1.3 we show a schematic representation of the set-up built to perform this procedure. First we generate efficient harmonic light with a

phase-matched BBO crystal, and we place a bandpass filter (Thorlabs, FGS900-A) to eliminate fundamental radiation. Then, we make sure that the generated harmonic light is TM- or TE-polarized with a polarizer (Thorlabs, GTH10M-A) and a half-wave plate. We perform this procedure for both polarizations. Then, the generated light faces the focusing lens placed in the set-up and goes through the hole detection arm, following the usual harmonic beam path. Now, before the light arrives at the PMT we need to use neutral density (ND) filters in order to attenuate the harmonic radiation generated by the BBO and be able to measure this light with the PMT. We perform the measurement and we obtain a given value in volts that we will call V_{PMT}. Then, we remove the ND filters and replace the PMT with a silicon photodiode (Thorlabs, S120C). We take the measurement and obtain a value of the signal in watts, that we will cal P_{PMT}. With this, we can calculate the responsivity of the PMT as:

$$R_{\mathrm{PMT}} = \frac{V_{\mathrm{PMT}}}{T_{\mathrm{ND}} P_{\mathrm{PMT}}} \,(\mathrm{V/W}) \tag{2.1.1}$$

where T_{ND} is the transmission of the ND filters at the given wavelength. We need to take it into account to make sure that the measurement performed with the photodiode "sees" the same as that taken with the PMT.

2. Measurement of the losses introduced by the detection arm. Notice that we are interested in the amount of harmonic signal just after the sample. We place the silicon photodiode at the sample place and take a measurement of the harmonic power (P_{Sample}). With this, we have the transmission of the detection arm as $T = P_{\mathrm{PMT}}/P_{\mathrm{Sample}}$, and we can calculate the harmonic power (P_{HG}) just after the sample through the following expression:

$$P_{\mathrm{HG}} = \frac{V_{\mathrm{HG}}}{T R_{\mathrm{PMT}}} \,(\mathrm{W}) \tag{2.1.2}$$

where V_{HG} is the value in volts measured with the oscilloscope of the harmonic signal arising from the GaAs wafer. Here we have to take into account the gain added by the PMT, which is changed by its power supply through which the control voltage can be modified. From the datasheet of the product, the following gain curve as a function of control voltage is obtained:

$$G(V) = 10^{8.64385619 logV + 6.301029996} \tag{2.1.3}$$

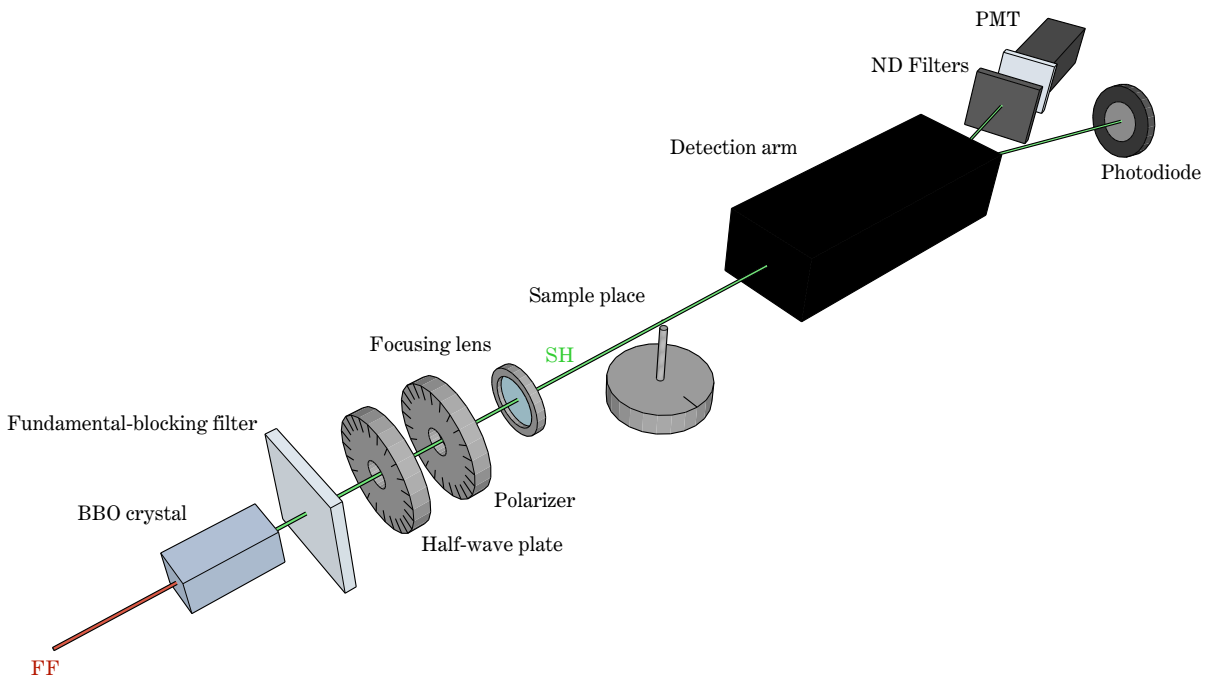

Figure 2.1.3: Schematic representation of the set-up built to measure responsivities of the PMT.

where V is the applied control voltage in volts. Then we define the parameter $g = G(V)/G(0.5V)$. In order to take into account the amplification of the signal added by changing the control voltage, we need to divide the signal measured in the oscilloscope by this value. We take as reference the gain at 0.5 V because it is the one we use to measure the responsivities.

3. Calculate the conversion efficiency. By dividing expression 2.1.2 by the power of the incident field just before the sample, which is measured in every experiment, we obtain the conversion efficiency of the process:

$$e_{\mathrm{HG}} = \frac{P_{\mathrm{HG}}}{P_{\mathrm{FF}}} \tag{2.1.4}$$

2.1.3 Beam characterization and calculus of incident intensity

The amount of generated SH and TH radiation depends on the incident peak intensity I_{FF} ($I_{\mathrm{SH}} \propto I_{\mathrm{FF}}^2$, $I_{\mathrm{TH}} \propto I_{\mathrm{FF}}^3$), so we need to precisely calculate it from the measured parameters. For a Gaussian beam, the pulse peak intensity can be given by:

$$I_{\mathrm{FF}} = \frac{2\sqrt{2ln2}}{\pi^{3/2}} \frac{P_{\mathrm{FF}}}{w_0^2 f_{\mathrm{rep}} \tau_{\mathrm{FWHM}}} \tag{2.1.5}$$

where P_{FF} is the average power of the fundamental field measured just before the sample, w_0 is the beam radius when the intensity drops to $1/e^2$ of the maximum value, which we call the beam waist, f_{rep} is the repetition rate, and τ_{FWHM} is the pulse duration at FWHM. The average power is measured in each experiment, and the repetition rate and pulse duration are known and have been already specified. To determine the beam waist we measure the beam diameter at the sample plane implementing a beam profiler (an Ophir CCD camera with the corresponding software - BeamGage).

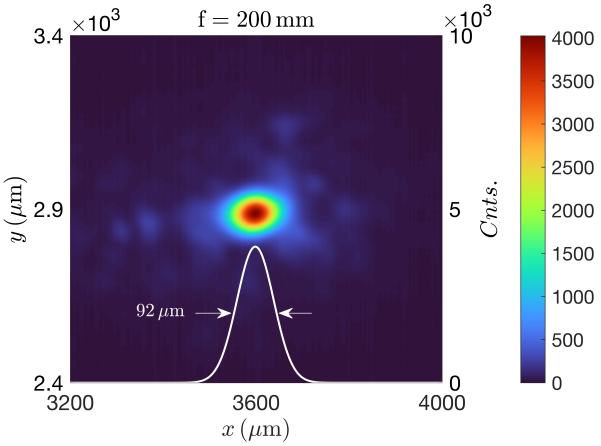

Figure 2.1.4: Measurement of the beam transverse profile generated by the fiber laser at the sample plane. The white curve corresponds to a Gaussian fit performed in the curve obtained from a cut in the x direction from which we obtain the beam diameter at FWHM.

In Fig. 2.1.4 we show measurements of the profile of the fiber laser beam at the sample plane. The white curve corresponds to a Gaussian fit performed to a cut of the experimental beam profile in the x direction. From this curve, we extracted a beam diameter at FWHM ($\mathrm{D_{FWHM}}$) of 92 μm, related to the beam waist through the expression: $\mathrm{D_{FWHM}} = w_0\sqrt{2ln2}$. So finally, we obtain the measured beam waist: $w_0 \sim 78\,\mu$m. In Table 2.1.2 we summarize the parameters of the laser corresponding to experimental conditions, used in the calculation of the incident peak intensity through Eq. 2.1.5. As it can be seen, typical incident pulse peak intensities used in the experiments were $\sim 1\,\mathrm{GW/cm^2}$.

	P_{FF}	f_{rep}	τ_{FWHM}	w_0	I_{FF}
Fiber laser	1.5 mW	1 kHz	13 ps	1 μm	1 GW/cm^2

Table 2.1.2: Fiber laser (FYLA PS50) parameters under experimental conditions.

2.2 Description of the sample

We use an undoped GaAs wafer of 500 μm thickness, grown in the (001) crystallographic direction, purchased from Wafer Technology Ltd. (United Kingdom). It has a diameter of 50.5 mm, it is double side polished and has a resistivity greater than 10^7 Ωcm. In Fig. 2.2.1 we represent schematically the geometric configuration of the sample for TM-polarized incident light, where $\mathbf{E}_\omega$, $\mathbf{H}_\omega$ and $\mathbf{S}_\omega$ are electric and magnetic fields and Poynting vector, respectively, at the fundamental frequency, and θ_{in} is the angle of incidence.

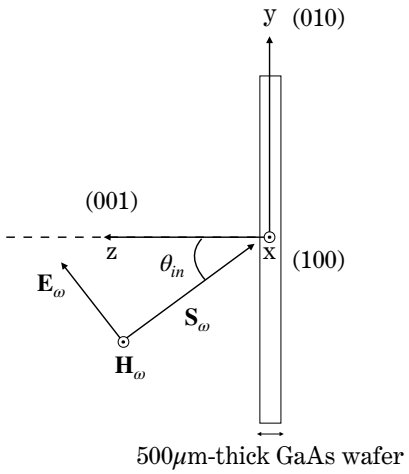

Figure 2.2.1: Schematic representation of the (001) GaAs wafer when TM-polarized light is incident at a certain angle θ_{in}.

2.3 Theoretical approach

For typical GaAs substrates, free carrier doping is rather low, ranging from 10^{14} cm^{-3} to 10^{17} cm^{-3}, so that in the visible and near-IR ranges the Drude portion may be neglected, and only bound electrons are assumed to play a role in SHG and THG. The dielectric function of

GaAs may be described using two Lorentzian functions, each describing a set of bound charges:

$$\varepsilon(\tilde{\omega}) = 1 - \frac{\tilde{\omega}_{p,b1}^2}{\tilde{\omega}^2 - \tilde{\omega}_{01}^2 + i\tilde{\gamma}_{b1}\tilde{\omega}} - \frac{\tilde{\omega}_{p,b2}^2}{\tilde{\omega}^2 - \tilde{\omega}_{02}^2 + i\tilde{\gamma}_{b2}\tilde{\omega}} \tag{2.3.1}$$

where $\tilde{\omega} = 1/\lambda$ and it has μm^{-1} units. As it can be seen, each oscillator can have its own plasma, resonant and damping frequency.

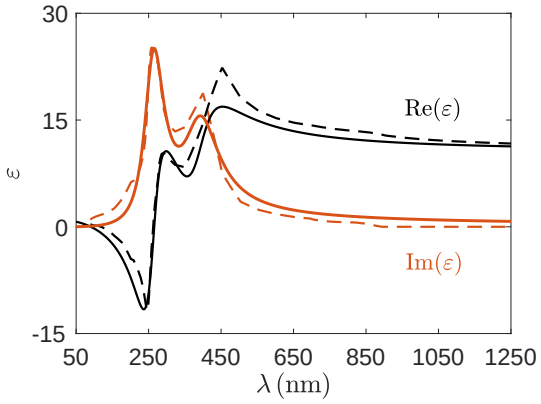

Figure 2.3.1: Real (black dashed curves) and imaginary (red dashed curves) parts of the complex dielectric constant of GaAs found in Palik's handbook [107]. The respective solid curves are the corresponding Lorentzian functions chosen to reproduce the data.

In Fig. 2.3.1 we have plotted data of the real $\text{Re}(\varepsilon)$ and imaginary $\text{Im}(\varepsilon)$ parts of the dielectric function of GaAs extracted from Palik's handbook [107]. It can be seen that the medium is transparent for wavelengths above $\sim 900\,\text{nm}$ and strongly absorptive below it. The solid curves in Fig. 2.3.1 correspond to fittings of the data through Eq. 2.3.1. From this, we obtain the parameters appearing in Eq. 2.3.1: $(\tilde{\omega}_{p,b1}, \tilde{\omega}_{01}, \tilde{\gamma}_{b1}) = (5, 2.55, 0.75)$ and $(\tilde{\omega}_{p,b2}, \tilde{\omega}_{02}, \tilde{\gamma}_{b2}) = (9.3, 3.8, 0.95)$. We recall that in our model, the dielectric constant merely serves the purpose of determining these parameters, which are inserted in dynamical equations of motion. In the case of GaAs, where only bound electrons trigger the nonlinearities, this equation is:

$$\ddot{\mathbf{P}}_{bj} + \tilde{\gamma}_{bj}\dot{\mathbf{P}}_{bj} + \tilde{\omega}_{0j}^2\mathbf{P}_{bj} + \mathbf{P}_{bj}^{\text{NL}} = \frac{n_{0,bj}e^2\lambda_0^2}{m_{bj}^* c^2}\mathbf{E} + \frac{e\lambda_0}{m_{bj}^* c^2}(\mathbf{P}_{bj}\cdot\nabla)\mathbf{E} + \frac{e\lambda_0}{m_{bj}^* c^2}\dot{\mathbf{P}}_{bj}\times\mathbf{H} \tag{2.3.2}$$

where $j = 1, 2$ represents two separate atomic species. Apart from the bulk nonlinearity introduced by the term $\mathbf{P}_{bj}^{\text{NL}} = \tilde{a}\mathbf{P}_{bj}\cdot\mathbf{P}_{bj} - \tilde{b}(\mathbf{P}_{bj}\cdot\mathbf{P}_{bj})\mathbf{P}_{bj}$, Eq. 2.3.2 contains also a surface

contribution triggered by the spatial derivatives of the fields $\frac{e\lambda_0}{m^*_{bj}c^2}(\mathbf{P}_{bj}\cdot\nabla)\mathbf{E}$, and a nonlinear contribution arising from the magnetic portion of the Lorentz force $\frac{e\lambda_0}{m^*_{bj}c^2}\dot{\mathbf{P}}_{bj}\times\mathbf{H}$. The total polarization inserted into Maxwell's equations is $\mathbf{P}_{\text{total}} = \mathbf{P}_{b1} + \mathbf{P}_{b2}$. GaAs is a non-centrosymmetric material, so $\mathbf{P}_b^{\text{NL}}$ contains both second ($P_i^{\text{NL}^{(2)}} = \sum_{j=1,3}\sum_{k=1,3}\tilde{a}_{i,j,k}P_jP_k$) and third ($P_i^{\text{NL}^{(3)}} = \sum_{j=1,3}\sum_{k=1,3}\sum_{l=1,3}\tilde{b}_{i,j,k,l}P_jP_kP_l$) order bulk nonlinearities, which are to be interpreted as three-component vectors given by:

$$\begin{pmatrix} P_{j,x}^{\text{NL}^{(2)}} \\ P_{j,y}^{\text{NL}^{(2)}} \\ P_{j,z}^{\text{NL}^{(2)}} \end{pmatrix} = \tilde{a}_j \begin{pmatrix} P_{j,z}P_{j,y} \\ P_{j,z}P_{j,x} \\ P_{j,y}P_{j,x} \end{pmatrix} \tag{2.3.3}$$

and

$$\begin{pmatrix} P_{j,x}^{\text{NL}^{(3)}} \\ P_{j,y}^{\text{NL}^{(3)}} \\ P_{j,z}^{\text{NL}^{(3)}} \end{pmatrix} = \tilde{b}_j \begin{pmatrix} (P_{j,x}^2 + P_{j,y}^2 + P_{j,z}^2)P_{j,x} \\ (P_{j,x}^2 + P_{j,y}^2 + P_{j,z}^2)P_{j,y} \\ (P_{j,x}^2 + P_{j,y}^2 + P_{j,z}^2)P_{j,z} \end{pmatrix} \tag{2.3.4}$$

as it was already outlined in Chapter 1.5.3. Due to the fact that the resonances are closely spaced, we assume that $\tilde{a}_1 \approx \tilde{a}_2 = \tilde{a}$ and $\tilde{b}_1 \approx \tilde{b}_2 = \tilde{b}$. However, the two electron spices probably have different densities and effective masses.

2.4 Results and discussion

Experiments have been carried out with picosecond pulses tuned at 1064 nm being incident on a GaAs wafer grown in the (001) crystallographic orientation, with typical peak pump pulse intensities of $\sim 1\,\text{GW/cm}^2$. We have performed measurements of the SH and TH generated signals as a function of incident angle and polarization.

In Figs. 2.4.1, 2.4.2 and 2.4.3 we show experimental results of the (a) transmitted and (b) reflected SHG conversion efficiencies (η_{SHG}) for the GaAs wafer as a function of incident angle (θ_{in}) and polarization, depicted with cross markers. As can be immediately inferred, a transmitted SH component is generated and propagated through a 500 μm-thick sample in the presence of strong absorption, corresponding to the propagation of the phase-locked component. Measurements are compared with numerical simulations, which are depicted with solid curves. Simulations were performed with incident pulses whose temporal duration ranged from 50 fs to 100 fs, were tuned at 1064 nm and were incident on a 10 μm-thick GaAs wafer assumed to

have (001) crystallographic characteristics. The method is ill-suited to model long substrates. Nevertheless, our simulations suggest that increasing pulse duration and medium thickness simultaneously yields only marginal changes to the overall aspects of the results. Peak pump pulse power densities of $\sim 2\,\mathrm{GW/cm^2}$ were used and the polarization of the incident fundamental pulse was selected to be either TE [$\mathbf{E} = (E_x, 0, 0)$], or TM [$\mathbf{E} = (0, E_y, E_z)$].

In Fig. 2.4.1 it can be seen that a TM-polarized SH component was measured, which is a clear indication of the contribution of the surface and Lorentz terms in this process. Let's see what happens with SHG if we neglect both surface and magnetic Lorentz terms in Eq. 2.3.2, and only take into account the bulk nonlinear contribution. Then, if we are incident with a TE-polarized field [$\mathbf{E} = (E_x, 0, 0)$], and we apply Eq. 2.3.3, we see that $\mathbf{P}^{\mathrm{NL}^{(2)}} = 0$, which means that no SH radiation is generated. If a TM-polarized incident field is used instead [$\mathbf{E} = (0, E_y, E_z)$], then a TE-polarized SH component is generated as $\mathbf{P}^{\mathrm{NL}^{(2)}} = \tilde{a}(P_z P_y, 0, 0)$. So, with this we can explain the presence of a bulk TE-polarized SH component generated when the sample was illuminated with TM-polarized light, as shown in Fig. 2.4.2. However, two other components were observed. When an incident TM-polarized field was used, a TM-polarized SH component was also detected, which arises from both surface and magnetic Lorentz contributions (Fig. 2.4.1). Apart from that, a TM-polarized SH component is triggered by the magnetic Lorentz nonlinearity when the fundamental field is TE-polarized (Fig. 2.4.3). With this, it is obvious that the surface and the magnetic Lorentz contributions to the total polarization, usually neglected in front of the bulk contribution, play a crucial role in the nonlinear response of a 500 μm-thick GaAs sample. Moreover, in our measurements surface and Lorentz component efficiencies are of order 10^{-7} and 10^{-8}. In contrast, bulk conversion efficiencies are of order 10^{-9}. As a result, it is clear that in our GaAs sample surface and Lorentz terms play a more important role than the bulk in the generation of the SH field. With this comparative experimental-theoretical study we extracted an effective mass of $m^*_{b1} = m^*_{b2} = 0.015 m_e$, and a second order nonlinear scaled coefficient of $\tilde{a} = 2.5 \cdot 10^{-6}$ was used.

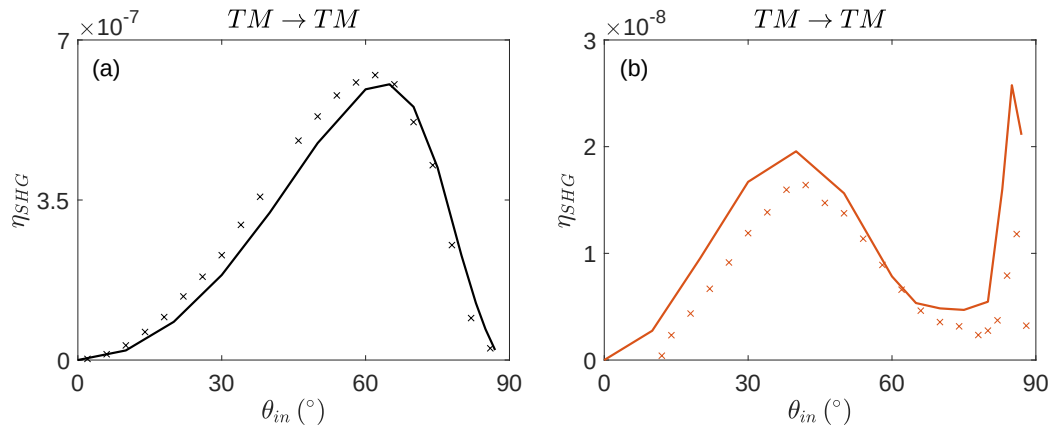

Figure 2.4.1: (a) Transmitted and (b) reflected angular dependence of the measured (cross markers) and predicted (solid curves) surface-generated TM-polarized SHG efficiencies triggered by a TM-polarized incident field.

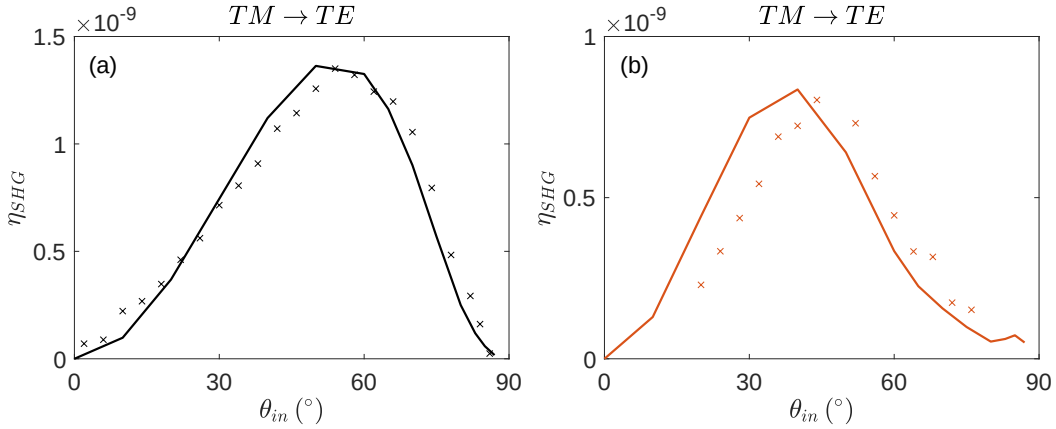

Figure 2.4.2: (a) Transmitted and (b) reflected angular dependence of the measured (cross markers) and predicted (solid curves) bulk-generated TE-polarized SHG efficiencies triggered by a TM-polarized incident field.

It can also be seen in Figs. 2.4.1, 2.4.2 and 2.4.3 that experimental and predicted results agree well regarding amplitude of the signal and peak position in most of the cases. However, there are some discrepancies between them. In Fig. 2.4.3(b), the result of the simulation shows a somewhat more complicated structure than the measured signal. In the bulk-generated SH component in the case of reflection (Fig. 2.4.2(b)), the measured SH peak is shifted to larger angles by approximately 10°, and the maximum amplitude predicted by the simulation is nearly a

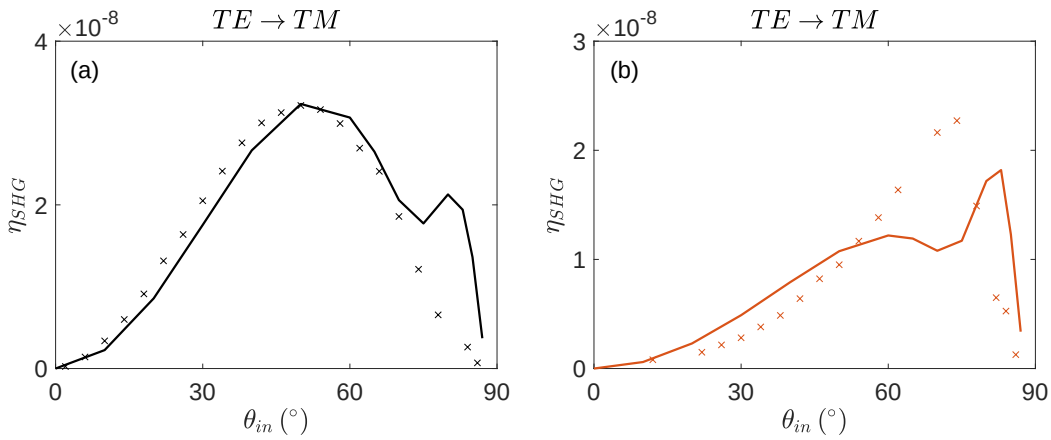

Figure 2.4.3: (a) Transmitted and (b) reflected angular dependence of the measured (cross markers) and predicted (solid curves) TM-polarized SHG efficiencies triggered by a TE-polarized incident field. The SH signal arises mostly from the magnetic Lorentz nonlinearity.

factor of 13 smaller than the measured signal (in the plot the predicted curve is multiplied by 13). We try to explain these issues with the following reasoning. In our calculations we have assumed a GaAs substrate of uniform composition from entrance to exit, having no relevant surface features. However, it is known that MBE-grown (molecular beam epitaxy) GaAs may display extended regions of space charges, or depletion layers, due to the existence of surface states that change the symmetry of the bulk inside a thin surface region [108]. In addition, the surface may be either Ga- or As-rich, or have a thin Gallium oxide layer that also displays a dielectric anisotropy [109] that may result in direction-dependent effective masses, damping coefficients and resonance frequencies. Notwithstanding this differences, we find that the nonlinear oscillator model exemplified by Eq. 2.3.2 predicts rather well surface SHG, with most discrepancies arising from the bulk-generated SH signal.

In Fig. 2.4.4 we have plotted the same results shown in Figs. 2.4.1, 2.4.2 and 2.4.3 but in a different configuration. In Figs. 2.4.4(a) and 2.4.4(b) we show measurements and simulations, respectively, of transmitted SHG efficiencies for the GaAs wafer for the three different polarization cases. As it can be seen, the measured ratio between them are well reproduced in the simulations. In Figs. 2.4.4(c) and 2.4.4(d) we plot the same situation for the reflection case.

Despite of some discrepancies already mentioned, the overall aspect of the measured results agree quite well with the simulations.

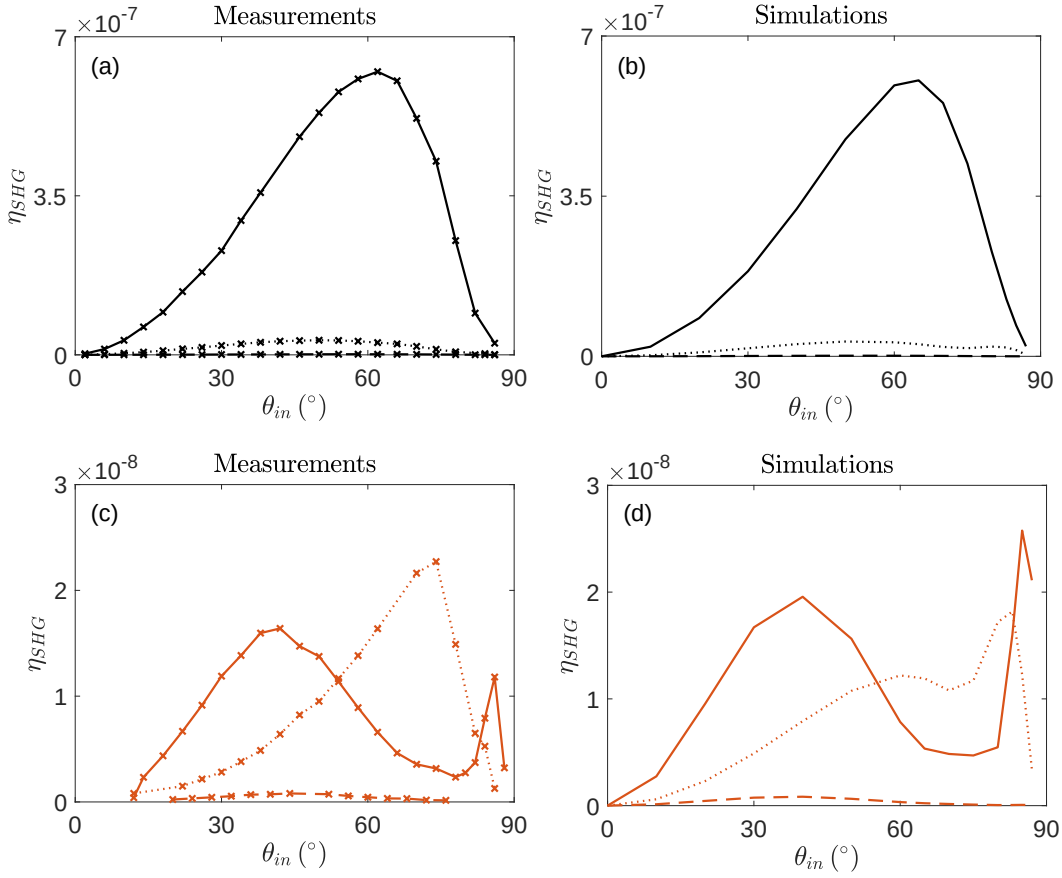

Figure 2.4.4: [(a) and (c)] Measured and [(b) and (d)] predicted SHG efficiencies as a function of incident angle obtained in transmission (black) and in reflection (red). Solid curves: SH generated by the surface and magnetic Lorentz contributions. Pointed curves: surface-generated SH. Dashed curves: SH generated by the bulk contribution.

Transmitted THG efficiencies (η_{THG}) were also measured as a function of incident angle. The results are summarized in Fig. 2.4.5, with cross markers, along with the numerical simulation results, depicted with solid curves, for TM- and TE-polarized pump pulses. As it can be seen, the measured data agrees relatively well with our predictions, in which we used $\tilde{b} = 10^{-7}$. In this case, the bulk contribution to the nonlinear polarization dominates the process, and based on Eq. 2.3.4, it is expected that THG is triggered by either a TM- or a TE-polarized pump generating a TM- and a TE-polarized TH, respectively, which is corroborated by our

experiments. Reflected THG is more than one order of magnitude smaller in both cases, and follows the angular dependence displayed by the transmitted THG. We remark that the TH is tuned directly to the absorption resonance located near 355 nm, where one would have no expectations to register any transmitted signal.

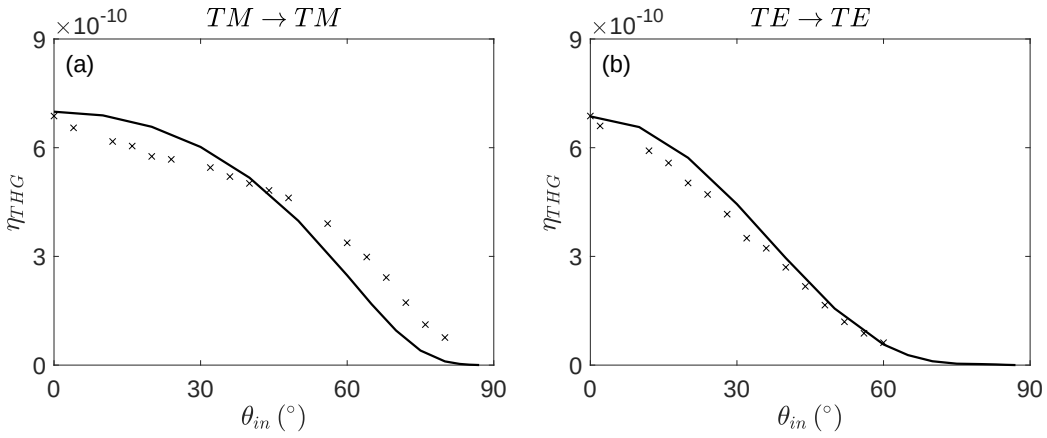

Figure 2.4.5: Angular dependence of the measured (cross markers) and predicted (solid curves) transmitted THG efficiencies as a function of incident pump polarization. (a) A TM-polarized pump generates a TM-polarized TH signal, and (b) a TE-polarized pump triggers a TE-polarized TH signal. Both of them arise mostly from the bulk contribution to the nonlinear polarization.

2.5 Conclusions and summary

In summary, we have experimentally demonstrated different components of SHG and THG in the opaque region of GaAs, corresponding to the phase-locked harmonic generation and we have identified and analyzed in detail surface and bulk nonlinear sources. We have shown that the experimental data fits well the numerical simulations performed using a theoretical model that includes different contributions to the nonlinear process arising from the bulk, surface and magnetic terms, in the presence of linear and nonlinear dispersion. The polarization dependence of the measured harmonics allows us to discern the relative contribution of each nonlinear term to the overall nonlinear conversion efficiency. A detailed study of these phenomena can be used to obtain relevant information about material parameters, such as effective mass of bound electrons, and second and third order oscillator parameters.

3
Harmonic generation from Si in the visible and UV

This chapter is divided in three main sections. In Section 3.1 we report measurements of SHG and THG from an amorphous silicon nanolayer and a crystalline silicon wafer performed in our laboratory. The objective of this study is to inspection the differences of the nonlinear response in amorphous and crystalline silicon. We explain the approach used for this experimental study in Section 3.1.1, and the samples in Section 3.1.2. Then, in Section 3.1.3, we explain how the theoretical model is adapted for the case of amorphous and crystalline silicon. Finally, we show the experimental and theoretical results of SHG and THG in Section 3.1.4. In Section 3.2, we introduce results obtained from a 1340 nm- and a 200 nm-thick undoped crystalline silicon membranes. Following the usual order, the experimental approach, a brief description of the samples and the theoretical approach are reported in Sections 3.2.1, 3.2.2 and 3.2.3, respectively. Then, results are shown in Section 3.2.4. Using experimental results and simulations we identify the effective mass of bound electrons, which determines SHG efficiency, and oscillator parameters that control third order processes. We can then accurately predict the nonlinear optical properties of complex structures, without including and artificially separating the effective $\chi^{(2)}$ into surface and volume contributions, and by simultaneously including effects of linear and nonlinear dispersion. For this reason, we conclude this chapter with Section 3.3, where preliminary

simulated results on SHG and THG from a nanostructure made of crystalline silicon nanowires are reported. The objective is to show that by studying simple samples, like a nanolayer or a wafer, and using our hydrodynamic model, we are able to predict the nonlinear response in more complex nanostructures which are nowadays designed and fabricated as they are able to enhance the nonlinear response of the material. This step is crucial in the field of nanophotonics in order to have an efficient nanodevice. Finally, we end up with some conclusions in Section 3.4.

3.1 Amorphous and crystalline silicon

3.1.1 Experimental approach

The study consisted on measuring SHG and THG efficiencies from an amorphous silicon nanolayer and a crystalline silicon wafer when being excited with two different laser sources. The first one consists of a fiber laser delivering picosecond pulses at 1064 nm, which was introduced in Chapter 2. The second one consists of a Ti:Sapphire oscillator (Coherent, Mira 900-F). It is a mode-locked femtosecond laser system emitting pulses at $\lambda = 800\,\text{nm}$, which is pumped by a continuous wave green laser (Coherent, Verdi). The pulses are 140 fs in duration at FWHM (τ_{FWHM}) and are emitted at a repetition rate (f_{rep}) of 76 MHz, with a CW output average power (P_{out}) of 1.7 W, corresponding to approximately 22 nJ/pulse. These parameters are summarized in Table 3.1.1.

	λ	τ_{FWHM}	f_{rep}	P_{out}	Energy/pulse
Ti:Sapphire	800 nm	140 fs	76 MHz	1.7 W	22 nJ

Table 3.1.1: Ti:Sapphire oscillator (Coherent, Mira 900-F) parameters.

The beam of this source was characterized with a CCD camera (Ophir CCD camera with the corresponding software - BeamGage). We obtained a beam waist $w_0 \sim 34\,\mu\text{m}$, corresponding to incident pulse peak intensities of $\sim 3.5\,\text{GW/cm}^2$. We also characterized the beam of the fiber laser source. A smaller beam waist than that obtained in Chapter 2 for the same laser source was measured because now a lens of focusing length f = 100 mm (Thorlabs, LA1509-C)

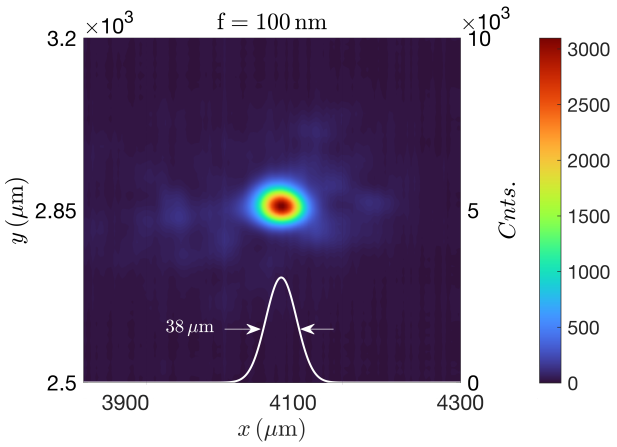

Figure 3.1.1: Measurement of the beam transverse profile generated by the fiber laser at the sample plane. The white curve correspond to a Gaussian fit performed in the curve obtained from a cut in the x direction from which we obtain the beam diameter at FWHM.

was used to focus the beam on the sample plane. With this, a higher fundamental pulse peak intensity could be used in the experiments. This measurement is shown in Fig. 3.1.1, where we show the beam transverse profile at the sample plane and the white curve corresponds to a Gaussian fit performed to a cut of the experimental beam profile in the x direction. From this we can extract a beam diameter at FWHM of $\sim 38\,\mu$m, corresponding to $w_0 \sim 32\,\mu$m. As a consequence we obtained a peak pump pulse intensity of $\sim 4.5\,\mathrm{GW/cm^2}$. In Table 3.1.2 we summarize the parameters of both laser sources under experimental conditions, where it can be seen that typical peak pump pulse intensities were $\sim 4\,\mathrm{GW/cm^2}$.

	P_{FF}	f_{rep}	τ_{FWHM}	w_0	I_{FF}
Ti:Sapphire	1 W	76 MHz	140 fs	34 μm	3.5 GW/cm^2
Fiber laser	1.5 mW	1 kHz	13 ps	32 μm	4.5 GW/cm^2

Table 3.1.2: Laser parameters under experimental conditions.

SHG and THG signals were measured using the same set-up described in Chapter 2. However, when pumping the samples at 800 nm, some of the elements had to be replaced. A B-coated lens with focusing length f = 100 mm (Thorlabs, LA1509-B) was used to focus the beam on the sample plane. For the detection of SHG at 400 nm, another filter (Thorlabs, FGB37-A) was used to attenuate the fundamental radiation, and the PMT was protected with a bandpass filter

centered at 400 nm (Thorlabs, FBH400-40). In order to accurately detect SH signals reaching the PMT when the Ti:Sapphire source was used in the experiments, a mechanical shopper (Scitec, 300CD Rotating Optical Chopper) was placed in the beam path before reaching the sample in order to modulate the fundamental signal at typical frequencies of order of 100 Hz with a duty cycle of 50%. On the other hand, when the fiber laser was used, the source was modulated so it delivered a train of N pulses which are repeated at a rate of 1 kHz. This way, the response of N pulses can be integrated on the PMT signal measurements and a larger signal is obtained. The amount of average power arriving at the sample depends on this number of pulses, as shown in Chapter 2.1.

Conversion efficiencies were estimated performing the same calibration procedure as that explained in Chapter 2.1.

3.1.2 Description of the samples

The crystalline silicon wafer was purchased from Biotain (Hong Kong, China). It consists of a 500 μm-thick undoped crystalline silicon wafer grown in the (100) crystallographic direction. It has a diameter of 50.8 mm, it is double side polished, and has a resistivity greater than 1000 Ωcm.

The amorphous silicon sample consisted on a 25 nm-thick nanolayer, and it was magnetron sputtered [31, 110] from a silicon target on transparent fused silica glass.

We performed X-Ray diffraction (XRD) measurements on both samples to prove their amorphous/crystalline properties. The diffraction patterns obtained from the amorphous silicon nanolayer and the crystalline silicon wafer are shown in Figs. 3.1.2(a) and 3.1.2(b), respectively. The diffraction patterns of a crystalline sample are very different with respect to an amorphous sample. A crystalline sample XRD results in very narrow intense peaks, corresponding to its crystal planes. On the contrary, an amorphous sample results in a very broad peak or shoulder with low intensity and at low angles. These characteristics are reflected in our results shown in Fig. 3.1.2. In Fig. 3.1.2(c) we show an schematic representation of the problem, where $\mathbf{E}_\omega$, $\mathbf{B}_\omega$ and $\mathbf{S}_\omega$ are electric and magnetic fields and Poynting vector at the fundamental frequency, re-

spectively. In the figure, TM-polarized light is incident with a certain angle θ_{in} to an amorphous silicon nanolayer or a crystalline silicon wafer having (100) crystallographic characteristics.

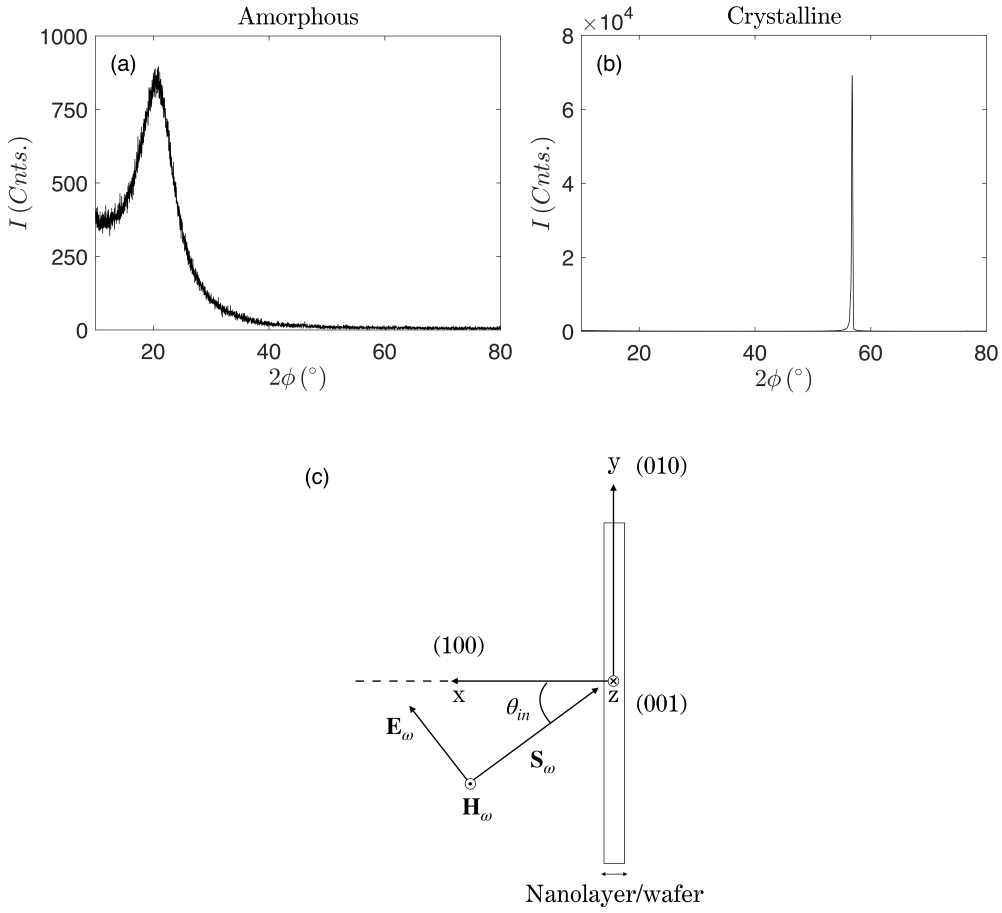

Figure 3.1.2: XRD measurements performed on the (a) 25 nm-thick amorphous silicon layer and (b) crystalline silicon wafer. (c) Schematic representation of the nanolayer/wafer when TM-polarized light is incident at a certain angle θ_{in}.

3.1.3 Theoretical approach

As well as in the case of GaAs, for typical silicon substrates, free carrier doping is rather low, so that they can be assumed to play a minor role in the linear and nonlinear properties of the material. This means that the dielectric constant of silicon can be described with the Lorentz model. In the case of amorphous silicon, just one Lorentzian resonance is enough to fit experimental data, while in its crystalline configuration, the dielectric function is accurately

described by taking into account two different bound spices. Then, the dielectric constant of amorphous ($\alpha-$Si) and crystalline silicon ($c-$Si) can be given by Eqs. 3.1.1 and 3.1.2, respectively:

$$\varepsilon_{\alpha-\mathrm{Si}}(\tilde{\omega}) = 1 - \frac{\tilde{\omega}_{p,b}^2}{\tilde{\omega}^2 - \tilde{\omega}_0^2 + i\tilde{\gamma}_b\tilde{\omega}} \tag{3.1.1}$$

$$\varepsilon_{c-\mathrm{Si}}(\tilde{\omega}) = 1 - \frac{\tilde{\omega}_{p,b1}^2}{\tilde{\omega}^2 - \tilde{\omega}_{01}^2 + i\tilde{\gamma}_{b1}\tilde{\omega}} - \frac{\tilde{\omega}_{p,b2}^2}{\tilde{\omega}^2 - \tilde{\omega}_{02}^2 + i\tilde{\gamma}_{b2}\tilde{\omega}} \tag{3.1.2}$$

where $\tilde{\omega} = 1/\lambda$ and it has $\mu\mathrm{m}^{-1}$ units. In Figs. 3.1.3(a) and 3.1.3(b) we have plotted data of the real $\mathrm{Re}(\varepsilon)$ and imaginary $\mathrm{Im}(\varepsilon)$ parts of the dielectric function of amorphous and crystalline silicon, respectively. The amorphous silicon sample was analyzed using a variable angle spectroscopic ellipsometer (Woollam, VASE), while the complex dielectric data of crystalline silicon was extracted from Palik's handbook [107]. These data have been fitted with Eqs. 3.1.1 and 3.1.2. From the fitting we have obtained $(\tilde{\omega}_{p,b}, \tilde{\omega}_0, \tilde{\gamma}_b) = (9, 2.8, 1.15)$ in the case of amorphous silicon and $(\tilde{\omega}_{p,b1}, \tilde{\omega}_{01}, \tilde{\gamma}_{b1}) = (3, 2.75, 0.1)$ and $(\tilde{\omega}_{p,b2}, \tilde{\omega}_{02}, \tilde{\gamma}_{b2}) = (11, 3.3, 0.75)$ in the case of crystalline silicon.

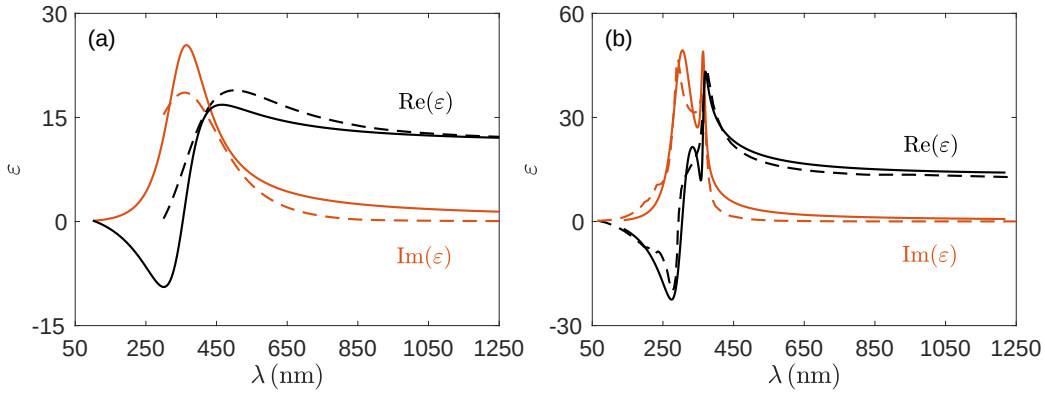

Figure 3.1.3: Real (black dashed curves) and imaginary (red dashed curves) parts of the complex dielectric constant of (a) amorphous and (b) crystalline silicon. The respective solid curves are the corresponding Lorentzian functions chosen to reproduce the data.

As we saw in Chapter 1.5, the dynamic equation of motion for semiconductors like silicon can be written as:

$$\ddot{\mathbf{P}}_{bj} + \tilde{\gamma}_{bj}\dot{\mathbf{P}}_{bj} + \tilde{\omega}_{0j}^2\mathbf{P}_{bj} + \mathbf{P}_{bj}^{\mathrm{NL}} = \frac{n_{0,bj}e^2\lambda_0^2}{m_{bj}^* c^2}\mathbf{E} + \frac{e\lambda_0}{m_{bj}^* c^2}(\mathbf{P}_{bj}\cdot\nabla)\mathbf{E} + \frac{e\lambda_0}{m_{bj}^* c^2}\dot{\mathbf{P}}_{bj}\times\mathbf{H} \tag{3.1.3}$$

where $j = 1$ in the case of amorphous silicon and $j = 1, 2$ in the case of crystalline silicon, corresponding to one or two Lorentzian resonances appearing in the dielectric response of the material. The total polarization inserted into Maxwell's equations is the sum $\mathbf{P}_{\text{total}} = \mathbf{P}_{b1} + \mathbf{P}_{b2}$. Silicon is a centrosymmetric material, so $\mathbf{P}_{bj}^{\text{NL}}$ contains only third order nonlinearities: $\mathbf{P}_{bj}^{\text{NL}} = -\tilde{b}_j(\mathbf{P}_{bj} \cdot \mathbf{P}_{bj})\mathbf{P}_{bj}$, and in the case of crystalline silicon, it is assumed that $\tilde{b}_1 \approx \tilde{b}_2 = \tilde{b}$, as the resonances are closely spaced. Apart from this third order bulk nonlinearity, Eq. 3.1.3 also contains a surface contribution triggered by the spatial derivatives of the fields $\frac{e\lambda_0}{m_{bj}^* c^2}(\mathbf{P}_{bj} \cdot \nabla)\mathbf{E}$, and a nonlinear contribution arising from the magnetic portion of the Lorentz force $\frac{e\lambda_0}{m_{bj}^* c^2}\dot{\mathbf{P}}_{bj} \times \mathbf{H}$.

3.1.4 Results and discussion

Experiments have been carried out pumping our samples with picosecond and femtosecond pulses tuned at 1064 nm and 800 nm, respectively. Typical incident pulse peak intensities used in the experiments were $\sim 4\,\text{GW/cm}^2$, and we recall that our set-up, schematically depicted in Fig. 2.1.1, allows us to take measurements as a function of fundamental and harmonic polarization, and incident angle. For what the simulations are concerned, 100 fs pulses tuned at either 800 nm or 1064 nm were incident on a free-standing 25 nm-thick amorphous silicon layer and on a 10 μm-thick crystalline silicon wafer assumed to have (100) crystallographic orientation, with pump pulse power densities of $\sim 4\,\text{GW/cm}^2$.

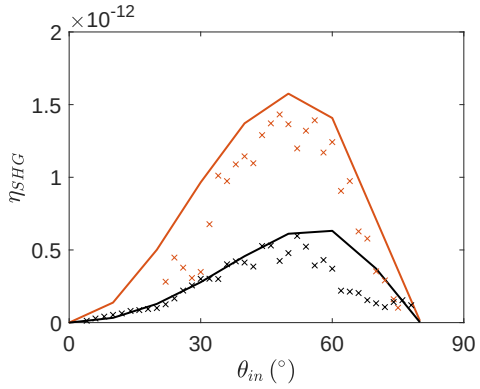

Figure 3.1.4: Transmitted (black) and reflected (red) angular dependence of the measured (cross markers) and predicted (solid curves) TM-polarized SHG efficiencies triggered by a TM-polarized pump pulse tuned at 800 nm.

We first introduce the results we have obtained on amorphous silicon. In Fig. 3.1.4 we show transmitted and reflected SHG efficiencies (η_{SHG}) as a function of incident angle when the sample is pumped at 800 nm. Both fundamental and SH fields were selected to be TM-polarized. It can be observed that the reflected experimental and theoretical curves agree well in shape and amplitude, having a maximum around 50° angle of incidence, leading to a conversion efficiency of $\sim 1.5 \cdot 10^{-12}$. The results for the transmission case are also satisfactory. Both measured and predicted maximum efficiencies correspond to $\sim 0.5 \cdot 10^{-12}$, and the shape of the curves are in good agreement. Another thing that is reproduced in both experimental and theoretical results is the ratio between transmitted and reflected efficiencies.

In Figs. 3.1.5(a) and 3.1.5(b) we show transmitted and reflected SHG efficiencies, respectively, as functions of incident angle when both fundamental and SH fields are TM-polarized, and pump wavelength is tuned at 1064 nm. Experimental efficiencies are depicted with cross markers and are shown in the left y-axis, while theoretical predictions are depicted with solid curves and shown in the right y-axis. In both cases experimental and simulated curves agree remarkably well, showing a maximum detected and predicted efficiency around 50° incident angle for both transmission and reflected cases. TM-polarized SHG efficiencies as a function of incident angle generated by a TE-polarized incident field tuned at 1064 nm are shown in Figs. 3.1.5(c) and 3.1.5(d) for transmission and reflection cases, respectively. Experimental and predicted curves are shown in a configuration similar to that in Figs. 3.1.5(a) and 3.1.5(b). Once again, both transmitted and reflected experimental and theoretical results agree remarkably well in shape and amplitude. From the experimental-theoretical comparison shown in Figs. 3.1.4 and 3.1.5 we extracted an effective mass for bound electrons of $m_b^* = 2.5 m_e$. We note that some discrepancies can be found between experimental and theoretical efficiencies in the 1064 nm pump wavelength case. However, we recall that our efficiencies are calculated making no assumptions about effective surface or volume nonlinearities. Once the effective mass and densities are fixed, the same values are used in all the cases. We also note that in the case of amorphous silicon, the TE-polarized SH component generated by a TM-polarized incident field is not observed, differently

from the GaAs case. We recall that this SH component is generated by the bulk nonlinearity, as it was shown in Chapter 2. As silicon is a centrosymmetric material, it is expected that this component is not observed, which is in agreement with our results.

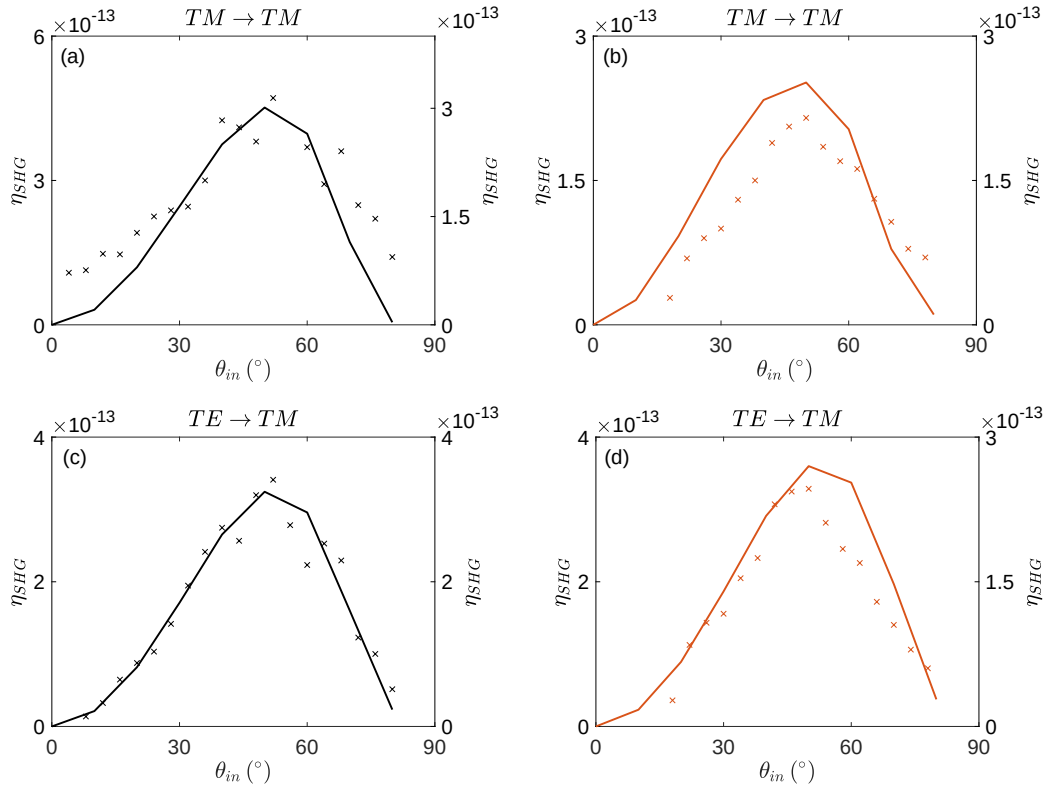

Figure 3.1.5: [(a)-(b)] (a) Transmitted and (b) reflected angular dependence of the measured (cross markers, left y-axis) and predicted (solid curves, right y-axis) TM-polarized SHG efficiencies triggered by a TM-polarized pump pulse tuned at 1064 nm. [(c)-(d)] (c) Transmitted and (d) reflected angular dependence of the measured (cross markers, left y-axis) and predicted (solid curves, right y-axis) TM-polarized SHG efficiencies triggered by a TE-polarized pump pulse tuned at 1064 nm.

Experimental and theoretical results of the angular dependence of THG efficiencies (η_{THG}) for the pump tuned at 1064 nm are shown in Fig. 3.1.6. A TM-polarized TH signals is detected when the incident field is TM-polarized, while a TE-polarized incident field generates a TE-polarized TH signal. These generated curves are shown in Figs. 3.1.6(a-b) and 3.1.6(c-d), respectively. Once again, both experimental and theoretical results agree remarkably well in

shape and amplitude showing a maximum efficiency at normal incidence. Simulations were obtained with $\tilde{b} = 1.2 \cdot 10^{-7}$.

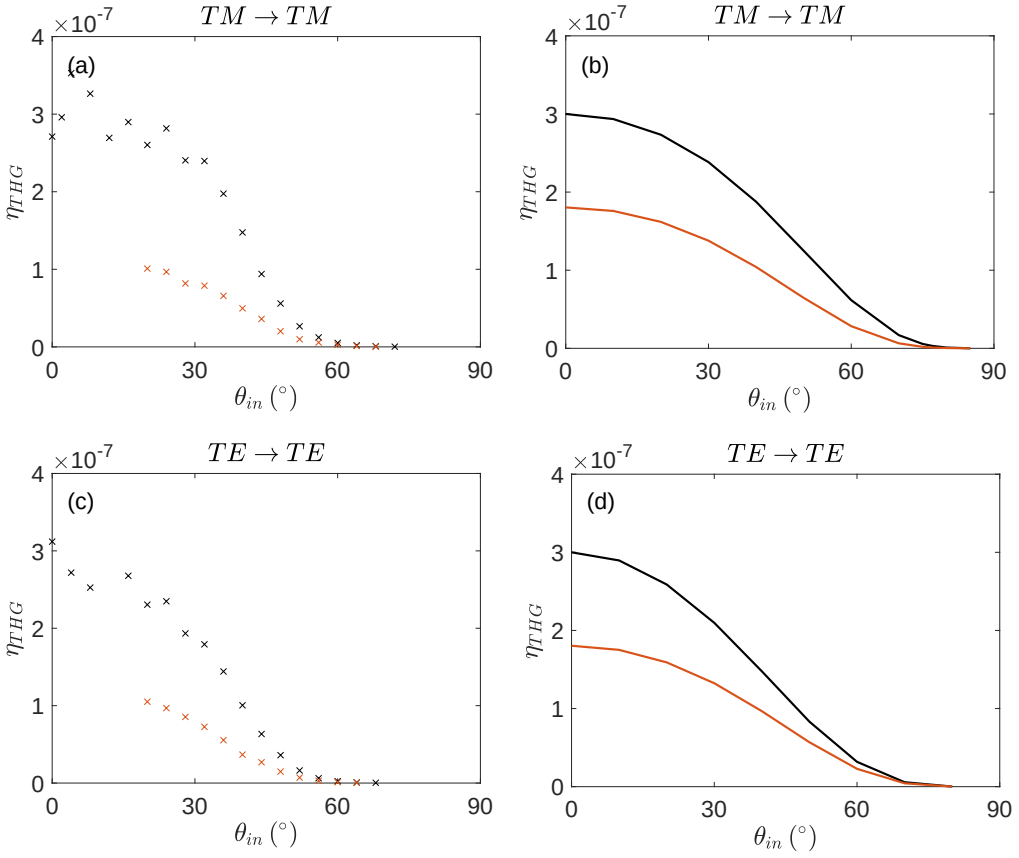

Figure 3.1.6: [(a)-(b)] Transmitted (black) and reflected (red) angular dependence of (a) measured and (b) predicted TM-polarized THG efficiencies triggered by a TM-polarized pump pulse tuned at 1064 nm. [(c)-(d)] Transmitted (black) and reflected (red) angular dependence of (c) measured and (d) predicted TE-polarized THG efficiencies triggered by a TE-polarized pump pulse tuned at 1064 nm.

We have also investigated the nonlinear signals in a 500 μm-thick crystalline silicon wafer grown in the (100) crystalographic direction. In Figs. 3.1.7(a) and 3.1.7(b) we show results of the angular dependence of the transmitted and reflected SHG efficiencies obtained from (a) experiments and (b) simulations. We note in the experimental results that the maximum of the reflected curve is shifted towards a larger angle of incidence with respect to the transmitted curve. This fact is well reproduced by the curves obtained with the simulations. Moreover, experimental and predicted curves agree well in amplitude and shape. From the comparison

between experimental and theoretical results we obtained an effective mass of bound electrons of $m^*_{b1} = m^*_{b2} = 2.5m_e$.

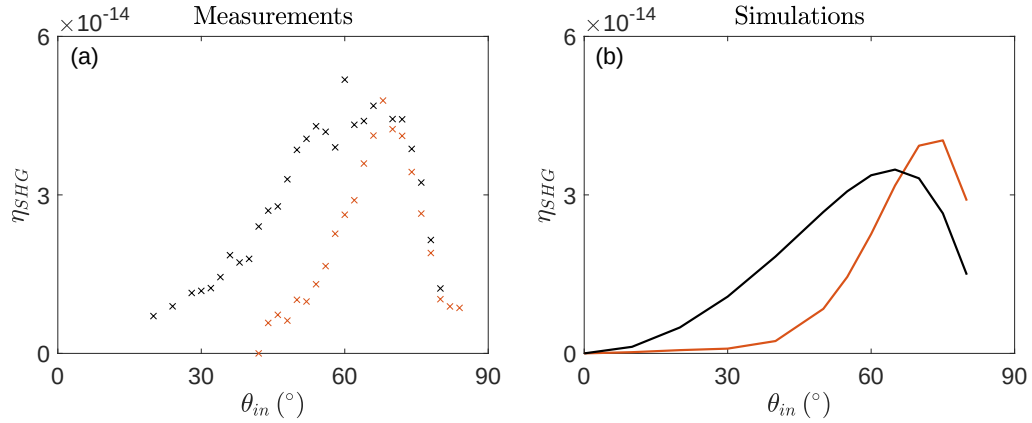

Figure 3.1.7: (a) Measured and (b) predicted SHG conversion efficiencies obtained from the crystalline silicon wafer in transmission (black) and in reflection (red) and as a function of incident angle when both fundamental and SH fields are TM-polarized.

In Fig. 3.1.8 we show experimental and simulated results of the angular dependence of THG efficiencies from the silicon wafer. As well as in the case of the GaAs wafer and the amorphous silicon nanolayer, a TM-polarized TH signal is detected when a TM-polarized field is incident on the sample, while a TE-polarized fundamental field generates a TE-polarized TH field. By matching experimental and predicted results we obtained a third order nonlinear parameter of $\tilde{b} = 3.6 \cdot 10^{-7}$. The amplitude of the transmitted signal depends on sample thickness because the pump is absorbed as it decays inside the sample. On the contrary, if the sample is thicker than a few tens of microns, reflected harmonic generation becomes independent of sample thickness, because the pump is absorbed faster than the round trip time necessary to trigger meaningful cavity effects. We note again that a transmitted TH generated at 355 nm is able to propagate through a 500 μm-thick wafer without being absorbed, which tells us that it corresponds to the phase-locked harmonic component.

Finally, in Fig. 3.1.9 we show measurements of the TH signal generated by the crystalline silicon wafer for TM-polarized incident and detected light taken with an spectrometer (Andor, Shamrock 303I) with an attached camera (Andor, DV420A-OE). This measurement was per-

formed in the same conditions as those shown in Fig. 3.1.8, but the TH light was collected by the above mentioned spectrometer instead of by the PMT. In the inset of the figure it can be seen that no fundamental light, tuned at 1064 nm was detected.

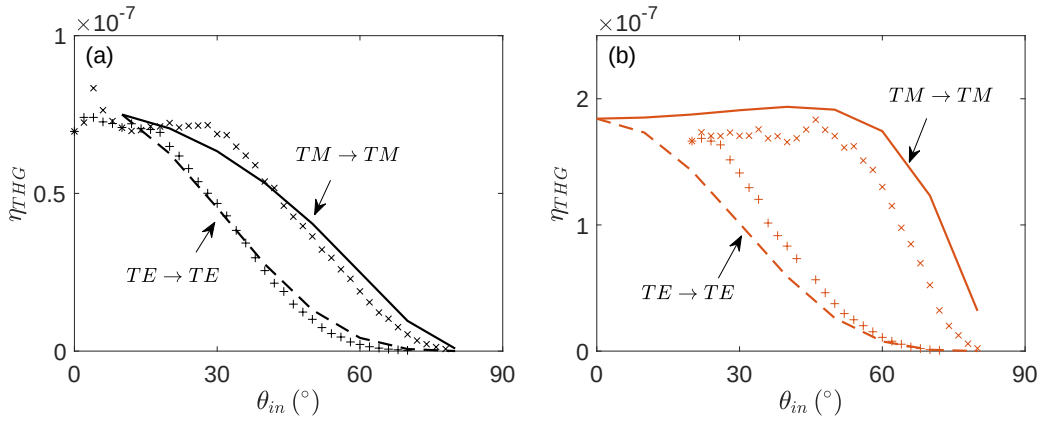

Figure 3.1.8: Measured (markers) and predicted (curves) THG efficiencies as a function of incident angle for the crystalline silicon wafer obtained in (a) transmission and (b) reflection. A TM-polarized TH signal is detected when the incident field is TM-polarized (cross markers, solid curves), while a TE-polarized fundamental field generates a TE-polarized TH (plus markers, dashed curves).

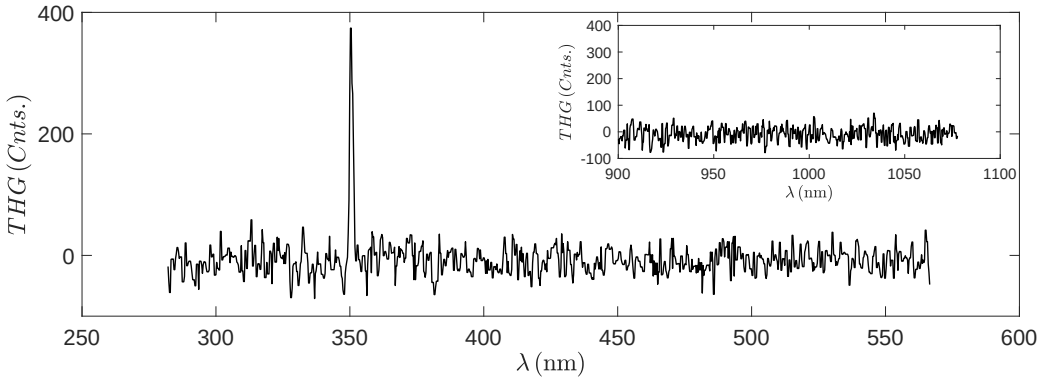

Figure 3.1.9: Spectroscopy measurement of the THG signal for the crystalline silicon wafer. A signal was detected at 355 nm, corresponding to the TH of incident pulses tuned at 1064 nm. Both incident and TH fields are TM-polarized.

3.2 Silicon membranes

3.2.1 Experimental approach

The nonlinear response of the silicon membranes was studied in a different laboratory (Charles M. Bowden Laboratory, Huntsville, Alabama), during a PhD stay abroad. There, a completely new set-up was built, taking as a reference the one described in Chapter 2.1. This new configuration was specially designed for wavelength dependence measurements, as we had access to a tunable femtosecond laser source in the laboratory. It consists of a Ti:Sapphire laser system (Coherent, Astrella) which pumps an optical parametric amplifier (OPA) (Coherent, Opera Solo). The system emits pulses of ~ 100 fs at 1 kHz repetition rate and can be set to operate at different wavelength ranges: 1160 nm to 1600 nm range with energies $> 220\,\mu$J/pulse; 480 nm to 1160 nm range with energies $> 50\,\mu$J/pulse; 290 nm to 480 nm range, with energies above $10\,\mu$J/pulse. In Table 3.2.1 we have summarized the above mentioned parameters in the 1160 nm to 1600 nm wavelength range, which was the most common one used in the experiments.

	λ	τ_{FWHM}	f_{rep}	P_{out}	Energy/pulse
OPA (Coherent, Opera Solo)	1160 nm − 1600 nm	100 fs	1 kHz	> 0.2 W	$> 220\,\mu$J

Table 3.2.1: Tunable femtosecond source parameters.

The calibration procedure performed to estimate SHG and THG efficiencies was carried out in a similar fashion as that described in Chapter 2.1. As light source we used the OPA tuned in the range from 350 nm to 750 nm (this would correspond to the light generated by the BBO crystal in the calibration procedure described in Chapter 2.1). Then, the responsivity of the PMT was measured for different wavelengths and calculated as $R_{\mathrm{PMT}} = V_{\mathrm{PMT}}/(T_{\mathrm{ND}} P_{\mathrm{PMT}})$, where V_{PMT} is the reading of the signal taken with the oscilloscope to which the PMT is connected, P_{PMT} is the power measured with a photodiode (Newport, 918D-UV-OD3) in front of the PMT, and T_{ND} is the transmission of the ND filters placed before the PMT. In order to have access to the responsivity for all possible wavelengths, we fitted our measurements to the PMT's responsivity provided in its datasheet, which is shown in Fig. 3.2.1 with a solid curve. Measurements

are depicted with cross markers. The transmission T of the detection arm also depended on wavelength and was calculated for each case with transmission values given by the datasheet of the elements (filters, lenses, polarizer, etc.) placed in the detection arm.

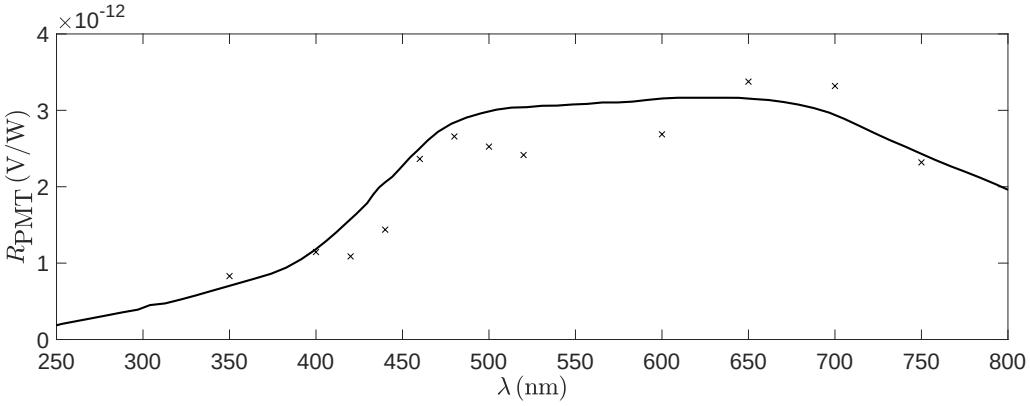

Figure 3.2.1: Measurements of the responsivity of the PMT (cross markers) fitted to Thorlabs' responsivity curve (solid curve).

Knife edge measurements were performed to characterize the size of the beam at the sample plane. This technique consists on placing a blade in front of the laser beam and measuring the power transmitted by the blade using a photodiode. This blade is displaced horizontally (x) from the position were the beam is totally blocked, to the position were the hole beam is transmitted (or the other way around). From this, a curve similar to that shown in Fig. 3.2.2 is obtained, where we show the measured power P as a function of the displacement of the blade x in mm. Pulses with 800 nJ of energy tuned at 1500 nm were used. This measurements are depicted with cross markers and can be fitted to a function of the form:

$$P(x) = A\left(erf\left(\frac{\sqrt{2}(x-x_0)}{w_0}\right)\right) + B \tag{3.2.1}$$

where A and B are parameters of the fitting, w_0 corresponds to the beam waist, and x_0 is the center point of the beam. From this we extracted a beam waist of $w_0 \sim 175\,\mu$m. The experiment was repeated for different input wavelengths, for which a similar beam waist was obtained. Typical incident energies per pulse used in the experiments were $E_{\mathrm{FF}} = 100$ nJ, which leads us to incident pulse peak intensities of $1.5\,\mathrm{GW/cm^2}$. However, the set-up allowed

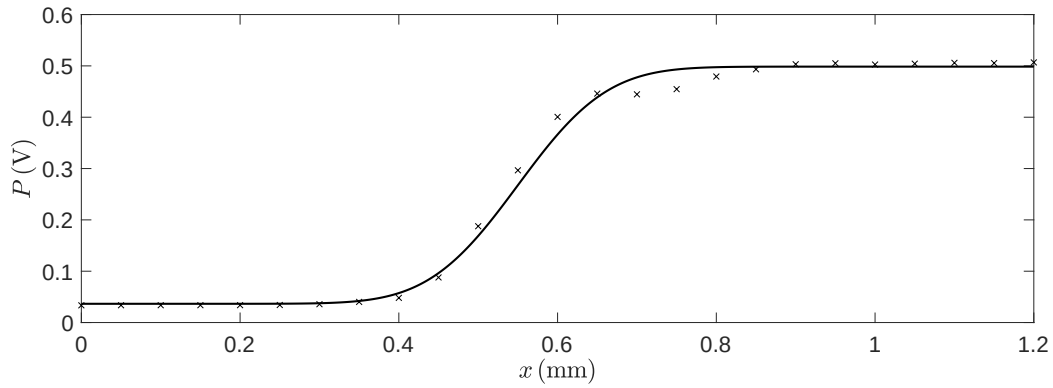

Figure 3.2.2: Knife edge measurements performed to the focused beam when the incident wavelength was tuned at 1500 nm. Measurements (cross markers) are fitted to an error function (solid curves) from which the beam waist w_0 of the beam can be extracted.

us to vary the energy per pulse so that higher peak pump pulse intensities could be used in the experiments. These parameters are summarized in Table 3.2.2.

	E_{FF}	f_{rep}	τ_{FWHM}	w_0	I_{FF}
OPA (Coherent, Opera Solo)	100 nJ	1 kHz	100 fs	175 μm	1.5 GW/cm^2

Table 3.2.2: Tunable femtosecond source parameters under experimental conditions.

In Fig. 3.2.3 we show an schematic representation of our experimental set-up. This set-up uses as starting point that described previously in Chapter 2.1. However, it contains a given amount of filters to eliminate the fundamental radiation instead of a dispersive prism as alignment with a multiwavelength system and pump-wavelength sweeps would be difficult with the prism configuration. Residual undesired frequency components coming from the OPA are eliminated placing a silicon wafer in the beam path. Then, ND filters are used to attenuate the fundamental energy per pulse. After that, with a pair of polarizers (Thorlabs, WP25L-UB and LPNIR100-MP2) we can control the power and the polarization of the incident field. Then, using colored glass longpass filters (usually two are enough) possible SH or TH radiation generated in elements of the set-up placed between the OPA and the sample is eliminated. Depending on the input wavelength range, the filters are chosen to have a suitable cut-on wavelength. The beam is focused on the sample plane and then collimated with a pair of calcium fluoride

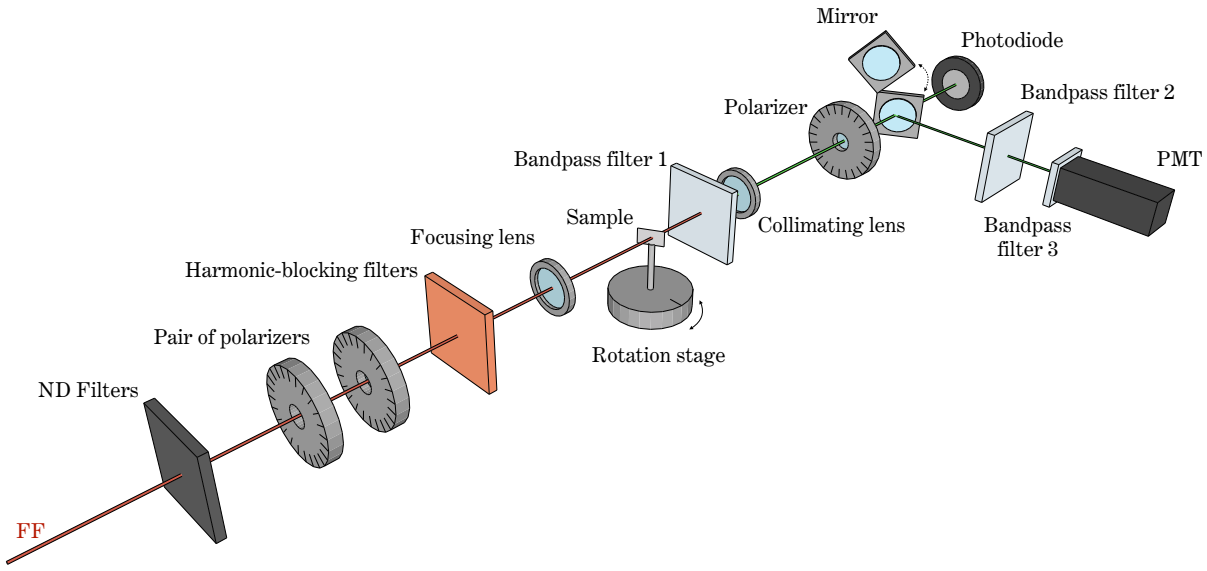

Figure 3.2.3: Schematic representation of the experimental set-up in its transmission configuration specifically built for wavelength dependence measurements of SH and TH signals arising from crystalline silicon membranes.

(CaF_2) lenses with focal length f = 500 mm (Thorlabs, LA5464). The sample is mounted on top of a motorized rotation stage (Newport, URS150BCC), again allowing measurements as a function of incident angle. With a polarizer (Thorlabs, WP25L-UB) the harmonic field is selected to be either TM- or TE-polarized. Then, a mirror (Thorlabs, PF10-03-F01) on a flip mount allows the selection of either a calibrated silicon photodiode (Newport, 918D-UV-OD3), or a PMT (Thorlabs, PMT1001) to enable easy measurements of the responsivity of the system. The electronic signal from the PMT is filtered and amplified by a low-noise preamplifier (SRS, SR530) before being measured with a digital oscilloscope (Agilent Technologies, DSO6104A) connected to a computer. As can be seen in Fig. 3.2.3, several bandpass filters are placed in different parts of the detection arm: (1) between the sample and the collimating lens, (2) between the mirror and the PMT, and (3) at the PMT. These filters have the role of eliminating the fundamental field, as well as SH or TH radiation depending on which harmonic frequency we want to detect. For this reason, the choice of these filters is crucial and depends on the incident wavelengths we are using. For spectral THG measurements with incident pulses tuned

in the range from 1000 nm to 1600 nm, which corresponds to TH signals laying between 333 nm and 533 nm, we use: (1) FGS900, (2) FGS900 × 2, and (3) FGS900. For TH generated from smaller input wavelengths, each of these filters is replaced by a FGUV11-UV. In the case of SHG, measurements were performed at a fixed wavelength due to availability of filters. For instance, for $\lambda_{in} = 1300$ nm, 1400 nm and 1500 nm, we use: (1) FGS900 × 2, (2) bandpass filter centered at the detection wavelength (Thorlabs, FBXXX-10) and (3) FESH0900. By choosing another combination of filters, one is able to measure harmonic signals at different wavelength ranges.

3.2.2 Description of the samples

We studied two different silicon samples consisting of a 200 nm- and a 1340 nm-thick (100) crystalline silicon membranes etched out [31] of silicon wafers purchased from Norcada (Alberta, Canada). In Fig. 3.2.4(a) an schematic representation of the 200 nm-thick membrane is shown, and in Fig. 3.2.4(b) we show the geometric representation of the problem for TM-polarized incident light, where $\mathbf{E}_\omega$, $\mathbf{H}_\omega$ and $\mathbf{S}_\omega$ are electric and magnetic fields and Pointing vector, respectively, at the fundamental frequency, and θ_{in} is the angle of incidence.

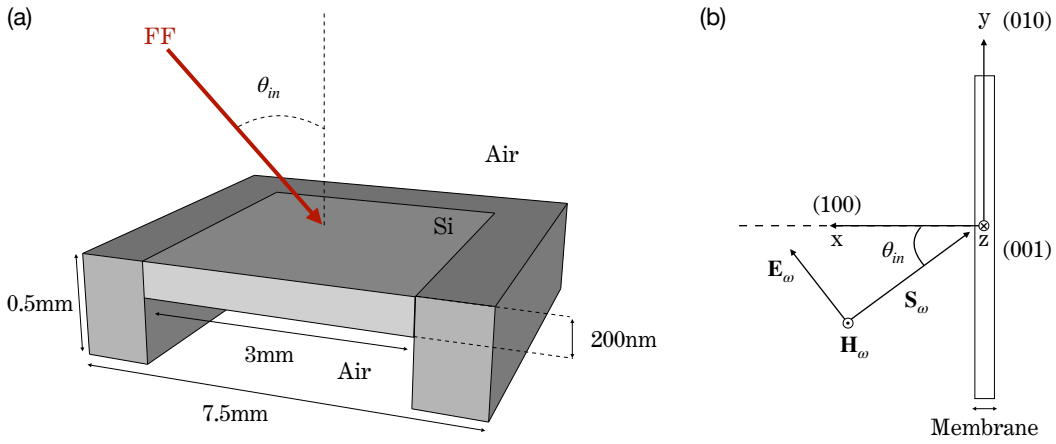

Figure 3.2.4: (a) Schematic representation of the 200 nm-thick silicon membrane. (b) Schematic representation of the silicon membrane when TM-polarized light is incident at a certain angle θ_{in}.

The membranes are supported by a silicon frame. In the case of the 1340 nm-thick membrane, this frame is 300 μm thick and has 10×10 mm dimensions. The membrane size is 4.8×4.8 mm. In the case of the 200 nm-thick membrane, the frame has 7.5×7.5 mm dimensions and is 500 μm-thick. The size of this membrane is 3×3 mm. These parameters are summarized in table 3.2.3.

Membrane thickness	Membrane size	Frame thickness	Frame size
200 nm	3×3 mm	500 μm	7.5×7.5 mm
1340 nm	4.8×4.8 mm	300 μm	10×10 mm

Table 3.2.3: Silicon membranes parameters.

3.2.3 Theoretical approach

The theoretical approach that was followed to perform numerical simulations of SHG and THG efficiencies generated by the silicon membranes mimics that for the crystalline silicon wafer case, described in section 3.1.3.

3.2.4 Results and discussion

Experiments have been carried out pumping our samples with tunable femtosecond pulses. Typically, the incident wavelength range used in the experiments was from 1160 nm to 1600 nm. However, smaller fundamental wavelengths could also be used by using other ports of the OPA. This allowed us to generate harmonic signals deeper in the UV. Typical incident pulse peak intensities used in the THG experiments were $\sim 1.5\,\mathrm{GW/cm^2}$, while for SHG measurements they were increased to $\sim 10\,\mathrm{GW/cm^2}$. We recall that our set-up, schematically depicted in Fig. 3.2.3, allows us to take measurements as a function of fundamental and harmonic polarization, and incident angle and wavelength. For what the simulations are concerned, tunable 100 fs pulses were incident on a free-standing 200 nm-thick or 1340 nm-thick crystalline silicon membrane assumed to have (100) crystallographic orientation, with pump pulse power densities of $\sim 1.5\,\mathrm{GW/cm^2}$, which were increased for the SHG case accordingly to experimental conditions.

In Fig. 3.2.5(a) we display linear pump transmittance as a function of incident wavelength for the 200 nm- and 1340 nm-thick membranes. These spectra were taken with a spectrometer (Shimadzu, UV-3101PC) and they consist of a series of Fabry-Perot resonances whose free

spectral range depends on thickness. In Fig. 3.2.5(b) we show the transmittance around the 1400 nm resonance peak, when low-intensity, 100 fs pulses, which are narrowband enough to resolve the resonances, were injected normal to the surface of the 1340 nm-thick membrane. Simulations (solid curve) and measurements (cross markers) of the linear transmittance agree well in terms of amplitude and peak location.

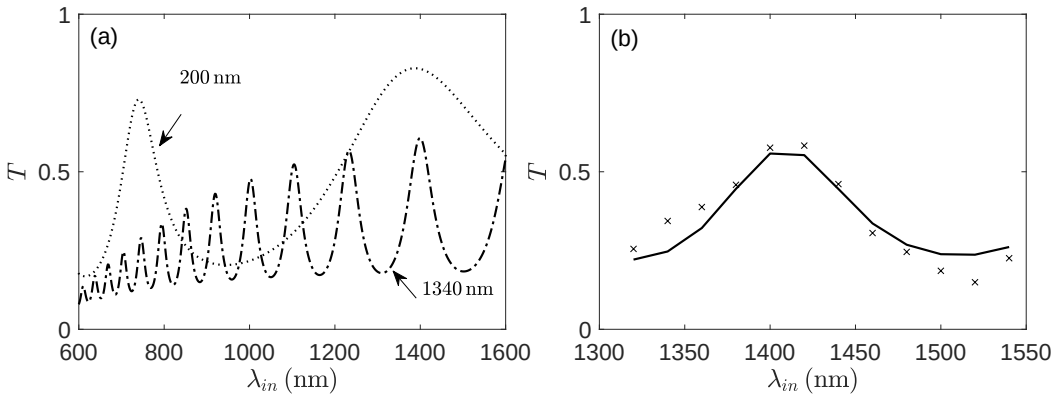

Figure 3.2.5: (a) Measured linear transmission as a function of incident pump wavelength for the 1340 nm- and 200 nm-thick silicon membranes. (b) Measured (cross markers) and simulated (solid curve) linear transmission as a function of incident pump wavelength for normally incident pulses tuned near the 1400 nm resonance wavelength for the 1340 nm-thick silicon membrane. Measurements in (a) were performed with a specrophotometer, while measurements in (b) were taken with the laser source used in the nonlinear experiments, with low-intensity pulses.

We go on now to introduce our experimental results regarding the nonlinear behavior of the two silicon membranes, which have been compared with the predictions of our numerical simulations.

Observations and predictions of SHG transmitted efficiencies (η_{SHG}) as a function of incident angle (θ_{in}) for the 1340 nm-thick membrane are depicted in Figs. 3.2.6(a)-(c), for three different incident wavelengths: 1300 nm, 1400 nm and 1500 nm, tuning the SH field at 650 nm, 700 nm and 750 nm, respectively. In all these cases, a TM-polarized incident field was used, and a TM-polarized SH was selected. The obtained SH curves show maxima peaking between 65° and 70°, and conversion efficiencies of order $10^{-12} - 10^{-13}$. According to the hydrodydamic approach adapted for the case of crystalline silicon in Chapter 3.1.3, SHG conversion efficiencies

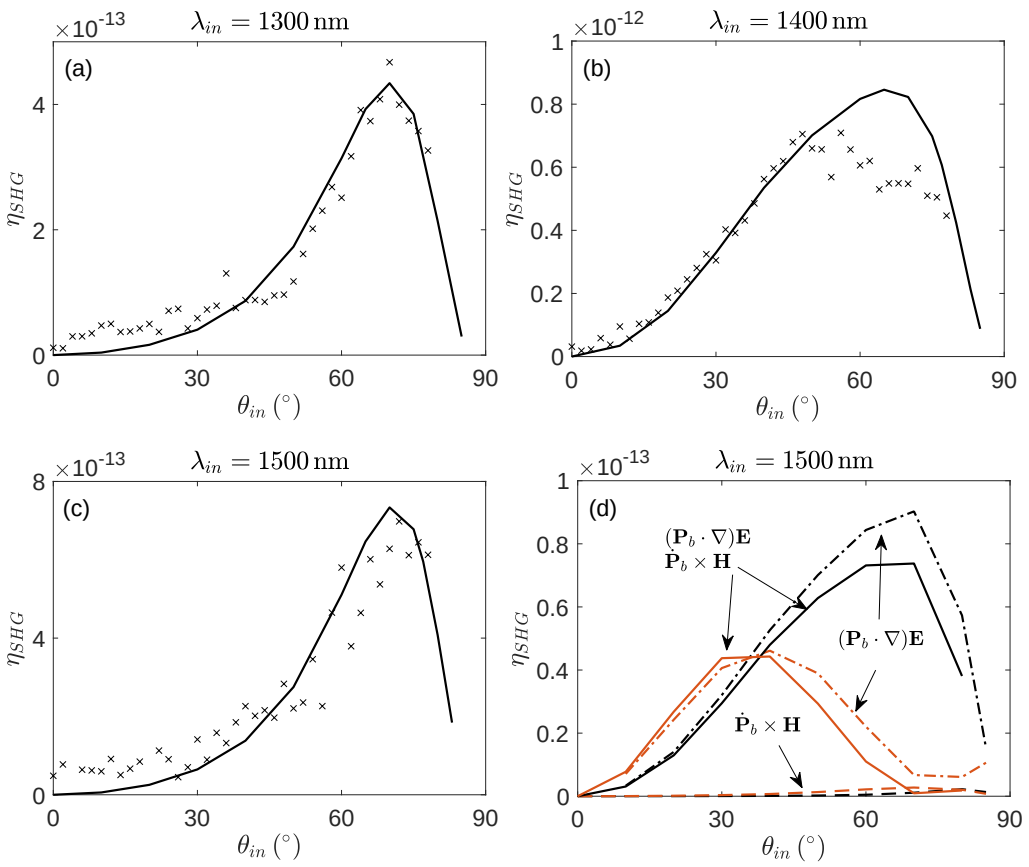

Figure 3.2.6: Angular dependence of transmitted SHG measured (cross markers) and predicted (solid curves) efficiencies for incident pulses tuned at (a) 1300 nm, (b) 1400 nm, and (c) 1500 nm, for the 1340 nm-thick silicon membrane. (d) Predictions of the transmitted (black) and reflected (red) SHG efficiencies for the 1340 nm-thick silicon membrane under three different scenarios: taking only the Lorentz (dashed curves) or the surface (dashed-pointed curves) contribution into account, and considering both terms (solid curves) in Eq. 3.1.3.

are completely determined by the spatial derivatives of the electric field, and by the magnetic component of the Lorentz force, which is almost never explicitly and specifically discussed, and which are multiplied by the factor $e\lambda_0/(m^*_{bj}c^2)$. By matching the simulated and measured conversion efficiencies we extracted an effective mass of bound electrons $m^*_{b1} = m^*_{b2} = 2.5m_e$.

The presence of the magnetic component of the Lorentz force is essential when the pump is TE-polarized, and can act as a catalyst when the field is TM-polarized. In fact, as we have seen in the previous chapter, a TE-polarized pump generated a TM-polarized SH signal thanks to the term $\frac{e\lambda_0}{m^*_{bj}c^2}\dot{\mathbf{P}}_{bj} \times \mathbf{H}$. For TM-polarized pumps, calculations show that while the individual

surface component may yield several orders of magnitude more SH signal than the magnetic Lorentz term, their combined effect can impact both quantitative and qualitative aspects of the interaction. This situations is represented in Fig. 3.2.6(d), where we show predictions of the transmitted and reflected SHG efficiencies obtained under three different scenarios: taking only either the surface or the magnetic Lorentz term into account, and considering both of them to contribute in the nonlinear polarization. SHG triggered only by the magnetic term (dashed

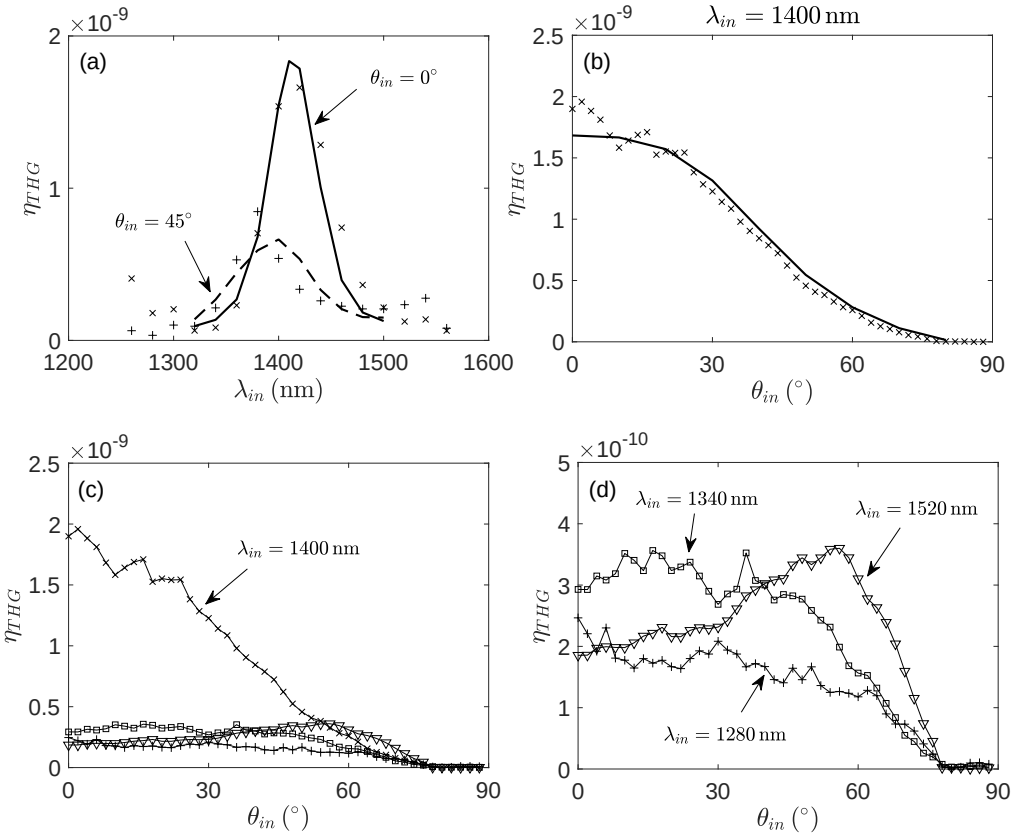

Figure 3.2.7: (a) Transmitted THG efficiencies as a function of pump wavelength for the 1340 nm-thick silicon membrane. Measurements were taken at normal incidence (cross markers) and at 45° incident angle (plus markers). Their corresponding simulations are depicted with a solid curve and a dashed curve, respectively. (b) Angular dependence of the measured (cross markers) and predicted (solid curve) transmitted THG efficiency for the 1340 nm-thick silicon membrane when incident pulses were tuned at 1400 nm. (c) Experimental results of the angular dependence of the transmitted THG efficiencies when pump pulses tuned at 1280 nm, 1340 nm, 1400 nm and 1520 nm are incident on the 1340 nm-thick silicon membrane. (d) The same results plotted in Fig. 3.2.7(c) but neglecting the 1400 nm pump wavelength case.

curves) is two orders of magnitude smaller than SH signals generated only by the surface term (dashed-pointed curves), and barely visible on the plot. Nevertheless, when both terms are present (solid curves) the peak of the transmitted SHG curve suffers almost a 20% reduction compared to what is generated by the surface, while the reflected SH peak shifts to smaller angles by a measurable amount. It is obvious then, that this term has a catalytic action and it should not be neglected.

In Fig. 3.2.7 we show experimental and simulated results of the transmitted TM-polarized THG efficiencies (η_{THG}) for the 1340 nm-thick crystalline silicon membrane when the incident field is TM-polarized. In Fig. 3.2.7(a) we report the spectral response at normal ($\theta_{in} = 0°$) and oblique ($\theta_{in} = 45°$) angles of incidence. A maximum THG efficiency of $2 \cdot 10^{-9}$ was obtained at 466 nm, with the pump tuned at 1400 nm at normal incidence. Simulations were obtained with $\tilde{b} = 1.5 \cdot 10^{-8}$ and agree well with experimental results in terms of amplitude and peak locations. The agreement between theory and experimental observations evident in Fig. 3.2.7(a) repeats in Fig. 3.2.7(b), where we show the angular response of the TH signal when incident pulses tuned to the peak of 1400 nm were used. In Fig. 3.2.7(c) we show experimental curves obtained in other spectral locations. Figure 3.2.7(d) is a zoom in of Fig. 3.2.7(c), neglecting the curve obtained pumping the sample at 1400 nm. Experimental results obtained using incident wavelengths of

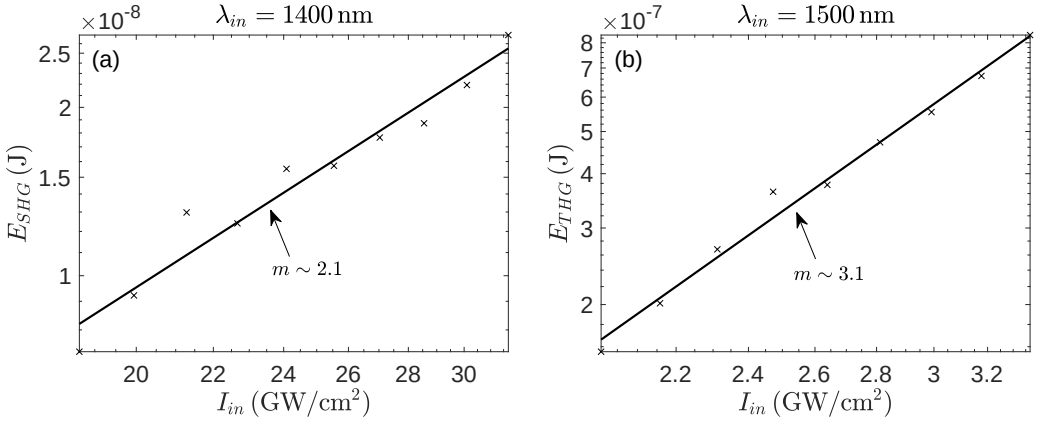

Figure 3.2.8: (a) SH and (b) TH measured energies as a function of incident pulse peak intensity for the 1340 nm silicon membrane and incident pulses tuned at 1400 nm and 1500 nm, respectively.

1280 nm, 1340 nm and 1520 nm are shown, tuning the TH signal at 426 nm, 446 nm and 506 nm, respectively.

Finally, SHG and THG energies (E_{SHG} and E_{THG}) were measured as a function of incident pulse peak intensity for the 1340 nm silicon membrane. In the case of SHG, incident pulses were tuned at 1400 nm, while for THG they were tuned at 1500 nm. These results are plotted in logarithmic scale in Fig. 3.2.8. A slope of $m \sim 2.1$ and $m \sim 3.1$ is found for the SHG and THG case, respectively, a result that gives us confidence on the fact that we are measuring SH and TH signals.

The second set of measurements consisted of detecting THG efficiencies carried out on a 200 nm-thick silicon membrane. This sample gives us the opportunity to directly address the nanoscale, and to simultaneously investigate THG in a cavity environment in the UV range, where nonlinear dispersion, absorption, and phase-locking come robustly into play. In Fig. 3.2.9(a) we show experimental and predicted results of the spectral response of the transmitted THG efficiency at normal and 45° incident angle when both incident and TH fields are TM-polarized. As it can be seen, predicted and observed data display remarkable agreement in the wavelength range above 300 nm (900 nm pump wavelength). However, we remark that THG predictions below 300 nm have the right trend but are somewhat lower than our experimental observations. This may be due to the fact that conversion efficiency is inversely proportional to the fourth power of the electron density and lattice constant ($\tilde{b}^2 \sim (L^4 n_{0,b}^4)^{-1}$), and the possibility that the third order coefficient may be somewhat dispersive and geometry dependent, which can account for stronger nonlinear gain.

In Figs. 3.2.9(b)-(d) we display the angular dependence of the transmitted THG when the carrier wavelength is tuned to 1000 nm, 900 nm and 810 nm, leaving the generated TH tuned at 333 nm, 300 nm and 270 nm, respectively, well in the UV range of the spectrum. The sharp drops that the observed TH curves display occur because the incident beam impinges on the substrate, with subsequent precipitous reduction in transmittance. The aperture of the 200 nm-thick membrane is smaller compared to that of the 1340 nm-thick sample (see Section 3.2.2),

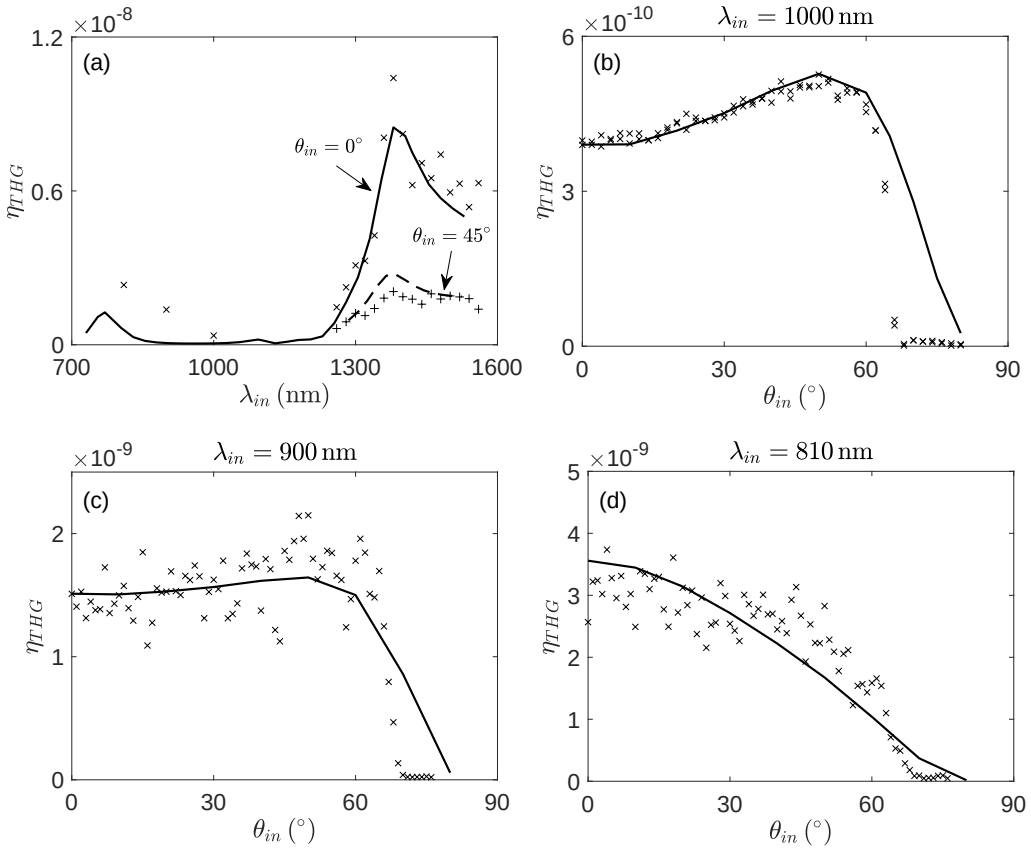

Figure 3.2.9: (a) Transmitted THG efficiencies as a function of incident wavelength for the 200 nm-thick silicon membrane. Measurements were taken at normal incidence (cross markers) and at 45° incident angle (plus markers). Their corresponding simulations are depicted with a solid curve and a dashed curve, respectively. [(b)-(d)] Angular dependence of the transmitted THG measured (cross markers) and predicted (solid curves) efficiencies for incident pulses tuned at (b) 1000 nm, (c) 900 nm, and (d) 810 nm, for the 200 nm-thick silicon membrane.

thus restricting the range of incident angles we could investigate without having the laser beam clipped by the membrane aperture. As it can be observed, this membrane is at least five times more efficient than the thicker counterpart, and that conversion efficiencies are still relatively large even when the TH signal is tuned to 270 nm. Predicted curves in Figs. 3.2.9(c) and 3.2.9(d) were obtained by slightly increasing the nonlinear gain coefficient to approximately match observed conversion efficiencies. We recall that this parameter can be expressed as $\tilde{b}_j = \tilde{\omega}_{p,bj}^2/(L^2e^2n_{0,bj}^2)$. For silicon, we have that $L \sim 2.6\,\text{Å}$, $n_{0,bj} \sim 10^{22}\,\text{cm}^{-3}$ and $\tilde{\omega}_{p,bj}$ lays between 250 nm and 450 nm. Combining these parameters, we obtain $\tilde{b} = 1.5 \cdot 10^{-8}$. However, we

recall also from Chapter 1.5.3 that this magnitude is flexible and is fully determined relying in experimental efficiencies.

3.3 Silicon nanowires

The study of basic silicon structures presented in the previous Sections 3.1 and 3.2, where we have shown SHG and THG results on an amorphous silicon nanolayer, a crystalline silicon wafer and in two crystalline silicon membranes, has allowed us to extract basic physical properties of the material. As we have seen, these are the effective mass of bound electrons, which determines SHG, and oscillator parameters $\tilde{b}$ which determine THG. Now, we will use this knowledge to predict harmonic generation in a more complex structure. Nowadays, the scientific interest has been towards the design of nanostructures capable of enhancing harmonic generation efficiencies. For this reason, our purpose now is to investigate the nonlinear response in a more complex structure made of silicon. This structure consists of a nanograting made of silicon nanowires having square cross section 230 nm × 230 nm, and a period of 1200 nm, which is schematically shown in Fig. 3.3.1 were θ_{in} is the incident angle.

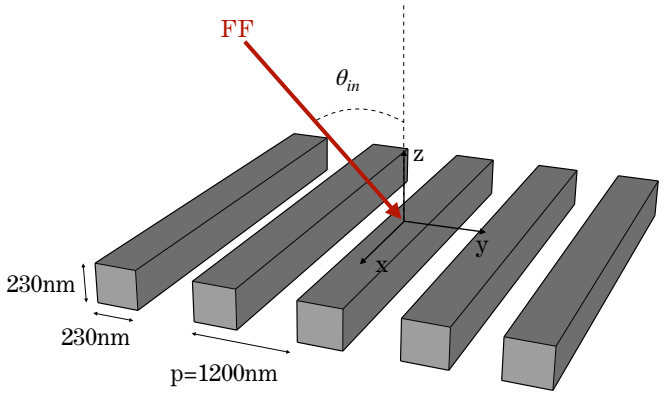

Figure 3.3.1: Schematic representation of the silicon grating. The nanowires have a cross section of 230 nm × 230 nm and a period of p = 1200 nm.

3.3.1 Results and discussion

We have simulated the linear, SHG and THG spectra for two different incident peak pump pulse intensities. In Fig. 3.3.2(a) we show predictions of the linear transmission T and reflection R spectra for this grating, for TM-polarized incident pulses. The solid and dashed curves are obtained with incident pulse peak intensities of $0.5\,\mathrm{GW/cm^2}$ and $8\,\mathrm{GW/cm^2}$, respectively. As it can be seen, the reflected (transmitted) peak (valley) of the curve obtained at higher incident peak intensities is shifted towards a larger incident wavelength with respect to the curves obtained at lower incident peak intensities.

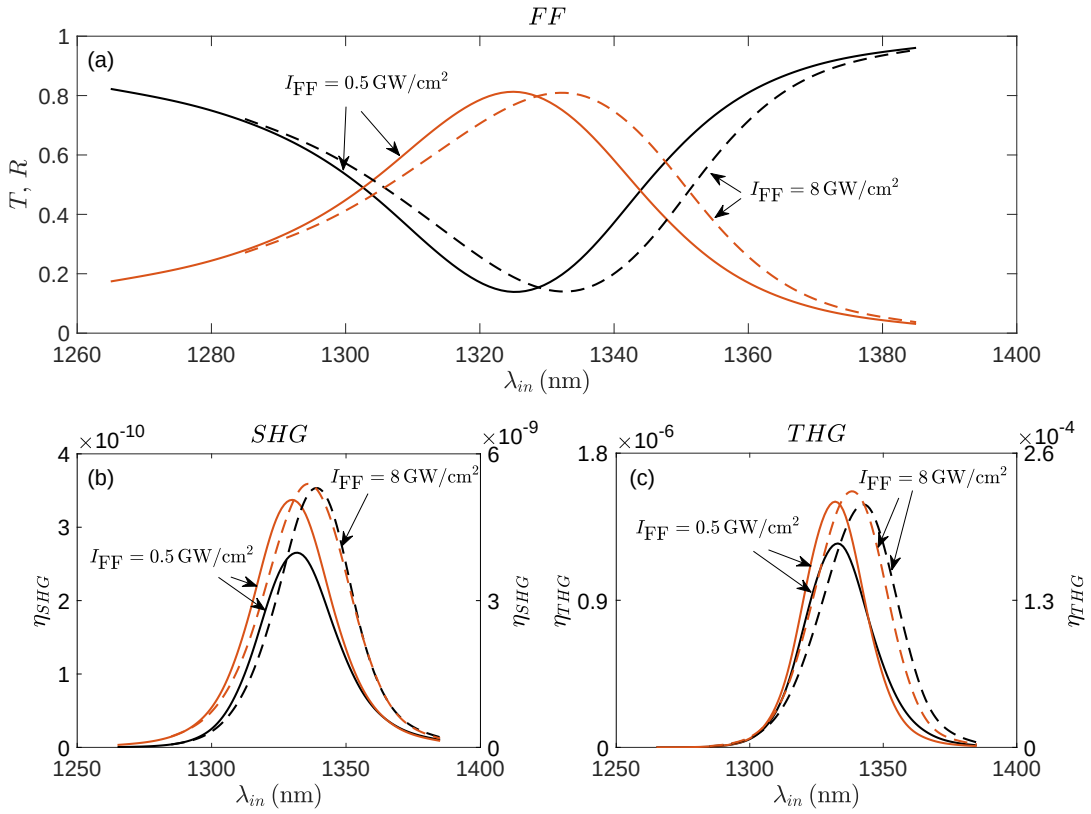

Figure 3.3.2: (a) Predictions of the linear transmitted (black) and reflected (red) spectra for the silicon grating when the incident peak pump pulse intensity is $0.5\,\mathrm{GW/cm^2}$ (solid curves) and $8\,\mathrm{GW/cm^2}$ (dashed curves). [(b)-(c)] Predictions of the transmitted (black) and reflected (red) (b) SHG and (c) THG conversion efficiencies as a function of incident wavelength. Solid curves correspond to incident peak intensities of $0.5\,\mathrm{GW/cm^2}$, efficiencies shown at the left y-axis; and dashed curves correspond to incident peak intensities of $8\,\mathrm{GW/cm^2}$, efficiencies shown at the right y-axis.

In Fig. 3.3.2(b) we have plotted numerical simulation results of the transmitted and reflected SHG efficiencies (η_{SHG}) as a function of incident wavelength from the silicon grating, when both incident and SH fields are TM-polarized. The solid curves are calculated with an incident peak pump pulse intensity of $0.5\,\mathrm{GW/cm^2}$, and the corresponding conversion efficiencies are shown in the left y-axis. They show a maximum transmitted and reflected efficiencies for $\lambda_{in} \sim 1332\,\mathrm{nm}$. The dashed curves are obtained by setting the incident pulse peak intensity at $8\,\mathrm{GW/cm^2}$, and the corresponding conversion efficiencies appear at the right y-axis. As it can be observed, these curves are redshifted, peaking at $\lambda_{in} \sim 1340\,\mathrm{nm}$ for the transmission case. Conversion efficiencies of order 10^{-10} and 10^{-9} are obtained for the low and high incident pulse peak intensity case, respectively, which have been obtained with electrons' effective masses of $m^*_{b1} = m^*_{b2} = 2.5m_e$.

Figure 3.3.2(c) presents the predicted results for TM-polarized THG efficiencies (η_{THG}) from the silicon grating when pump pulses are TM-polarized. Once again, two different fundamental peak pulse intensities have been used. The redshifting of the curves generated with higher intensities is also observed in this case. As it can be seen, THG conversion efficiencies of order 10^{-6} and 10^{-4} are obtained for incident peak intensities of $0.5\,\mathrm{GW/cm^2}$ and $8\,\mathrm{GW/cm^2}$, respectively. These values are obtained with $\tilde{b} \sim 10^{-8}$. There is no doubt that these efficiencies have to be corroborated with experimental results, with which effective masses and nonlinear oscillator parameters can be readjusted. So, the next step would be to prepare a sample of this kind and measure its nonlinear response. In fact, this nanograting is already under preparation.

3.4 Conclusions and summary

In summary, we have studied nonlinear frequency conversion in suspended silicon membranes of 200 nm and 1340 nm thickness, in a 500 μm silicon wafer, and in a 25 nm-thick amorphous silicon nanolayer in the visible and UV ranges, in regimes where this material tends to be opaque, and where nonlinear dispersion and phase-locking dominate the dynamics. Our results thus suggest that the entire UV range is available for the development of relatively efficient light sources. Our theoretical approach is in remarkable agreement with measured results, and sheds light on

the dynamical aspects of surface, second order phenomena, as well as third order nonlinearities. The identification of basic parameters like the effective mass of bound electrons, which drives SHG, and nonlinear oscillator parameters, which control THG, has allowed us to make accurate predictions about conversion efficiencies in more complicated geometrical arrangements. With this, we have reported preliminary results of predicted SHG and THG efficiencies from a silicon nanograting, which shows an impressive enhancement of conversion efficiencies. However, this study should be completed with experimental observations.

4
SHG and THG from ITO: nonlocal effects and hot electrons

In this chapter we report a comparative experimental and theoretical study of SHG and THG from a 20 nm-thick ITO layer in proximity of its ENZ condition, which was carried out in collaboration with ICFO (Institut de ciències fotòniques). Thanks to using a tunable OPA we are able to record both spectral and angular dependence of the generated harmonic signals close to this particular point. We discuss how nonlocal effects, which blueshift the ENZ resonance by tens of nanometers and are determined by the Fermi energy, and the variation of the effective mass of conduction electrons due to temperature, which redshifts the plasma frequency, can alter the SH response. We refer to this variation of the effective mass as the hot electron contribution. We also briefly debate the influence of this contribution to THG. After that, we show numerical simulations that predict that the presence of nonlocal effects not only can cause a blueshift of the ENZ resonance, but they also can induce an anisotropic response in ITO.

This chapter is structured as follows. In Section 4.1 we explain the experimental conditions under which measurements were taken, as well as the experimental set-up built to measure SHG and THG efficiencies arising from the ITO nanolayer. In Section 4.2 we describe the sample and how it was fabricated. After that, in Section 4.3 we explain how the theoretical model explained in Chapter 1.5 has been adapted to the particular case of conductive oxides like ITO. Then, in

Section 4.4 we report the experimental and theoretical results obtained of harmonic generation in ITO and finally, in Section 4.5 the chapter is ended with some conclusions.

4.1 Experimental approach

The measurements that are reported in this chapter were taken in collaboration with ICFO, which gave us the opportunity to work with a tunable femtosecond source, similar to the one used in Chapter 3.2. A Ti:Sapphire laser system (Coherent, Astrella) pumps an OPA (Light conversion, TOPAS), which operates in a wavelength range from 1140 nm to 1600 nm, delivering pulses with energies exceeding 500 μJ/pulse generated at a repetition rate of 1 kHz. FROG (frequency-resolved optical grating) measurements were performed to determine the pulse width. Depending on the wavelength, pulses with duration between 50 and 102 fs were incident to the samples. In the following table we summarize the above mentioned parameters:

	λ	τ_{FWHM}	f_{rep}	P_{out}	Energy/pulse
OPA (TOPAS)	1140 nm − 1600 nm	50 − 102 fs	1 kHz	> 0.5 W	$> 500\,\mu$J

Table 4.1.1: Tunable femtosecond source parameters.

Knife edge measurements were performed to characterize the size of the beam at the sample plane. Depending on the wavelength, beam waists were between 4.2 mm and 4.8 mm. With this, the typical power densities that we used in the experiments were between 1 and 2 GW/cm^2. These parameters are summarized in Table 4.1.2 for four different wavelengths. For the SHG measurements, the fundamental beam was directed onto the sample under these conditions, while in the THG experiments, a 50 cm uncoated CaF_2 lens was introduced in the beam path to increase the fundamental beam intensity, leading to a focal spot size of 145 μm at 1240 nm.

	λ_{in}	P_{FF}	τ_{FWHM}	w_0	I_{FF}
OPA (TOPAS)	1140 nm	17.35 mW	83 fs	3.7 mm	0.9 GW/cm^2
	1200 nm	18.4 mW	102 fs	4 mm	1 GW/cm^2
	1300 nm	30.8 mW	50 fs	4.3 mm	2 GW/cm^2
	1400 nm	24.8 mW	52 fs	4.7 mm	1.3 GW/cm^2

Table 4.1.2: Tunable femtosecond source parameters under experimental conditions for SHG.

Measurements were performed using the same set-up described in Chapter 2.1. However, as we are now dealing with different wavelengths, some of the filters were replaced or added. First, a longpass filter (Thorlabs, FELH1100) was used to remove undesired frequency components coming from the OPA, and the pulses were attenuated using ND filters. Second, a superachromatic waveplate was employed to prepare and control the input beam polarization. Third, the longpass filter used to eliminate harmonic radiation generated by elements in the optical path placed before the sample had, in this case, a higher cut-on wavelength (Thorlabs, FGL850). The filters placed after the sample to attenuate fundamental radiation were also replaced (Thorlabs, FELH1100).

Experimental efficiencies were obtained by performing a calibration procedure similar to that explained in Chapter 2.1. We took the measurement at 620 nm by tuning the OPA at 1240 nm and generating efficient SH light with the phase-matched BBO crystal. The responsivity was calculated as $R_{\mathrm{PMT}} = V_{\mathrm{PMT}}/(T_{\mathrm{ND}} P_{\mathrm{PMT}})$, where V_{PMT} is the signal read taken with the oscilloscope to which the PMT is connected, P_{PMT} is the power measured with a photodiode in front of the PMT, and T_{ND} is the transmission of the ND filters placed before the PMT. A more extensive description of this method can be found in Chapter 2.1. This procedure should have been repeated for all input wavelengths used in the experiments, as the responsivity of the PMT may depend on it. In fact, this is what was done in the study of the silicon membranes, shown in Chapter 3.2. However, we did not expect a strong variation because the scanned range of frequencies was not very broad, so we assumed the responsivity of the PMT to be constant in the range of wavelengths that we studied. The transmission T of the detection arm also depends on incident wavelength. In Fig. 4.1.1(a) we show the input power used in the experiments for different incident wavelength. In Fig. 4.1.1(b) we have plotted the transmission T of the detection arm as a function of incident wavelength. As it was determined in Chapter 2.1, this transmission is defined as $T = P_{\mathrm{PMT}}/P_{\mathrm{Sample}}$, where P_{PMT} and P_{Sample} are the power generated by the BBO crystal measured in front of the PMT and at the sample plane, respectively.

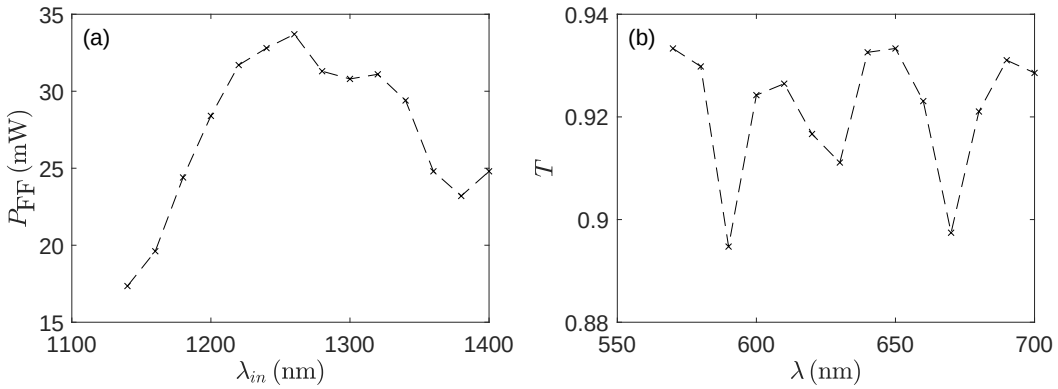

Figure 4.1.1: (a) Measurements of the incident average power and (b) measurement of the transmission of the detection arm as a function of wavelength.

4.2 Description of the samples

The ITO sample consists of a 20 nm-thick layer on top of a fused silica substrate. The ITO nanolayer was magnetron sputtered [31, 110] from an ITO target on transparent fused silica glass. The electro-optical properties of deposited ITO films depend on a number of processing conditions, including substrate temperature, sputtering power, deposition pressure, oxygen partial pressure, and post-annealing. The sample was fabricated at room temperature with a power of 100 W and Ar sputter pressure of 5 mTorr. The sputtered ITO typically has an ENZ crossing above 1800 nm. The samples were post-annealed in vacuum so that a zero-crossing of the real part of the dielectric constant is blueshifted.

The samples were analyzed using a variable angle spectroscopic ellipsometer (Woollam, VASE). Additional, angular TM-polarized transmission measurements were made to verify the spectral location of the ENZ crossing point. The resistivity of ITO is attributed to oxygen vacancy and film crystallinity. Therefore, the deposition conditions as well as the post-annealing process allow one to tune the ENZ wavelength. Our 20 nm-thick sample was annealed at 600°C and displays an ENZ condition near 1260 nm. An schematic representation of the geometry of the problem is shown in Fig. 4.2.1 for TM-polarized incident light, where $\mathbf{E}_\omega$, $\mathbf{H}_\omega$ and $\mathbf{S}_\omega$ are

electric and magnetic fields and Pointing vector, respectively, at the fundamental frequency, and θ_{in} is the angle of incidence.

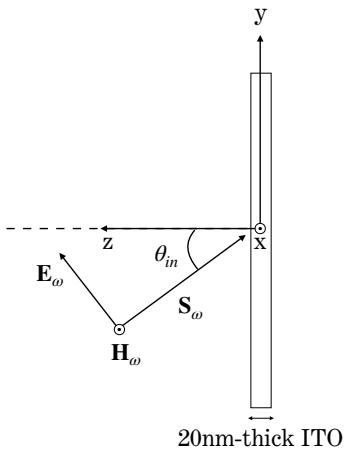

Figure 4.2.1: Schematic representation of the ITO nanolayer when TM-polarized light is incident at a certain angle θ_{in}.

4.3 Theoretical approach

The situation in conductive oxides like ITO is different from that of semiconductors like GaAs and silicon because now, free electrons also contribute to the linear and nonlinear optical response of the material. As a consequence, a Drude portion must be added in the dielectric function of this material:

$$\varepsilon(\tilde{\omega}) = 1 - \frac{\tilde{\omega}_{p,f}}{\tilde{\omega}^2 + i\tilde{\gamma}_f\tilde{\omega}} - \frac{\tilde{\omega}_{p,b}^2}{\tilde{\omega}^2 - \tilde{\omega}_0^2 + i\tilde{\gamma}_b\tilde{\omega}} \tag{4.3.1}$$

where $\tilde{\omega} = 1/\lambda$ and it has μm^{-1} units. In Eq. 4.3.1 it can be seen that now a Drude portion and a Lorentzian resonance describe the complex dielectric constant.

The ENZ wavelength in ITO may depend on the deposition conditions as well as the post-annealing process. So, in this case, the samples were analyzed using a variable angle spectroscopic ellipsometer (Woollam, VASE), from which data of the real and imaginary parts of the dielectric constant was extracted and is shown in Fig. 4.3.1 with dashed curves. This data was fitted with Eq. 4.3.1 and the following values were obtained for plasma and resonant frequencies and damping coefficients: $(\tilde{\omega}_{p,b}, \tilde{\omega}_0, \tilde{\gamma}_b) = (11.5, 7, 0.01)$ for bound electrons, and

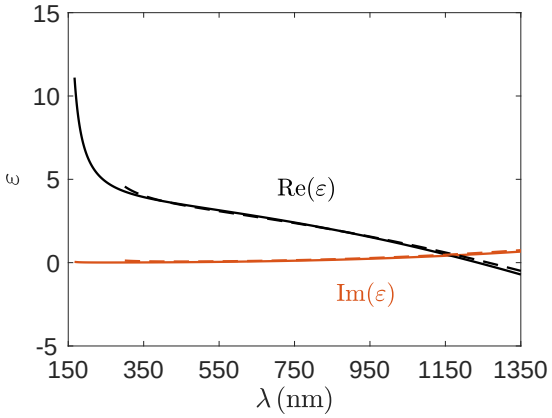

Figure 4.3.1: Real (black dashed curves) and imaginary (red dashed curves) parts of the complex dielectric constant of our ITO sample measured with a variable angle spectroscopic ellipsometer. The respective solid curves are a Drude-Lorentz fit to the data corresponding to Eq. 4.3.1.

$(\tilde{\omega}_{p,f}, \tilde{\gamma}_f) = (1.5785, 0.1105)$ for free carriers. It was also obtained that the real part of the dielectric constant crosses zero at 1260 nm. This is shown in Fig. 4.3.1, where it can be seen that the curve is strongly indicative of the fact that material dispersion is Drude-like above 450 nm, and Lorentz-like at smaller wavelengths. The absorption resonance becomes discernible in the data near 300 nm. However, the presence of the Lorentz resonance ascribes a nonlinear third order response that supplements and competes with the hot electron nonlinearity, which in turn accounts for a dynamic redshift of the free electron plasma frequency.

As it was shown in Chapter 1.5 the dynamics of free and bound electrons can be described with the following equations:

$$\begin{aligned}\ddot{\mathbf{P}}_f + \tilde{\gamma}_f \dot{\mathbf{P}}_f = \frac{n_{0,f} e^2 \lambda_0^2}{m_{0,f}^* c^2}\mathbf{E} - \frac{e\lambda_0}{m_{0,f}^* c^2}(\nabla \cdot \mathbf{P}_f)\mathbf{E} + \frac{e\lambda_0}{m_{0,f}^* c^2}\dot{\mathbf{P}}_f \times \mathbf{H} \\ + \frac{5E_F}{3m_{0,f}^* c^2}[\nabla(\nabla \cdot \mathbf{P}_f) + \frac{1}{2}\nabla^2 \mathbf{P}_f] - \frac{1}{n_{0,f} e\lambda_0}[(\nabla \cdot \dot{\mathbf{P}}_f)\dot{\mathbf{P}}_f + (\dot{\mathbf{P}}_f \cdot \nabla)\dot{\mathbf{P}}_f]\end{aligned} \tag{4.3.2}$$

$$\ddot{\mathbf{P}}_b + \tilde{\gamma}_b \dot{\mathbf{P}}_b + \tilde{\omega}_0^2 \mathbf{P}_b + \mathbf{P}_b^{\mathrm{NL}} = \frac{n_{0,b} e^2 \lambda_0^2}{m_b^* c^2}\mathbf{E} + \frac{e\lambda_0}{m_b^* c^2}(\mathbf{P}_b \cdot \nabla)\mathbf{E} + \frac{e\lambda_0}{m_b^* c^2}\dot{\mathbf{P}}_b \times \mathbf{H} \tag{4.3.3}$$

Equation 4.3.3 describes the dynamics of bound electrons, were $\mathbf{P}_b^{\mathrm{NL}} = -\tilde{b}(\mathbf{P}_b \cdot \mathbf{P}_b)\mathbf{P}_b$ as ITO is a centrosymmetric material. A part from the third order bulk contribution, Eq. 4.3.3 also accounts for surface and magnetic nonlinearities through the terms $\frac{e\lambda_0}{m_b^* c^2}(\mathbf{P}_b \cdot \nabla)\mathbf{E}$ and $\frac{e\lambda_0}{m_b^* c^2}\dot{\mathbf{P}}_b \times \mathbf{H}$, respectively. Equation 4.3.2 represents the behaviour of free electrons, and it contains a

quadrupole-like Coulomb term, $-\frac{e\lambda_0}{m_f^* c^2}(\nabla \cdot \mathbf{P}_f)\mathbf{E}$, the magnetic Lorentz force, $\frac{e\lambda_0}{m_f^* c^2}\dot{\mathbf{P}}_f \times \mathbf{H}$, convective terms $-\frac{1}{n_{0,f} e\lambda_0}[(\nabla \cdot \dot{\mathbf{P}}_f)\dot{\mathbf{P}}_f + (\dot{\mathbf{P}}_f \cdot \nabla)\dot{\mathbf{P}}_f]$, and nonlocal effects due to pressure and viscosity, $\frac{5E_F}{3m_f^* c^2}\nabla(\nabla \cdot \mathbf{P}_f + \frac{1}{2}\nabla^2 \mathbf{P}_f)$. However, in the case of conductive oxides like ITO, a term in Eq. 4.3.2 is missing if we want to take into account the contribution of hot electrons in the nonlinear polarization. This contribution is given by the fact that the effective mass of free electrons is now a function of temperature.

In conductive oxides the description of hot carriers is typically done by implementing the two-temperature model, which couples the lattice temperature to that of the free electron gas. However, if the electron temperature is only a few thousand degrees Kelvin, as in the case of ITO, the temperature dependence of the free electron's effective mass may be quantified by an expression that connects linearly the electron effective mass to the electron gas temperature (T_e) [111]:

$$m_f^*(T_e) \approx m_{0,f}^* + K_B T_e = m_{0,f}^* + K_B \Lambda \int \mathbf{J} \cdot \mathbf{E} dt \tag{4.3.4}$$

where K_B is Boltzmann's constant, Λ is a constant of proportionality, $m_{0,f}^*$ is the free electron's rest mass for no applied field and $\Lambda \int \mathbf{J} \cdot \mathbf{E}$ represents absorption. For convenience, we assume the simplified form $\mathbf{J} = \sigma_0 \mathbf{E}$, where σ_0 is the conductivity. Using Eq. 4.3.4, the leading term on the right hand side of Eq. 4.3.2 may be written as:

$$\begin{aligned} \frac{n_{0,f} e^2 \lambda_0^2}{m_f^*(T_e) c^2}\mathbf{E} &= \frac{n_{0,f} e^2 \lambda_0^2}{m_{0,f}^* c^2}\left(1 + \frac{\Lambda}{m_{0,f}^*}\int \mathbf{J} \cdot \mathbf{E} dt\right)^{-1}\mathbf{E} \\ &\approx \frac{n_{0,f} e^2 \lambda_0^2}{m_{0,f}^* c^2}\left(1 - \frac{\Lambda\sigma_0}{m_{0,f}^*}\int \mathbf{E} \cdot \mathbf{E} dt + \left(\frac{\Lambda\sigma_0}{m_{0,f}^*}\right)^2 (\mathbf{E} \cdot \mathbf{E})^2 + ...\right)\mathbf{E} \end{aligned} \tag{4.3.5}$$

For simplicity, we introduce a parameter $\tilde{\Lambda}$ proportional to the product of $\frac{\Lambda\sigma_0}{m_{0,f}^*}$ and the temporal duration of the pulse, so that Eq. 4.3.5 takes the following form:

$$\frac{n_{0,f} e^2 \lambda_0^2}{m_f^*(T_e) c^2}\mathbf{E} \approx \tilde{\omega}_{p,f}^2 \mathbf{E} - \tilde{\Lambda}(\mathbf{E} \cdot \mathbf{E})\mathbf{E} \tag{4.3.6}$$

where $\tilde{\omega}_{p,f}^2 = 4\pi n_{0,f} e^2 \lambda_0^2/(m_{0,f}^* c^2)$ is the scaled free electron plasma frequency in CGS units. Equation 4.3.6 tells that the coefficient $\tilde{\Lambda}$ determines the spatiotemporal dynamics of the redshift impressed upon the plasma frequency, and it includes to Eq. 4.3.2 cubic nonlinearities. We note

that the effective mass appears in all but one term on the right-hand side of Eq. 4.3.2. However, additional nonlinear contributions beyond Eq. 4.3.6 to the rest of the terms in Eq. 4.3.2 are of higher order and for our purposes in this study will be neglected. The parameter $\tilde{\Lambda}$ is generally dispersive, but for simplicity we assume it to be nearly constant in the range of wavelengths of interest. Its magnitude can vary substantially ranging from 10^{-7} to 10^{-9}, and is determined relying on experimental conversion efficiencies.

After adding the hot electron contribution, the polarization equation describing the dynamics of free electrons in ITO can be expressed as:

$$\begin{aligned}\ddot{\mathbf{P}}_f + \tilde{\gamma}_f \dot{\mathbf{P}}_f = \frac{n_{0,f} e^2 \lambda_0^2}{m_{0,f}^* c^2}\mathbf{E} - \tilde{\Lambda}(\mathbf{E}\cdot\mathbf{E})\mathbf{E} - \frac{e\lambda_0}{m_{0,f}^* c^2}(\nabla\cdot\mathbf{P}_f)\mathbf{E} \\ + \frac{e\lambda_0}{m_{0,f}^* c^2}\dot{\mathbf{P}}_f \times \mathbf{H} + \frac{5E_F}{3m_{0,f}^* c^2}[\nabla(\nabla\cdot\mathbf{P}_f) + \frac{1}{2}\nabla^2\mathbf{P}_f] \\ - \frac{1}{n_{0,f} e\lambda_0}[(\nabla\cdot\dot{\mathbf{P}}_f)\dot{\mathbf{P}}_f + (\dot{\mathbf{P}}_f\cdot\nabla)\dot{\mathbf{P}}_f]\end{aligned} \tag{4.3.7}$$

4.4 Results and discussion

Experiments have been performed pumping our ITO nanolayer with femtosecond pulses tuned in the 1140 nm-1600 nm wavelength range, with incident pulse peak intensities ranging from 1 GW/cm^2 to 2 GW/cm^2. Our experiments include measurements of SHG and THG efficiencies as a function of incident angle, wavelength and polarization. Simulations were performed with pulses 100 fs in duration, and incident power densities were set to be $\sim$ 1 GW/cm^2, but were allowed to vary somewhat consistently with experimental conditions.

In the first experiment, we recorded the SHG efficiency (η_{SHG}) as a function of fundamental wavelength around the ENZ condition, for a fixed incident angle of 60° and TM-polarized fundamental and SH fields. The spectral response of the SH generated both in transmission and in reflection is shown in Fig. 4.4.1(a), depicted with cross markers. The curves show a clear spectral dependence of the SHG conversion efficiency and its enhancement near the ENZ condition, appearing close to 1240 nm. In this regard, it is important to note that the locations of the transmitted and reflected maxima clearly do not coincide most likely because transmission

depends more on propagation through the bulk material, while the reflected component partially benefits from conditions at the surface. This shift, as well as the amplitude of the curves, is well reproduced by the numerical predictions, which are depicted with solid curves. Since ITO is a centrosymmetric material, SH sources are found mainly in the free electron components. Nonlocal effects, given by the term $\Sigma[\nabla(\nabla\cdot\mathbf{P}_f)+\frac{1}{2}\nabla^2\mathbf{P}_f]$ where $\Sigma=\frac{5E_F}{3m^*_{0,f}c^2}$, which blueshift the ENZ resonance, and the hot electron contribution, given by the term $-\tilde{\Lambda}(\mathbf{E}\cdot\mathbf{E})\mathbf{E}$, which redshifts the plasma frequency, may change the SHG response, altering the position of the maxima in the SHG spectrum. The effective free electron mass and density were chosen to be $m^*_{0,f}=0.033m_e$ and $n_{0,f}\sim 10^{20}\,\mathrm{cm}^{-3}$, which combine a Fermi energy that imparts a blueshift of nearly 50 nm to the SHG peak spectral position, which corresponds to $\Sigma=3.48\cdot10^{-5}$. The magnitude of the hot electron parameter was chosen so that its effect is to redshift the SHG spectra by approximately 15 nm, for a net blueshift of $\sim$ 35 nm, which corresponds to $\tilde{\Lambda}\sim10^{-9}$. We highlight that the agreement that we find between predictions and experiments is quite extraordinary and extends to the relative locations of transmitted and reflected SH maxima. This ratio is not maintained if, for instance, we arbitrarily set to zero the magnetic Lorentz contribution, although the peaks remain similarly shifted with respect to each other. By the same token, artificially eliminating Coulomb and convective terms instead leads to a completely different SH response, an indication that one should be wary of using models that merely insert effective, dispersionless surface and/or volume nonlinearities in order to reproduce the shape of experimental curves, if not the amplitudes.

The contrasting actions that nonlocal effects and hot electrons can have in the SHG spectra are shown in Fig. 4.4.1(b), were we show predictions of the transmitted SHG efficiencies as a function of incident wavelength under three different scenarios. The dashed curve is obtained by neglecting both contributions, and shows a peak at 1260 nm incident wavelength. When the hot electron contribution, with $\tilde{\Lambda}=10^{-9}$, is introduced, the SHG peak is redshifted by approximately 15 nm. This situation is exemplified by the pointed curve. Finally, if both contributions are taken into account, with $\tilde{\Lambda}=10^{-9}$ and $\Sigma=3.48\cdot10^{-5}$, the solid curve is

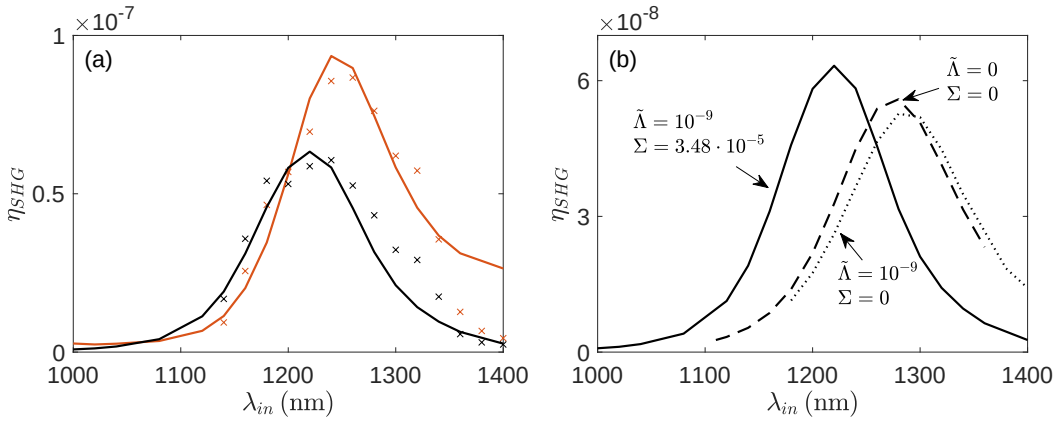

Figure 4.4.1: (a) Transmitted (black) and reflected (red) SHG efficiencies as a function of pump wavelength and at an incident angle of 60° from the ITO nanolayer. Measurements are plotted with cross markers and predictions are depicted with solid curves. (b) Predictions of the transmitted SHG efficiency from the ITO nanolayer under three different scenarios. The dashed curve is obtained neglecting both the hot electron contribution and nonlocal effects; the pointed curve is calculated introducing the hot electron contribution with $\tilde{\Lambda} = 10^{-9}$; the solid curve is obtained by taking both contributions into account with $\tilde{\Lambda} = 10^{-9}$ and $\Sigma = 3.48 \cdot 10^{-5}$ in Eq. 4.3.2.

obtained, which shows a blueshift of the SHG peak of ~ 35 nm with respect to the dashed curve. This situation corresponds to the black, solid curve, shown in Fig. 4.4.1(a). With this, it is obvious then that taking this contributions into account, apart from the above mentioned ones, is crucial to properly predict the SHG response in our ITO nanolayer.

A second set of experiments on SHG from the ITO nanolayer is shown in Fig. 4.4.2, where we show the angular dependence of the transmitted SHG efficiencies when the sample is pumped at different input wavelengths: above (1300 nm), and at (1240 nm) the ENZ condition. Their simulated counterparts are plotted with solid curves. By examining this angular dependence, features that may be ascribed to nonlocal effects can be revealed. The peak SHG efficiencies, which occur near 70°, and the shape of the curves depend on the magnitude of the nonlocal coefficient, and to an extent, they are counteracted by pump absorption and electron cloud heating. In Fig. 4.4.2(b) we plot SHG efficiency as a function of angle at 1300 nm, which displays a clear shoulder below 40°. The predicted transmitted SHG curve, depicted with a solid curve, displays a slight shoulder below 40° before peaking at 70°. However, the dashed curve can be

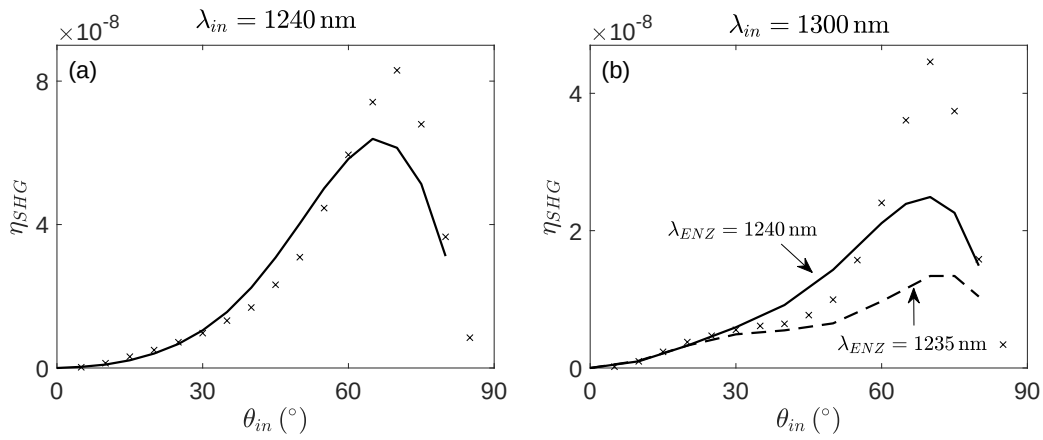

Figure 4.4.2: Measured (markers) and predicted (solid curves) transmitted SHG efficiencies as a function of incident angle for the ITO nanolayer when the pump wavelength is tuned at (a) 1240 nm and (b) 1300 nm. The curve with the prominent shoulder (dashed curve) in (b) is calculated with an ENZ crossing point near 1235 nm.

obtained by either artificially increasing the Fermi energy, and thus the nonlocal coefficient, or using a material dispersion curve that displays a slightly blueshifted ENZ crossing point, in either case without modifying either $m^*_{0,f}$ or $n_{0,f}$ so as not to affect SH gain. Specifically it was obtained by tuning the zero crossing point at 1235 nm. Given the evident and quite remarkable qualitative and quantitative agreement between our experimental observations and our predictions, in terms of spectral response, peak locations, the ratio of reflected/transmitted maxima, and angular dependence, including the ability to reproduce the shoulder shown in Fig. 4.4.2(b), the model appears to clearly and accurately capture the most prominent aspects of the electromagnetic response of conducting oxides such as ITO.

The changes that nonlocal effects can have on the optical response of conductive oxides like ITO are not only those illustrated in Figs. 4.4.1 and 4.4.2. Nonlocal effects can also induce additional absorption resonances and anisotropic dielectric response: longitudinal ($\langle\varepsilon_{zz}\rangle$) and transverse ($\langle\varepsilon_{yy}\rangle$) effective dielectric functions are modulated differently along the propagation direction, and display different ENZ crossing points. The former is illustrated in Fig. 4.4.3(a), where we depict linear pump absorption spectra (A) for 100 fs, TM-polarized pulses incident at 60° on a 20 nm-thick ITO film, for local ($\Sigma = 0$) and nonlocal ($\Sigma \neq 0$) regimes. The absorption

is calculated as the total scattered (transmitted and reflected) pump energy subtracted from the total energy contained in the incident pulse. As it can be seen, for the pump field, nonlocal effects manifest themselves primarily with a blueshifted main peak and additional absorption resonances, highlighted by the arrows near 700 nm and 900 nm. As we will see later, these additional resonances can be correlated directly to longitudinal, resonant oscillations of the free electron gas.

Our numerical simulations reveal an anisotropic response in the presence of nonlocal effects. At low incident power densities, in a two-dimensional geometry (invariant in the x-direction, see Fig. 3.2.4(b)) only linear, nonlocal effects survive. In this case, Eq. 4.3.7 may be written as follows:

$$\begin{aligned}\ddot{\mathbf{P}}_f + \tilde{\gamma}_f \dot{\mathbf{P}}_f = \frac{n_{0,f} e^2 \lambda_0^2}{m_{0,f}^* c^2} \mathbf{E} \\ + \frac{5E_F}{3m_{0,f}^* c^2} \left[\left(\frac{\partial}{\partial y}\mathbf{j} + \frac{\partial}{\partial z}\mathbf{k} \right) \left(\frac{\partial P_y}{\partial y} + \frac{\partial P_z}{\partial z} \right) + \frac{1}{2} \left(\frac{\partial^2}{\partial y^2} + \frac{\partial^2}{\partial z^2} \right) (P_y \mathbf{j} + P_z \mathbf{k}) \right]\end{aligned} \tag{4.4.1}$$

By Fourier transforming Eq. 4.4.1 and separating the polarization's vector components, we get:

$$\begin{aligned} P_y &= \frac{\frac{n_{0,f} e^2 \lambda_0^2}{m_{0,f}^* c^2} E_y - \Sigma \tilde{k}_y \tilde{k}_z P_z}{-\tilde{\omega}^2 - i\tilde{\gamma}_f \tilde{\omega} + \frac{3}{2}\Sigma \tilde{k}_y^2 + \frac{1}{2}\Sigma \tilde{k}_z^2} \\ P_z &= \frac{\frac{n_{0,f} e^2 \lambda_0^2}{m_{0,f}^* c^2} E_z - \Sigma \tilde{k}_y \tilde{k}_z P_y}{-\tilde{\omega}^2 - i\tilde{\gamma}_f \tilde{\omega} + \frac{3}{2}\Sigma \tilde{k}_z^2 + \frac{1}{2}\Sigma \tilde{k}_y^2} \end{aligned} \tag{4.4.2}$$

where $\tilde{k}_{y,z} = \lambda_0 k_{y,z}$. In Eq. 4.4.2 it can be seen that, in the absence of nonlocal effects ($\Sigma = 0$), the local Drude model is recovered. Equation 4.4.2 may be solved and put into the usual form: $\begin{pmatrix} P_y \\ P_z \end{pmatrix} = \begin{pmatrix} \chi_{yy}^{(1)} & \chi_{yz}^{(1)} \\ \chi_{zy}^{(1)} & \chi_{zz}^{(1)} \end{pmatrix} \begin{pmatrix} E_y \\ E_z \end{pmatrix}$.

In the discussion that follows the off-diagonal terms will be neglected, in view of the relatively small magnitude of Σ. The form of Eq. 4.4.2 thus demonstrates that even if the medium is assumed to be isotropic, nonlocal effects intervene by introducing an intrinsic anisotropy that affects propagation. This is illustrated in Fig. 4.4.4, where we plot the retrieved complex dielectric constant of ITO under different conditions by means of a method that we call numerical ellipsometry which will be explained in Chapter 6.

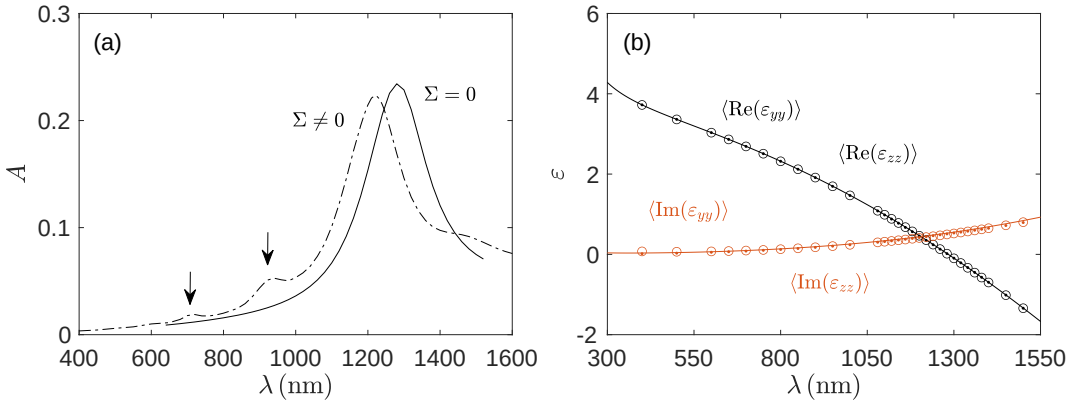

Figure 4.4.3: (a) Calculated local (solid curve) and nonlocal (dashed-pointed curve) pump absorption spectra at 60° incident angle. (b) Retrieved complex longitudinal (circe markers) and transverse (pointed markers) local dielectric constants. The solid curves represent our measured data fitted using a local Drude-Lorentz model, corresponding to that shown in Fig. 4.3.1.

In Fig. 4.4.3(b) we plot the measured complex dielectric function of our 20 nm-thick ITO layer, fitted with the local, isotropic Drude-Lorentz model, as it was shown in Fig. 4.3.1. Also shown in Fig. 4.4.3(b) are the spatially averaged, retrieved complex dielectric constants at low power densities (1 MW/cm^2) and in the local approximation. As it can be seen, there is excellent agreement between the experimentally retrieved data and our theoretical predictions. Also, based on the results shown in Fig. 4.4.3(b), one may also conclude that medium response is local and isotropic ($\langle \varepsilon_{yy} \rangle = \langle \varepsilon_{zz} \rangle$), notwithstanding the presence of the ENZ crossing point.

The introduction of nonlocal effects causes ε_{yy} and ε_{zz} to display unusual spatial inhomogeneities (Figs. 4.4.4(a-b)), while the effective dispersion $\langle \varepsilon_{yy} \rangle$ and $\langle \varepsilon_{zz} \rangle$ exhibit discordant ENZ crossing points (Figs. 4.4.4(c-d)). In Figs. 4.4.4(a) and 4.4.4(b) we plot the retrieved complex longitudinal and transverse dielectric constants, respectively, as a function of the longitudinal coordinate z, for the propagation snapshot that corresponds to the peak of the pulse reaching the ITO layer. The layer starts at $z = 0$ and finishes at $z = 0.02\,\mu$m. The carrier wavelength is 1230 nm and the incident angle is 60°. Besides edge effects, in Fig. 4.4.4(a) Re(ε_{zz}) displays the expected drop to near-zero values inside the medium. On the other hand, in Fig. 4.4.4(b) the complex ε_{yy} exhibits oscillatory behavior with periodicity on only a few nanometers. A

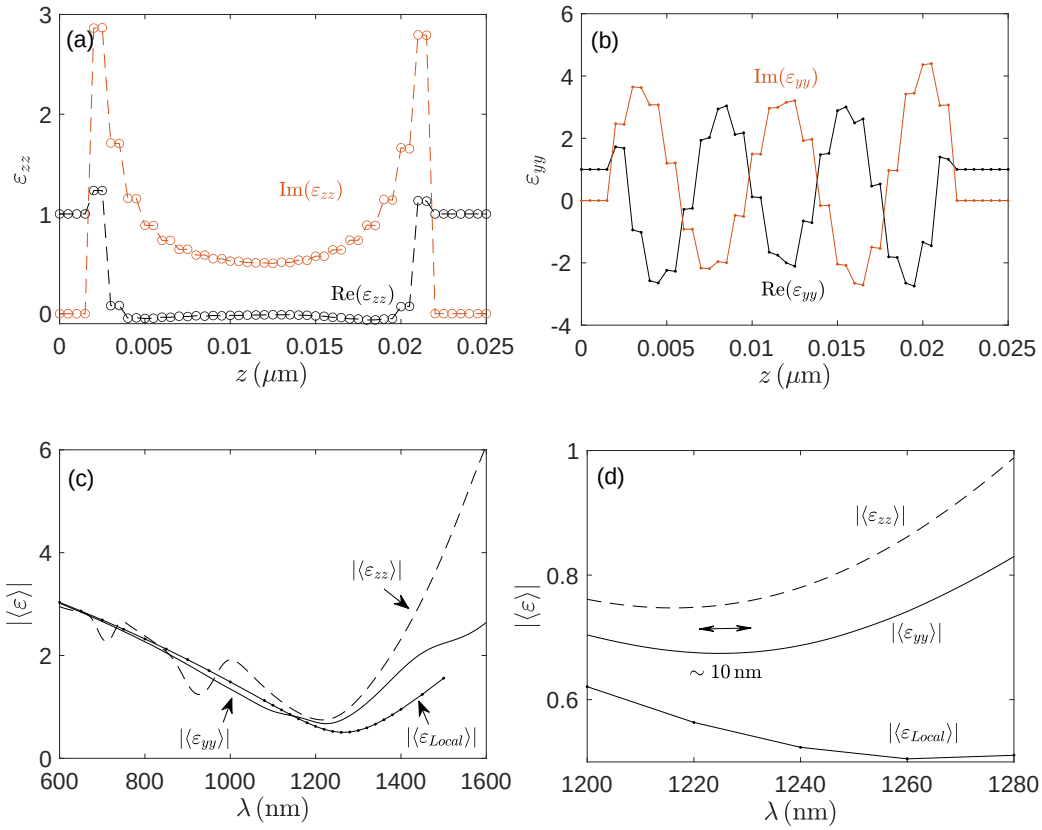

Figure 4.4.4: [(a)-(b)] Retrieved complex (a) longitudinal and (b) transverse nonlocal dielectric constants, respectively, at 60° incident angle as a function of the longitudinal coordinate. (c) Total local (solid curve with pointed markers) and nonlocal longitudinal (dashed curve) and transverse (solid curve) averaged over the thickness of the layer. (d) Fig. 4.4.4(c) in the 1200 nm-1280 nm wavelength range.

physically meaningful way to view these rapid oscillations is to note that since we are dealing with mostly free electrons, nonlocal effects induce currents that alternate direction inside the layer on the scale of the Fermi wavelength, as predicted and reported before for a CdO layer [100]. In general, the connection between conductivity and dielectric constant may be quantified as follows: $\sigma_{yy} = -i\omega_0 \frac{\varepsilon_{yy}-1}{4\pi} = \frac{\omega_0}{4\pi}\left(\mathrm{Im}(\varepsilon_{yy}) - i(\mathrm{Re}(\varepsilon_{yy})-1)\right)$, and similarly for σ_{zz}. The sign of the imaginary part thus governs the direction of local current flow. However, from an effective medium standpoint their overall significance may be dismissed, as the averages $\langle \mathrm{Im}(\varepsilon_{yy,zz})\rangle$ are greater than zero in all cases we have investigated.

In Fig. 4.4.4(c) we plot the magnitudes of the total, local, and nonlocal effective dielectric constants predicted using our numerical ellipsometry method. The minimum in each curve, easily identified in Fig. 4.4.4(d), where we plot the same results as in Fig. 4.4.4(c) but in a shorter wavelength range, represents the ENZ crossing point. The longitudinal dielectric constant displays the same kind of modulation that pump absorption displays in Fig. 4.4.3(a), an indication that it drives the dynamics. In Fig. 4.4.4(d) it can be seen that, in addition to an evident degree of anisotropy, the nonlocal curves are blueshifted with respect to the local dielectric constant and with respect to each other, with crossing points that are mismatched by nearly 10 nm. It is also important to note that at certain wavelengths the difference between $\langle \varepsilon_{yy} \rangle$ and $\langle \varepsilon_{zz} \rangle$ approaches zero. These points are typically referred to as isotropic points, because they represent the wavelengths for which the medium acts as if it were isotropic.

Finally, in Fig. 4.4.5(a) we show experimental (cross markers) and simulated (solid curve) results of the transmitted THG efficiency (η_{THG}) as a function of incident angle when the sample is pumped at the ENZ condition. We recall that for these measurements, higher incident pulse peak intensities were used. The minimum that occurs at relatively small angles is a unique feature of the angular dependence of THG from an ITO layer that had been previously predicted to occur [112]. Although we consider all sources of THG, including cascading from both free and bound electrons, second order sources, i.e., Coulomb, Lorentz, and convective and nonlocal terms in Eqs. 4.3.7 and 4.3.3, there are two main fonts of TH signal: (i) hot electrons, via the term $-\tilde{\Lambda}(\mathbf{E}\cdot\mathbf{E})\mathbf{E}$, and (ii) the bound electron nonlinear polarization component given by $\mathbf{P}_b^{\mathrm{NL}} = -\tilde{b}(\mathbf{P}_b\cdot\mathbf{P}_b)\mathbf{P}_b$. Accordingly, the relative amounts of THG triggered by either nonlinear term depends on the relative amplitudes of the scaled coefficients $\tilde{\Lambda}$ and $\tilde{b}$, which have been chosen to be $\tilde{\Lambda} \sim 10^{-8}$ and $\tilde{b} = 10^{-8}$, as well as proximity to the ENZ condition. These two types of nonlinearities behave differently because they are active in different wavelength ranges, tend to respond in different ways at large intensities, but give similar qualitative contributions at low intensities. This can be seen in Fig. 4.4.5(b), where we have plotted our predictions for transmitted THG spectra using an incident pulse peak power density of 20 GW/cm^2, and

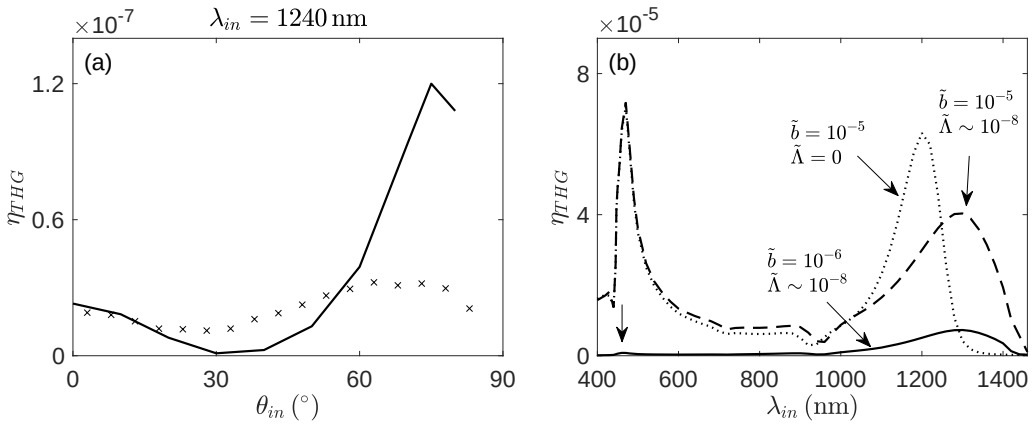

Figure 4.4.5: (a) Angular dependence of the measured (cross markers) and predicted (solid curves) transmitted THG efficiencies for the ITO nanolayer when incident pulses are tuned at 1240 nm. (b) Predictions of the transmitted THG efficiencies as a function of pump wavelength and scaled third order coefficients $\tilde{b}$ and $\tilde{\Lambda}$: the solid curve is obtained with $\tilde{b} = 10^{-6}$ and $\tilde{\Lambda} \sim 10^{-8}$, the dashed curve is calculated with $\tilde{b} = 10^{-5}$ and $\tilde{\Lambda} \sim 10^{-8}$, while the pointed curve refers to the case when $\tilde{b} = 10^{-5}$ and $\tilde{\Lambda} = 0$.

as a function of the scaled third order coefficients $\tilde{\Lambda}$ and $\tilde{b}$. Reflection curves display similar behavior. The solid curve is obtained with $\tilde{\Lambda} \sim 10^{-8}$ and $\tilde{b} = 10^{-6}$. As it is shown in Fig. 4.3.1, the dielectric constant of the sample may display an absorption resonance near 150 nm, with a corresponding nonlinearity capable of significantly enhancing the THG even under condition of high absorption. The TH peak that arises from the Lorentzian portion of the dielectric response resonance is identified by an arrow, and is one order of magnitude smaller compared to the TH originating at the ENZ resonance. The spectrum exemplified by the dashed curve is obtained by increasing $\tilde{b}$ by one order of magnitude, so that we may ascertain the relative impact of the bound electron resonance with respect to the hot electron contribution. This increase translates to a two order of magnitude increase in conversion efficiency at the bound electron resonance, which now dominates over the TH signal originating at the ENZ peak. Finally, the pointed curve is obtained by turning off the hot electron contribution. This curve suggests that the hot electrons govern THG by shifting and distorting the ENZ resonance, and by contributing little near the Lorentz resonance.

The disagreement between measurements and predictions in Fig. 4.4.5(a) may be for at least two reasons: (i) theoretical and (ii) experimental. From a theoretical point of view, precise location and maximum amplitude of the bound electron resonance are not known very well, notwithstanding the agreement apparent in Fig. 4.3.1 for $\lambda > 300\,\text{nm}$. In fact, in the wavelength range shown, the fitting parameters we use for the Lorentzian portion of the dielectric response are not unique. The amplitude at resonance $\tilde{\omega}_0$ depends on the combination of effective bound electron mass m_b^* and damping coefficient $\tilde{\gamma}_b$. The location of the resonance determines the nonlinear parameter $\tilde{b} \propto \frac{\omega_0^2}{L^2}$, and the amplitude determines the long-wavelength behavior of the effective third order nonlinearity. At long wavelengths, the effective third order coefficient is triggered by the electron gas. So, at this stage we do not have enough information to state the magnitudes of these parameters with any certainty. Further studies are required to extract these parameters from the spectral response over a wide range of wavelengths. However, from the experimental point of view, a direct extension of the measurements to include spectral TH signal dependence is not a straightforward task, at least at the stage we were when this study was performed. The main problem was related to the prospect of making accurate calibration measurements at UV wavelengths partly because transmittance values at wavelengths below 400 nm decrease significantly the amount of the TH signal reaching the PMT. Moreover, the sensitivity of the PMT is drastically reduced at these wavelengths. In order to accomplish proper calibration, a TH signal must first be generated with enough intensity, which was not possible for all wavelengths in our set-up. In fact, as already stated, the experimental THG efficiency was approximated using the calibration done for the SH measurements. So, we cannot rely, in this case, on experimental values of THG efficiencies to fully determine the values of $\tilde{b}$ and $\tilde{\Lambda}$.

4.5 Conclusions and summary

In summary, we have presented experimental results on the spectral and angular response of SHG and THG from a 20 nm-thick ITO layer close to its ENZ crossing point. The results suggest

that transmitted and reflected SHG spectra display maxima that are shifted by approximately 20 nm with respect to each other. This relative shift has not been reported before and persists even in the absence of nonlocal effects and constant plasma frequency. Additional simmulations suggest that this shift may depend on sample thickness. We have also explored the angular dependence of THG and observed a minimum at approximately 30° angle of incidence.

Moreover, we have predicted that nonlocal effects can induce anisotropic medium response and that at sufficiently large intensities, we are able to discriminate between third order free and bound electron contributions to THG.

5
SHG and THG from gold: bound and hot electrons

In this chapter we report experimental and theoretical results on SHG and THG from a 20 nm- and a 70 nm-thick gold layers. We discuss the relative roles that bound and hot electrons play in THG. In other words, how the third order bulk contribution to the nonlinear polarization and an intensity dependent free electron density affect the TH response. We conclude that our measured efficiencies suggest that the TH signal originates mostly from hot electrons.

The comparison between measurements and simulations has allowed us to extract basic physical intrinsic properties of this material like the effective mass of free and bound electrons and the nonlinear oscillator parameter $\tilde{b}$. This knowledge allows us to make accurate predictions about conversion efficiencies in more complicated geometrical arrangements, which are able to enhance several orders of magnitude harmonic generation conversion efficiencies. For this reason, in this chapter we also report experimental observations and numerical simulations of SHG and THG from a gold nanograting which exhibits a plasmonic resonance in the near-IR. From our results we obtain an increase of more than three orders of magnitude for SHG, while we report a THG conversion efficiency enhancement factor of 3200.

This chapter is structured in the following way. In Section 5.1 we report the study done with the gold nanolayers, and it includes a description of the experimental approach and the

samples. We also show how the theoretical model described in Chapter 1.5 is applied to the particular case of metals like gold, and finally experimental and theoretical results on SHG and THG are reported. In Section 5.2 we present the research done with the gold nanograting. This section is structured as the previous one. First we introduce the experimental approach, then a description of the samples, after that we include a description of the theoretical approach and finally we show our results. Then, the chapter is ended with some conclusions in Section 5.3.

5.1 Gold nanolayers

5.1.1 Experimental approach

We have measured SHG and THG efficiencies from a 20 nm- and a 70 nm-thick gold nanolayers as a function of incident angle and wavelength. These experiments were performed using the experimental set-up described in Chapter 2.1, and the harmonic signals were generated exciting the samples with two different laser sources, which have also been introduced in previous chapters: a Ti:Sapphire oscillator (Coherent, Mira 900-F) delivering femtosecond pulses tuned at 800 nm and a fiber laser (FYLA PS50) delivering picosecond pulses tuned at 1064 nm. The coated focusing lens (see Fig. 2.1.1) was chosen depending on fundamental wavelength and the amount of incident pulse peak intensities desired in the experiments. For SHG measurements, the samples were excited at both 800 nm and 1064 nm with a lens of focal length f = 200 mm: Thorlabs, LA1708-B and LA1708-C for the case of incident pulses tuned at 800 nm and 1064 nm, respectively. THG experiments were performed using incident 1064 nm light focused on the sample plane by means of a lens with focusing length f = 100 mm (Thorlabs, LA1509-C). Measurements of the beam waist were performed in order to estimate peak pump pulse intensities, which have been shown in Chapters 2.1 and 3.1.1. In Table 5.1.1 we collect the parameters, where it can be seen that typical incident pulse peak intensities used in the experiments were $\sim 1\,\mathrm{GW/cm^2}$ for SHG and $\sim 4.5\,\mathrm{GW/cm^2}$ for THG.

The bandpass filters used to attenuate the fundamental radiation after the sample, as well as the bandpass/laser line filters centered at the harmonic wavelength we want to detect placed at

the PMT were also chosen depending on incident/harmonic wavelength and have already been specified in previous chapters.

	Fiber laser		Ti:Sapphire
	f = 100 mm	f = 200 mm	f = 200 mm
P_{FF}	1.5 mW		1 W
f_{rep}	1 kHz		76 MHz
τ_{FWHM}	13 ps		140 fs
w_0	32 μm	78 μm	71 μm
I_{FF}	4.5 GW/cm^2	1 GW/cm^2	1 GW/cm^2

Table 5.1.1: Laser parameters under experimental conditions.

5.1.2 Description of the samples

The samples consist of a 20 nm- and a 70 nm-thick gold layers on top of a fused silica substrate. The gold films were deposited from a gold target on transparent fused silica glass using a magnetron sputtering system [31, 110]. The target power was 100 W and deposition pressure 3 mTorr. The samples were analyzed using a variable angle spectroscopic ellipsometer (Woollam, VASE). In Fig. 5.1.1 we show an schematic representation of the problem when TM-polarized light is incident with a certain angle θ_{in} to the gold nanolayer, where $\mathbf{E}_\omega$, $\mathbf{B}_\omega$ and $\mathbf{S}_\omega$ are electric and magnetic fields and Poynting vector at the fundamental frequency, respectively.

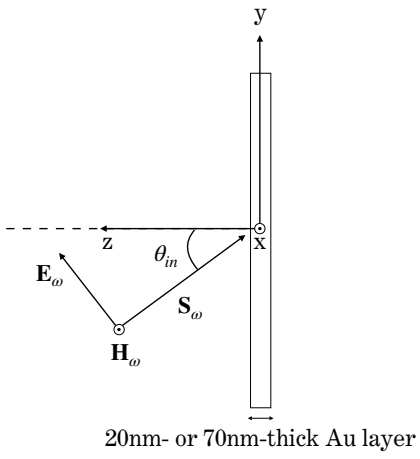

Figure 5.1.1: Geometric representation of TM-polarized light incident to a 20 nm- or 70 nm-thick gold nanolayer.

5.1.3 Theoretical approach

As well as in the case of ITO, in metals like gold both free and bound electrons contribute to the linear and nonlinear response of the material. This means that its complex dielectric constant is given by a Drude portion followed by one or more Lorentzian resonances. In the case of gold nanolayers, two Lorentzian resonances are enough to describe it, as shown in Eq. 5.1.1:

$$\varepsilon(\tilde{\omega}) = 1 - \frac{\tilde{\omega}_{p,f}}{\tilde{\omega}^2 + i\tilde{\gamma}_f\tilde{\omega}} - \frac{\tilde{\omega}^2_{p,b1}}{\tilde{\omega}^2 - \tilde{\omega}^2_{01} + i\tilde{\gamma}_{b1}\tilde{\omega}} - \frac{\tilde{\omega}^2_{p,b2}}{\tilde{\omega}^2 - \tilde{\omega}^2_{02} + i\tilde{\gamma}_{b2}\tilde{\omega}} \tag{5.1.1}$$

where $\tilde{\omega} = 1/\lambda$ and it has μm^{-1} units.

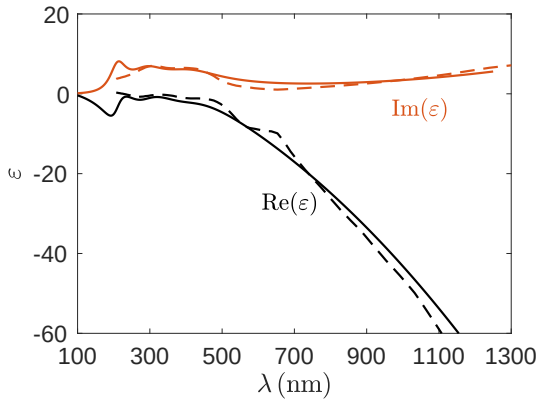

Figure 5.1.2: Real (black dashed curve) and imaginary (red dashed curve) parts of the complex dielectric constant of gold extracted from our ellipsometry measurements. These data have been fitted with Eq. 5.1.1, which is depicted with solid curves.

In Fig. 5.1.2 we have plotted data of the real and imaginary parts of the dielectric constant of gold extracted from our ellipsometry measurements, which is depicted with dashed curves. These data have been fitted with Eq. 5.1.1. This fitting is plotted with solid curves, and from it we have obtained that $(\tilde{\omega}_{p,b1}, \tilde{\omega}_{01}, \tilde{\gamma}_{b1}) = (3, 2.75, 0.1)$ and $(\tilde{\omega}_{p,b2}, \tilde{\omega}_{02}, \tilde{\gamma}_{b2}) = (11, 3.3, 0.75)$ for bound electrons, and $(\tilde{\omega}_{p,f}, \tilde{\gamma}_f) = (6.45, 0.05)$ for free electrons. These parameters are useful because they will be introduced in the dynamic equations of motion used to perform the numerical simulations.

As it was shown in Chapter 1.5 the dynamics of free and bound electrons can be described by:

$$\begin{aligned}\ddot{\mathbf{P}}_f + \tilde{\gamma}_f \dot{\mathbf{P}}_f = \frac{n_{0,f} e^2 \lambda_0^2}{m_{0,f}^* c^2}\mathbf{E} - \frac{e\lambda_0}{m_{0,f}^* c^2}(\nabla \cdot \mathbf{P}_f)\mathbf{E} + \frac{e\lambda_0}{m_{0,f}^* c^2}\dot{\mathbf{P}}_f \times \mathbf{H} \\ + \frac{5E_F}{3m_{0,f}^* c^2}[\nabla(\nabla \cdot \mathbf{P}_f) + \frac{1}{2}\nabla^2 \mathbf{P}_f] - \frac{1}{n_{0,f} e\lambda_0}[(\nabla \cdot \dot{\mathbf{P}}_f)\dot{\mathbf{P}}_f + (\dot{\mathbf{P}}_f \cdot \nabla)\dot{\mathbf{P}}_f]\end{aligned} \tag{5.1.2}$$

$$\ddot{\mathbf{P}}_{bj} + \tilde{\gamma}_{bj}\dot{\mathbf{P}}_{bj} + \tilde{\omega}_{0j}^2 \mathbf{P}_{bj} + \mathbf{P}_{bj}^{\mathrm{NL}} = \frac{n_{0,bj} e^2 \lambda_0^2}{m_{bj}^* c^2}\mathbf{E} + \frac{e\lambda_0}{m_{bj}^* c^2}(\mathbf{P}_{bj} \cdot \nabla)\mathbf{E} + \frac{e\lambda_0}{m_{bj}^* c^2}\dot{\mathbf{P}}_{bj} \times \mathbf{H} \tag{5.1.3}$$

The dynamics of bound electrons are described through Eq. 5.1.3, where j=1,2 represent two separate atomic spices, and $\mathbf{P}_b^{\mathrm{NL}} = -\tilde{b}(\mathbf{P}_b \cdot \mathbf{P}_b)\mathbf{P}_b$ as gold is a centrosymmetric material. A part from the third order bulk contribution, Eq. 5.1.3 also accounts for surface and magnetic nonlinearities through the terms $\frac{e\lambda_0}{m_b^* c^2}(\mathbf{P}_b \cdot \nabla)\mathbf{E}$ and $\frac{e\lambda_0}{m_b^* c^2}\dot{\mathbf{P}}_b \times \mathbf{H}$, respectively. Equation 5.1.2 describes the dynamics of free electrons, and it contains a quadrupole-like Coulomb term, $-\frac{e\lambda_0}{m_f^* c^2}(\nabla \cdot \mathbf{P}_f)\mathbf{E}$, the magnetic Lorentz force, $\frac{e\lambda_0}{m_f^* c^2}\dot{\mathbf{P}}_f \times \mathbf{H}$, convective terms $-\frac{1}{n_{0,f} e\lambda_0}[(\nabla \cdot \dot{\mathbf{P}}_f)\dot{\mathbf{P}}_f + (\dot{\mathbf{P}}_f \cdot \nabla)\dot{\mathbf{P}}_f]$, and nonlocal effects due to pressure and viscosity, $\frac{5E_F}{3m_f^* c^2}\nabla(\nabla \cdot \mathbf{P}_f + \frac{1}{2}\nabla^2 \mathbf{P}_f)$. In Eq. 5.1.2 a term is missing if we want to take into account the contribution of hot electrons in the nonlinear polarization. In the case of metals, we refer to hot electrons to those that may be temporally excited from the valence into the conduction band, provoking a transient increase of the free electron density n_f. In other words, Eq. 5.1.2 can be adapted to describe a time-varying free electron density triggered by interband transitions in metals. From Chapter 1.5.2, we recover the continuity equation for free electrons:

$$n_f(\mathbf{r}, t) = n_{0,f} + \frac{1}{e}\nabla \cdot \mathbf{P}_f \tag{5.1.4}$$

If the free electron density is allowed to vary as a function of applied intensity, Eq. 5.1.4 can be modified in the following way:

$$n_f(\mathbf{r}, t) = n_{0,f} + \frac{1}{e}\nabla \cdot \mathbf{P}_f + \tilde{\Lambda}(\mathbf{E} \cdot \mathbf{E}) \tag{5.1.5}$$

where $\tilde{\Lambda}$ is a scaled parameter that measures changes in the free electron density as a function of incident light intensity. It is generally dispersive, and depends on field fluence and absorption.

For simplicity we parametrize it, and assume it to be nearly constant in the range of wavelength of interest, ranging from $10^{-7} - 10^{-9}$ magnitudes.

With this correction, the polarization equation for free electrons in metals becomes:

$$\begin{aligned}\ddot{\mathbf{P}}_f + \tilde{\gamma}_f \dot{\mathbf{P}}_f = \frac{n_{0,f} e^2 \lambda_0^2}{m^*_{0,f} c^2}\mathbf{E} + \tilde{\Lambda}(\mathbf{E}\cdot\mathbf{E})\mathbf{E} - \frac{e\lambda_0}{m^*_{0,f}c^2}(\nabla\cdot\mathbf{P}_f)\mathbf{E} + \frac{e\lambda_0}{m^*_{0,f}c^2}\dot{\mathbf{P}}_f \times \mathbf{H} \\ + \frac{5E_F}{3m^*_{0,f}c^2}[\nabla(\nabla\cdot\mathbf{P}_f) + \frac{1}{2}\nabla^2\mathbf{P}_f] - \frac{1}{n_{0,f}e\lambda_0}[(\nabla\cdot\dot{\mathbf{P}}_f)\dot{\mathbf{P}}_f + (\dot{\mathbf{P}}_f\cdot\nabla)\dot{\mathbf{P}}_f]\end{aligned} \tag{5.1.6}$$

5.1.4 Results and discussion

The angular dependence of SHG and THG efficiencies were obtained by pumping the nanolayers with 13 ps and 140 fs pulses tuned at 1064 nm and 800 nm, respectively. Typical pump pulse power densities used in SHG experiments were measured to be $\sim 1\,\mathrm{GW/cm^2}$. For the detection of TH signals it was increased to $\sim 4.5\,\mathrm{GW/cm^2}$. For what the simulations are concerned, pulses tuned at either 800 nm or 1064 nm with 100 fs temporal duration were used, with peak intensities of $\sim 1\,\mathrm{GW/cm^2}$. These intensities were increased in the THG case accordingly to experimental conditions.

In Fig. 5.1.3 we plot and compare experimentally measured (cross markers) and predicted (solid curves) transmitted and reflected SHG efficiencies (η_{SHG}) at 800 nm and 1064 nm fundamental wavelengths, respectively, as functions of the incident angle (θ_{in}) for the 20 nm-thick gold layer. In both cases, a TM-polarized fundamental field was incident on the samples and a TM-polarized SH was selected. The agreement between predicted and measured values is good and occurs notwithstanding the fact that simulations are carried out using incident 100 fs pulses. This confirms that rapid convergence is achieved as a function of incident pulse duration for flat structures that display no geometrical spectral features. It is evident that experimental and theoretical results agree well in both cases, in shape, amplitude, and peak locations. Moreover, in the case of Fig. 5.1.3(a) the agreement also occurs in the ratio between transmitted and reflected curves, and the relative angular position of the maxima. As it can be seen in both figures, at longer wavelengths the main transmitted peak shifts to larger incident angles, field penetration depth decreases and surface charge discontinuities, exemplified by Coulomb

$\left(-\frac{e\lambda_0}{m^*_{0,f}c^2}(\nabla\cdot\mathbf{P}_f)\mathbf{E}\right)$ and convective $\left(-\frac{1}{n_{0,f}e\lambda_0}\left[(\nabla\cdot\dot{\mathbf{P}}_f)\dot{\mathbf{P}}_f+(\dot{\mathbf{P}}_f\cdot\nabla)\dot{\mathbf{P}}_f\right]\right)$ terms, increase and become the main source of SHG, although the magnetic contribution encompasses both nonlinear surface and volume currents.

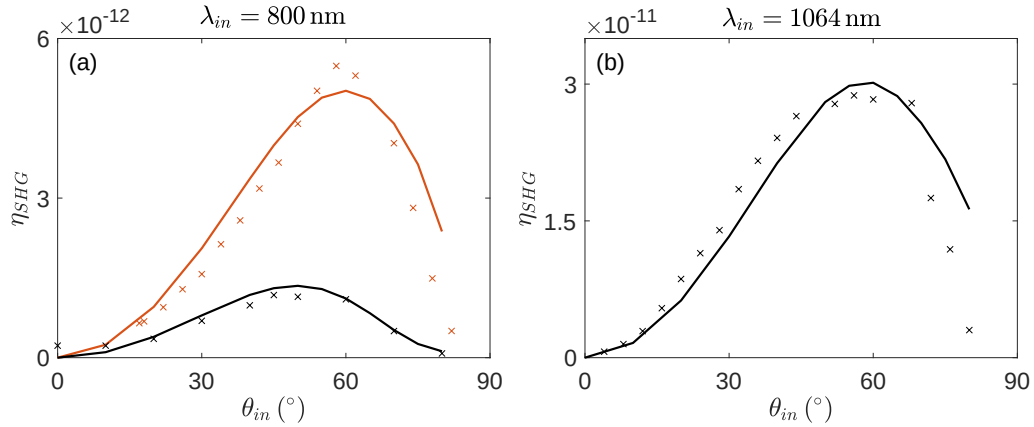

Figure 5.1.3: Transmitted (black) and reflected (red) SHG efficiencies as a function of incident angle for the 20 nm-thick gold nanolayer when the pump field is tuned at (a) 800 nm, and (b) 1064 nm. Measurements and predictions are depicted with cross markers and solid curves, respectively.

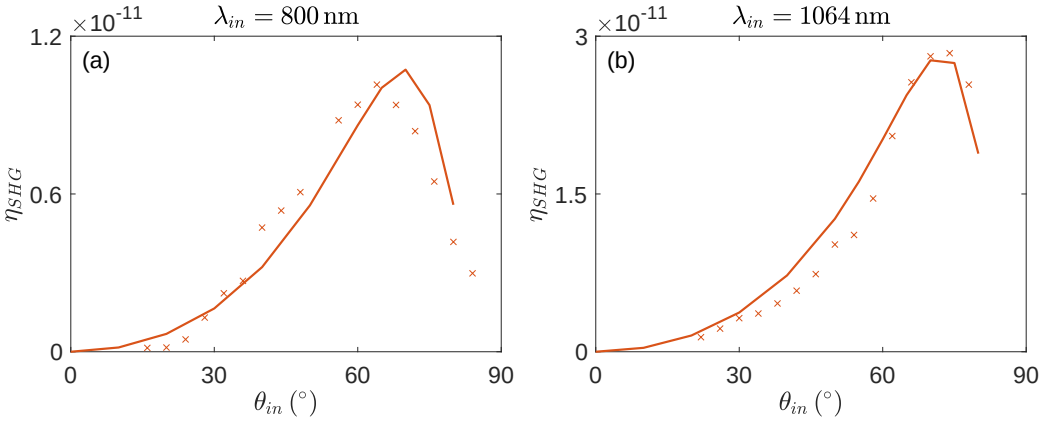

Figure 5.1.4: Measured (cross markers) and predicted (solid curves) reflected SHG efficiencies as a function of incident angle for the 70 nm-thick gold nanolayer when the incident field is tuned at (a) 800 nm, and (b) 1064 nm.

The reflected SHG conversion efficiencies as a function of incident angle for 800 nm and 1064 nm pulsed laser sources for the 70 nm-thick gold layer are plotted in Fig. 5.1.4. Transmis-

sion is negligible in both cases. Both incident and SH fields were selected to be TM-polarized. As it can be observed, once again experimental and theoretical results agree quite well qualitatively and quantitatively. Peak SHG performance shifts from $\sim 60^\circ$ at 800 nm, to $\sim 75^\circ$ at 1064 nm, reflecting changes in field penetration depth in the two different spectral ranges. The transparent, 20 nm-thick layer was used to monitor transmitted and reflected SH signals, as the fields carry information about combined surface and volume currents excited on and inside the sample. On the other hand, the opaque, 70 nm-thick gold layer supports mostly surface currents, with reflected conversion efficiencies that are largest at larger angles. By comparing experiments and simulations of SHG efficiencies we extracted effective masses of $m^*_{0,f} = m^*_{bj} = m_e$. The density of free electrons is similar to that of bound electrons as each atom yields one free electron, although lower d-shell electrons may also contribute at short enough wavelengths, so $n_{0,f} \sim 10^{22}\,\mathrm{cm}^{-3}$.

As has been already mentioned, a system described by combined Drude and Lorentz electrons illuminated by a pulsed pump laser source has at least two main THG sources: interband transitions (Lorentz resonances, with nonlinear interactions governed by the parameter $\tilde{b}$) and hot electrons, whose relative strength is determined by $\tilde{\Lambda}$. Experimental and predicted results of the transmitted THG efficiencies (η_{THG}) are shown in Fig. 5.1.5(a), where we have plotted the angular dependence of the signal generated by the 20 nm-thick gold layer when it is pumped at 1064 nm. A TM- and a TE-polarized TH was detected when the incident field was TM- or TE-polarized, respectively. The angular dependence of THG is different compared to SHG because the inherent nonlinearity in this case is triggered by the bulk, with conversion efficiencies of order 10^{-8}. By introducing a scaled coefficient $\tilde{b}$ of order 10^{-8} in the simulations, predicted efficiencies of order 10^{-11} were obtained, clearly inadequate to explain our observations. Instead, what was required to reproduce the conversion efficiencies that we observed is the introduction of the hot electron contribution. The simulated curves in Fig. 5.1.5(a) were obtained with $\tilde{b} \sim 10^{-8}$ and $\tilde{\Lambda} \sim \cdot 10^{-8}$.

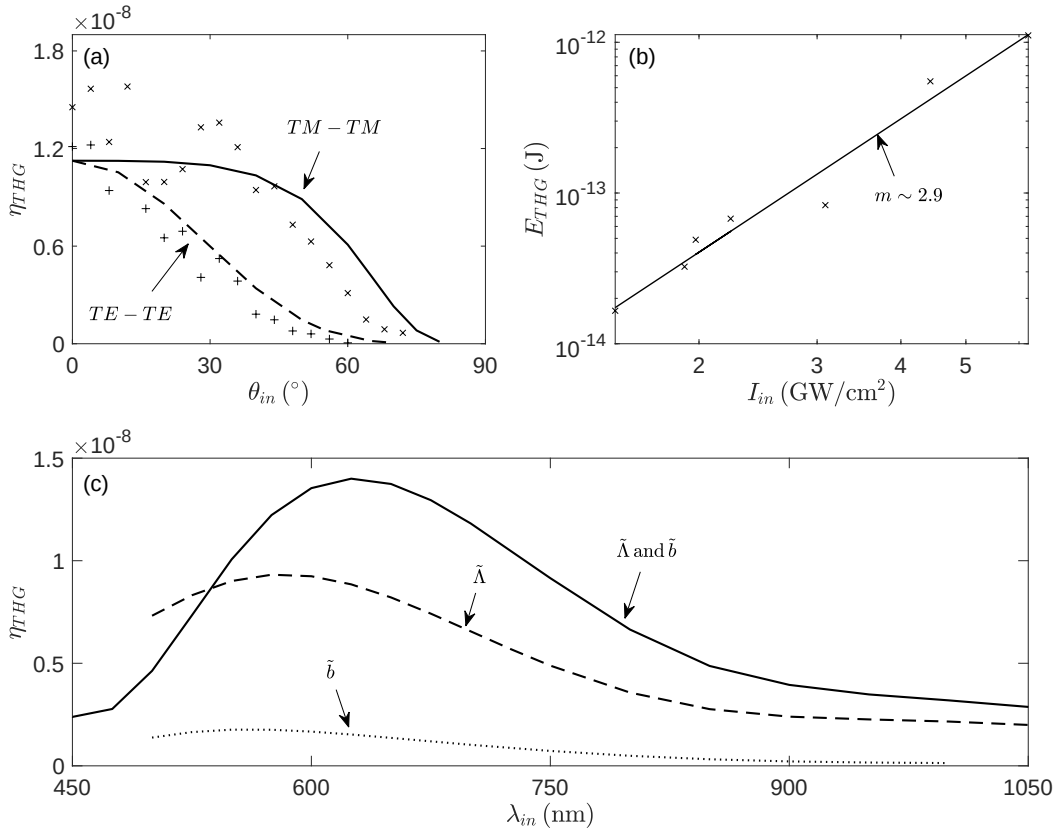

Figure 5.1.5: (a) Angular dependence of the transmitted THG efficiencies for the 20 nm-thick gold nanolayer. A TM-polarized TH was measured when the incident field was TM-polarized (cross markers), and a TE-polarized TH was detected when the fundamental field was TE-polarized (plus markers). Their corresponding predictions are depicted with a solid curve and a dashed curve, respectively. (b) Measured THG energy as a function of incident pulse peak intensity. (c) Predictions of the reflected THG efficiencies as a function of incident wavelength for the 20 nm-thick gold nanolayer obtained under three different scenarios: taking only into account either the bound electron or the hot electron contribution (pointed curve and dashed curve, respectively), and taking both terms into account (solid curve) in Eqs. 5.1.6 and 5.1.3.

The detected THG energy (E_{THG}) as a function of incident pulse peak intensity is shown in Fig. 5.1.5(b) in logarithmic scale. Measurements were performed at normal incidence with TM-polarized pulses tuned at 1064 nm. A slope of $m \sim 2.9$ is obtained, which is in agreement with THG.

In Fig. 5.1.5(c) we show the predicted, reflected THG spectral response for 100 fs pulses incident at 55° on a 20 nm-thick gold layer. The transmitted signal is predicted to display similar behavior. In this example the parameters are chosen arbitrarily so that each nonlinear

contribution yields similar THG conversion efficiency when the other is turned off. Then we combine them together to ascertain the interplay between these two different TH sources. The figure suggests that separately, each type of third order nonlinearity yields qualitatively and quantitatively a similar response, with a TH peak for pump wavelengths of $\sim 600\,\text{nm}$. However, their combined response redshifts the TH peak. This prediction runs counter intuition because an increased free electron density should blueshift the plasma frequency, with expected similar outcome for the TH peak. It is obvious that the two components interfere and conspire to instead redshift the peak, an effect that encapsulates a cautionary tale for any experimental result that may be extrapolated without the benefit of proper assumptions and theoretical support.

5.2 Gold nanograting

5.2.1 Experimental approach

The nonlinear response of the gold nanograting was analyzed with two different sets of experiments. First, the harmonic generated signals were studied pumping the gold nanograting with the Ti:Sapphire source. So pulses 140 fs in duration tuned at 800 nm were used, although the wavelength could be tuned in the $790\,\text{nm} - 810\,\text{nm}$ range. This source has been introduced in the first part of this chapter, as well as in Chapter 3.1.1. The second set of experiments was performed using the laser system described in Chapter 3.2.1, so tunable pulses 100 fs in duration were used in this case. In Table 5.2.1 we summarize some parameters of the femtosecond sources corresponding to the conditions under which experiments were taken:

	P_{FF}	f_{rep}	τ_{FWHM}	w_0	I_{FF}
Ti:Sapphire	1 W	76 MHz	140 fs	34 μm	3.5 GW/cm^2
OPA (Coherent, Opera Solo)	100 nJ	1 kHz	100 fs	175 μm	1.5 GW/cm^2

Table 5.2.1: Parameters of the femtosecond sources under experimental conditions.

The set-up used to perform the first set of measurements on the gold nanograting is a modification of that described in Chapter 2.1 and it is schematically shown in Fig. 5.2.1. Differently from the first version, this set-up does not include a dispersive prism. Instead, we only use

bandpass filters to eliminate the fundamental field radiation. In Chapter 3.2.1, we described an experimental set-up that did not include a dispersive prism either. In that case, the reason was that alignment with a multiwavelength system and pump-wavelength sweeps would be difficult with the prism configuration. Now, the prism is removed because we aim to detect harmonic light deep in the UV, at 266 nm. If only bandpass filters are used to remove fundamental radiation, the alignment of the set-up can be done at any wavelength, as they will not be dispersed differently. In contrast, using a dispersive prism requires generating light at the harmonic wavelength we want to detect in order to perform a proper alignment of the experimental set-up. As we did not possess a light source at 266 nm in our laboratory, we decided to change the prism configuration shown in Chapter 2.1 to another structure more similar to that shown in Chapter 3.2.1.

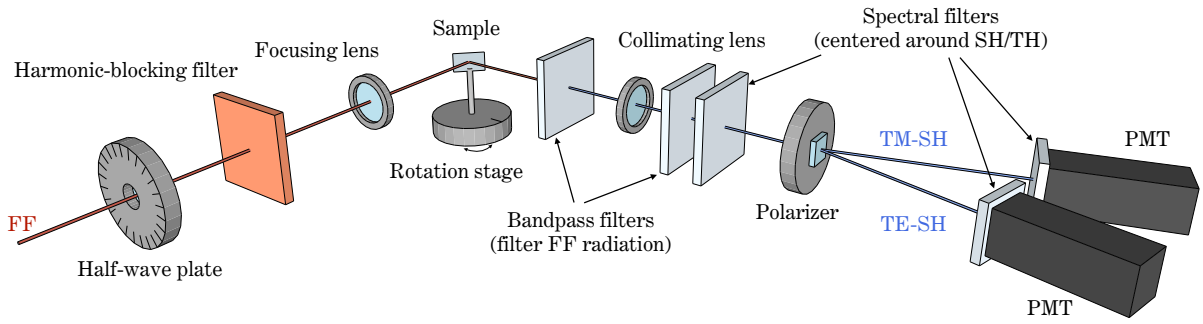

Figure 5.2.1: Schematic representation of the experimental set-up in its reflection configuration built to measure SH and TH signals arising from the gold nanograting.

We need to make sure that the total optical density added by the bandpass filters at the fundamental wavelength is greater than the harmonic generation efficiency in order to ensure there is no pump leakage to the filters. We also need to confirm that they are able to eliminate SH or TH radiation in case we want to detect TH or SH signals, respectively. Moreover, this set-up allows us to detect TM- and TE-polarized harmonic signals simultaneously. The first part of this set-up (the elements placed before the sample) is the same as the set-up shown in Fig. 2.1.1. A half-wave plate working at 800 nm allows us to select TM- or TE- polarized incident light, a longpass filter eliminates SH or TH radiation previous to the sample, and with a lens (Thorlabs,

LA1708-B) we focus the beam on the sample plane. In this case, the sample is mounted on top of a motorized rotation stage (OptoSigma, OSMS-40YAW), which is controlled with 1-axis stage controller (OptoSigma, GSC-01-P). The controller can be connected to a computer and, by means of a software provided also by OptoSigma, we are allowed to control the rotation angle. After the sample, we place two bandpass colored glass filters (Thorlabs, FGB37-A) when we want to detect SH signals. In between these two filters, a plano-convex lens (Thorlabs, LA4380-UV) with focal length f = 100 nm is used to collimate the beam. Then, we use another bandpass filter (Thorlabs, FBH400-40). In the case we want to detect TH radiation, we use just one filter which we place between the sample and the collimating lens (Chroma, ET262-20bp). To select the polarization of the harmonic field, in this set-up we use a polarizer (Thorlabs, WPA10) that is able to separate the harmonic radiation in its TM- and a TE-polarized components. Each component is collected by two different PMTs, in which another bandpass filter (Thorlabs, FBH400-40) is placed in each of them when SH radiation is wanted to be detected. In the case of TH signal detection, this bandpass filter is replaced by a UV bandpass filter (Eksma Optics, NSH filter). Both of the PMTs were provided by Hamamatsu (Hamamatsu, H10722-113 and H10722-04) and their performance is very similar. Their sensitivity peaks at 400 nm, however, the absolute value of the sensitivity of the second PMT (the one that is not used in the version of the set-up described in Chapter 2.1) is greater. One of the reasons of choosing this new PMT is the desire of measuring harmonic signals at 266 nm (TH of 800 nm). Usually, optics do not have a good performance at this wavelength range. An important percentage of the signal can be lost through the different optical elements, including the filters, which are able to eliminate the fundamental beam but usually only transmit the 50% or less of the field at 266 nm. So, we need the PMT to have the better possible response at this range of wavelengths in order to optimize the detection. Finally, the PMTs were connected to their power supplies and to an oscilloscope were the reading of the signal was taken.

Conversion efficiencies were estimated following the calibration procedure described in Chapter 2.1. However, the responsivity at 266 nm could not be measured as described due to the lack of

a light source at this wavelength. As a consequence, it is estimated relying on the responsivity curve provided by the PMT's datasheet and scaled with respect to the values obtained at the other wavelengths.

The second set of experiments was performed with the femtosecond source and the set-up described in Chapter 3.2.1. This allowed us to complete the study by analyzing the nonlinear response of the sample when pumped at different wavelengths.

5.2.2 Description of the sample

The grating consists of periodic parallel nanogrooves etched on the surface of a thick gold layer substrate of thickness $t = 200\,\text{nm}$, having a period $p = 610\,\text{nm}$, channel width $a = 385\,\text{nm}$, and depth $w = 50\,\text{nm}$. These parameters are displayed in Fig. 5.2.2(a), where we show an schematic representation of the sample.

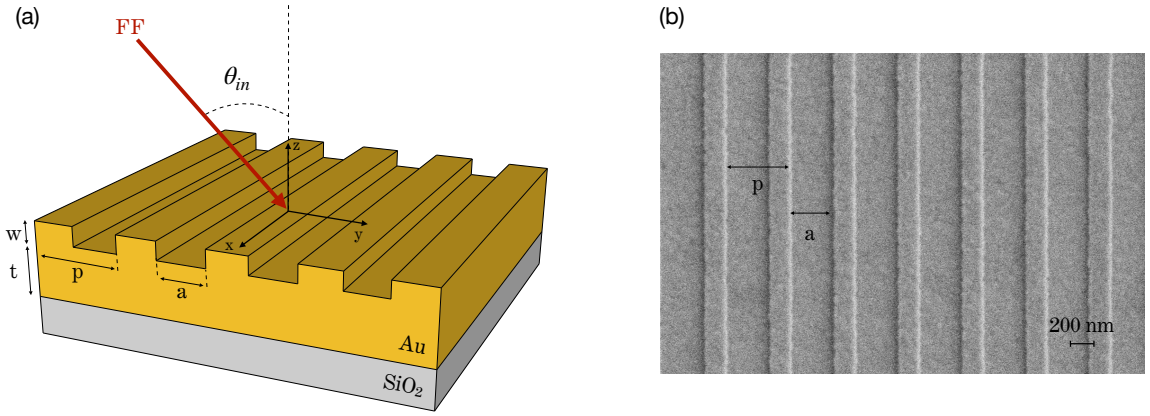

Figure 5.2.2: (a) Schematic representation of the gold nanograting and (b) SEM image of the fabricated nanograting.

Such a grating was fabricated by first depositing a 200 nm-thick gold layer on top of a SiO_2 substrate. Subsequently, we performed electron-beam lithography [31] on a PMMA (poly methyl methacrylate) resist and deposited an additional thickness of gold that would ultimately form the grooves. Finally, the resist was removed with acetone. In Fig. 5.2.2(b) we show a SEM (Scaning electron microscope) image of the fabricated nanograting.

5.2.3 Theoretical approach

The theoretical approach that was followed to perform numerical simulations of SHG and THG efficiencies generated by the gold nanograting departs from that developed for the gold nanolayers, described previously in this chapter, in Section 5.1.3. However, in order to represent the dielectric response more accurately in the $200\,\mathrm{nm} - 300\,\mathrm{nm}$ wavelength range, a third Lorentzian functions was added to the complex dielectric constant of the material:

$$\varepsilon(\tilde{\omega}) = 1 - \frac{\tilde{\omega}_{p,f}}{\tilde{\omega}^2 + i\tilde{\gamma}_f\tilde{\omega}} - \frac{\tilde{\omega}^2_{p,b1}}{\tilde{\omega}^2 - \tilde{\omega}^2_{01} + i\tilde{\gamma}_{b1}\tilde{\omega}} - \frac{\tilde{\omega}^2_{p,b2}}{\tilde{\omega}^2 - \tilde{\omega}^2_{02} + i\tilde{\gamma}_{b2}\tilde{\omega}} - \frac{\tilde{\omega}^2_{p,b3}}{\tilde{\omega}^2 - \tilde{\omega}^2_{03} + i\tilde{\gamma}_{b3}\tilde{\omega}} \qquad (5.2.1)$$

where $\tilde{\omega} = 1/\lambda$ and it has $\mu\mathrm{m}^{-1}$ units, and $(\tilde{\omega}_{p,b1}, \tilde{\omega}_{01}, \tilde{\gamma}_{b1}) = (3.4, 2.45, 1.25)$, $(\tilde{\omega}_{p,b2}, \tilde{\omega}_{02}, \tilde{\gamma}_{b2}) = (4.79, 3.45, 1.45)$ and $(\tilde{\omega}_{p,b3}, \tilde{\omega}_{03}, \tilde{\gamma}_{b3}) = (6.35, 4.75, 1.25)$ for bound electrons, and $(\tilde{\omega}_{p,f}, \tilde{\gamma}_f) = (7.1, 0.05)$ for free electrons. This means that now we are considering three different bound electron spices in Eq. 5.1.3 instead of two, so j=1,2,3.

Another difference between the theoretical approach used to simulate the nonlinear response of the gold nanograting and the gold nanolayers is found on the dynamic polarization equation of bound electrons. At resonance, the plasmonic grating confines the fields near the surface, producing an intense field close to the corners of the grating, as it can be seen in Fig. 5.2.3 where we show electric and magnetic field distributions in between two grooves of the nanograting. The presence of the intense field at the edges of the grating is responsible for pump absorption and the simultaneous enhancement of nonlinear interactions. So, we choose to expand the bound electron's bulk term up to seventh order, neglecting even order nonlinearities because the system is centrosymmetric:

$$\mathbf{P}^{\mathrm{NL}}_{bj} = -\tilde{b}_j(\mathbf{P}_{bj}\cdot\mathbf{P}_{bj})\mathbf{P}_{bj} + \tilde{\vartheta}_j(\mathbf{P}_{bj}\cdot\mathbf{P}_{bj})^2\mathbf{P}_{bj} - \tilde{\delta}_j(\mathbf{P}_{bj}\cdot\mathbf{P}_{bj})^3\mathbf{P}_{bj} \qquad (5.2.2)$$

where $\tilde{b}_j$ has already been defined and $\tilde{\vartheta}_j = \tilde{b}_j/(n^2_{0,bj}e^2L^2)$, $\tilde{\delta}_j = \tilde{b}_j/(n^4_{0,bj}e^4L^4)$. These parameters are real and depend on linear oscillator parameters like resonance frequency $\tilde{\omega}_{0j}$ and lattice constant L. The lattice constant is determined using average orbital diameters. For gold we can approximate $L \sim 1\,\text{Å}$. Since each gold atom contributes approximately one free electron to

the electron density, then it is reasonable to assume that the bound electron density may be approximated with the free electron density, which is $n_{0,f} \sim 5.8 \cdot 10^{22}\,\mathrm{cm}^{-3}$. This is then sufficient to determine $\tilde{b}_j$, $\tilde{\vartheta}_j$ and $\tilde{\delta}_j$, although their values can be readjusted according to experimental conversion efficiencies, as we do for the parameter $\tilde{b}$.

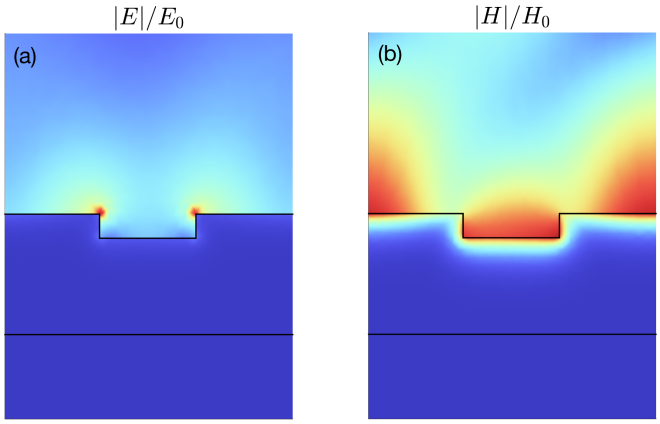

Figure 5.2.3: (a) Electric and (b) magnetic field distributions at 800 nm and 16° angle of incidence between two grooves normalized with respect incident electric and magnetic field amplitudes.

5.2.4 Results and discussion

A first set of nonlinear measurements was taken pumping the sample with femtosecond pulses tuned in the 790 nm − 800 nm wavelength range, with incident peak intensities of $\sim 3.5\,\mathrm{GW/cm^2}$. A second set of experiments was performed exciting the nanograting with femtosecond pulses tuned at 1000 nm and 1100 nm with peak intensities of $\sim 1.5\,\mathrm{GW/cm^2}$. SHG and THG signals were collected as a function of incident angle and wavelength. Simulations were performed with pulses being 200 fs in duration, with variable peak pump pulse power densities modulated between $1\,\mathrm{GW/cm^2}$ and $4\,\mathrm{GW/cm^2}$, which were incident to a nanograting having the following dimensions: $p = 605\,\mathrm{nm}$, $a = 385\,\mathrm{nm}$ and $w = 62\,\mathrm{nm}$.

In Fig. 5.2.4(a) we show the theoretical spectral response of the grating in reflection as a function of incident angle which is calculated by means of a rigorous coupled wave analysis (RCWA). The resonance is seen to shift from 700 nm up to 1100 nm when the angle of the

incident beam varies from 0° to 50°. The linear characterization of the grating was performed using a supercontinuum laser source (FYLA SCT 1000) by measuring the reflected spectrum as a function of incident angle with a high-resolution spectrometer (Andor, Kymera 328i). These measurements are plotted in Fig. 5.2.4(a) for TM-polarized incident light with black dots and are in excellent agreement with our simulations. As expected, no resonances appear when the sample is illuminated with TE-polarized light. In Fig. 5.2.4(b) we show an example of a resonance located near 800 nm, corresponding to the dashed line in Fig. 5.2.4(a). Measurements and simulations of the linear reflection are plotted with cross markers and a solid curve, respectively, and are normalized to the value obtained from the unpatterned gold layer.

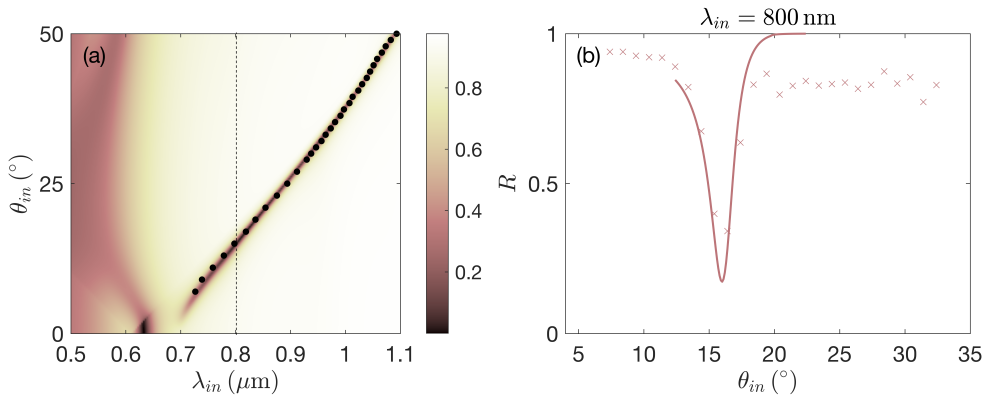

Figure 5.2.4: (a) Simulations of the gold grating linear reflection as a function of incident angle and wavelength. Experimental measurements of the central resonance wavelength as a function of incident angle are shown with black dots. (b) Experimental (cross markers) and simulated (solid curve) linear reflection of the gold grating as a function of incident angle for an incident wavelength of 800 nm, normalized to the value obtained from the unpatterned gold layer.

In Fig. 5.2.5 we show the spectral response of TM-polarized SH emission from the gold grating when the incident field was TM-polarized. Figure 5.2.5(a) shows measurements of the reflected SHG efficiency (η_{SHG}) when the incident wavelength is varied around 800 nm and the incident angle (θ_{in}) was fixed at 16°. SH efficiencies obtained from the gold grating are shown with cross markers and correspond to the left y-axis, while the right y-axis corresponds to the square markers curve which was obtained illuminating the unpatterned portion of the same

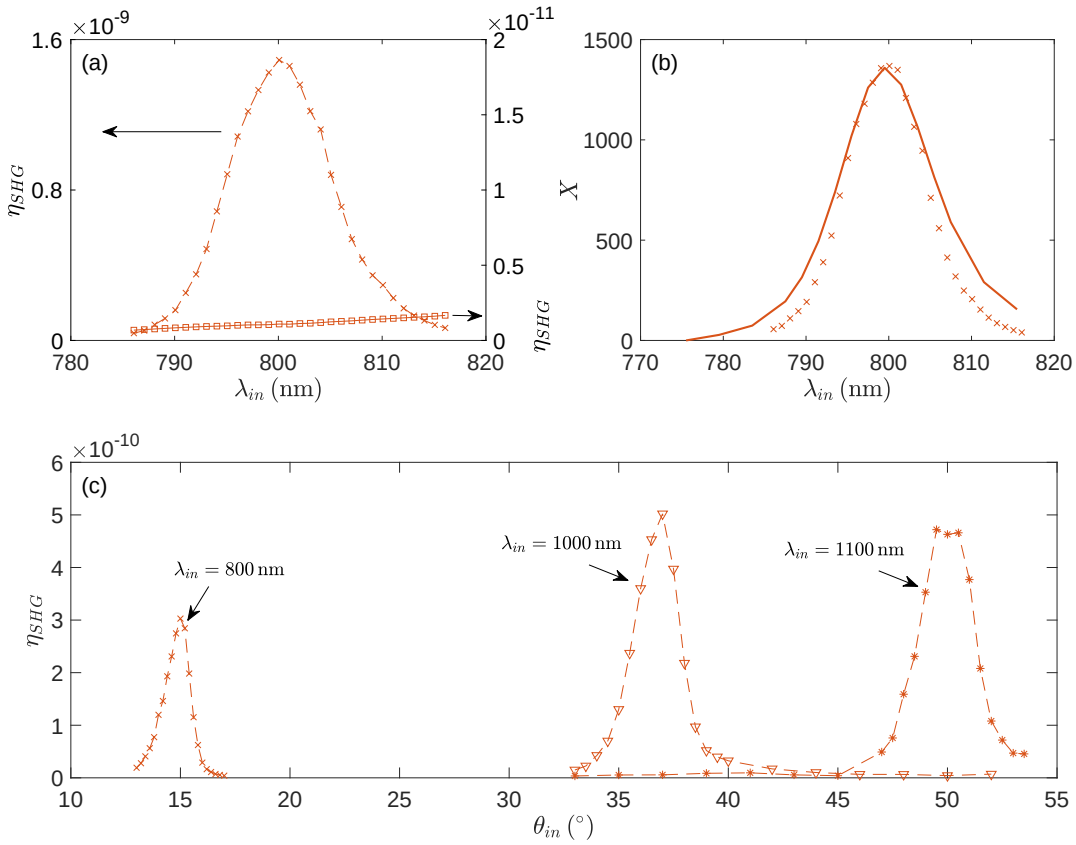

Figure 5.2.5: (a) Experimental results of the reflected SHG efficiency from the gold grating (cross markers, left y-axis) and the unpatterned gold layer (square markers, right y-axis) as a function of pump wavelength when the incident angle is fixed at 16°. (b) Experimental (cross markers) and predicted (solid curve) SHG enhancement factor in reflection for the gold grating as a function of pump wavelength when the incident angle is 16°. (c) Experimental results of the reflected SHG efficiency as a function of incident angle when the sample is pumped at three different wavelengths.

sample, which was used as a reference. In the case of the grating, a maximum SHG efficiency of $\sim 1.5 \cdot 10^{-9}$ was measured, while illuminating the unpatterned gold under the same experimental conditions yielded to a maximum efficiency of $\sim 1.2 \cdot 10^{-12}$. Cross markers in Fig. 5.2.5(b) show experimental results of the enhancement factor X of the SH signal, which is obtained scaling the SHG efficiency coming from the gold grating to the SHG efficiency originating from the unpatterned portion of the gold sample. We obtained a maximum enhancement factor of 1400. The simulated counterpart is depicted with a solid curve, which was obtained with $m^*_{0,f} = m^*_{bj} = m_e$. These results clearly show excellent agreement between theory and experimental

observations, with near-perfect resolution of shape, width, and maximum amplitude of the spectral response.

Since the resonance wavelength changes by varying the angle of incidence, similar enhancement is expected to occur at different wavelengths by merely tilting the sample. SHG efficiency was also measured at two alternative incident angles and wavelengths, again when TM-polarized incident and SH fields were selected. We measured the reflected SHG efficiency at 37° incident angle, where the laser carrier wavelength maps the resonance located around 1000 nm, and at 50° by tuning the fundamental wavelength around 1100 nm. The combined results of the three measured wavelengths are shown in Fig. 5.2.5(c). We note that the conversion efficiency in the case of an incident wavelength of 800 nm is smaller than that shown in Fig. 5.2.5(a). This is due to the fact that the SH (or TH) light emitted by the grating is diffracted. This is schematically shown in Fig. 5.2.6 for the case of (a) SH and (b) TH wavelengths, where m is the order of diffraction. As it can be seen, three orders of diffraction are expected in both cases. For instance, in the case of SHG, when we are incident at 16° and 800 nm, we expect a zeroth diffraction order emitting at an angle θ_{ref} of 16°, a first diffraction order at 63° and an additional order expected to emit at a negative angle of −24°. Experimentally, we were able to detect two of them, because

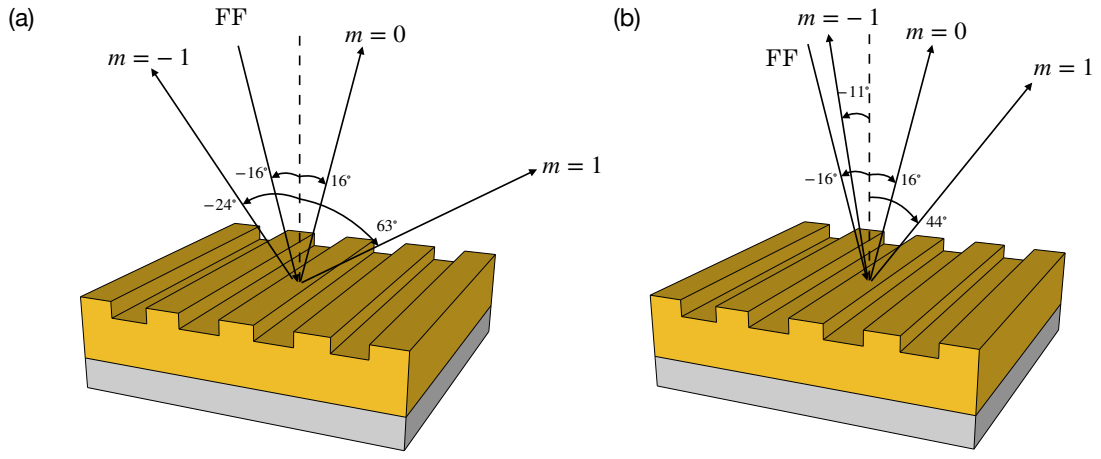

Figure 5.2.6: Schematic representation of the diffraction orders for (a) SH and (b) TH wavelengths.

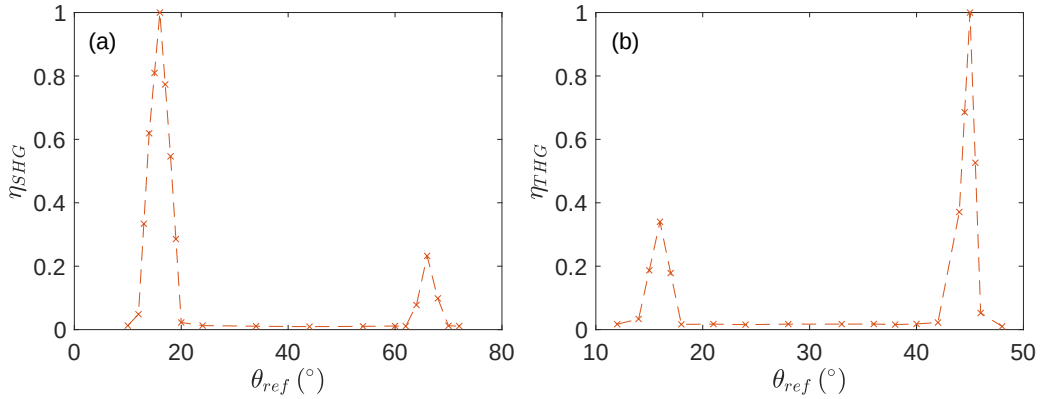

Figure 5.2.7: Measurement of (a) SHG and (b) THG normalized conversion efficiencies at the zeroth and first diffraction orders.

our set-up detects signals propagating away from the grating only on one side of the incident beam. This can also be seen in Fig. 5.2.7, where we show measurements of normalized (a) SHG and (b) THG conversion efficiencies at the zeroth and first diffraction orders. The relative intensity between the different orders of the SH emission is the same as the linear diffraction result obtained by illuminating the grating with radiation at 400 nm at 16°. In Figs. 5.2.5(a) and 5.2.5(b) we plot the total efficiency, calculated by adding up the signal detected from the two diffraction orders. On the contrary, in Fig. 5.2.5(c) we plot the efficiency obtained by detecting only the zeroth diffraction order.

Measurements of the spectral response of the reflected THG efficiency (η_{THG}) when the incident angle was fixed at 16° are shown in Fig. 5.2.8(a), where it has been plotted with cross markers and the efficiency values correspond to the left y-axis. Again, we measured the TH response under the same experimental conditions from the unpatterend gold layer, which is depicted with square markers and whose efficiencies are shown in the right y-axis. TM-polarized incident light was used, for which a TM-polarized TH signal was detected. As it can be seen, a resonance around 800 nm was measured in the case of the grating. In Fig. 5.2.8(b) we show the enhancement factor, obtained as in the case of SHG. Measurements are plotted with cross markers, while the solid curve correspond to the predicted result. As it was discussed in previous

chapters, THG has two different sources: hot electrons and bound electron contributions. Tuning the pump at 800 nm places it in a regime dominated by the third order nonlinearity of free electrons, i.e., the term $\tilde{\Lambda}(\mathbf{E}\cdot\mathbf{E})\mathbf{E}$. In contrast, the third harmonic signal at 266 nm is subject to the nonlinear dispersion of bound electrons and interband transitions, driven by the term $-\tilde{b}_j(\mathbf{P}_{bj}\cdot\mathbf{P}_{bj})\mathbf{P}_{bj}+\tilde{\vartheta}_j(\mathbf{P}_{bj}\cdot\mathbf{P}_{bj})^2\mathbf{P}_{bj}-\tilde{\delta}_j(\mathbf{P}_{bj}\cdot\mathbf{P}_{bj})^3\mathbf{P}_{bj}$. Once again, the comparison between experimental results and simulations is in excellent agreement in terms of shape, spectral width, and maximum amplitude, with an enhancement factor of nearly 4000.

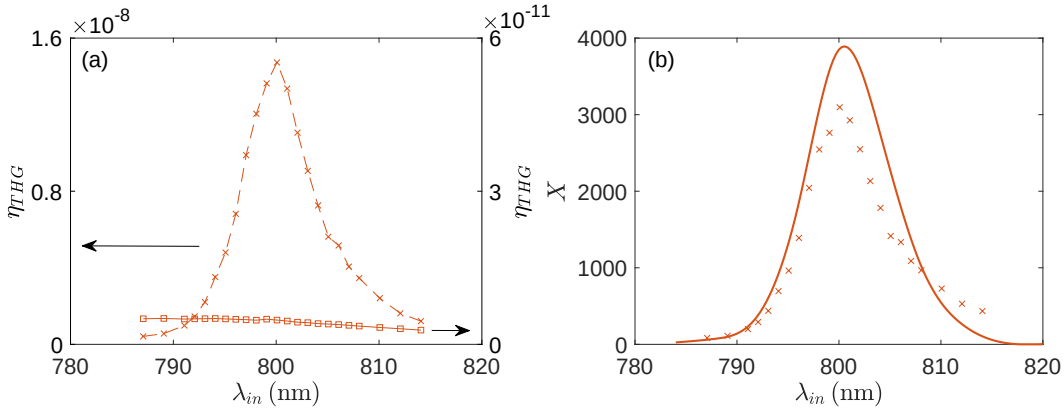

Figure 5.2.8: (a) Experimental results of the reflected THG efficiency from the gold grating (cross markers, left y-axis) and the unpatterned gold layer (square markers, right y-axis) as a function of pump wavelength when the incident angle is fixed at 16°. (b) Experimental (cross markers) and predicted (solid curve) THG enhancement factor in reflection for the gold grating as a function of pump wavelength when the incident angle is 16°.

Despite the reported enhanced performance of the nanograting with respect to the gold nanolayers, our predictions suggest that it may be possible to harness significantly larger THG enhancement factors with slight geometrical modifications. This situation is depicted in Fig. 5.2.9, where we plot the results of numerical simulations using 200 fs pulses incident on a grating having the same periodicity, and by gradually increasing the width of the channel. Aside from a sligh redshift of the resonance, Fig. 5.2.9(b) shows that the THG enhancement factor can easily be increased by nearly a factor of two without significant geometrical modifications. On the other hand, in Fig. 5.2.9(a) it can be seen that SHG efficiencies are not affected appreciа-

bly when the width of the channel is changed because they depend mostly on surface charge densities, currents, and spatial derivatives of the field rather than field localization.

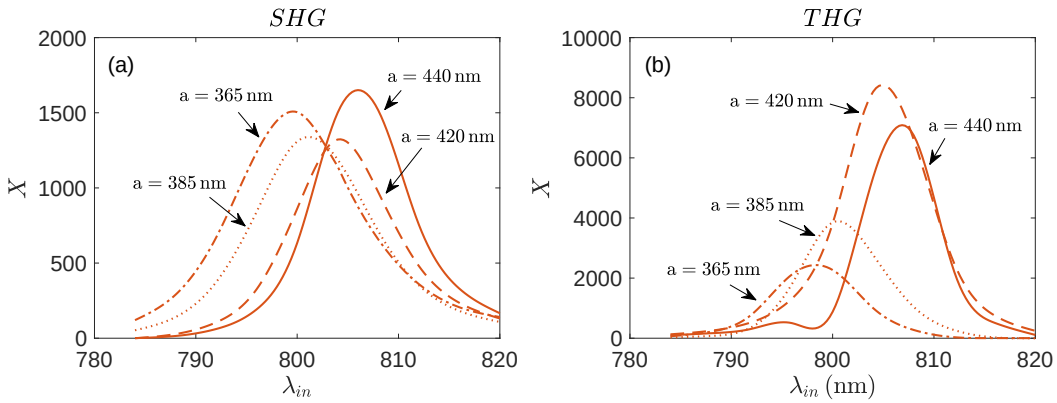

Figure 5.2.9: Predicted (a) SHG and (b) THG enhancement factors relative to a flat gold mirror as a function of incident wavelength for different channel widths.

5.3 Conclusions and summary

In summary, we have reported experimental observations of SHG and THG in transparent and opaque gold nanolayers. We have used our theoretical approach to model light-matter interactions, and make no assumptions about effective surface or volume nonlinearities. Instead, we have relied on temporal and spatial derivatives and mere knowledge of the effective electron mass to determine the relative magnitudes of surface and volume contributions. In doing so, we have found remarkable agreement with experimental observations. We also have reported observations of TM- and TE-polarized, transmitted THG efficiencies from the 20 nm-thick gold layer, and we have attributed the generated TH signal mostly to hot electron dynamics. This combined experimental-theoretical study has provided us with knowledge that we can use to predict harmonic generation in more complex structures. Thus, we have also reported SH and TH emissions from a gold nanograting at different wavelengths and have compared their efficiency to the efficiencies triggered by a flat gold mirror, and we have found unprecedented agreement between our simulations and experimental observations of both SHG and THG at visible and UV wavelengths. This comparison shows impressive enhancement in the SHG and THG conversion

efficiencies by more than three orders of magnitude. Moreover, we have also shown predictions that simple geometrical rearrangements can improve THG conversion efficiencies, leaving open the possibility that optimization can significantly increase TH emission in the UV range.

6
Experimental-numerical ellipsometry

In this chapter we present a practical, combined experimental and theoretical approach based on our hydrodynamic model that uses experimental results of harmonic generation conversion efficiencies to retrieve complex, linear and nonlinear dispersion curves. From our experimental results on harmonic generation efficiencies in silicon, ITO and gold, presented in Chapters 3, 4 and 5, respectively, we are able to extract bulk nonlinear dispersion from the equations of motion, like the third-order nonlinear susceptibilities. However, the method is not limited to third order processes and extraction of the bulk, second order response is straightforward and can be done in similar fashion. Based on our assessment of THG efficiencies in silicon, we predict $\chi^{(3)}_{\omega}$ and $\chi^{(3)}_{3\omega}$ of order $10^{-17}\,\mathrm{m}^2/\mathrm{V}^2$ in the visible and near-IR ranges, with respective peaks of $10^{-14}\,\mathrm{m}^2/\mathrm{V}^2$ and $10^{-16}\,\mathrm{m}^2/\mathrm{V}^2$ in the UV range. Similarly, gold's $\chi^{(3)}_{\omega}$ and $\chi^{(3)}_{3\omega}$ are of order 10^{-17}-$10^{-16}\,\mathrm{m}^2/\mathrm{V}^2$, and predict $\chi^{(3)}_{\omega} \sim 10^{-17}\,\mathrm{m}^2/\mathrm{V}^2$ and $\chi^{(3)}_{3\omega} \sim 10^{-18}\,\mathrm{m}^2/\mathrm{V}^2$ for ITO. These results clearly suggest that judicious exploitation of the nonlinear dispersion of ordinary semiconductors has the potential to transform devise physics in spectral regions that extend well into the UV range.

The structure of the chapter is as follows. In Section 6.1 we explain the theoretical method we use to retrieve the linear and nonlinear dispersion of the materials that have been studied in this thesis, which is based on the hydrodynamic model explained in detail in Chapter 1.5. Then,

in Section 6.2 we present the results that we have obtained from this study in silicon, gold and ITO. Finally, in Section 6.3 we finish the chapter with some conclusions.

6.1 Theoretical approach

When intense light interacts with a nonlinear material, its index of refraction can be modified, and under certain conditions it may be written in terms of the fundamental field intensity as: $n = n_0 + n_2 I$. This is a well known third order process known as the Kerr effect, which was introduced in Chapter 1.1.5. When nonlinear interactions occur in a bulk dielectric, for instance, the value of n_2 can be directly related to the third order susceptibility. The classical method to determine the value (magnitude and sign) of n_2 is the z-scan technique, developed by Sheik-Bahae *et al.* [113, 114]. By moving the sample and measuring transmittance along the longitudinal direction on the focal plane of a focused Gaussian beam, this technique allows one to infer the nonlinear coefficient both in amplitude and sign. Different z-scan theories have been proposed in the literature. However, they usually do not take into account the origin and nature of all relevant nonlinearities present in the problem, in order to extract accurate information from experimental measurements, and thus obtain the desired, accurate values of the nonlinear coefficient. As we have seen in this thesis, in metals, semiconductors and conductive oxides samples with nanoscale dimensions, new linear and nonlinear sources become relevant, such as nonlocal effects, magnetic dipole and electric quadrupole nonlinearities, convection, hot electrons, and phase-locking. Therefore, different terms introduced in the equations of motion contribute to the nonlinear susceptibility and add to beam dynamics. Our technique utilizes the constitutive relations to extract the complex nonlinear dispersion, to which we refer to as numerical ellipsometry. In a simplified terminology, the method to retrieve nonlinear dispersion consists of taking the following steps: first, we perform a calculation in the linear regime (low power densities) using a pulse only a few femtoseconds in duration, incident normal to the surface, and extract spatially averaged, complex polarizations and fields inside a 20 nm-thick layer of material when the peak of the pulse reaches the layer. With this, we estimate a spatially-

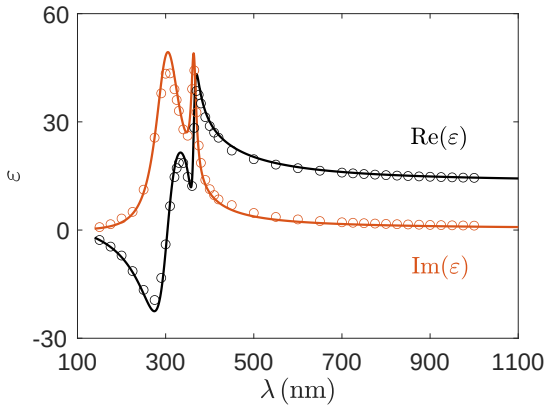

Figure 6.1.1: Real (black) and imaginary (red) parts of the complex dielectric constant of crystalline silicon. The solid curves correspond to the Lorentzian fits shown in Fig. 3.1.2. The markers correspond to the calculated results.

averaged complex dielectric constant at any given carrier wavelength. Then, we perform the same calculation in the nonlinear regime, to once again estimate spatially-averaged polarization and field inside the same layer of material. Finally, we calculate $\chi^{(3)}_{\omega}$ and $\chi^{(3)}_{3\omega}$ using the constitutive relations.

For a coordinate system invariant in the x-direction, the polarization of the system can be written as:

$$\begin{pmatrix} P^{\mathrm{L}}_y \\ P^{\mathrm{L}}_z \end{pmatrix} = \begin{pmatrix} \chi^{(1)}_{yy} & \chi^{(1)}_{yz} \\ \chi^{(1)}_{zy} & \chi^{(1)}_{zz} \end{pmatrix} \begin{pmatrix} E^{\mathrm{L}}_y \\ E^{\mathrm{L}}_z \end{pmatrix} \tag{6.1.1}$$

Neglecting the off-diagonal terms we estimate the spatially averaged, complex transverse ($\varepsilon^{\mathrm{L}}_{yy}$) and longitudinal ($\varepsilon^{\mathrm{L}}_{zz}$) dielectric constants at any given carrier wavelength:

$$\begin{aligned} \langle \varepsilon^{\mathrm{L}}_{yy} \rangle &= 1 + 4\pi \frac{\langle P^{\mathrm{L}}_y \rangle}{\langle E^{\mathrm{L}}_y \rangle} \\ \langle \varepsilon^{\mathrm{L}}_{zz} \rangle &= 1 + 4\pi \frac{\langle P^{\mathrm{L}}_z \rangle}{\langle E^{\mathrm{L}}_z \rangle} \end{aligned} \tag{6.1.2}$$

where $P^{\mathrm{L}}_{y,z}$ and $E^{\mathrm{L}}_{y,z}$ are complex polarization and field amplitudes, respectively, the super-index L stands for linear, and the brackets indicate spatial averages.

For planar structures and arbitrary angle of incidence, the fields are uniform along the transverse coordinate, and so it suffices to perform an average along the longitudinal coordinate: $\langle \varepsilon^{\mathrm{L}}_{yy,zz} \rangle = \frac{1}{d} \int_0^d \varepsilon^{\mathrm{L}}_{yy,zz} dz$, where d is layer thickness. This straightforward procedure allows us

to reconstruct, and verify, the linear material dispersion. In the absence of nonlocal effects, $\langle\varepsilon^{\mathrm{L}}_{yy}\rangle = \langle\varepsilon^{\mathrm{L}}_{zz}\rangle = \langle\varepsilon^{\mathrm{L}}\rangle$, as it was discussed in Chapter 4. The results of this calculation are reported in Fig. 6.1.1 in the case of silicon, for instance, with circle markers. As it can be seen, they agree quite well with the analytical Lorentzian functions, which correspond to Eq. 3.1.2 and which are depicted with solid curves.

The second important step consists of performing the same calculation in the nonlinear regime, to once again estimate spatially-averaged polarization and field inside the same layer of material, such that $\langle\varepsilon^{\mathrm{NL}}\rangle = 1 + 4\pi\frac{\langle P^{\mathrm{NL}}\rangle}{\langle E^{\mathrm{NL}}\rangle}$. Now, if we wish to retrieve $\chi^{(3)}_{\omega}$, in the undepleted pump approximation we may write:

$$\mathbf{P}^{\mathrm{NL}}_{\omega} = \chi^{(1)}_{\omega}\mathbf{E}^{\mathrm{NL}}_{\omega} + \chi^{(3)}_{\omega}|\mathbf{E}^{\mathrm{NL}}_{\omega}|^2\mathbf{E}^{\mathrm{NL}}_{\omega} \tag{6.1.3}$$

For simplicity, spatial averages are now implied and bracket symbols dropped. Additional considerations and terms are needed on the right hand side of Eq. 6.1.3 if either the pump is allowed to deplete, or if surface, magnetic, and/or higher order nonlinearities come into play. In Eq. 6.1.3 a linear calculation is required to obtain $\chi^{(1)}_{\omega} = \frac{\mathbf{P}^{\mathrm{L}}_{\omega}}{\mathbf{E}^{\mathrm{L}}_{\omega}}$, where $\mathbf{P}^{\mathrm{L}}_{\omega}$ and $\mathbf{E}^{\mathrm{L}}_{\omega}$ are the linear, spatially-averaged polarization and field at the fundamental frequency. Removing vector notation, we can write:

$$\chi^{(3)}_{\omega} = \frac{P^{\mathrm{NL}}_{\omega} - \frac{P^{\mathrm{L}}_{\omega}}{E^{\mathrm{L}}_{\omega}}E^{\mathrm{NL}}_{\omega}}{|E^{\mathrm{NL}}_{\omega}|^2 E^{\mathrm{NL}}_{\omega}} = \frac{\varepsilon^{\mathrm{NL}}_{\omega} - \varepsilon^{\mathrm{L}}_{\omega}}{4\pi|E^{\mathrm{NL}}_{\omega}|^2} \tag{6.1.4}$$

In order to extract $\chi^{(3)}_{3\omega}$, the procedure mirrors that used to recover $\chi^{(3)}_{\omega}$. We first write the expression for the third order polarization as:

$$\mathbf{P}^{\mathrm{NL}}_{3\omega} = \chi^{(1)}_{3\omega}\mathbf{E}^{\mathrm{NL}}_{3\omega} + \chi^{(3)}_{3\omega}(\mathbf{E}^{\mathrm{NL}}_{\omega}\cdot\mathbf{E}^{\mathrm{NL}}_{\omega})\mathbf{E}^{\mathrm{NL}}_{\omega} \tag{6.1.5}$$

Once again, the right hand side of Eq. 6.1.5 should be modified if additional nonlinearities become relevant, and a linear calculation is required to obtain $\chi^{(1)}_{3\omega} = \frac{\mathbf{P}^{\mathrm{L}}_{3\omega}}{\mathbf{E}^{\mathrm{L}}_{3\omega}}$, where $\mathbf{P}^{\mathrm{L}}_{3\omega}$ and $\mathbf{E}^{\mathrm{L}}_{3\omega}$ are the linear, spatially-averaged, complex polarization and field at the TH frequency, respectively. In contrast, $\mathbf{E}^{\mathrm{NL}}_{3\omega}$ is the field generated at the TH wavelength when pumping at the fundamental frequency, which is necessarily nonlinear, while $\mathbf{E}^{\mathrm{NL}}_{\omega}$ is now the nonlinear pump

field. So, again removing vector notation, Eq. 6.1.5 may be inverted to yield:

$$\chi^{(3)}_{3\omega} = \frac{P^{\mathrm{NL}}_{3\omega} - \frac{P^{\mathrm{L}}_{3\omega}}{E^{\mathrm{L}}_{3\omega}} E^{\mathrm{NL}}_{3\omega}}{(E^{\mathrm{NL}}_{\omega})^3} \tag{6.1.6}$$

In the case of silicon and other similarly undoped semiconductors it is possible to derive analytical expressions for $\chi^{(3)}_{\omega}$ and $\chi^{(3)}_{3\omega}$ using a similar approach as that outlined in Chapter 1.5. Provided the pump remains undepleted and no other nonlinearities or effects enter the picture, the scaled expressions for the third order nonlinear susceptibilities for a two-resonance system may be written as follows in Gaussian units:

$$\begin{aligned}\chi^{(3)}_{\omega} = &\frac{\frac{3\tilde{b}}{4\pi^2}\left(\frac{\tilde{\omega}^2_{p,b1}}{(4\pi)^2}\right)^3}{\left(\tilde{\omega}^2_{01} - \tilde{\omega}^2 + i\gamma_{b1}\tilde{\omega}\right)^3\left(\tilde{\omega}^2_{01} - \tilde{\omega}^2 - i\gamma_{b1}\tilde{\omega}\right)} \\ &+\frac{\frac{3\tilde{b}}{4\pi^2}\left(\frac{\tilde{\omega}^2_{p,b2}}{(4\pi)^2}\right)^3}{\left(\tilde{\omega}^2_{02} - \tilde{\omega}^2 + i\gamma_{b2}\tilde{\omega}\right)^3\left(\tilde{\omega}^2_{02} - \tilde{\omega}^2 - i\gamma_{b2}\tilde{\omega}\right)}\end{aligned} \tag{6.1.7}$$

$$\begin{aligned}\chi^{(3)}_{3\omega} = &\frac{\frac{3\tilde{b}}{4\pi^2}\left(\frac{\tilde{\omega}^2_{p,b1}}{(4\pi)^2}\right)^3}{\left(\tilde{\omega}^2_{01} - \tilde{\omega}^2 + i\gamma_{b1}\tilde{\omega}\right)^3\left(\tilde{\omega}^2_{01} - 9\tilde{\omega}^2 - i3\gamma_{b1}\tilde{\omega}\right)} \\ &+\frac{\frac{3\tilde{b}}{4\pi^2}\left(\frac{\tilde{\omega}^2_{p,b2}}{(4\pi)^2}\right)^3}{\left(\tilde{\omega}^2_{02} - \tilde{\omega}^2 + i\gamma_{b2}\tilde{\omega}\right)^3\left(\tilde{\omega}^2_{02} - 9\tilde{\omega}^2 - i3\gamma_{b2}\tilde{\omega}\right)}\end{aligned} \tag{6.1.8}$$

where $\tilde{\omega}$ is a scaled frequency and $\tilde{\omega}_{p,bj}$ is the scaled plasma frequency. In MKS system, $\chi^{(3)}_{\omega,3\omega,\mathrm{MKS}} = \frac{4\pi}{(3\cdot 10^4)^2}\chi^{(3)}_{\omega,3\omega}$. For damping coefficients and resonant and plasma frequencies, we use values extracted from the linear dielectric constant of the material, as indicated in Chapter 1.5.3, while the parameter $\tilde{b}$ is obtained from experimental results.

6.2 Results and discussion

In Fig. 6.2.1(a) we have plotted numerical results of the nonlinear dispersion of crystalline silicon $\chi^{(3)}_{\omega,\mathrm{MKS}}$ calculated using Eq. 6.1.4 through markers in the visible and near-IR ranges, which are compared with the analytical results obtained with Eq. 6.1.7, depicted with solid curves. Figure 6.2.1(b) shows contrast extended well into the IR range. Both figures show remarkably good agreement between analytical results derived using the nonlinear oscillator model, and

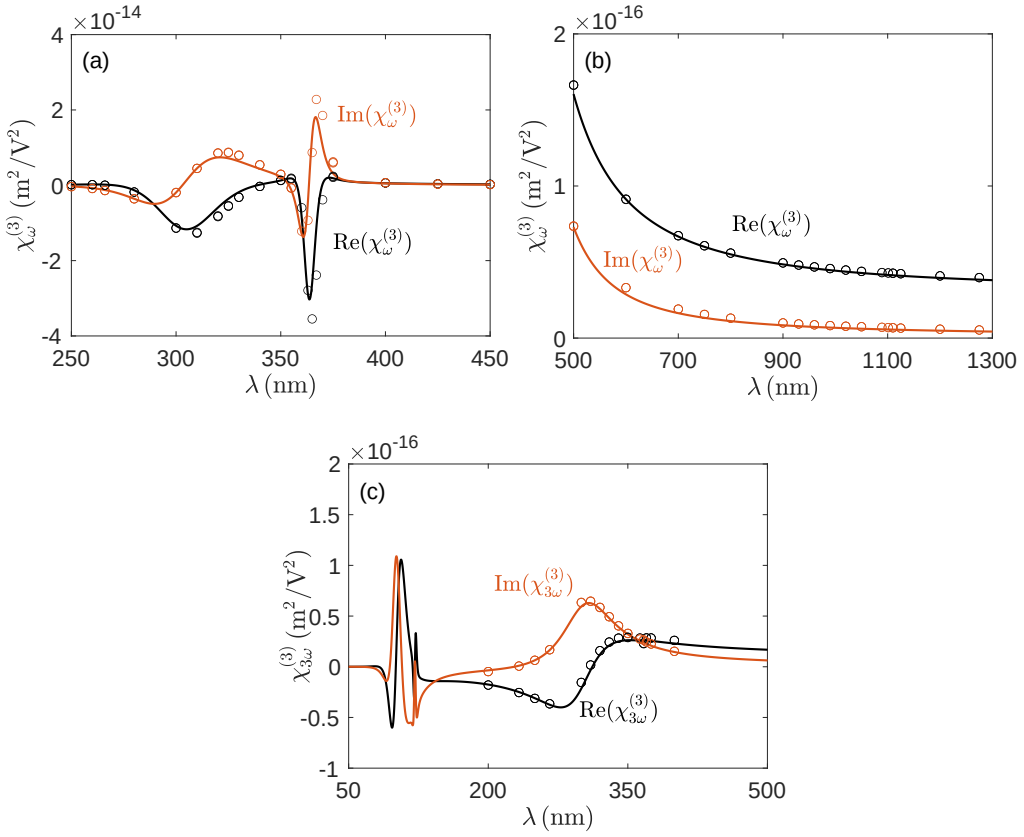

Figure 6.2.1: [(a)-(b)] Real (black) and imaginary (red) part of the complex $\chi^{(3)}_{\omega,\mathrm{MKS}}$ obtained analytically from Eq. 6.1.7 (solid curves) and calculated with Eq. 6.1.4 (markers), in different wavelength regions. (c) Real (black) and imaginary (red) parts of the complex $\chi^{(3)}_{3\omega,\mathrm{MKS}}$ calculated analytically from Eq. 6.1.8 (solid curves) and calculated with Eq. 6.1.6 (markers).

the simulations performed using ultrashort pulses. We note that while in the near-IR range the magnitude of $\chi^{(3)}_{\omega,\mathrm{MKS}}$ is of order $10^{-17}\,\mathrm{m}^2/\mathrm{V}^2$ and decreasing at longer wavelengths, its magnitude increases three orders of magnitude near resonance at UV. The comparison between Eqs. 6.1.6 and 6.1.8 for $\chi^{(3)}_{3\omega,\mathrm{MKS}}$ is shown in Fig. 6.2.1(c), with maximum values occurring near resonance. Again, the comparison between analytical and retrieved values is noteworthy. The nonlinear dispersion exhibited by silicon in Fig. 6.2.1 is consistent with the THG efficiencies reported in Chapter 3.1.4 (Fig. 3.1.8).

The third order nonlinear susceptibility of gold has also been extracted relying on experimental results of THG in gold nanolayers, reported in Chapter 5.1.4. In this case the situation is

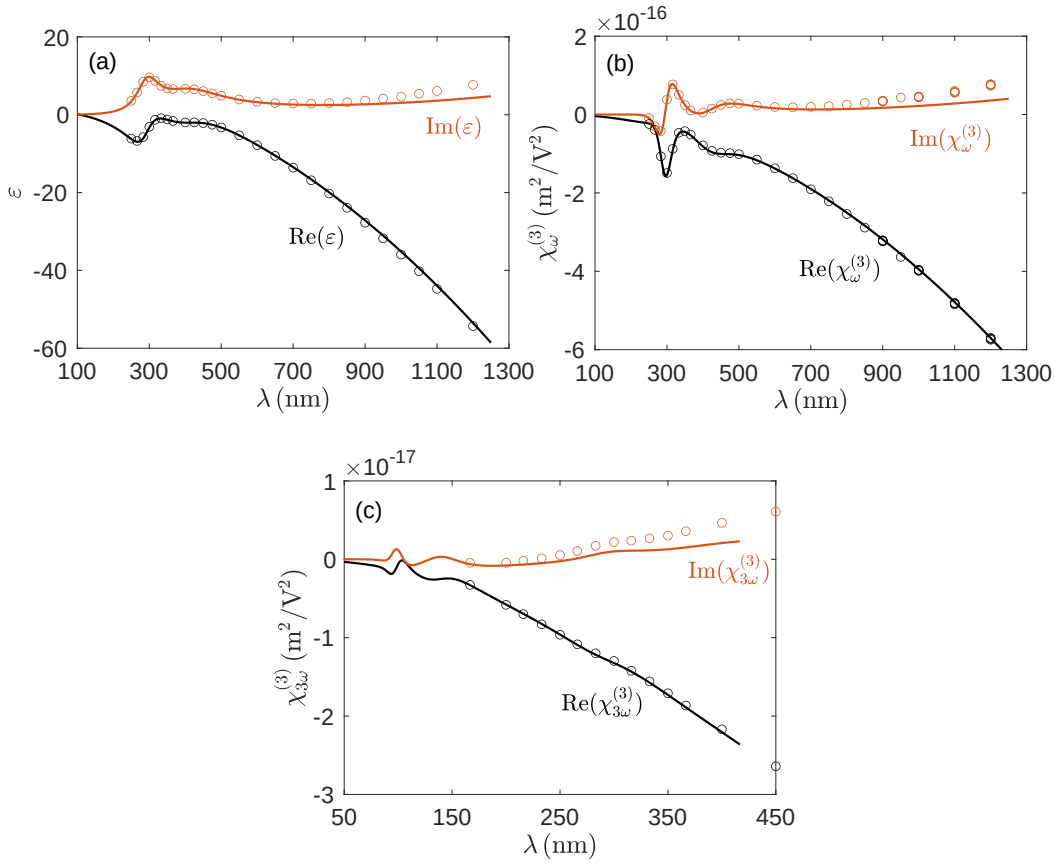

Figure 6.2.2: (a) Real (black) and imaginary (red) parts of the complex dielectric constant of gold. The solid curves correspond to the Drude-Lorentz fits shown in Fig. 5.1.2. Markers correspond to the calculated results. (b) Real (black) and imaginary (red) parts of the complex $\chi_{\omega}^{(3)}$ obtained analytically from Eq. 6.2.1 (solid curves) and calculated with Eq. 6.1.4 (markers). (c) Real (black) and imaginary (red) parts of the complex $\chi_{3\omega}^{(3)}$ obtained analytically (solid curves) and from our simulations (markers).

different because now, we have a third order contribution of hot electrons. Accordingly, Eq. 6.1.7 is modified as follows, with a similar alteration to Eq. 6.1.8:

$$\chi_{\omega}^{(3)} = \frac{3\tilde{\Lambda}}{-\tilde{\omega}^2 - i\tilde{\gamma}_f\tilde{\omega}} + \frac{\frac{3\tilde{b}}{4\pi^2}\left(\frac{\tilde{\omega}_{p,b1}^2}{(4\pi)^2}\right)^3}{\left(\tilde{\omega}_{01}^2 - \tilde{\omega}^2 + i\gamma_{b1}\tilde{\omega}\right)^3\left(\tilde{\omega}_{01}^2 - 9\tilde{\omega}^2 - i3\gamma_{b1}\tilde{\omega}\right)} + \frac{\frac{3\tilde{b}}{4\pi^2}\left(\frac{\tilde{\omega}_{p,b2}^2}{(4\pi)^2}\right)^3}{\left(\tilde{\omega}_{02}^2 - \tilde{\omega}^2 + i\gamma_{b2}\tilde{\omega}\right)^3\left(\tilde{\omega}_{02}^2 - 9\tilde{\omega}^2 - i3\gamma_{b2}\tilde{\omega}\right)} \tag{6.2.1}$$

In Fig. 6.2.2(a) we show with solid curves gold's linear dielectric constant data found in [107], fitted using one Drude and two Lorentzian functions, along with the data retrieved using

our model, which is represented with markers. As it can be seen, the agreement between the simulations and the analytical results is notable. In Figs. 6.2.2(b) and 6.2.2(c) we show the real and imaginary parts of the third order nonlinear susceptibility $\chi^{(3)}_{\omega,\mathrm{MKS}}$ and $\chi^{(3)}_{3\omega,\mathrm{MKS}}$, respectively. Analytical results are plotted with solid curves, while the retrieved values from our simulations are depicted with markers. The overall agreement between analytical and numerical results is once again quite remarkable, despite of some disagreement in the imaginary part for wavelengths longer than $1\,\mu$m.

Finally, we have also been able to retrieve the nonlinear dispersion in ITO. In this case, nonlocal effects become relevant and $\langle\varepsilon_{yy}\rangle \neq \langle\varepsilon_{zz}\rangle$, as already discussed in Chapter 4. In Fig. 6.2.3(a) and 6.2.3(b) we have plotted the retrieved transverse and longitudinal dielectric constants, respectively, using our approach, for an incident angle of 65°. The solid curves correspond to the real and imaginary parts of the measured local dielectric constant, coinciding to that displayed in Fig. 4.3.1. As it can be seen, additional absorption resonances appear due to nonlocal effects, also discussed previously in Chapter 4.

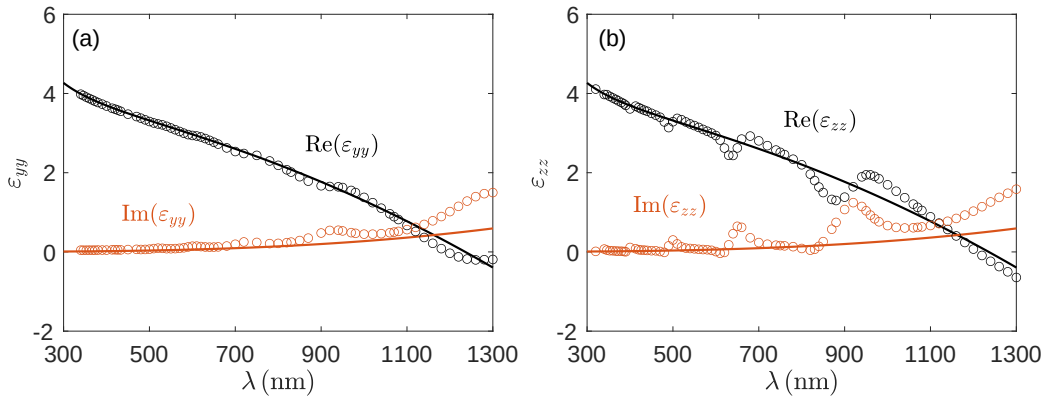

Figure 6.2.3: Real (black) and imaginary (red) parts of the complex (a) transverse (ε_{yy}) and (b) longitudinal (ε_{zz}) dielectric constant obtained from the calculations (markers). The solid curves correspond to the Drude-Lorentz fits shown in Fig. 4.3.1.

No analytical solutions equivalent to Eq. 6.2.1 are known in the presence of nonlocal effects. At oblique incidence, an expansion of the term $-\tilde{b}(\mathbf{P}_{bj}\cdot\mathbf{P}_{bj})\mathbf{P}_{bj}$ must be carried out into its vector and frequency components. Assuming the simultaneous presence of the fundamental and

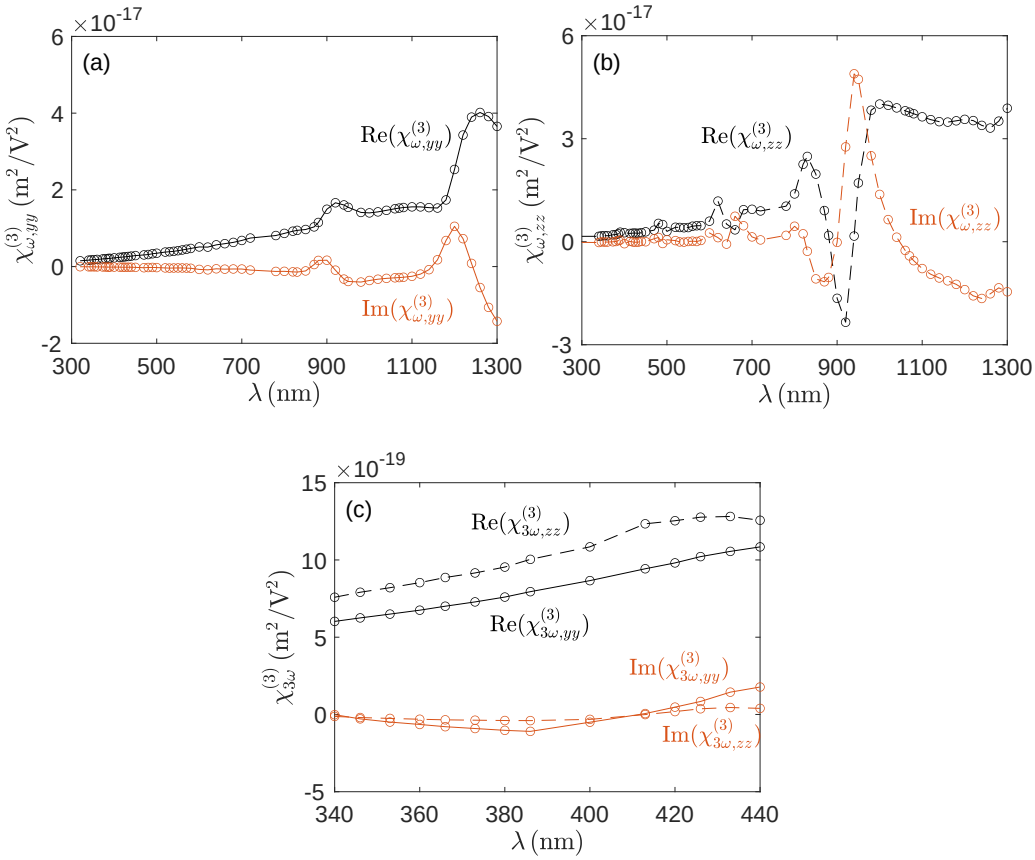

Figure 6.2.4: Real (black) and imaginary (red) parts of the complex (a) transverse $\chi^{(3)}_{\omega,yy}$ and (b) longitudinal $\chi^{(3)}_{\omega,zz}$ obtained from our calculations. (c) Real (black) and imaginary (red) parts of the complex transverse $\chi^{(3)}_{3\omega,yy}$ (solid curves with markers) and longitudinal $\chi^{(3)}_{3\omega,zz}$ (dashed curves with markers).

its generated harmonics, the total polarization can be written as:

$$\begin{aligned}\mathbf{P}_{bj} = \mathbf{j}\left(P_{\omega,y}e^{-i\omega t} + (P_{\omega,y})^* e^{i\omega t} + P_{2\omega,y}e^{-2i\omega t} + (P_{2\omega,y})^* e^{2i\omega t} + P_{3\omega,y}e^{-3i\omega t} + (P_{3\omega,y})^* e^{3i\omega t}\right) \\ +\mathbf{k}\left(P_{\omega,z}e^{-i\omega t} + (P_{\omega,z})^* e^{i\omega t} + P_{2\omega,z}e^{-2i\omega t} + (P_{2\omega,z})^* e^{2i\omega t} + P_{3\omega,z}e^{-3i\omega t} + (P_{3\omega,z})^* e^{3i\omega t}\right)\end{aligned} \tag{6.2.2}$$

for a coordinate system invariant in the x-direction. With this, Eqs. 6.1.4 and 6.1.6 take the following form:

$$\begin{aligned}\chi^{(3)}_{\omega,yy} &= \frac{P^{NL}_{\omega,y} - \chi^{(1)}_{\omega} E^{NL}_{\omega,y}}{|E^{NL}_{\omega,y}|^2 E^{NL}_{\omega,y} + \frac{1}{3}|E^{NL}_{\omega,z}|(E^{NL}_{\omega,y})^* + \frac{2}{3}|E^{NL}_{\omega,z}|^2 E_{\omega,y}} \\ \chi^{(3)}_{\omega,zz} &= \frac{P^{NL}_{\omega,z} - \chi^{(1)}_{\omega} E^{NL}_{\omega,z}}{|E^{NL}_{\omega,z}|^2 E^{NL}_{\omega,z} + \frac{1}{3}|E^{NL}_{\omega,y}|(E^{NL}_{\omega,z})^* + \frac{2}{3}|E^{NL}_{\omega,y}|^2 E_{\omega,z}}\end{aligned} \tag{6.2.3}$$

and

$$\chi^{(3)}_{3\omega,yy} = \frac{P^{NL}_{3\omega,y} - \chi^{(1)}_{3\omega} E^{NL}_{3\omega,y}}{(E^{NL}_{\omega,y})^3 + (E^{NL}_{\omega,z})^2 E^{NL}_{\omega,y}}$$
$$\chi^{(3)}_{3\omega,zz} = \frac{P^{NL}_{3\omega,z} - \chi^{(1)}_{3\omega} E^{NL}_{3\omega,z}}{(E^{NL}_{\omega,z})^3 + (E^{NL}_{\omega,y})^2 E^{NL}_{\omega,z}} \tag{6.2.4}$$

At normal incidence, Eqs. 6.2.3 and 6.2.4 yield Eqs. 6.1.4 and 6.1.6, respectively, as the longitudinal component of the electric field vanishes. The curves that correspond to Eq. 6.2.3 are plotted in Figs. 6.2.4(a) and 6.2.4(b), while Eqs. 6.2.4 are displayed in Fig. 6.2.4(c). The strong oscillatory behavior that characterizes especially the longitudinal nonlinear response in Fig. 6.2.4(b) is triggered by the nonlocal resonances seen in the linear response of Fig. 6.2.3(b). The THG data used to retrieve the nonlinear dispersion in Fig. 6.2.4 is that shown in Fig. 4.4.5, in Chapter 4.4.

6.3 Conclusions and summary

In summary, we have presented a combined experimental and numerical method that can be used to predict complex nonlinear dispersion curves in almost any material, based exclusively on the experimental determination of harmonic generation conversion efficiencies. Our hydrodynamic approach faithfully duplicates linear dispersion, and predicts the wavelength dependence nonlinear response. The method is particularly useful when the analytical solutions are not available, as is the case for conductive oxides like ITO, which displays nonlocal effects that trigger an effective anisotropy, and it is extendable to second order bulk nonlinearities.

7
Conclusions

In this thesis we have developed an extensive experimental-theoretical study of nonlinear frequency conversion of light in different materials and structures with nanoscale dimensions. The experimental study has focused most of the effort and has been performed thanks to the developement of optical set-ups capable of measuring SHG and THG conversion efficiencies arising from different samples made of semicondutors (GaAs wafers, amorphous silicon nanolayers, crystalline silicon wafers, and silicon membranes), conductive oxides (ITO nanolayers), and metals (gold nanolayers and nanograting). We have performed different kind of experiments analysing the angular, spectral and polarization dependence of the harmonic generated signals, measuring absolute values of very low harmonic generation conversion efficiencies (down to 10^{-13}). The experimental results have been compared with numerical simulations based on the hydrodynamic-Maxwell model explained in Chapter 1.5, which was developed by Dr. Michael Scalora, USA, and has been adapted in this thesis for each particular case. This way we have been able to understand linear and nonlinear optical properties of metals and semiconductors, and obtain quantitative comparisons between measurements and simulations providing valuable information of the material parameters. The model accounts for competing surface, magnetic, and bulk nonlinearities arising from both free and bound electrons, and it also preserves linear and nonlinear material dispersion, nonlocal effects due to pressure and viscosity, and the influence of hot

electrons: variations in the conduction electron's effective mass or density. This approach does not make assumptions about effective surface and volume nonlinearities to determine harmonic generation conversion efficiencies. Instead, we rely on temporal and spatial derivatives and mere knowledge of the effective mass of electrons to determine the relative amplitudes of surface and volume contributions to SHG, and on oscillator parameters to estimate THG efficiencies.

In Chapter 2 we have presented results of phase-locked SHG and THG in the opaque region of a 500 μm-thick GaAs wafer. This component corresponds to the particular solution of the inhomogeneous equation driven by the nonlinear polarization term. Differently from the homogeneous solution, the phase-locked component is captured by the pump and experiences its same effective dispersion. Under pulse illumination and under phase-mismatched conditions, the two components walk off. The wafer was illuminated at 1064 nm, so that both SH and TH generated fields fell in the absorption region of the semiconductor. As a consequence, the inhomogeneous component was the only able to propagate through the 500 μm of semiconductor. By performing experiments of harmonic generation conversion efficiencies as a function of incident angle and polarization we have analyzed in detail surface and bulk nonlinear sources. We have concluded that a TM-polarized incident pulse generates a TM-polarized SH field due to the surface contribution. A bulk-generated TE-polarized SH signal is triggered by a TM-polarized incident field, and TE-polarized incident pulse generates a TM-polarized SH field due to the magnetic Lorentz nonlinearity.

In Chapter 3 we have reported our results on nonlinear frequency conversion from different silicon samples: a 25 nm-thick amorphous silicon nanolayer, a 500 μm-thick crystalline silicon wafer and a 1340 nm- and a 200 nm-thick crystalline silicon membranes. The study has been performed in the visible and UV ranges, in regimes where this material tends to be opaque, and where nonlinear dispersion and phase-locking dominate the dynamics. By comparing experimental and numerical results we have been able to extract basic physical properties of the material, which we have used to predict nonlinear conversion efficiencies generated by a more complex structure which we have chosen to be crystalline silicon nanowires. Our predictions show that conversion

efficiencies can he enhanced in this type of nanostructure. However, experimental results are needed in order to be able to complete this study. A sample of this characteristics is under preparation, and its nonlinear frequency conversion response will be studied experimentally in the near future.

In our experiments we have been able to measure transmission efficiencies of order 10^{-7}-10^{-10} for the SH signal, and 10^{-10} for the TH for the case of GaAs, and of order of $10^{-12} - 10^{-13}$ for the SH signal, and $10^{-9} - 10^{-7}$ for the TH signal for the case of silicon. The fact is that propagation phenomena and nonlinear frequency conversion studies below the absorption edge of semiconductors are still lacking, primarily because these processes are thought to be uninteresting and inefficient due to absorption and to the naturally high degree of phase-mismatch. However, as our numerical predictions on silicon nanowires suggest, harmonic generation conversion efficiencies in absorbing materials at visible and UV wavelengths can be remarkably and surprisingly high, and thus can be useful for realizing coherent sources and for the many other potential applications that semiconductors find in optical technology.

In Chapter 4 we have studied the angular and wavelength dependence of SHG and THG conversion efficiencies arising from a 20 nm-thick ITO nanolayer near its ENZ condition which falls in the IR regime. The excitation of the ENZ mode requires TM-polarized light at oblique incidence causing an enhancement of the electric field component inside the film and a formation of an absorption peak in the spectrum. As a consequence, a peak is also expected in the SH response, which is demonstrated in our experimental and theoretical results. In our numerical predictions we take into account the fact that in conductive oxides, the effective mass of conduction electrons can be a function of temperature, giving birth to what we call the hot electron contribution. Our experimental and theoretical results show that both nonlocal effects and hot electrons can alter the SH response by blue-shifting or red-shifting the absorption peak. Not only this, but our simulations also suggest that the presence of nonlocal effects in a nanolayer of ITO can induce additional absorption resonances and an anisotropic dielectric response. We

expect our theoretical model to be applicable to other nonlinear interactions in ENZ materials and provide deeper understanding of the phenomenon.

In Chapter 5 we have analyzed harmonic generation in samples of gold having a different configuration. First, we have studied both experimentally and theoretically harmonic generation conversion efficiencies from a transparent and an opaque gold nanolayers. The transparent, 20 nm-thick layer is used to monitor transmitted and reflected SH signals, as the fields carry information about combined surface and volume currents excited on and inside the sample. On the other hand, the opaque, 70 nm-thick gold layer supports mostly surface currents. We also use the transparent nanolayer to measure transmitted THG efficiencies. The hydrodynamic model described in Chapter 1.5 is adapted to describe the nonlinear response in metals by taking into account the variation of the free electron's density due to interband transitions, to which we refer as the hot electron contribution. Our results on THG suggest that this contribution is essential in order to explain the observed conversion efficiencies, while leaving the SH response almost unchanged. By matching experimental and simulated conversion efficiencies, we are able to extract the effective mass of electrons and oscillator parameters to predict the SH and TH response in a gold nanograting. These predictions report a three orders of magnitude enhancement on SHG and THG in both visible and UV ranges, which is corroborated by our experimental observations. Moreover, our predicted results show that simple geometrical rearrangements can improve THG conversion efficiencies, leaving open the possibility that optimization can significantly increase TH emission in the UV range.

In Chapter 6 we have reported a theoretical method based on experimental conversion efficiencies and our hydrodynamic approach that allows us to extract nonlinear dispersion curves. We have seen that the method can be particularly useful when the analytical solutions are not available, as in the case of ITO. We have reported results on third order nonlinear susceptibilities, although the approach is extendable to second order bulk nonlinearities. Our experimental results for THG in silicon suggest that it is possible to exploit large nonlinear response in the visible and UV ranges, thus opening up new prospects for silicon photonics.

Future work

With all these studies we have been able to understand nonlinear frequency conversion at the nanoscale in simple geometrical arrangements, like nanolayers and wafers, made of materials which are in the forefront of nowadays technology. This understanding involves the distinction of the different nonlinear processes that trigger harmonic generation conversion efficiencies, as well as basic physical parameters of the materials. In the near future our group will do a step forward and will apply the experimental-theoretical approach developed in this thesis to study more complex geometries, were strong field confinement by plasmonic resonances in metallic nanostructures or in metamaterials, as well as Mie resonances in semiconductors can boost harmonic generation conversion efficiencies. The group will also try to apply topological photonics to nonlinear materials with the purpose of enhancing nonlinear effects. As it was stated at the very beginning of this thesis, the capability to efficiently generate harmonics at the nanoscale will have an enormous impact in the fields of nanomedicine and nanotechnology, since it would allow one to realize much more compact devices and to interrogate matter in extremely confined volumes.

These kind of studies have already started with this thesis, mostly in the case of the gold nanograting presented in Chapter 5.2. Our numerical results suggested that simple geometrical rearrangements can improve THG conversion efficiencies, leaving open the possibility that optimizations can significantly increase TH emission in the UV range. However, the same geometrical changes that appear to improve THG did not seem to affect the 1400-fold increase in SHG efficiencies. The usual emission from the bare metal layer shows a characteristic angular dependence that favors maximum SH emission at large angles and maximum THG at normal incidence. However, photonic devices often require small angle applications. By using a suitable grating with the appropriate periodicity, one may thus achieve SH and TH emissions from the metal grating at almost any desired angle, with enhancement factors that are larger than three orders of magnitude with respect to the emission from the bare surface. With this study we

concluded that metals should not be discounted as suitable frequency converters, while more optimized, complex topologies may catalyze further improvements in conversion efficiencies.

Bibliography

[1]T. H. Maiman, "Stimulated optical radiation in ruby", Nature **187**, 493–494 (1960).

[2]P. A. Franken, A. E. Hill, C. W. Peters, and G. Weinreich, "Generation of optical harmonics", Phys. Rev. Lett. **7**, 118 (1961).

[3]J. A. Armstrong, N. Bloembergen, J. Ducuing, and P. S. Pershan, "Interactions between light waves in a nonlinear dielectric", Phys. Rev. **127**, 1918 (1962).

[4]N. Bloembergen and P. S. Pershan, "Light waves at the boundary of nonlinear media", Phys. Rev. **128**, 606 (1962).

[5]J. A. Armstrong, "Measurement of picosecond laser pulse width", Appl. Phys. Lett. **10**, 16 (1967).

[6]I. Freund and M. Deutsch, "Second-harmonic microscopy of biological tissue", Optics Letters **11**, 94–96 (1986).

[7]J. A. Squier, M. Müller, G. J. Brakenhoff, and K. R. Wilson, "Third harmonic generation microscopy", Optics Express **3**, 315–324 (1998).

[8]R. W. Boyd, *Nonlinear optics* (Academic Press, 2003).

[9]J. A. Giordmaine, "Mixing of light beams in crystals", Phys. Rev. Lett. **8**, 19 (1962).

[10]Y. J. Ding and J. B. Khurgin, "Second-harmonic generation based on quasi-phase matching: a novel configuration", Optics Letters **21**, 1445–1447 (1996).

[11]D. T. Reid, "Engineered quasi-phase-matching for second-harmonic generation", J. Opt. A, Pure Appl. Opt. **5**, S97 (2003).

[12]G. D. Boyd and C. K. N. Patel, "Enhancement of optical second-harmonic generation (SHG) by reflection phase matching in ZnS and GaAs", Appl. Phys. Lett. **8**, 313 (1996).

[13]U. K. Sapaev and D. T. Reid, "General second-harmonic pulse shaping in grating-engineered quasi-phase-matched nonlinear crystals", Optics Express **13**, 3264–3276 (2005).

[14]J. I. Dadap, J. Shan, K. B. Eisenthal, and T. F. Heinz, "Second-harmonic rayleigh scattering from a sphere of centrosymmetric material", Phys. Rev. Lett. **83**, 4045 (1999).

[15]K. N. Reddy, P. Y. Chen, A. I. Fernández-Domínguez, and Y. Sivan, "Revisiting the boundary conditions for second-harmonic generation at metal-dielectric interfaces", J. Opt. Soc. Am. B **34**, 1824–1832 (2017).

[16]D. Timbrell, J. W. You, Y. S. Kivshar, and N. C. Panoiu, "A comparative analysis of surface and bulk contributions to second-harmonic generation in centrosymmetric nanoparticles", Sci. Rep. **8**, 3586 (2018).

[17]N. Bloembergen, H. J. Simon, and C. H. Lee, "Total reflection phenomena in second-harmonic generation of light", Phys. Rev. **181**, 1261 (1969).

[18]E. Adler, "Nonlinear optical frequency polarization in a dielectric", Phys. Rev. **134**, A728 (1964).

[19]S. S. Jha, "Theory of optical harmonic generation at a metal surface", Phys. Rev. **140**, A2020 (1965).

[20]W. H. Glenn, "Second-harmonic generation by picosecond optical pulses", IEEE J. Quantum Electron **QE-5**, 284–290 (1969).

[21]J. T. Manassah and O. R. Cockings, "Induced phase modulation of a generated second-harmonic signal", Optics Letters **12**, 1005–1007 (1987).

[22]L. D. Noordam, H. J. Bakker, M. P. de Boer, and H. B. van Linden van den Heuvell, "Second-harmonic generation of femtosecond pulses: observation of phase-mismatch effects", Opt. Lett. **15**, 24 (1990).

[23]W. Su, L. Qian, H. Luo, X. Fu, H. Zhu, T. Wang, K. Beckwitt, Y. Chen, and F. Wise, "Induced group-velocity dispersion in phase-mismatched second-harmonic generation", J. Opt. Soc. Am. B **23**, 57–55 (2006).

[24]M. Mlejnek, E. M. Wright, J. V. Moloney, and N. Bloembergen, "Second harmonic generation of femtosecond pulses at the boundary of a nonlinear dielectric", Phys. Rev. Lett. **83**, 2934 (1999).

[25]V. Roppo, M. Centini, C. Sibilia, M. Bertolotti, D. de Ceglia, M. Scalora, N. Akozbek, M. J. Bloemer, J. W. Haus, O. G. Kosareva, and V. P. Kandidov, "Role of phase matching in pulsed second-harmonic generation: walk-off and phase-locked twin pulses in negative-index media", Phys. Rev. A **76**, 033829 (2007).

[26]N. Akozbek, A. Iwasaki, A. Becker, M. Scalora, S. L. Chin, and C. M. Bowden, "Third-harmonic generation and self-channeling in air using high-power femtosecond laser pulses", Phys. Rev. Lett. **89**, 143901 (2007).

[27]E. Fazio, F. Pettazzi, M. Centini, M. Chauvet, A. Belardini, M. Alonzo, C. Sibilia, M. Bertolotti, and M. Scalora, "Complete spatial and temporal locking in phase-mismatched second-harmonic generation", Optics Express **17**, 3141–3147 (2009).

[28]M. Centini, V. Roppo, E. Fazio, F. Pettazzi, C. Sibilia, J. W. Haus, J. V. Foreman, N. Akozbek, M. J. Bloemer, and M. Scalora, "Inhibition of linear absorption in opaque materials using phase-locked harmonic generation", Phys. Rev. Lett. **101**, 113905 (2008).

[29]V. Roppo, C. Cojocaru, F. Raineri, G. D'Aguanno, J. Trull, Y. Halioua, R. Raj, I. Sagnes, R. Vilaseca, and M. Scalora, "Field localization and enhancement of phase-locked second- and third-order harmonic generation in absorbing semiconductor cavities", Phys. Rev. A **80**, 043834 (2009).

[30]V. Roppo, J. V. Foreman, N. Akozbek, M. A. Vincenti, and M. Scalora, "Third harmonic generation at 223 nm in the metallic regime of gap", Appl. Phys. Lett. **98**, 111105 (2011).

[31]J. W. Haus, *Fundamentals and applications of nanophotonics* (Elsevier, 2016).

[32]M. Mesch, B. Metzger, M. Hentschel, and H. Giessen, "Nonlinear plasmonic sensing", Nano Lett. **16**, 3155–3159 (2016).

[33]L. Ghirardini, A.-L. Baudrion, M. Monticelli, D. Petti, P. Biagioni, L. Duò, G. Pellegrini, P.-M. Adam, M. Finazzi, and M. Celebrano, "Plasmon-enhanced second harmonic sensing", Nano Lett. **16**, 3155–3159 (2016).

[34]V. Kravtsov, R. Ulbricht, J. M. Atkin, and M. B. Raschke, "Plasmonic nanofocused four-wave mixing for femtosecond near-field imaging", Nat. Nanotech **11**, 459–464 (2016).

[35]G. Deka, C.-K. Sun, K. Fujita, and S.-W. Chu, "Nonlinear plasmonic imaging techniques and their biological applications", Nanophotonics **6**, 31–49 (2017).

[36]Q. Zhao, J. Zhou, F. Zhang, and D. Lippens, "Mie resonance-based dielectric metamaterials", Mater. Today **12**, 60–69 (2009).

[37]G. Barbillon, T. Noblet, B. Busson, A. Tadjeddine, and C. Humbert, "Localised detection of thiophenol with gold nanotriangles highly structured as honeycombs by nonlinear sum frequency generation spectroscopy", J. Mater. Sci. **53**, 4554–4562 (2018).

[38]J.-A. Huang, Y.-Q. Zhao, X.-J. Zhang, L.-F. He, T.-L. Wong, Y.-S. Chui, W.-J. Zhang, and S.-T. Lee, "Ordered Ag/Si nanowires array: wide-range surface-enhanced raman spectroscopy for reproducible biomolecule detection", Nano Lett. **13**, 5039–5045 (2013).

[39]Y. Salamin, P. Ma, B. Baeuerle, A. Emboras, Y. Fedoryshyn, W. Heni, B. Cheng, A. Josten, and J. Leuthold, "100GHz plasmonic photodetector", ACS Photonics **5**, 3291–3297 (2018).

[40]C. Haffner, W. Heni, Y. Fedoryshyn, J. Niegemann, A. Melikyan, D. L. Elder, B. Baeuerle, Y. Salamin, A. Josten, U. Koch, C. Hoessbacher, F. Ducry, L. Juchli, A. Emboras, D. Hillerkuss, M. Kohl, L. R. Dalton, C. Hafner, and J. Leuthold, "All-plasmonic mach–zehnder modulator enabling optical high-speed communication at the microscale", Nature Photonics **9**, 525–528 (2015).

[41]I. Vangelidis, A. Theodosi, M. J. Beliatis, K. K. Gandhi, A. Laskarakis, P. Patsalas, S. Logothetidis, S. R. P. Silva, and E. Lidorikis, "Plasmonic organic photovoltaics: unraveling plasmonic enhancement for realistic cell geometries", ACS Photonics **5**, 1440–1452 (2018).

[42]X. Chen, J. Fang, X. Zhang, Y. Zhao, and M. Gu, "Optical/electrical integrated design of core–shell aluminum-based plasmonic nanostructures for record-breaking efficiency enhancements in photovoltaic devices", ACS Photonics **4**, 2102–2110 (2017).

[43]F. Brown, R. E. Parks, and A. M. Sleeper, "Nonlinear optical reflection from a metallic boundary", Phys. Rev. Lett. **14**, 1029 (1965).

[44]N. Bloembergen, R. K. Chang, and C. H. Lee, "Second-harmonic generation of light in reflection from media with inversion symmetry", Phys. Rev. Lett. **16**, 986 (1966).

[45]N. Bloembergen, R. K. Chang, S. S. Jha, and C. H. Lee, "Optical second-harmonic generation in reflection from media with inversion symmetry", Phys. Rev. **174**, 813 (1968).

[46]J. Rudnick and E. A. Stern, "Second-harmonic radiation from metal surfaces", Phys. Rev. B **4**, 4274 (1971).

[47]J. E. Sipe, V. C. Y. So, M. Fukui, and G. I. Stegeman, "Analysis of second-harmonic generation at metal surfaces", Phys. Rev. B **21**, 4389 (1980).

[48]A. Liebsch, "Second-harmonic generation at simple metal surfaces", Phys. Rev. Lett. **61**, 1233 (1988).

[49]D. Krause, C. W. Teplin, and C. T. Rogers, "Optical surface second harmonic measurements of isotropic thin-film metals: Gold, silver, copper aluminum, and tantalum", J. of Appl. Phys. **96**, 3626 (2004).

[50]J. Butet, J. Duboisset, G. Bachelier, I. Russier-Antoine, E. Benichou, C. Jonin, and P.-F. Brevet, "Optical second harmonic generation of single metallic nanoparticles embedded in a homogeneous medium", Nano Lett. **10**, 1717–1721 (2010).

[51]J. Butet, G. Bachelier, I. Russier-Antoine, C. Jonin, E. Benichou, and P.-F. Brevet, "Optical second harmonic generation of single metallic nanoparticles embedded in a homogeneous medium", Phys. Rev. Lett. **105**, 077401 (2010).

[52]M. Zavelani-Rossi, M. Celebrano, P. Biagioni, D. Polli, M. Finazzi, L. Duò, G. Cerullo, M. Labardi, M. Allegrini, J. Grand, and P.-M. Addam, "Near-field second-harmonic generation in single gold nanoparticles", Appl. Phys. Lett. **92**, 093119 (2008).

[53]Y. Zhang, N. K. Grady, C. Ayala-Orozco, and N. J. Halas, "Three-dimensional nanostructures as highly efficient generators of second harmonic light", Nano Lett. **11**, 5519–5523 (2011).

[54]M. D. McMahon, R. Lopez, R. F. Haglund, J. E. A. Ray, and P. H. Bunton, "Second-harmonic generation from arrays of symmetric gold nanoparticles", Phys. Rev. B **73**, 041401(R) (2006).

[55]Y. Zeng, W. Hoyer, J. Liu, S. W. Koch, and J. V. Moloney, "Classical theory for second-harmonic generation from metallic nanoparticles", Phys. Rev. B **79**, 235109 (2009).

[56]F. X. Wang, F. J. Rodríguez, W. M. Albers, R. Ahorinta, J. E. Sipe, and M. Kauranen, "Surface and bulk contributions to the second-order nonlinear optical response of a gold film", Phys. Rev. B **80**, 233402 (2009).

[57]H. B. Liao, R. F. Xiao, J. S. Fu, H. Wang, K. S. Wong, and G. K. L. Wong, "Origin of third-order optical nonlinearity in Au:SiO_2 composite films on femtosecond and picosecond time scales", Opt. Lett. **23**, 388–290 (1998).

[58]D. D. Smith, Y. Yoon, R. W. Boyd, J. K. Campbell, L. A. Baker, R. M. Crooks, and M. George, "Z-scan measurement of the nonlinear absorption of a thin gold film", J. of Appl. Phys. **86**, 6200 (1999).

[59]S. Debrus, J. Lafait, M. May, N. Pinçon, D. Prot, C. Sella, and J. Venturini, "Z-scan determination of the third-order nonlinearity of gold:silica nanocomposites", J. of Appl. Phys. **88**, 4469 (2000).

[60]R. West, Y. Wang, and T. Goodson, "Nonlinear absorption properties in novel gold nanostructured topologies", J. Phys. Chem. B. **107**, 3419–3426 (2003).

[61]A. I. Ryasnyanskiy, B. Palpant, S. Debrus, U. Pal, and A. Stepanov, "Third-order nonlinear-optical parameters of gold nanoparticles in different matrices", Journal of Luminescence **127**, 181–185 (2007).

[62]R. W. Boyd, Z. Shi, and I. D. Leon, "The third-order nonlinear optical susceptibility of gold", Opt. Comm. **326**, 74–79 (2014).

[63]E. J. Stanton, J. Chiles, N. Nader, G. Moody, N. Volet, L. Chang, J. E. Bowers, S. W. Nam, and R. P. Mirin, "Efficient second harmonic generation in nanophotonic GaAs-on-insulator waveguides", Opt. Express **28**, 9521–9532 (2020).

[64]P. S. Kuo, J. Bravo-Abad, and G. S. Solomon, "Second-harmonic generation using quasi-phasematching in a GaAs whispering-gallery-mode microcavity", Nat. Commun. **5**, 3109 (2014).

[65]S. Buckley, M. Radulaski, J. Petykiewicz, K. G. Lagoudakis, J.-H. Kang, M. Brongersma, K. Biermann, and J. Vučković, "Second-harmonic generation in GaAs photonic crystal cavities in (111)B and (001) crystal orientations", ACS Photonics **1**, 516–523 (2014).

[66]D. V. Thourhout, J. V. Campenhout, P. Rojo-Romeo, P. Regreny, C. Seassal, P. Binetti, X. J. M. Leijtens, R. Notzel, M. K. Smit, L. D. Cioccio, C. Lagahe, J. M. Fedeli, and R. Baets, "A photonic interconnect layer on CMOS", Proc. 33rd European Conf. Optical Communications paper **6.3.1** (2007).

[67]L. Tsybeskov, D. J. Lockwood, and M. Ichikawa, "Silicon photonics: CMOS going optical", Proc. IEEE **97**, 1161–1165 (2009).

[68]M. A. Foster, A. C. Turner, R. Salem, M. Lipson, and A. L. Gaeta, "Broad-band continuous-wave parametric wavelength conversion in silicon nanowaveguides", Opt. Express **15**, 12949–12958 (2007).

[69]M. Lipson, "Guiding, modulating, and emitting light on silicon-challenges and opportunities", J. Lightwave Technol. **23**, 4222–4238 (2005).

[70]Y.-H. Kuo, H. Rong, V. Sih, S. Xu, M. Paniccia, and O. Cohen, "Demonstration of wavelength conversion at 40Gb/s data rate in silicon waveguides", Opt. Express **14**, 11721–11726 (2006).

[71]M. A. Foster, R. Salem, D. F. Geragthy, A. C. Turner-Foster, M. Lipson, and A. L. Gaeta, "Silicon-chip-based ultrafast optical oscilloscope", Nature **156**, 81–84 (2008).

[72]C. Koos, P. Vorreau, T. Vallaitis, P. Dumon, W. Bogaerts, R. Baets, B. Esembeson, I. Biaggio, T. Michinobu, F. Diederich, W. Freude, and J. Leuthold, "All-optical high-speed signal processing with silicon-organic hybrid slot waveguides", Nat. Photonics **3**, 216–219 (2009).

[73]J. T. Robinson, L. Chen, and M. Lipson, "On-chip gas detection in silicon optical microcavities", Opt. Express **16**, 4296–4301 (2008).

[74]A. W. Elshaari, W. Pernice, K. Srinivasan, O. Benson, and V. Zwiller, "Hybrid integrated quantum photonic circuits", Nat. Photonics **14**, 285–298 (2020).

[75]H. W. K. Tom, T. F. Heinz, and Y. R. Shen, "Second-harmonic reflection from silicon surfaces and its relation to structural symmetry", Phys. Rev. Lett. **51**, 1983 (1983).

[76]N. Bloembergen, K. Burns, and M. Matsuoka, "Reflected third harmonic generated by picosecond laser pulses", Opt. Comm. **1**, 195–198 (1969).

[77]W. K. Burns and N. Bloembergen, "Third harmonic generation in absorbing media of cubic or isotropic symmetry", Phys. Rev. B **4**, 3437 (1971).

[78]C. C. Wang, J. Bomback, W. T. Donlon, C. R. Huo, and J. V. James, "Optical third-harmonic generation in reflection from crystalline and amorphous samples of silicon", Phys. Rev. Lett. **57**, 1647 (1986).

[79]M. Cazzanelli, F. Bianco, E. Borga, G. Pucker, M. Ghulinyan, E. Degoli, E. Luppi, V. Véniard, S. Ossicini, D. Modotto, S. Wabnitz, R. Pierobon, and L. Pavesi, "Second-harmonic generation in silicon waveguides strained by silicon nitride", Nat. Materials **11**, 148–154 (2012).

[80]J.-H. Zhao, Q.-D. Chen, Z.-G. Chen, G. Jia, W. Su, Y. Jiang, Z.-X. Yan, T. V. Dolgova, O. A. Aktsipetrov, and H.-B. Sun, "Enhancement of second-harmonic generation from silicon stripes under external cylindrical strain", Opt. Lett. **34**, 3340–3342 (2009).

[81]C. Castellan, A. Trenti, C. Vecchi, A. Marchesini, M. Mancinelli, M. Ghulinyan, G. Pucker, and L. Pavesi, "On the origin of second harmonic generation in silicon waveguides with silicon nitride cladding", Scientific Reports **9**, 1088 (2019).

[82]C. Monat, B. Corcoran, C. Grillet, D. J. Moss, B. J. Eggleton, T. P. White, L. O'Faolain, and T. F. Krauss, "Green light emission in silicon through slow light enhanced third-harmonic generation in photonic crystal waveguides", Nat. Photonics **3**, 206–210 (2009).

[83]M. R. Shcherbakov, D. N. Neshev, B. Hopkins, A. S. Shorokhov, I. Staude, E. V. Melik-Gaykazyan, M. Decker, A. A. Ezhov, A. E. Miroshnichenko, I. Brener, A. A. Fedyanin, and Y. S. Kivshar, "Enhanced third-harmonic generation in silicon nanoparticles driven by magnetic response", Nano Lett. **14**, 6488–6492 (2014).

[84]W. Tong, C. Gong, X. Liu, S. Yuan, Q. Huang, J. Xia, and Y. Wang, "Enhanced third harmonic generation in a silicon metasurface using trapped mode", Opt. Express **24**, 19661–19670 (2016).

[85]S. Sederberg, C. J. Firby, and A. Y. Elezzabi, "Efficient, broadband third-harmonic generation in silicon nanophotonic waveguides spectrally shaped by nonlinear propagation", Opt. Express **27**, 4990–5004 (2019).

[86]M. Z. Alam, I. D. Leon, and R. W. Boyd, "Large optical nonlinearity of indium tin oxide in its epsilon-near-zero region", Science **352**, 795 (2016).

[87]T. S. Luk, D. de Ceglia, S. Liu, G. A. Keeler, R. P. Prasankumar, M. A. Vincenti, M. Scalora, M. B. Sinclair, and S. Campione, "Enhanced third harmonic generation from epsilon-near-zero modes of ultrathin films", Appl. Phys. Lett. **106**, 151103 (2015).

[88]A. Capretti, Y. Wang, N. Engheta, and L. D. Negro, "Enhanced third-harmonic generation in Si-compatible epsilon-near-zero indium tin oxide nanolayers", Opt. Lett. **40**, 1500–1503 (2015).

[89]A. Capretti, Y. Wang, N. Engheta, and L. D. Negro, "Comparative study of second-harmonic generation from epsilon-near-zero indium tin oxide and titanium nitride nanolayers excited in the near-infrared spectral range", ACS Photonics **2**, 1584–1591 (2015).

[90]M. A. Vincenti, M. Kamandi, D. de Ceglia, C. Guclu, M. Scalora, and F. Capolino, "Second-harmonic generation in longitudinal epsilon-near-zero materials", Phys. Rev. B **96**, 045438 (2017).

[91]M. A. Vincenti, D. de Ceglia, A. Ciattoni, and M. Scalora, "Singularity-driven second- and third-harmonic generation at ε-near-zero crossing points", Phys. Rev. A **84**, 063826 (2011).

[92]M. A. Vincenti, D. de Ceglia, J. W. Haus, and M. Scalora, "Harmonic generation in multi-resonant plasma films", Phys. Rev. A **88**, 043812 (2013).

[93]C. Rizza, A. Ciattoni, and E. Palange, "Two-peaked and flat-top perfect bright solitons in nonlinear metamaterials with epsilon near zero", Phys. Rev. A **83**, 053805 (2011).

[94]A. Ciattoni, C. Rizza, and E. Palange, "Extreme nonlinear electrodynamics in metamaterials with very small linear dielectric permittivity", Phys. Rev. A **81**, 043839 (2010).

[95]A. Ciattoni and E. Spinozzi, "Efficient second-harmonic generation in micrometer-thick slabs with indefinite permittivity", Phys. Rev. A **85**, 043806 (2012).

[96]M. A. Vincenti, S. Campione, D. de Ceglia, F. Capolino, and M. Scalora, "Gainassisted harmonic generation in near-zero permittivity metamaterials made of plasmonic nanoshells", New J. Phys. **14**, 103016 (2012).

[97]D. de Ceglia, S. Campione, M. A. Vincenti, F. Capolino, and M. Scalora, "Lowdamping epsilon-near-zero slabs: nonlinear and nonlocal optical properties", Phys. Rev. B **87**, 155140 (2013).

[98]O. Reshef, I. D. Leon, M. Z. Alam, and R. W. Boyd, "Nonlinear optical effects in epsilon-near-zero media", Nat. Rev. Mater. **4**, 535–551 (2019).

[99]K. Ellmer, "Past achievements and future challenges in the development of optically transparent electrodes", Nature Photonics **6**, 809–817 (2012).

[100]D. D. Ceglia, M. Scalora, M. A. Vincenti, S. Campione, K. Kelley, E. L. Runnerstrom, J.-P. Maria, G. A. Keeler, and T. S. Luk, "Viscoelastic optical nonlocality of low-loss epsilon-near-zero nanofilms", Sci. Rep. **8**, 9335 (2018).

[101]Y. Yang, K. Kelley, E. Sachet, S. Campione, T. S. Luk, J.-P. Maria, M. B. Sinclair, and I. Brener, "Femtosecond optical polarization switching using a cadmium oxide-based perfect absorber", Nat. Photonics **11**, 390–395 (2017).

[102]D. de Ceglia, M. A. Vincenti, N. Akozbek, M. J. Bloemer, and M. Scalora, "Nested plasmonic resonances: extraordinary enhancement of linear and nonlinear interactions", Opt. Express **25**, 3980 (2017).

[103]M. Scalora, M. A. Vincenti, D. de Ceglia, V. Roppo, M. Centini, N. Akozbek, and M. J. Bloemer, "Second- and third-harmonic generation in metal-based structures", Phys. Rev. A **82**, 043828 (2010).

[104]M. Scalora, M. A. Vincenti, D. de Ceglia, C. M. Cojocaru, M. Grande, and J. W. Haus, "Nonlinear duffing oscillator model for third harmonic generation", J. Opt. Soc. Am. B **32**, 2129–2138 (2015).

[105]I. Tokatly and O. Pankratov, "Hydrodynamic theory of an electron gas", Phys. Rev. B **60**, 15550 (1999).

[106]D. de Ceglia, M. Scalora, M. A. Vincenti, S. Campione, K. Kelley, E. L. Runnerstrom, J.-P. Maria, G. A. Keeler, and T. S. Luk, "Viscoelastic optical nonlocality of low-loss epsilon-near-zero nanofilms", Scientific Reports **8**, 9335 (2018).

[107]E. D. Palik, *Handbook of optical constants of solids* (Academic Press, 1985).

[108]J. Qi, *Nonlinear optical spectroscopy of gallium arsenide interfaces* (University of Pennsylvania, 1995).

[109]M. Rabiena, W. Henrion, M. Hong, J. P. Mannaerts, and M. Fleischer, "Optical properties of gallium oxide thin films", Appl. Phys. Lett. **81**, 250–252 (2002).

[110]`https://korvustech.com/magnetron-sputtering/`.

[111]D. M. Riffe, "Temperature dependence of silicon carrier effective masses with application to femtosecond reflectivity measurements", J. Opt. Soc. Am. B **19**, 1092–1100 (2002).

[112]M. Scalora, M. A. Vincenti, D. de Ceglia, N. Akozbek, M. J. Bloemer, C. D. Angelis, J. W. Haus, R. Vilaseca, J. Trull, and C. Cojocaru, "Harmonic generation from metal-oxide and metal-metal boundaries", Phys. Rev. A **98**, 023837 (2018).

[113]M. Sheik-bahae, A. A. Said, and E. W. V. Stryland, "High-sensitivity, single-beam n_2 measurements", Optics Letters **14**, 955–957 (1989).

[114]M. Sheik-Bahae, A. Said, T.-H. Wei, D. Hagan, and E. V. Stryland, "Sensitive measurement of optical nonlinearities using a single beam", IEEE J. Quantum Electron **26**, 1760 (1990).

[115]M. Scalora and M. E. Crenshaw, "A beam propagation method that handles reflections", Opt. Commun. **108**, 191–196 (1994).

Appendix A
List of publications and research activities

A.1 Publications

1. **L. Rodríguez-Suné**, J. Trull, M. Scalora, R. Vilaseca, and C. Cojocaru, "Harmonic generation in the opaque region of GaAs: the role of the surface and magnetic nonlinearities", Opt. Express **23**, 26120-26130 (2019).

2. **L. Rodríguez-Suné**, M. Scalora, A. S. Johnson, C. Cojocaru, N. Akozbek, Z. J. Coppens, D. Perez-Salinas, S. Wall, and J. Trull, "Study of second and third harmonic generation from an indium tin oxide nanolayer: Influence of nonlocal effects and hot electrons", APL Photonics **5**, 010801 (2020).

3. M. Scalora, J. Trull, D. de Ceglia, M. A. Vincenti, N. Akozbek, Z. Coppens, **L. Rodríguez-Suné**, and C. Cojocaru, "Electrodynamics of conductive oxides: Intensity-dependent anisotropy, reconstruction of the effective dielectric constant, and harmonic generation", Phys. Rev. A **101**, 053828 (2020).

4. **L. Rodríguez-Suné**, J. Trull, C. Cojocaru, N. Akozbek, D. de Ceglia, M. A. Vincenti, and M. Scalora, "Harmonic generation from gold nanolayers: bound and hot electron contributions to nonlinear dispersion", Opt. Express **29**, 8581-8591 (2021).

5. **L. Rodríguez-Suné**, J. Trull, N. Akozbek, D. de Ceglia, M. A. Vincenti, M. Scalora, and C. Cojocaru, "Retrieving Linear and Nonlinear Optical Dispersions of Matter: Combined Experimental-Numerical ellipsometry in Silicon, Gold and Indium Tin Oxide", Front. Photon. **2**, 746341 (2021).

6. K. A. Hallman, **L. Rodríguez-Suné**, J. Trull, C. Cojocaru, M. A. Vincenti, N. Akozbek, R. Vilaseca, and M. Scalora, "Harmonic generation from silicon membranes at visible and ultraviolet wavelengths", Opt. Express **31**, 792-801 (2023).

7. S. Mukhopadhyay, **L. Rodríguez-Suné**, C. Cojocaru, M. A. Vincenti, K. Hallman, G. Leo, M. Belchovski, D. de Ceglia, M. Scalora, and J. Trull, "Three orders of magnitude of second and third harmonic generation in the visible and ultraviolet ranges from plasmonic gold nanogratings", APL Photonics **8**, 046108 (2023).

A.2 Proceedings

1. **L. R. Suñé**, J. F. Trull, M. Scalora, and C. Cojocaru, "Surface and bulk harmonic generation in the opaque region of GaAs", Proc. SPIE 11026, Nonlinear Optics and Applications XI, 1102600 (30 April 2019).

2. C. Cojocaru, **L. R. Suñé**, M. Scalora, and J. Trull, "Phase Locked Harmonic Generation in the Opaque Region of GaAs", IEEE 2019, 21st International Conference on Transparent Optical Network (ICTON), Angers, France (19 September 2019).

3. **L. Rodríguez-Suné**, M. Scalora, A. S. Johnson, C. Cojocaru, N. Akozbek, Z. J. Coppens, D. Perez-Salinas, S. Wall, and J. Trull, "Second harmonic generation from an ITO nanolayer: experiment versus theory", Proc. SPIE 11345, Nanophotonics VIII, 113451R (1 April 2020).

4. **L. Rodríguez-Suné**, M. Scalora, A. S. Johnson, C. Cojocaru, N. Akozbek, Z. J. Coppens, D. Perez-Salinas, S. Wall, and J. Trull, "Experimental and theoretical study of second

harmonic generation from an ITO nanolayer", IEEE 2020, 22nd International Conference on Transparent Optical Networks (ICTON), Bari, Italy (22 September 2020).

5. **L. Rodríguez-Suné**, J. Trull, C. Cojocaru, N. Akozbek, D. de Ceglia, M. A. Vincenti, and M. Scalora, "Harmonic generation from gold nanolayers: bound and hot electron contributions", Proc. SPIE 11770, Nonlinear Optics and Applications XII, 117700X (6 May 2021).

6. **L. Rodríguez-Suné**, J. Trull, N. Akozbek, D. de Ceglia, M. A. Vincenti, M. Scalora, and C. Cojocaru, "Second and third harmonic generation from gold nanolayers: experiment versus theory", EPJ Web of Conferences **255**, 07003 (18 November 2021).

7. **L. Rodríguez-Suné**, M. Scalora, C. Cojocaru, N. Akozbek, R. Vilaseca, and J. Trull, "Experimental and theoretical study of second and third harmonic generation in amorphous silicon," Proc. SPIE 12143, Nonlinear Optics and its Applications 2022, 1214307 (25 May 2022).

8. **L. Rodríguez-Suné**, M. Scalora, C. Cojocaru, N. Akozbek, R. Vilaseca, and J. Trull, "Towards harmonic generation enhancement on silicon", EPJ Web of Conferences **266**, 05010 (13 October 2022).

A.3 Conferences

1. J. Trull, **L. Rodríguez-Suné**, M. Scalora, and C. Cojocaru, "Surface and bulk harmonic generation in the opaque region of GaAs", invited talk, Emerging Trends in Nonlinear Optics (ETNO), 10-12 of September 2018, Brescia, Italy.

2. **L. Rodríguez-Suné**, J. Trull, M. Scalora, C. Cojocaru, "Surface and bulk harmonic generation in the opaque region of GaAs", oral presentation, SPIE Optics + Optoelectronis, 1-4 of April 2019, Prague, Czech Republic.

3. M. Scalora, **L. Rodríguez-Suné**, J. Trull, C. Cojocaru, and M.A. Vincenti, and D. De Ceglia, "Surface-mediated SHG from a GaAs etalon in the visible and UV ranges", oral presentation, SPIE Optics + Optoelectronis, 1-4 of April 2019, Prague, Czech Republic.

4. C. Cojocaru, **L. Rodríguez-Suné**, M. Scalora, R. Vilaseca, and J. Trull, "Surface and bulk harmonic generation in the opaque region of GaAs", invited talk, Photonics & Electromagnetics Research Symposium (PIERS), 17-20 of June 2019, Rome, Italy.

5. **L. Rodríguez-Suné**, J. Trull, M. Scalora, R. Vilaseca, and C. Cojocaru, "Surface and bulk harmonic generation in the opaque region of GaAs", poster, Conference on Lasers and Electro-Optics-Int Quantum Electronics Conference CLEO/Europe-IQEC, 24-27 of June 2019, Munich, Germany.

6. C. Cojocaru, **L. Rodríguez-Suné**, M. Scalora, and J. Trull, "Surface and bulk harmonic generation in the opaque region of GaAs", invited talk, International Conference on Transparent Optical Networks (ICTON), 7-11 of July 2019, Angers, France.

7. **L. Rodríguez-Suné**, J. Trull, M. Scalora, and C. Cojocaru, "Surface and bulk harmonic generation in the opaque region of GaAs: experiment versus theory", oral presentation, Ultrafast Science and Technology (USTS), 6-8 of November 2019, Madrid, Spain.

8. C. Cojocaru, **L. Rodríguez-Suné**, M. Scalora, and J. Trull, "Harmonic generation in the opaque region of GaAs: the role of surface and magnetic nonlinearities", invited talk, Complex Materials for Nonlinear Optics Workshop (CMNO), 29-31 January 2020, Zurich, Switzerland.

9. **L. Rodríguez-Suné**, M. Scalora, A. S. Johnson, C. Cojocaru, N. Akozbek, Z. J. Coppens, D. Perez-Salinas, S. Wall, and J. Trull, "Second harmonic generation from an ITO nanolayer: experiment versus theory", oral presentation, SPIE Photonics Europe, 6-10 of April 2020, Online.

10. **L. Rodríguez-Suné**, M. Scalora, A. S. Johnson, C. Cojocaru, N. Akozbek, Z. J. Coppens, D. Perez-Salinas, S. Wall, and J. Trull, "Experimental and theoretical study of second harmonic generation from an ITO nanolayer", oral presentation, International Conference on Transparent Optical Networks (ICTON), 19-23 of July 2020, Online.

11. C. Cojocaru, L. Rodríguez-Suné, M. Scalora, and J. Trull, "Harmonic generation in the opaque region of semiconductors: the role of the surface and magnetic nonlinearities", invited talk, International Conference on Transparent Optical Networks (ICTON), 19-23 of July 2020, Online.

12. C. Cojocaru, **L. Rodríguez-Suné**, M. Scalora, N. Akozbek, M. A. Vincenti, D. de Ceglia, and J. Trull, "Harmonic generation in the opaque region of semiconductors: the role of the surface and magnetic nonlinearities", invited talk, SPIE Optics + Photonics, 24 of August-4 of September 2020, Online.

13. C. Cojocaru, **L. Rodríguez-Suné**, M. Scalora, N. Akozbek, and J. Trull, "Harmonic generation at nanoscale in strategic materials for nanophotonics", keynote talk, SPIE Optics + Optoelectronics, 19-29 of April 2021, Online.

14. **L. Rodríguez-Suné**, J. Trull, C. Cojocaru, N. Akozbek, D. de Ceglia, M. A. Vincenti, and M. Scalora, "Harmonic generation from gold nanolayers: bound and hot electron contributions", oral presentation, SPIE Optics + Optoelectronics, 19-29 of April 2021, Online.

15. **L. Rodríguez-Suné**, C. Cojocaru, M. Scalora, and J. Trull, "Nonlinear optics at the nanoscale: experiment versus theory", poster, Conference on Lasers and Electro-Optics-Int Quantum Electronics Conference CLEO/Europe-IQEC, 21-25 of June 2021, Online.

16. C. Cojocaru, **L. Rodríguez-Suné**, M. Scalora, N. Akozbek, and J. Trull, "Harmonic generation at nanoscale in strategic materials for nanophotonics", invited talk, SPIE Optics + Photonics, 1-5 of August 2021, Online.

17. **L. Rodríguez-Suné**, J. Trull, C. Cojocaru, N. Akozbek, D. de Ceglia, M. A. Vincenti, and M. Scalora, "Second and third harmonic generation from gold nanolayers: experiment versus theory", oral presentation, EOS Annual Meeting (EOSAM), 13-17 of September 2021, Rome, Italy.

18. **L. Rodríguez-Suné**, C. Cojocaru, M. Scalora, N. Akozbek, D. de Ceglia, M. A. Vincenti, R. Vilaseca, and J. Trull, "Experimental and theoretical study of second and third harmonic generation from gold nanolayers", oral presentation, National Optics Meeting (RNO), 22-24 of November 2021, Online.

19. **L. Rodríguez-Suné**, M. Scalora, C. Cojocaru, N. Akozbek, R. Vilaseca, and J. Trull, "Combined experimental-theoretical study of harmonic generation in silicon at nanoscale", oral presentation, XXXVIII Reunión Bienal de la RSEF 11–15 of June 2022, Murcia, Spain.

20. S. Mukhopadhyay, J. Trull, **L. Rodríguez-Suné**, M. Scalora, M. A. Vincenti, G. Leo, and C. Cojocaru, "Nonlinear conversion efficiency enhancement in gold grating nanostructure", oral presentation, XXXVIII Reunión Bienal de la RSEF 11–15 of June 2022, Murcia, Spain.

21. M. Scalora, **L. Rodríguez-Suné**, K. Hallman, M.A. Vincenti, N. Akozbek, J. Trull, and C. Cojocaru "Harmonic generation from silicon membranes in the visible and UV ranges", invited talk, SPIE Optics + Photonics, 21–25 of Agust 2022, San Diego, USA.

22. M. Scalora, S. Mukhopadhyay, **L. Rodríguez-Suné**, K. Hallman, M. A. Vincenti, D. de Ceglia, N. Akozbek, J. Trull, and C. Cojocaru "Harmonic generation from metal surfaces and gratings: free electron spill-out layer as an epsilon-near-zero boundary layer", invited talk, SPIE Optics + Photonics, 21–25 of Agust 2022, San Diego, USA.

23. **L. Rodríguez-Suné**, M. Scalora, C. Cojocaru, N. Akozbek, R. Vilaseca, and J. Trull "Towards harmonic generation enhancement on silicon", oral presentation, European Optical Society Annual Meeting (EOSAM), 12-16 September 2022, Porto, Portugal.

24. **L. Rodríguez-Suné**, M. Scalora, C. Cojocaru, N. Akozbek, R. Vilaseca, and J. Trull, "Experimental and theoretical study of second and third harmonic generation in amorphous silicon", oral presentation, SPIE Photonics Europe, 3-7 of April 2022, Strasbourg, France.

25. **L. Rodríguez-Suné**, S. Mukhhopadhyay, J. Trull, M. Scalora, M. A. Vincenti, G. Leo, and C. Cojocaru, "Nonlinear conversion efficiency enhancement in gold grating nanostructure", oral presentation, SPIE Photonics Europe, 3-7 of April 2022, Strasbourg, France.

26. J. Trull, C. Cojocaru, **L. Rodriguez- Suné**, and M. Scalora. "Harmonic generation in nanolayers with femtosecond pulses", invited talk, Ultrafast Science & Technology Spain (USTS2022) 16-18 November 2022, Málaga, Spain.

27. C. Cojocaru, **L. Rodríguez-Suné**, J. Trull, and M. Scalora, "Harmonic generation at the nanoscale in femtosecond regime", invited talk, International Symposium on Ultrafast Intense laser Science, 11-16 of Decemner 2022, Honolulu, Hawaii, USA.

28. **L. Rodríguez-Suné**, K. A. Hallman, J. Trull, C. Cojocaru, M. A. Vincenti, N. Akozbek, R. Vilaseca, and M. Scalora "Harmonic generation from silicon membranes at visible and ultraviolet wavelengths", oral presentation, Conference on Lasers and Electro-Optics-Int Quantum Electronics Conference CLEO/Europe-IQEC, 26–29 of June 2023.

29. S. Mukhopadhyay, **L. Rodríguez-Suné**, C. Cojocaru, M. A. Vincenti, K. Hallman, G. Leo4, M. Belchovski, D. de Ceglia, M. Scalora, and J. Trull "Strong nonlinear efficiency enhancement in the visible and UV ranges from plasmonic gold nanogratings", oral presentation, Conference on Lasers and Electro-Optics-Int Quantum Electronics Conference CLEO/Europe-IQEC, 26–29 of June 2023.

30. M. Scalora, M. Belchovski, **L. Rodríguez-Suné**, S. Mukhopadhyay, K. Hallman, R. Vilaseca, C. Cojocaru, J. Trull, and M. A. Vincenti "Linear and Nonlinear Optical Properties

of Aluminum", poster, Conference on Lasers and Electro-Optics-Int Quantum Electronics Conference CLEO/Europe-IQEC, 26–29 of June 2023.

31. C. Cojocaru, S. Mukhopadhyay, **L. Rodríguez-Suné**, M. A. Vincenti, R. Vilaseca, M. Scalora, and J. Trull "Large enhancement of the nonlinear efficiency in the visible and UV ranges from plasmonic gold nanogratings", invited talk, International Conference on Transparent Optical Networks (ICTON), 3-6 of July 2023, Bucharest, Romania.

32. S. Mukhopadhyay, **L. Rodríguez-Suné**, C. Cojocaru, M. A. Vincenti, K. Hallman, G. Leo4, M. Belchovski, D. de Ceglia, M. Scalora, and J. Trull "Large enhancement in visible to UV nonlinear frequency conversion by a plasmonic gold nanograting", oral presentation, International Conference on Metamaterials, Photonic Crystals and Plasmonics (META), 18-21 of July 2023, Paris, France.

33. M. Scalora, S. Mukhopadhyay, **L. Rodríguez-Suné**, K. Hallman, M. A. Vincenti, D. de Ceglia, N. Akozbek, J. Trull, and C. Cojocaru" "Harmonic generation from metal/vacuum interfaces: free electron spill-out layer as an epsilon-near-zero boundary layer", invited talk, International Congress on Artificial Materials for Novel Wave Phenomena – Metamaterials 2023, Sep. 11–16, 2023, Crete, Greece.

A.4 Research projects

1. Investigadora. Analysis of second and third harmonic generation in absorptive materials. Coordinador científic: C. Cojocaru. 20/09/2019-19/03/2022. Durada: 2 anys i 6 mesos. Finançament: 186.580,00€. Àmbit: Estatal. Entitat on es desenvolupa: Física. Entitat finançadora: US Army RDECOM.

2. Investigadora. Generación Óptica de Armónicos en Materiales Estratégicos para la Nanofotónica. Coordinador científic: J. Trull. 01/06/2020-31/05/2023. Durada: 3 anys. Finançament: 104.060,00€. Àmbit: Estatal. Entitat on es desenvolupa: Física. Entitat finançadora: Agencia estatal de investigación.

Appendix B
Optical elements

In Chapters 2, 3, 4 and 5 we described the experimental set-ups built to measure harmonic signals from our samples, and we indicated with which optical elements these set-ups were formed. In this Appendix, we show transmission/reflection and optical density (OD) curves of these optical elements, as well as the main characteristics of the detectors that have been used.

B.1 Filters

In this section we show the spectral transmission and OD curves for the longpass filters used to eliminate harmonic signals before the sample (Thorlabs, FGL610, FGL850, FELH1100), bandpass filters to attenuate the fundamental field radiation (Thorlabs, FGS900, FGS900-A, FESH0900, FGB37-A, FGUV11-UV), and bandpass/laser line filters centered around the harmonic wavelength (Thorlabs, FL532-10, FL355-10, FBH400-40, FB500-10, Chroma, ET262-20bp, Eksma Optics, NSH filter).

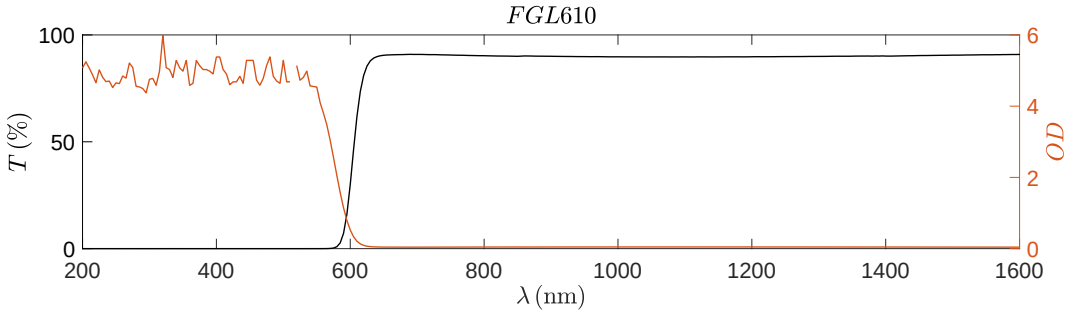

Figure B.1.1: Spectral transmission (black, left y-axis) and OD (red, right y-axis) curves of the longpass filter with cut-on wavelength at 610 nm used to eliminate harmonic radiation before the sample. Data are extracted from Thorlabs.

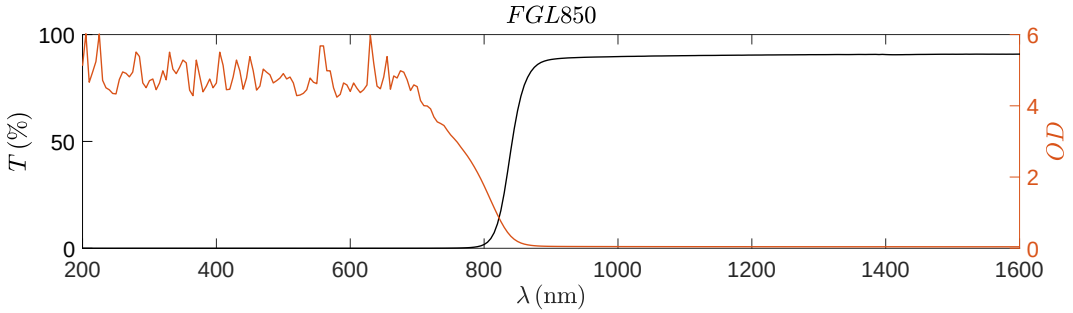

Figure B.1.2: Spectral transmission (black, left y-axis) and OD (red, right y-axis) curves of the longpass filter with cut-on wavelength at 850 nm used to eliminate harmonic radiation before the sample. Data are extracted from Thorlabs.

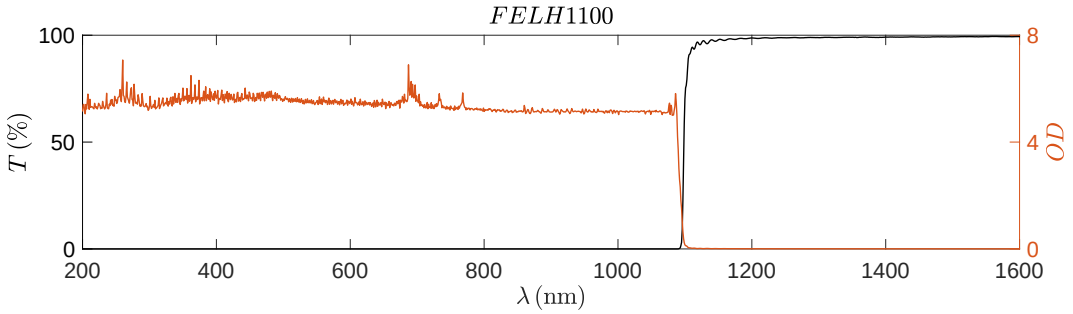

Figure B.1.3: Spectral transmission (black, left y-axis) and OD (red, right y-axis) curves of the longpass filter with cut-on wavelength at 1100 nm used to eliminate undesired frequency components coming from OPA (Light conversion, TOPAS). Data are extracted from Thorlabs.

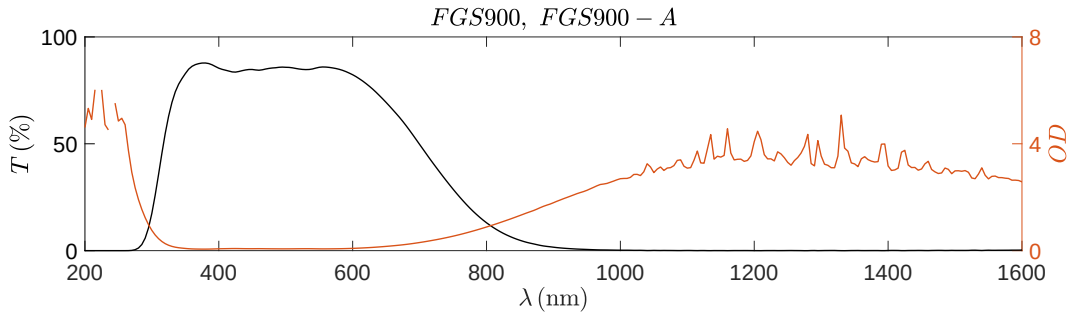

Figure B.1.4: Spectral transmission (black, left y-axis) and OD (red, right y-axis) curves of the bandpass colored glass filter used to attenuate fundamental radiation after the sample. Data are extracted from Thorlabs.

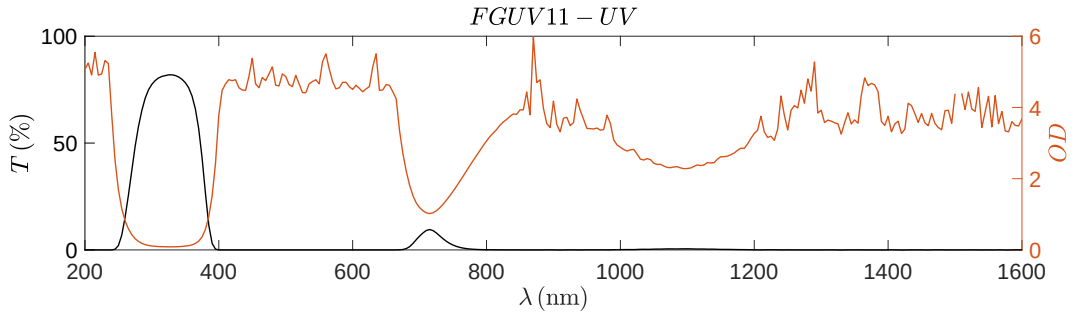

Figure B.1.5: Spectral transmission (black, left y-axis) and OD (red, right y-axis) curves of the bandpass colored glass filter used to attenuate fundamental radiation after the sample. Data are extracted from Thorlabs.

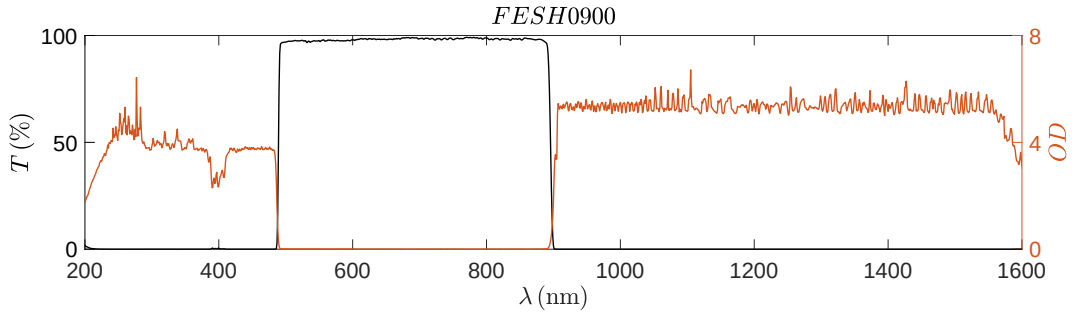

Figure B.1.6: Spectral transmission (black, left y-axis) and OD (red, right y-axis) curves of the hard-coated edgepass filter used to attenuate fundamental radiation after the sample. Data are extracted from Thorlabs.

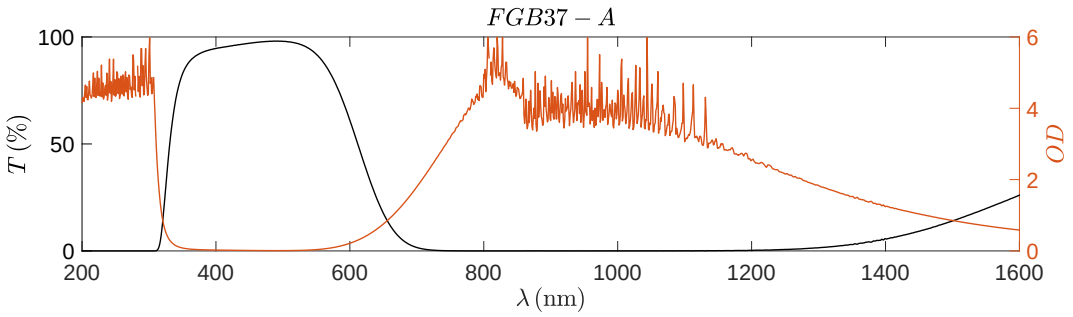

Figure B.1.7: Spectral transmission (black, left y-axis) and OD (red, right y-axis) curves of the bandpass colored glass filter used to attenuate fundamental radiation after the sample. Data are extracted from Thorlabs.

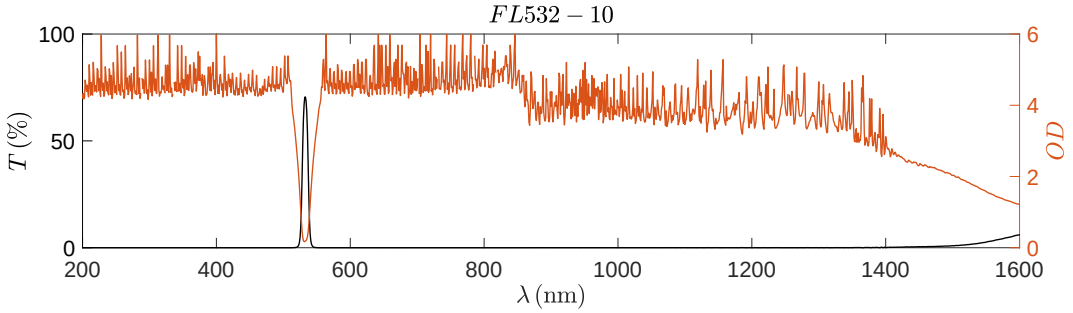

Figure B.1.8: Spectral transmission (black, left y-axis) and OD (red, right y-axis) curves of the laser line filter centered at 532 nm with bandpass at FWHM of 10 nm used to select SH radiation for $\lambda_{in} = 1064$ nm. Data are extracted from Thorlabs.

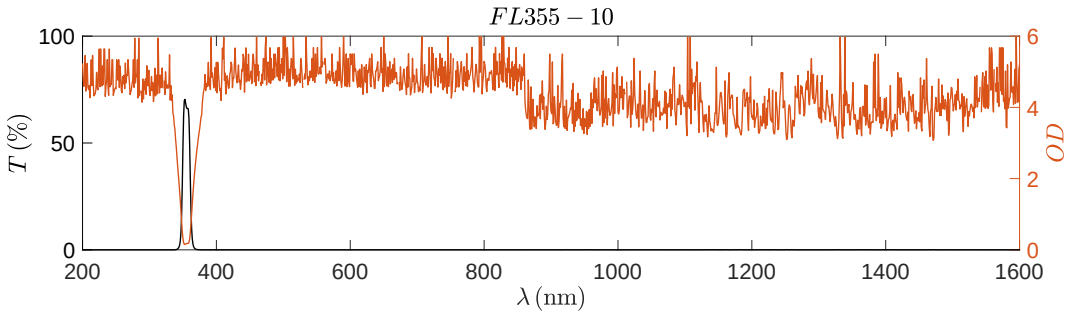

Figure B.1.9: Spectral transmission (black, left y-axis) and OD (red, right y-axis) curves of the laser line filter centered at 355 nm with bandpass at FWHM of 10 nm used to select TH radiation for $\lambda_{in} = 1064$ nm. Data are extracted from Thorlabs.

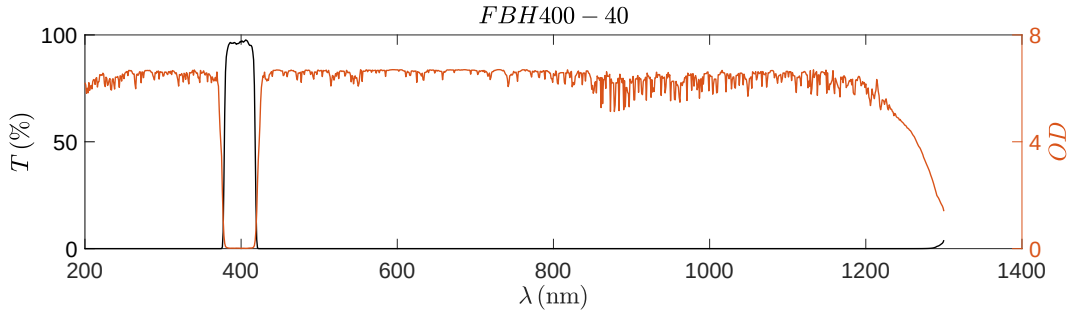

Figure B.1.10: Spectral transmission (black, left y-axis) and OD (red, right y-axis) curves of the hard-coated bandpass filter centered at 400 nm with bandpass at FWHM of 40 nm used to select SH radiation for $\lambda_{in} = 800\,\mathrm{nm}$. Data are extracted from Thorlabs.

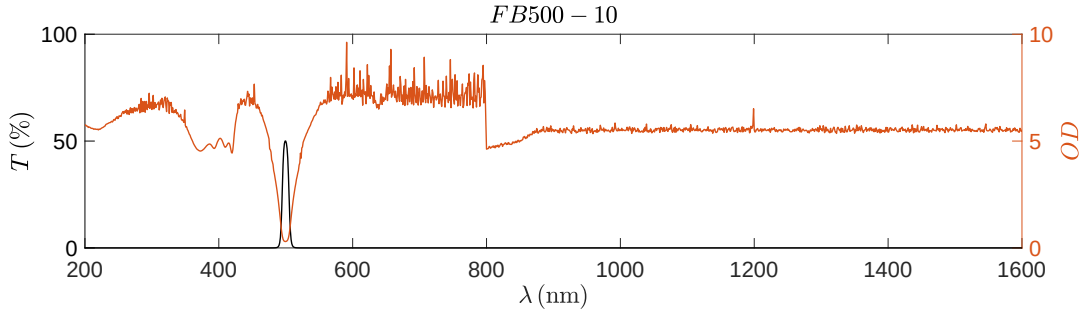

Figure B.1.11: Spectral transmission (black, left y-axis) and OD (red, right y-axis) curves of the bandpass filter centered at 500 nm with bandpass at FWHM of 10 nm used to select SH or TH radiation. Data are extracted from Thorlabs.

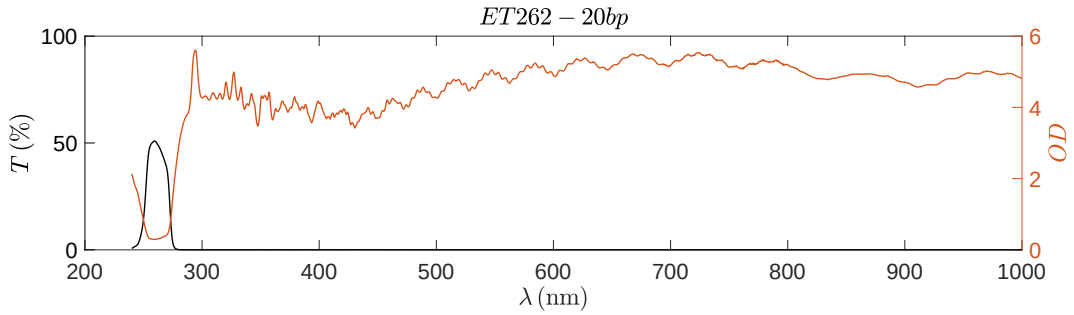

Figure B.1.12: Spectral transmission (black, left y-axis) and OD (red, right y-axis) curves of the bandpass filter centered at 262 nm with bandpass at FWHM of 20 nm TH radiation for $\lambda_{in} = 800\,\mathrm{nm}$. Data are extracted from Chroma.

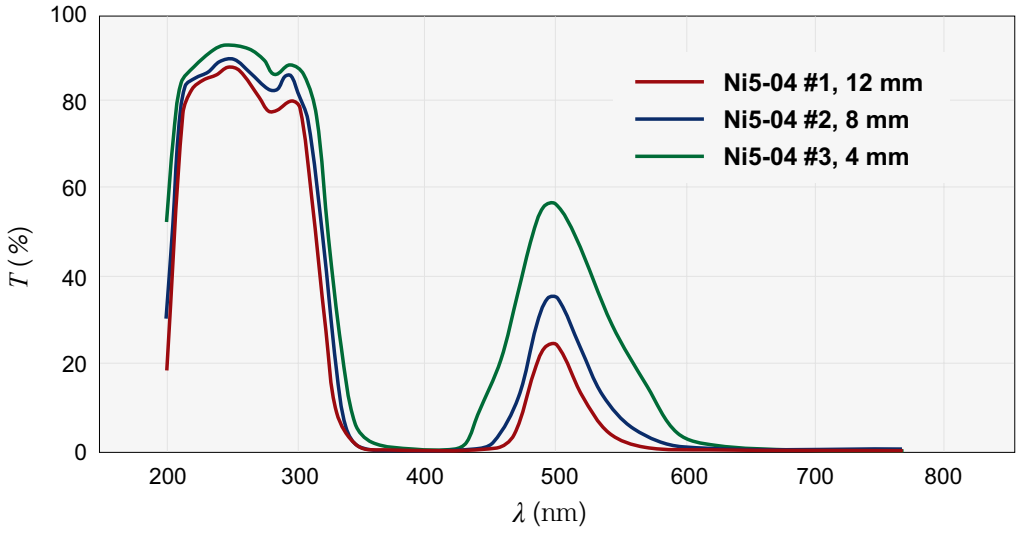

Figure B.1.13: Spectral transmission curve of the NSH bandpass filter used to select TH radiation for $\lambda_{in} = 800\,\text{nm}$. Our filter corresponds to the green curve. The figure is extracted from Eksma Optics.

B.2 Lenses

In this section we show the spectral transmission and reflection curves for the CaF_2 lens (Thorlabs, LA5464) and coated lenses (Thorlabs, LA4380-UV, LA1509-B, LA1708-B, LA1509-C and LA1708-C).

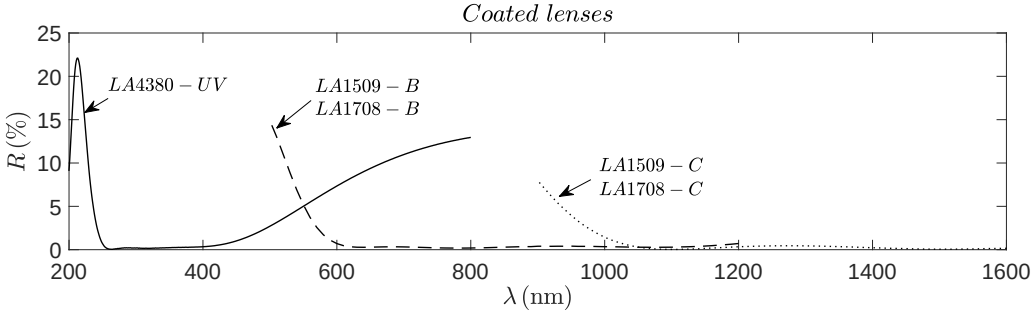

Figure B.2.1: Spectral reflection curves for the lenses used to focus and collimate the beam. These lenses are UV-coated (Thorlabs, LA4380-UV), B-coated (Thorlabs, LA1509-B and LA1708-B) and C-coated (Thorlabs, LA1509-C and LA1708-C). Data are extracted from Thorlabs.

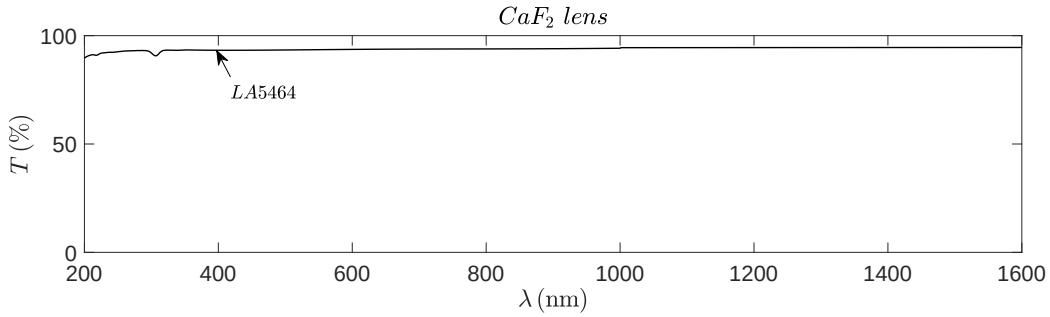

Figure B.2.2: Spectral transmission curve of the CaF_2 lens used to focus and collimate the beam. Data are extracted from Thorlabs.

B.3 Mirrors

In this section we show the spectral reflection curve of the mirror used to select either if the harmonic signal is detected with the PMT or with a silicon photodiode in the set-up described in Chapter 3.2.1.

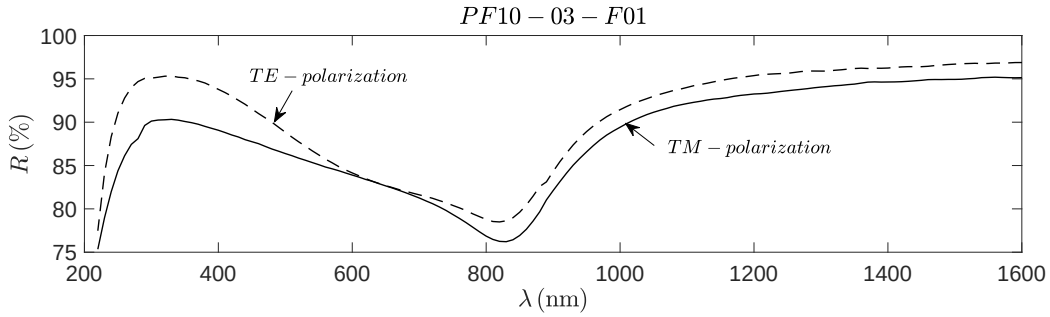

Figure B.3.1: Spectral reflection curve of the mirror for TM- (solid curve) and TE-polarized (dashed curve) light. Data are extracted from Thorlabs.

B.4 Polarizers

In this section we show the spectral transmission curves of the polarizers used to control the incident energy per pulse and the harmonic polarization.

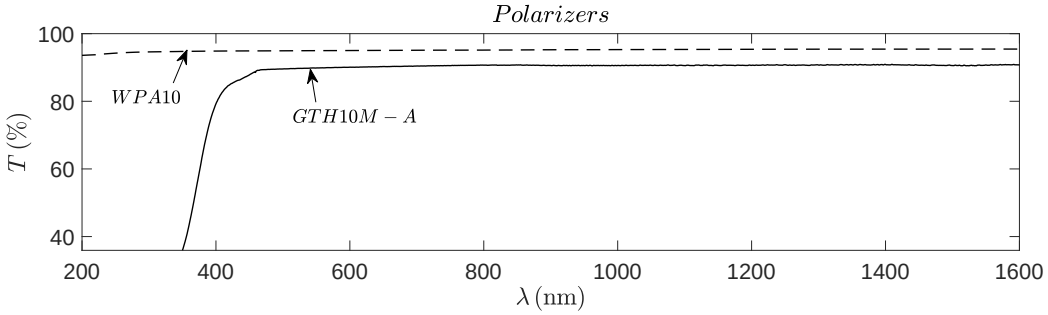

Figure B.4.1: Spectral transmission curves of the polarizers used to select the harmonic polarization (Thorlabs, GTH10M-A) and (Thorlabs, WPA10). Data are extracted from Thorlabs.

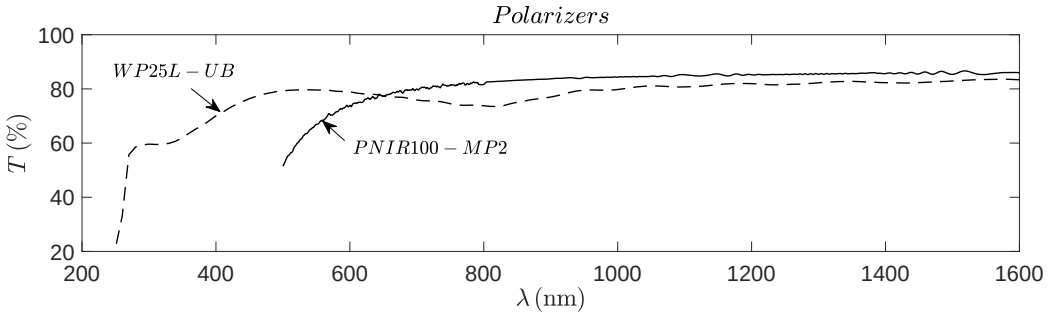

Figure B.4.2: Spectral transmission curves of the polarizers used to control the incident energy per pulse (Thorlabs, WP25L-UB, PNIR100-MP2) and select the harmonic polarization (Thorlabs, WP25L-UB). Data are extracted from Thorlabs.

B.5 Detectors

In this section we show the spectral responsivity curves of the PMTs (Hamamatsu, H10722-04), (Hamamatsu, H10722-113) and (Thorlabs, PMT1001), as well as the responsivity curve for the silicon photodiode used in the calibration procedure (Thorlabs, S120C).

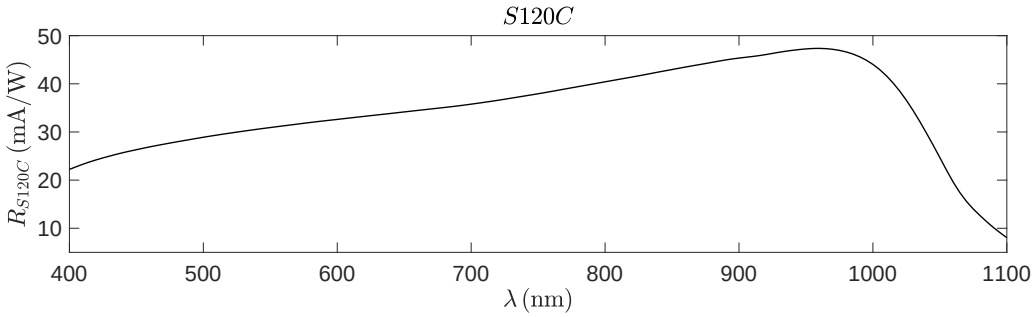

Figure B.5.1: Spectral responsivity curve of the silicon photodiode used in the calibration procedure. It is able to measure in the power range of 50 nW-50 mW and it has a resolution of 1 nW. Data are extracted from Thorlabs. The photodiode used in the set-up described in Chapter 3.2.1 (Newport, 918D-UV-OD3) has a similar response and it is enhanced in the UV.

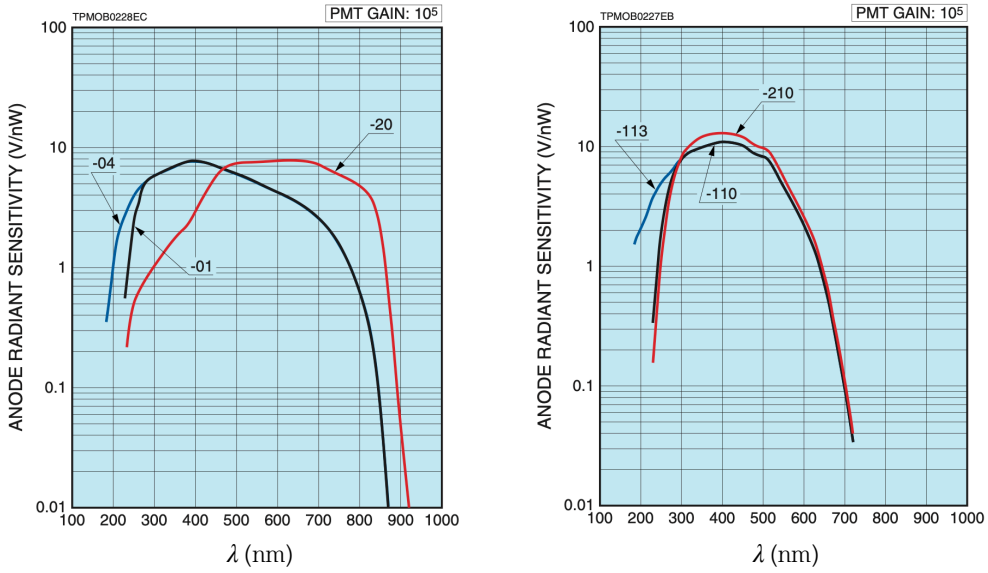

Figure B.5.2: Spectral responsivity curve of the PMTs (Hamamatsu, H10722-113, H10722-04) used to detect the harmonic signal. The figure is extracted from Hamamatsu.

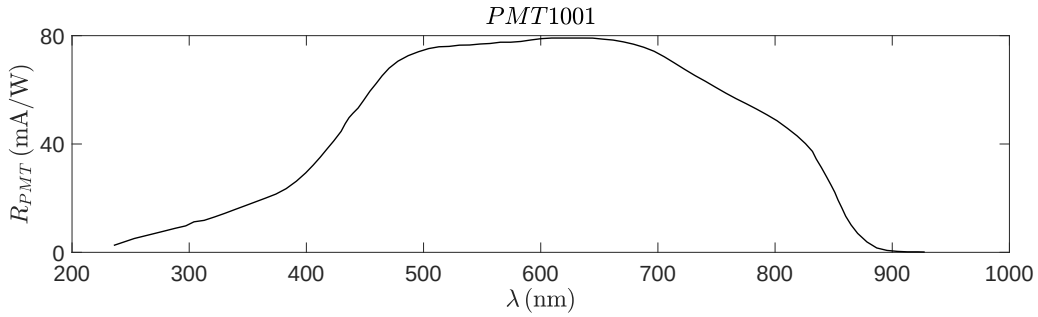

Figure B.5.3: Spectral responsivity curve of the PMT used to detect the harmonic signal. Data are extracted from Thorlabs.

Appendix C
Method of solution

In Chapter 1.5 we saw the dynamic polarization equations which together with Maxwell's equations are solved and numerical simulations results for SHG and THG conversion efficiencies are obtained. In this appendix we outline the method of solution of these equations by examining the propagation of a field coupled to a single Lorentz oscillator that contains a generic nonlinear term $\mathbf{P}^{\mathrm{NL}}$. Neglecting the nonlinear spring term and the magnetic portion of the Lorentz force, we have (in CGS units):

$$\begin{aligned} \nabla \times \mathbf{E} &= -\frac{1}{c}\frac{\partial \mathbf{H}}{\partial t} \\ \nabla \times \mathbf{H} &= \frac{1}{c}\frac{\partial \mathbf{E}}{\partial t} + \frac{4\pi}{c}\frac{\partial \mathbf{P}}{\partial t} \\ \ddot{\mathbf{P}} + \gamma\dot{\mathbf{P}} + \omega_0^2\mathbf{P} + \mathbf{P}^{\mathrm{NL}} &= \frac{n_{0,b}e^2}{m_b^*}\mathbf{E} \end{aligned} \tag{C.0.1}$$

Our approach is based on calculating the fields' spatial derivatives with high accuracy using FFTs (fast Fourier transforms), while material equations are integrated using a modified, second order accurate, predictor-corrector method. Without loss of generality, we assume the incident field is TM-polarized, and decompose the electric and magnetic fields as products of generic, complex envelope functions and terms that contain free-space carrier wave-vector and angular frequency that correspond to initial conditions for a pulse located in free space approaching the structure. The preservation of all spatial and temporal derivatives accounts for dynamical changes to the instantaneous phases and amplitudes of the fields. The **E** field is polarized on the

$y-z$ plane, and the $\mathbf{H}$ field is polarized along the x direction, and may be written as follows:

$$\mathbf{E} = E_y\mathbf{j} + E_z\mathbf{k} =$$

$$(E_y^{\omega}(y,z,t)e^{i(\mathbf{k}\cdot\mathbf{r}-\omega t)} + E_y^{2\omega}(y,z,t)e^{2i(\mathbf{k}\cdot\mathbf{r}-\omega t)} + E_y^{3\omega}(y,z,t)e^{3i(\mathbf{k}\cdot\mathbf{r}-\omega t)} + c.c.)\mathbf{j} \tag{C.0.2}$$

$$+(E_z^{\omega}(y,z,t)e^{i(\mathbf{k}\cdot\mathbf{r}-\omega t)} + E_z^{2\omega}(y,z,t)e^{2i(\mathbf{k}\cdot\mathbf{r}-\omega t)} + E_z^{3\omega}(y,z,t)e^{3i(\mathbf{k}\cdot\mathbf{r}-\omega t)} + c.c.)\mathbf{k}$$

$$\mathbf{H} = H_x\mathbf{i} = (H_x^{\omega}(y,z,t)e^{i(\mathbf{k}\cdot\mathbf{r}-\omega t)} + H_x^{2\omega}(y,z,t)e^{2i(\mathbf{k}\cdot\mathbf{r}-\omega t)} + H_x^{3\omega}(y,z,t)e^{3i(\mathbf{k}\cdot\mathbf{r}-\omega t)} + c.c.)\mathbf{i} \tag{C.0.3}$$

where $k_z = |\mathbf{k}|cos\theta_i$, $k_y = -|\mathbf{k}|sin\theta_i$, $|\mathbf{k}| = \omega/c$, and θ_i is the incident angle. This choice of carrier wave vector indicates the pulse is at first traveling along the $-y+z$ direction.

Substituting Eqs. C.0.2 and C.0.3 into Eqs. C.0.1, for each harmonic component, the field, current, and polarization envelopes obey coupled equations of motion of the type:

$$\begin{aligned}
\frac{\partial H_{\hat{x}}}{\partial\tau} &= i\beta(H_{\hat{x}} + E_{\hat{z}}sin\theta_i + E_{\hat{y}}cos\theta_i) - \frac{\partial E_{\hat{z}}}{\partial\hat{y}} + \frac{\partial E_{\hat{y}}}{\partial\hat{z}},\\
\frac{\partial E_{\hat{y}}}{\partial\tau} &= i\beta(E_{\hat{y}} + H_{\hat{x}}cos\theta_i) + \frac{\partial H_{\hat{x}}}{\partial\hat{z}} - 4\pi(J_{\hat{y}} - i\beta P_{\hat{y}}),\\
\frac{\partial E_{\hat{z}}}{\partial\tau} &= i\beta(E_{\hat{z}} + H_{\hat{x}}sin\theta_i) - \frac{\partial H_{\hat{x}}}{\partial\hat{y}} - 4\pi(J_{\hat{z}} - i\beta P_{\hat{z}}),\\
\frac{\partial J_{\hat{y}}}{\partial\tau} &= (2i\beta - \tilde{\gamma})J_{\hat{y}} + (\beta^2 + i\tilde{\gamma}\beta - \beta_0^2)P_{\hat{y}} + \frac{\pi\omega_p^2}{\omega_r^2}E_{\hat{y}} + P_{\hat{y}}^{\mathrm{NL}},\\
\frac{\partial J_{\hat{z}}}{\partial\tau} &= (2i\beta - \tilde{\gamma})J_{\hat{z}} + (\beta^2 + i\tilde{\gamma}\beta - \beta_0^2)P_{\hat{z}} + \frac{\pi\omega_p^2}{\omega_r^2}E_{\hat{z}} + P_{\hat{z}}^{\mathrm{NL}},\\
\frac{\partial P_{\hat{y}}}{\partial\tau} &= J_{\hat{y}},\\
\frac{\partial P_{\hat{z}}}{\partial\tau} &= J_{\hat{z}}
\end{aligned} \tag{C.0.4}$$

where we have used the scaled coordinates $\hat{z} = \frac{z}{\lambda_r}$, $\hat{y} = \frac{y}{\lambda_r}$, and $\hat{x} = \frac{x}{\lambda_r}$, scaled frequencies $\beta = \frac{2\pi\omega}{\omega_r}$ (for the fundamental field) and $\beta_0 = \frac{2\pi\omega_0}{\omega_r}$; and damping coefficient $\tilde{\gamma} = \gamma\frac{\lambda_0}{c}$, where $\lambda_r = 1\,\mu$m is a reference wavelength such that $\omega_r = \frac{2\pi c}{\lambda_r}$, and $P_{\hat{y}}^{\mathrm{NL}}$ and $P_{\hat{z}}^{\mathrm{NL}}$ are generic, nonlinear polarization components yet to be determined. Equations C.0.4 are solved in the time domain using a modified FFT pulse propagation method, which we discuss in some detail next. The electric and magnetic field equations can be put into a Schrödinger-like form:

$$\begin{aligned}
\frac{\partial H_{\hat{x}}}{\partial\tau} &= V_{H_{\hat{x}}}H_{\hat{x}} - \frac{\partial E_{\hat{z}}}{\partial\hat{y}} + \frac{\partial E_{\hat{y}}}{\partial\hat{z}},\\
\frac{\partial E_{\hat{y}}}{\partial\tau} &= V_{E_{\hat{y}}}E_{\hat{y}} + \frac{\partial H_{\hat{x}}}{\partial\hat{z}},\\
\frac{\partial E_{\hat{z}}}{\partial\tau} &= V_{E_{\hat{z}}}E_{\hat{z}} - \frac{\partial H_{\hat{x}}}{\partial\hat{y}}
\end{aligned} \tag{C.0.5}$$

The potentials in Eqs. C.0.5 are $V_{H_{\hat{x}}} = i\beta(1 + E_{\hat{z}}sin\theta_i + E_{\hat{y}}cos\theta_i)/H_{\hat{x}}$, $V_{E_{\hat{y}}} = i\beta(1 + H_{\hat{x}}cos\theta_i - 4\pi(J_{\hat{y}} - i\beta P_{\hat{y}}))/E_{\hat{y}}$, and $V_{E_{\hat{z}}} = i\beta(1 + H_{\hat{x}}sin\theta_i - 4\pi(J_{\hat{z}} - i\beta P_{\hat{z}}))/E_{\hat{z}}$. As a result, the equations can be solved using the classic, split-step beam propagation method adapted for the time domain [115]. The split-step algorithm usually calls for separation of free-space and material equations with differential equations that are first order in time. Equations C.0.5 are already first order in time, have no approximations, and can be immediately separated into free-space and material equations and integrated in the time domain. The formal solutions of the free-space propagator may be derived from the free-space equations, obtained by setting the effective potentials equal to zero. Then, Eqs. C.0.5 are Fourier transformed in space, resulting in:

$$\begin{aligned} \frac{\partial \tilde{H}_{\hat{x}}}{\partial \tau} &= -ik_{\hat{y}}\tilde{E}_{\hat{z}} + ik_{\hat{z}}\tilde{E}_{\hat{y}}, \\ \frac{\partial \tilde{E}_{\hat{y}}}{\partial \tau} &= ik_{\hat{z}}\tilde{H}_{\hat{x}}, \\ \frac{\partial \tilde{E}_{\hat{z}}}{\partial \tau} &= -ik_{\hat{y}}\tilde{H}_{\hat{x}} \end{aligned} \tag{C.0.6}$$

Equations C.0.6 may be integrated simultaneously using a midpoint trapezoidal method, so that:

$$\begin{aligned} \tilde{H}_{\hat{x}}(\delta\tau) &= \tilde{H}_{\hat{x}}(0) - \frac{ik_{\hat{y}}\delta\tau}{2}(\tilde{E}_{\hat{z}}(0) + \tilde{E}_{\hat{z}}(\delta\tau)) + \frac{ik_{\hat{z}}\delta\tau}{2}(\tilde{E}_{\hat{y}}(0) + \tilde{E}_{\hat{y}}(\delta\tau)), \\ \tilde{E}_{\hat{y}}(\delta\tau) &= \tilde{E}_{\hat{y}}(0) + \frac{ik_{\hat{z}}\delta\tau}{2}(\tilde{H}_{\hat{x}}(0) + \tilde{H}_{\hat{x}}(\delta\tau)), \\ \tilde{E}_{\hat{z}}(\delta\tau) &= \tilde{E}_{\hat{z}}(0) - \frac{ik_{\hat{y}}\delta\tau}{2}(\tilde{H}_{\hat{x}}(0) + \tilde{H}_{\hat{x}}(\delta\tau)) \end{aligned} \tag{C.0.7}$$

Solving for $\tilde{H}_{\hat{x}}(\delta\tau)$,

$$\tilde{H}_{\hat{x}}(\delta\tau) = \tilde{H}_{\hat{x}}(0)\frac{1 - \frac{(k_{\hat{y}}^2 + k_{\hat{z}}^2)\delta\tau^2}{4}}{1 + \frac{(k_{\hat{y}}^2 + k_{\hat{z}}^2)\delta\tau^2}{4}} + \frac{(ik_{\hat{z}}\tilde{E}_{\hat{y}}(0) - ik_{\hat{y}}\tilde{E}_{\hat{y}}(0))\delta\tau}{1 + \frac{(k_{\hat{y}}^2 + k_{\hat{z}}^2)\delta\tau^2}{4}} \tag{C.0.8}$$

Equation C.0.8 is then substituted back into the second and third of Eqs. C.0.7 to extract the electric fields. All fields are then inverse Fourier transformed.

The propagation step inside the medium is performed by integrating the material equations, written in terms of generic envelope functions as:

$$\begin{aligned}
\frac{\partial H_{\hat{x}}}{\partial \tau} &= i\beta(H_{\hat{x}} + E_{\hat{z}} sin\theta_i + E_{\hat{y}} cos\theta_i), \\
\frac{\partial E_{\hat{y}}}{\partial \tau} &= i\beta(E_{\hat{y}} + H_{\hat{x}} cos\theta_i) - 4\pi(J_{\hat{y}} - i\beta P_{\hat{y}}), \\
\frac{\partial E_{\hat{z}}}{\partial \tau} &= i\beta(E_{\hat{z}} + H_{\hat{x}} sin\theta_i) - 4\pi(J_{\hat{z}} - i\beta P_{\hat{z}}), \\
\frac{\partial J_{\hat{y}}}{\partial \tau} &= (2i\beta - \tilde{\gamma})J_{\hat{y}} + (\beta^2 + i\tilde{\gamma}\beta - \beta_0^2)P_{\hat{y}} + \frac{\pi\omega_p^2}{\omega_r^2}E_{\hat{y}} E_{\hat{y}} + P_{\hat{y}}^{\mathrm{NL}}, \\
\frac{\partial J_{\hat{z}}}{\partial \tau} &= (2i\beta - \tilde{\gamma})J_{\hat{z}} + (\beta^2 + i\tilde{\gamma}\beta - \beta_0^2)P_{\hat{z}} + \frac{\pi\omega_p^2}{\omega_r^2}E_{\hat{z}} + P_{\hat{z}}^{\mathrm{NL}}, \\
\frac{\partial P_{\hat{y}}}{\partial \tau} &= J_{\hat{y}}, \\
\frac{\partial P_{\hat{z}}}{\partial \tau} &= J_{\hat{z}}
\end{aligned} \tag{C.0.9}$$

Although we have neglected magnetic currents and polarizations, which typically characterize magnetically active and negative index materials, for example, they may be reintroduced in straightforward fashion by adding magnetic sources. Then, an approach similar to the solution of Eq. C.0.6 may be employed to solve Eqs. C.0.9. For instance, one may first obtain estimates (the prediction step) of all fields, currents, and polarizations at $\tau = \delta\tau$ with an Euler method, using only their initial values at $\tau = 0$. Using these predictions, the solutions for the currents at $\tau = \delta\tau$ are immediate and second order accurate, as follows:

$$\begin{aligned}
J_{\hat{y},\hat{z}}(\delta\tau) &= J_{\hat{y},\hat{z}}(0)\frac{1 + (2i\beta - \tilde{\gamma})\frac{\delta\tau}{2} + (\beta^2 + i\tilde{\gamma}\beta - \beta_0^2)\frac{\delta\tau^2}{4}}{1 - (2i\beta - \tilde{\gamma})\frac{\delta\tau}{2} - (\beta^2 + i\tilde{\gamma}\beta - \beta_0^2)\frac{\delta\tau^2}{4}} \\
&+ \frac{(\beta^2 + i\tilde{\gamma}\beta - \beta_0^2)P_{\hat{y},\hat{z}}(0)\delta\tau + \pi\frac{\omega_p^2}{\omega_r^2}(E_{\hat{y},\hat{z}}(0) + E_{P,\hat{y},\hat{z}}(\delta\tau))\frac{\delta\tau}{2} + (P_{\hat{y},\hat{z}}^{\mathrm{NL}} + P_{P,\hat{y},\hat{z}}^{\mathrm{NL}}(\delta\tau))\frac{\delta\tau}{2}}{1 - (2i\beta - \tilde{\gamma})\frac{\delta\tau}{2} - (\beta^2 + i\tilde{\gamma}\beta - \beta_0^2)\frac{\delta\tau^2}{4}}
\end{aligned} \tag{C.0.10}$$

$E_{P,\hat{y},\hat{z}}(\delta\tau)$ and $P_{P,\hat{y},\hat{z}}^{\mathrm{NL}}(\delta\tau)$ are first order accurate, predicted estimates of the fields and nonlinear polarizations at time $\tau = \delta\tau$. Once the currents are known, the polarizations may be found using the usual, second order accurate trapezaidal rule:

$$P_{\hat{y},\hat{z}}(\delta\tau) = P_{\hat{y},\hat{z}}(0) + (J_{\hat{y},\hat{z}}(\delta\tau) + J_{\hat{y},\hat{z}}(0))\frac{\delta\tau}{2} \tag{C.0.11}$$

In turn, knowledge of more accurate currents and polarizations at time $\delta\tau$ allows second order accurate estimates of all electric and magnetic fields. The process is then repeated several times, although one or two cycles usually suffice for the results to converge.

The energy refraction angle (i.e., the direction of energy flow) may be calculated by monitoring the normalized, transverse, and longitudinal electromagnetic momenta inside the medium as functions of time:

$$\begin{aligned} M_{\hat{y}}(\tau) &= \frac{1}{c^2}\int_{\hat{z}=0}^{\hat{z}=\infty}\int_{\hat{y}=-\infty}^{\hat{y}=\infty} S_{\hat{y}}(\hat{y},\hat{z},\tau)d\hat{y}d\hat{z} \\ M_{\hat{z}}(\tau) &= \frac{1}{c^2}\int_{\hat{z}=0}^{\hat{z}=\infty}\int_{\hat{y}=-\infty}^{\hat{y}=\infty} S_{\hat{z}}(\hat{y},\hat{z},\tau)d\hat{y}d\hat{z} \end{aligned} \tag{C.0.12}$$

where $S_{\hat{y}}$ and $S_{\hat{z}}$ are the components of the Poynting vector. The energy refraction angle may be calculated as $\theta_{ref} = \tan^{-1}(M_{\hat{y}}/M_{\hat{z}})$.

In order to solve the full nonlinear problem, the linear data may be reproduced dynamically in a numerical integration scheme by solving a set of coupled equations that contains: (1) an equation that described the polarization of free electrons, $\mathbf{P}_f$, and (2) a set of equations that account for the bound electron polarizations $\mathbf{P}_{bj}$. The linear equations are then modified to include nonlinear contributions in the high intensity regime, as shown in Eqs. 1.5.24 and 1.5.13.